Search for Supersymmetry in Final States Containing two Hadronically Decaying Taus with the ATLAS Detector at $\sqrt{s} = 8$ and 13 TeV

Dissertation der Fakultät für Physik
der
Ludwig-Maximilians-Universität München

vorgelegt von
Christopher Bock
geboren in Flensburg

München, September 2016

Erstgutachter: Prof. Dr. Dorothee Schaile
Zweitgutachter: Prof. Dr. Martin Faessler

Tag der mündlichen Prüfung: 9. November 2016
Tag der Abgabe: 19. September 2016

My colleagues in elementary particle theory in many lands [and I] are driven by the usual insatiable curiosity of the scientist, and our work is a delightful game. I am frequently astonished that it so often results in correct predictions of experimental results. How can it be that writing down a few simple and elegant formulae, like short poems governed by strict rules such as those of the sonnet or the waka, can predict universal regularities of Nature?

Murray Gell-Mann

Zusammenfassung

In dieser Arbeit werden zwei Analysen vorgestellt die sich mit der Suche nach supersymmetrischen Teilchen in Proton-Proton Kollisionen auseinander setzen. Im Endzustand werden in beiden Analysen mindestens zwei hadronisch zerfallende Taus, sowie fehlende transversale Energie erwartet. Die genutzten Daten wurden mit dem ATLAS Detektor am LHC aufgenommen. Zwei Datensätze werden analysiert, der eine wurde bei einer Schwerpunktsenergie von 8 TeV im Jahr 2012 aufgezeichnet, der andere bei einer Schwerpunktsenergie von 13 TeV im Jahr 2015.

Die erste Analyse nutzt den bei einer Schwerpunktsenergie von 8 TeV aufgezeichneten Datensatz. Er umfasst Daten entsprechend einer integrierten Luminosität von 20.3 fb^{-1}. Gesucht wird nach supersymmetrischen Teilchen die über die elektroschwache Wechselwirkung produziert werden und anschließend in Endzustände mit mindestens zwei hadronisch zerfallenden Taus, fehlender transversaler Energie und wenig bis garkeine Jets zerfallen. Spezielles Augenmerk wird auf die Validierung des Di-Boson Untergrunds, die Kombination des Kanals in dem beide Taus hadronisch zerfallen mit dem in dem eines leptonisch zerfällt, sowie auf eine Abschätzung der Sensitivität der Analyse bei einer Schwerpunktsenergie von 13 TeV gelegt. Da, verglichen mit der Erwartung aus Abschätzungen aus dem Standard Modell, kein Überschuss an Ereignissen gefunden wurde, werden mithilfe der CL_s-Methode neue Grenzen auf den untersuchten Prozess gesetzt. Modellunabhängig kann ein sichtbarer Wirkungsquerschnitt größer als 0.37 fb ausgeschlossen werden. Modellabhängige Ausschlussgrenzen werden für drei Szenarien des phänomenologisch motivierten minimalen supersymmetrischen Standardmodells (pMSSM), sowie zwei vereinfachte Modelle berechnet. In einem der vereinfachten Modelle werden Charginos in Paaren produziert und zerfallen über Staus oder Tau-Sneutrinos in Neutrinos, Taus und das leichteste Neutralino. Im anderen vereinfachten Modell wird ein Chargino zusammen mit dem nächstleichtesten Neutralino produziert und zerfällt, genau wie im anderen vereinfachten Modell, über Staus oder Tau-Sneutrinos in Neutrinos, Taus und das leichteste Neutralino. Eines der untersuchten pMSSM Szenarien ist so gewählt, dass vorwiegend Paare von Staus produziert werden die wiederum in Taus zerfallen. Die anderen beiden pMSSM Szenarien sind so ausgewählt, dass vorwiegend die drei zuvor genannten Prozesse miteinander konkurrieren, die Paarproduktion von Charginos, die assoziierte Produktion eines Charginos mit einem nächstleichtesten Neutralino, sowie die Paarproduktion von Staus. In einem der Modelle ist die Masse des Staus fix, im anderen wird sie auf die Hälfte der Summe der Massen des leichtesten Neutralinos und des leichtesten Charginos gesetzt. Betrachtet man die beiden Produktionskanäle der vereinfachten Modelle gemeinsam, so kann man $\tilde{\chi}_1^{\pm}/\tilde{\chi}_1^0$ Massen bis zu

410/140 GeV ausschliessen. Betrachtet man nur die Paarproduktion von Charginos, so kann man $\tilde{\chi}_1^{\pm}/\tilde{\chi}_1^0$ Massen bis zu 345/90 GeV ausschliessen. Im Fall des pMSSM Modells in dem vorwiegend Paare von Staus produziert werden ist die vorgestellte Analyse auf große Teile des Phasenraumes noch nicht sensitiv, da der Wirkungsquerschnitt fü r die Paarproduktion von Staus zu klein ist. In den verbleibenden beiden pMSSM Modellen können vergleichbare Ausschlussgrenzen auf die Masse des leichtesten Charginos gesetzt werden: ein Bereich von 100 GeV bis 350 GeV kann ausgeschlossen werden.
Die zweite Analyse verwendet den bei einer Schwerpunktsenergie von 13 TeV im Jahr 2015 aufgezeichneten Datensatz. Er umfasst Daten entsprechend einer integrierten Luminosität von 3.2 fb^{-1}. Es wird nach supersymmetrischen Teilchen gesucht, die über die starke Wechselwirkung produziert werden und in Endzustände zerfallen die sich durch mindestens zwei hadronisch zerfallende Taus, fehlende transversale Energie und, im Gegensatz zur ersten Analyse, Jets auszeichnen. Der Schwerpunkt der Analyse liegt dabei auf der Entwicklung einer Signalregion die speziell auf komprimierte Massenspektren sensitiv ist, sowie der Abschätzung des Untergrunds aus Multi-Jet Ereignissen. Verglichen mit einer Abschätzung aus dem Standard Modell konnte kein Überschuss an Ereignissen festgestellt werden. Deswegen werden Ausschlussgrenzen auf den untersuchten Prozess mithilfe der CL_s-Methode berechnet. Modellunabhängig kann ein Wirkungsquerschnitt von 1.07 fb ausgeschlossen werden. Modellabhängige Ausschlussgrenzen werden für ein vereinfachtes Modell, sowie ein gauge-mediated-symmetry-breaking, GMSB, Modell berechnet. Im vereinfachten Modell werden Gluinos in Paaren produziert und zerfallen danach asymmetrisch über ein leichtestes Chargino und ein nächstleichtestes Neutralino. Diese zerfallen wiederum über Staus und ihre Sneutrinos in Endzustände die Neutralinos, Jets, Taus und Netrinos enthalten. Im GMSB Modell werden außerdem Squarks in Paaren produziert und zerfallen via Neutralinos und Staus oder Sleptonen in Endzustände die sich durch Quarks und bis zu vier Taus auszeichnen. Weitere Prozesse sind im GMSB Modell möglich, aber der Wirkungsquerschnitt ist für diese vernachlässigbar. Gluino Massen bis zu 1550 GeV können im vereinfachten Modell ausgeschlossen werden, während Massen des leichtesten Neutralinos bis zu 750 GeV ausgeschlossen werden können. Für das GMSB Modell können sogar Gluino Massen bis 2.2 TeV ausgeschlossen werden für große Werte von $\tan\beta$, während für kleinere Werte immerhin noch Gluino Massen bis 2.0 TeV ausgeschlossen werden können.

Abstract

Two analyses will be presented searching for the production of supersymmetric particles decaying into final states containing at least two hadronically decaying taus and missing transverse energy in proton-proton collisions. The collisions were recorded by the ATLAS experiment at the LHC. Two different datasets are analyzed, one recorded at a center-of-mass energy of 8 TeV in 2012 and one recorded at a center-of-mass energy of 13 TeV in 2015.

The first analysis is performed using data collected at a center-of-mass energy of 8 TeV, corresponding to an integrated luminosity of 20.3 fb^{-1}. The electroweak production of supersymmetric particles which decay into final states containing at least two hadronically decaying taus, missing transverse energy, as well as few to no jets, is studied. Particular attention is paid to the validation of the diboson background, the combination with the channel where one of the two taus decays hadronically and the other one leptonically, as well as the estimate of the sensitivity of the analysis at $\sqrt{s} = 13$ TeV. No excess over the Standard Model expectation is found, thus limits are set using the CL$_s$ method. Model independent limits on the cross section are computed, the observed upper limit on the visible cross section is 0.37 fb. Model dependent limits are computed for three different pMSSM scenarios as well as two simplified models. One of the simplified models is characterized by chargino pair production, decaying via intermediate staus or tau sneutrinos into neutrinos, taus and the lightest neutralino. The other simplified model is characterized by the associated production of a lightest chargino and a next-to-lightest neutralino, also decaying via intermediate staus into taus, neutrinos and the lightest neutralino. The parameters of one of the pMSSM models are chosen such that the dominant process is the direct pair production of staus decaying into taus. The parameters of the other two pMSSM models are chosen such that the three processes compete. For one of the pMSSM models the stau mass is chosen to be fixed, while for the other it is chosen to be halfway between the $\tilde{\chi}_1^{\pm}$ and $\tilde{\chi}_1^0$ mass. In the case of simultaneous $\tilde{\chi}_1^{\pm}\tilde{\chi}_1^{\mp}$ and $\tilde{\chi}_1^{\pm}\tilde{\chi}_2^0$ production, $\tilde{\chi}_1^{\pm}/\tilde{\chi}_1^0$ masses of up to 410/140 GeV and in the case of $\tilde{\chi}_1^{\pm}$ pair production alone, $\tilde{\chi}_1^{\pm}/\tilde{\chi}_1^0$ masses of up to 345/90 GeV can be excluded. The presented analysis is not yet sensitive to large parts of the phase-space of the pMSSM model targeting direct-stau pair production, because the cross section is too small. In the other two pMSSM parameter planes, similar lightest chargino mass ranges can be excluded, namely approximately 100 GeV $-$ 350 GeV.

The second analysis makes uses of data collected throughout 2015 at a center-of-mass energy of 13 TeV, corresponding to an integrated luminosity of 3.2 fb^{-1}. The strong

production of supersymmetric particles is studied which decay into final states containing at least two hadronically decaying taus, missing transverse energy, as well as jets. The focus of the analysis is on the development of the signal region targeting low mass-splittings and the estimate of the multi-jet contribution to the signal, as well as control regions. Again, no excess over the Standard Model expectation is found and thus limits are set using the CL_s method. The obtained model independent observed upper limit on the visible cross section, $\langle\sigma_{\text{vis}}\rangle^{95}_{\text{obs}}$, is 1.07 fb. Model dependent limits are interpreted in two models: a simplified model of gluino pair production, subsequently decaying asymmetrically via a lightest chargino and a next-to-lightest neutralino which decay via staus or tau sneutrinos into final states containing lightest neutralinos, jets, taus as well as tau neutrinos; and a gauge-mediated-symmetry-breaking, GMSB, model where, in addition to the previous process, squarks are produced in pairs and decay via intermediate neutralinos and staus/sleptons into a pair of quarks and up to four taus. Other processes are possible as well in the GMSB modell, but they are sub-dominant for most of the studied phase-space. In the first model gluino masses up to 1550 GeV can be excluded while masses of the lightest neutralino up to 750 GeV can be excluded. In case of the GMSB model gluino masses up to 2.2 TeV can be excluded for large values of $\tan\beta$, while for lower values only gluino masses up to 2.0 TeV can be excluded.

Contents

1. Introduction **1**

2. Theoretical Foundation **3**
2.1. The Standard Model of Particle Physics . . . 3
2.1.1. Particle Content of the Standard Model of Particle Physics . . . 7
2.1.2. Successes of the Standard Model . . . 9
2.2. Problems of the Standard Model of Particle Physics . . . 11
2.2.1. Gravity . . . 11
2.2.2. Unification of Forces . . . 12
2.2.3. Dark Matter . . . 12
2.2.4. Neutrino Masses . . . 16
2.2.5. Matter-Antimatter-Asymmetry . . . 17
2.2.6. Higgs Mass and Naturalness . . . 18
2.3. Supersymmetry . . . 18

3. Statistical Interpretation **24**

4. The LHC and ATLAS **28**
4.1. The Large Hadron Collider . . . 28
4.2. The ATLAS detector . . . 31
4.2.1. Inner Detector . . . 32
4.2.2. Calorimeters . . . 34
4.2.3. Muon Spectrometer . . . 36
4.2.4. Magnets . . . 36
4.2.5. Forward Detectors . . . 38
4.2.6. Trigger and Data Acquisition . . . 38
4.3. Computing and the Grid . . . 39

5. Dataset **40**
5.1. Simulation of Datasets . . . 40
5.1.1. Calorimeter Simulation . . . 41
5.1.2. Performance of Substructure Observables in Fast Simulation . . . 41
5.2. Data Taken Using ATLAS . . . 42

6. Object Definitions and Discriminating Variables **45**
6.1. Primary Vertex and Pile-up . . . 45
6.2. Electrons . . . 46
6.3. Muons . . . 47

6.4. Taus . . . 49
6.5. Jets . . . 51
6.6. Missing Transverse Energy . . . 54
6.7. Overlap Removal Procedure . . . 54
6.8. Event Cleaning Procedure . . . 54
6.9. Discriminating Variables . . . 56

7. Searching for Electroweak Production of Supersymmetric Particles at $\sqrt{s} = 8$ TeV 58
7.1. Targeted Signal Processes and Models . . . 58
7.2. Event Selection . . . 61
7.3. Background Estimate . . . 63
7.3.1. Multi-jet Estimate . . . 64
7.3.2. W+Jets Estimate . . . 65
7.3.3. The Diboson Background . . . 67
7.3.4. Remaining Backgrounds . . . 74
7.3.5. Fitting Procedure . . . 76
7.4. Uncertainties . . . 76
7.5. Results . . . 79
7.6. Interpretation . . . 80
7.6.1. Simplified Models . . . 82
7.6.2. Direct-Stau Production . . . 82
7.6.3. pMSSM . . . 84
7.7. Tau + Light Lepton Channels . . . 86
7.7.1. Motivation . . . 87
7.7.2. Expected Significance Using Di-Tau SR . . . 90
7.7.3. Cut and Count Based Optimization . . . 91
7.7.4. Improvement When Combining all Three Channels . . . 97
7.8. Estimating the Sensitivity at $\sqrt{s} = 13$ TeV . . . 97
7.9. Summary . . . 101

8. ATLAS Results on the Search for Supersymmetry After Run I and the pMSSM Summary Paper 104
8.1. Idea of the Analysis . . . 104
8.2. Results . . . 106

9. Searching for Strong Production of Supersymmetric Particles at $\sqrt{s} = 13$ TeV108
9.1. Targeted Signal Processes and Models . . . 108
9.2. Event Selection . . . 110
9.3. Background Estimate . . . 115
9.3.1. Vector-Boson and Top-Quark Backgrounds . . . 115
9.3.2. Multi-jet Estimate . . . 118
9.3.3. Fitting Procedure . . . 127
9.4. Uncertainties . . . 127

9.5. Results . . . 128
9.6. Interpretation . . . 129
9.7. Summary . . . 130

10. Conclusions and Summary **133**

A. Appendix **138**
A.1. Datasets Used . . . 138
A.1.1. Run I Analysis . . . 138
A.1.2. Run II Analysis . . . 139
A.2. Tau + Light Lepton Channels . . . 140
A.2.1. Signal-over-Background-Ratios . . . 140
A.2.2. Combination of all Three Channels . . . 143
A.2.3. The Choice of the Transverse Mass Variable . . . 143
A.2.4. Further Optimizations Investigated . . . 143
A.3. Estimating the Sensitivity at $\sqrt{s} = 13$ TeV . . . 149
A.4. The Search for Strongly Produced Taus . . . 150
A.4.1. QCD Estimate . . . 150
A.4.2. Comparison Between Jet-Fake and OS-SS Methods . . . 158

1. Introduction

The Standard Model of particle physics, developed throughout the second half of the 20th century, is one of the most successful theories to date. It describes an overwhelming lot of experimental results correctly, like e.g. the baryonic particle zoo, but also predicted several particles which have been discovered years later: the W and Z bosons, the top quark, the τ neutrino, as well as the Higgs boson. In addition, predictions of observables made by the Standard Model were found to match with experimental results with an unprecedented precision at the Large Electron Positron Collider and many other experiments, building strong confidence in the Standard Model of particle physics.
However despite its successes, the Standard Model also has a few shortcomings. For instance the Standard Model neither provides a viable candidate to explain the observed Dark Matter nor the observed Dark Energy in the universe. In its current form the Standard Model also cannot explain why neutrinos are massive, they are predicted to be massless, while neutrino oscillations indicate that neutrinos are massive. Another, arguably more cosmetic, issue with the Standard Model is that it requires an unnaturally precise fine-tuning of parameters, meaning that slight deviations from the fine-tuned values of the Standard Model parameters render the Standard Model unstable and not viable anymore.
As a result, the common belief nowadays is that there must be an extension of the Standard Model which includes the Standard Model. The most prominent example being the Supersymmetric Standard Model, which introduces in addition to the symmetries already present in the Standard Model a symmetry between fermions and bosons, doubling the number of degrees of freedom in the model. Since supersymmetric particles have not been observed yet, supersymmetry must be broken and thus supersymmetric particles must be heavier than Standard Model particles. If, however, the lightest supersymmetric particle is neutral and stable it becomes a perfect candidate for cold Dark Matter.
This thesis focuses on the search for supersymmetry with two hadronically decaying taus and large missing transverse energy in the final state. The analysis will use 20.3 fb^{-1} of data taken with the ATLAS detector throughout 2012 at $\sqrt{s} = 8$ TeV[1] and 3.2 fb^{-1} of data recorded throughout 2015 at $\sqrt{s} = 13$ TeV. The 2012 dataset will be used in an analysis searching for the production of supersymmetric particles via the electroweak interaction, while the 2015 dataset will be used to search for the production of supersymmetric particles via the strong interaction, consequently the first analysis vetoes jets, while the second requires jets.

[1] Throughout this thesis natural units will be used such that $c = \hbar = 1$ and in formulas Einstein's sum convention will be used.

The outline of this thesis is as follows: chapter 2 will briefly introduce the theoretical framework, while chapter 3 describes the basics of the statistical concepts used later in this work to interpret the results. Subsequent Chapter 4 describes the LHC and the ATLAS experiment whose data is to be used throughout this thesis. Throughout chapter 5 the simulation of datasets will be briefly summarized. In chapter 6 physical objects and observables used throughout the following chapters will be defined. Chapter 7 details the search for electroweak production of supersymmetric particles, at a center of mass energy of $\sqrt{s} = 8$ TeV, with two hadronically decaying taus and large missing transverse energy in the final state, followed by chapter 8, summarizing results from the ATLAS collaboration's search for supersymmetry in Run I. Subsequently chapter 9 shifts the focus towards Run II of the LHC. The data taken throughout 2015 at $\sqrt{s} = 13$ TeV will be analyzed, looking for the production of supersymmetric particles via the strong interaction. Chapter 10 will conclude and summarize this thesis.

2. Theoretical Foundation

In the following the current state of the Standard Model shall be summarized based on [1, 2]. Emphasis will be put on the successes as well as the shortcomings of the Standard Model of particle physics as well as how an supersymmetric extension of the Standard Model can solve these.

2.1. The Standard Model of Particle Physics

The Standard Model of particle physics is arguably one of the most successful physics theories to date. Nearly all experimental results in the field of particle physics obtained in laboratory experiments can be accurately described by the Standard Model. It has been developed throughout the second half of the 20th century. The two most important developments in its history, from a theory point of view, were the unification of the electromagnetic and the weak force in 1968 and the inclusion of the strong force into the theory in 1973 which lead to its current formulation.

The Standard Model is a *renormalizeable quantum field theory* and describes the constituents of known ordinary matter and their interactions, consequently the Standard Model is also a gauge theory. It can be written down in terms of an *action* $\mathcal{S}$ which is the time and space integral over the Lagrange density $\mathcal{L}$. According to the *Hamilton principle*, the action $\mathcal{S}$ should be minimized. This leads to the *Euler-Lagrange* equations which describe the dynamics of the system:

$$\frac{\partial}{\partial x_\mu}\left(\frac{\partial \mathcal{L}}{\partial\left(\partial\Phi/\partial x_\mu\right)}\right) - \frac{\partial \mathcal{L}}{\partial \Phi} = 0, \tag{2.1}$$

where Φ describes the considered field while x_μ denotes the space-time four vector.

A priory there is no reason to exclude any term from the Lagrange density, so every term one can think of is allowed in the Lagrangian unless disproven by the experiment. Consequently the exact form of a Lagrangian density describing a physical system has to be determined experimentally. In the case of elementary particle physics it has been

found that the Lagrange density has a $SU(3)_{QCD} \otimes SU(2)_L \otimes U(1)_Y$ symmetry[1].
The most general form of the Standard Model Lagrangian obeying this symmetry looks as follows:

$$\mathcal{L} = \mathcal{L}_{EW} + \mathcal{L}_{QCD}, \tag{2.2}$$

$$\mathcal{L}_{EW} = \sum_k \bar{\psi}_k^L i\gamma_\mu D_{EW}^{\mu,L} \psi_k^L + \sum_k \bar{\psi}_k^R i\gamma_\mu D_{EW}^{\mu,R} \psi_k^R - \tfrac{1}{4} B_{\mu\nu} B^{\mu\nu} - \tfrac{1}{4} \vec{W}_{\mu\nu} \vec{W}^{\mu\nu}, \tag{2.3}$$

$$\mathcal{L}_{QCD} = \bar{\psi} \left(i\gamma_\mu D_{QCD}^{\mu} - m \right) \psi - \tfrac{1}{4} \vec{G}_{\mu\nu} \vec{G}^{\mu\nu}, \tag{2.4}$$

where the sum in the electroweak Lagrangian extends over all leptons and quarks. The covariant derivatives are:

$$D_{EW}^{\mu,L} = \partial^\mu + ig \tfrac{\vec{\tau}}{2} \vec{W}^\mu + ig' \tfrac{Y}{2} B^\mu, \tag{2.5}$$

$$D_{EW}^{\mu,R} = \partial^\mu + ig' \tfrac{Y}{2} B^\mu, \tag{2.6}$$

$$D_{QCD}^{\mu} = \partial^\mu + ig_s \tfrac{1}{2} \vec{\lambda} \vec{G}^\mu, \tag{2.7}$$

with g, g' and g_s being the coupling strengths of the weak, the electromagnetic and the strong interaction respectively, $\vec{\tau}$ denotes the Pauli matrices and the hypercharge is denoted by Y. The field strength tensors are given by:

$$B^{\mu\nu} = \partial^\mu B^\nu - \partial^\nu B^\mu, \tag{2.8}$$

$$\vec{W}^{\mu\nu} = \partial^\mu \vec{W}^\nu - \partial^\nu \vec{W}^\mu - g \vec{W}^\mu \times \vec{W}^\nu, \tag{2.9}$$

$$\vec{G}^{\mu\nu} = \partial^\mu \vec{G}^\nu - \partial^\nu \vec{G}^\mu - g_s \vec{G}^\mu \times \vec{G}^\nu, \tag{2.10}$$

where the possibility to unify the weak and the electromagnetic interaction, as Salam, Glashow and Weinberg showed, has already been exploited to yield the electroweak Lagrangian $\mathcal{L}_{EW}$. Their combined symmetry group is the $SU(2)_L \otimes U(1)_Y$ group.
According to Noether's theorem, symmetries give rise to conserved charges. If the symmetry is in addition a local one, spin-1 gauge bosons emerge. The gauge bosons are the mediators of the corresponding interactions: electromagnetic interactions are mediated by the massless photon γ, weak interactions are mediated by the $W^\pm$ and Z bosons, while the strong interaction is mediated by the massless gluons g. The $W^\pm$ and Z bosons

[1] It can actually be mathematically shown that the simple assumption of two entirely distinct gauge groups $SU(2)_L$ and $U(1)_{QED}$ does not work, $U(1)_{QED}$ being the symmetry group associated to the electrical charge Q. If two groups are distinct from each other their generators commute. By applying an infinitesimal $U(1)_{QED}$ rotation followed by an infinitesimal $SU(2)_L$ rotation onto e.g. the lightest left-chiral lepton doublet $\left(1 - \frac{i}{2}\vec{\alpha}\vec{\tau}\right)(1 - iQ\beta))\,(\nu; e)_L = \left(1 - \frac{i}{2}\vec{\alpha}\vec{\tau}\right)\left(1 - \frac{i}{2}\beta\,(q_\nu + q_e) - \frac{i}{2}\,(q_\nu - q_e)\,\tau^3\right)(\nu; e)_L$, it can be inferred that the generators of both groups only commute if $q_e = q_\nu$, because the Pauli matrices do not commute. This is not the case, proving that the simple $SU(2)_L \otimes U(1)_{QED}$ symmetry is not realized in nature, instead the electroweak $SU(2)_L \otimes U(1)_Y$ symmetry with respect to the hypercharge Y is realized.

and the photon are results of the mixing of the electroweak $SU(2)_L \otimes U(1)_Y$ group generators, the W^1, W^2, W^3 and B fields which are massless (more details on how they mix and obtain their mass will be discussed later in this section). Each boson couples to the charge associated with its symmetry group, which is: the hypercharge Y in case of the B field, the weak isospin I_3 in terms of the weakly interacting fields $\vec{W}$ and the color charge in case of the strong interaction. This in turn also implies that the bosons might couple amongst each other as long as they carry the corresponding charge, the photon (a mixture of W^3 and B) might for example interact with the $W^\pm$ (a mixture of W^1 and W^2).
Subsequent experiments revealed that the weak interaction violates parity maximally. Only left-chiral fermions take part in the weak interaction, while right-chiral fermions do not interact weakly. Consequently left-chiral fermions have a non zero weak isospin component, while the weak isospin vanishes in case of right-chiral particles, because the weak interaction couples to the weak isospin. Chirality is a fundamental property of a particle. It determines how the wave function of a particle transforms when being rotated. In the case of massless particles this is identical to the handedness of the particle which is the projection of the spin onto the direction of motion of the particle.
If the electroweak $SU(2)_L \otimes U(1)_Y$ symmetry weren't broken, the electroweak bosons would all be massless. Nature however decided differently, the observed weakly interacting bosons, the $W^\pm$ and Z bosons are massive. Consequently the $SU(2)_L \otimes U(1)_Y$ symmetry of the electroweak interaction cannot be exact, but instead is broken. As a result, the physically observed electroweak bosons are a mixture of the electroweak $\vec{W}$ and B fields[2]. The mixing is characterized by the Weinberg angle θ_W, a parameter of the theory which can only be measured, not predicted. Breaking of the $SU(2)_L \otimes U(1)_Y$ symmetry is introduced into the model by the Higgs mechanism, which introduces an additional complex scalar field ϕ into the theory as follows:

$$\mathcal{L}_{Higgs} = \left|D_H^\mu \phi\right|^2 - V(\phi) - \textstyle\sum_j c_j \bar{q}_{j,L} \phi q_{j,R} - \sum_k f_k \bar{\psi}_{k,L} \phi \psi_{k,R} + h.c., \tag{2.11}$$

$$D_H^\mu = \partial^\mu + ig\frac{\vec{\tau}}{2}\vec{W}^\mu + ig'\frac{Y}{2}B^\mu, \tag{2.12}$$

where the last two terms, including their hermitian conjugate, give quarks and charged leptons their mass by coupling them to the Higgs boson[3], while the first term gives mass to the weak gauge bosons by also coupling them to the Higgs boson. The symmetry

[2] This can be shown by measuring the so-called left-right asymmetry $A_{LR} = \frac{\sigma_L - \sigma_R}{\sigma_L + \sigma_R}$, σ_L being the production cross section of left-chiral fermion pairs in the final state, in $f^+f^- \to f'^+f'^-$ events when using a polarized $f^\pm$ beam at $E_{cm}^2 = M_Z^2$. If the W^3 and Z bosons coincide, this A_{LR} should become one. Measuring it at the SLAC using a polarized $e^\pm$ beam, it however turned out to be far from one. Consequently the Z boson is a mixture of the neutral W^3 and B fields.

[3] It is important to stress again, that this does not include neutrinos. Neutrinos are strictly massless in the Standard Model, because a coupling to the Higgs field would require right-handed neutrinos to exist. Their existence however could neither be proven nor falsified to date since neutrinos only interact via the weak interaction and therefore only left-handed neutrinos can be detected. If right-handed neutrinos exist, neutrino masses can be explained by a coupling to the Higgs. If not, another mechanism will be needed to generate neutrino masses.

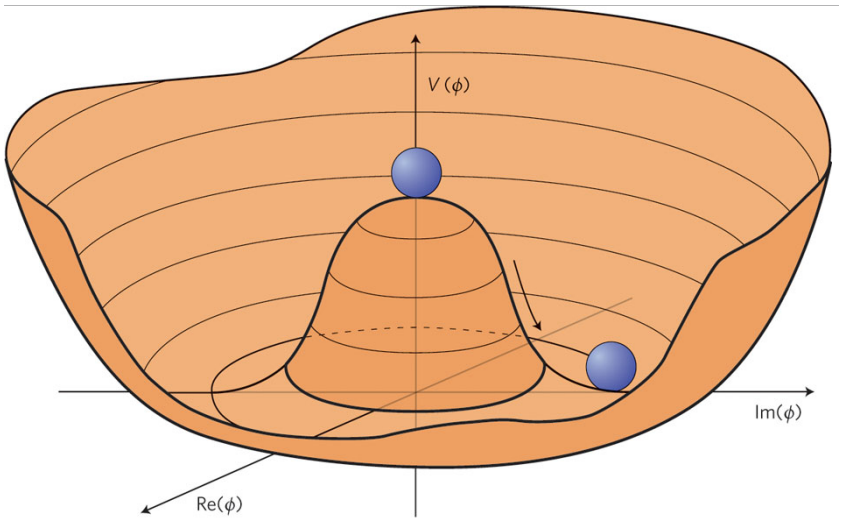

Figure 2.1.: Illustration of the Mexican-hat shaped Higgs-potential $V(\phi) = -\mu^2\phi^\dagger\phi + \frac{\lambda}{2}\left(\phi^\dagger\phi\right)^2$, with $\lambda > 0$ and $\mu^2 < 0$. The blue spheres indicate the state of the system at the point of spontaneous symmetry breaking and in the ground-state ϕ_0. Figure from [3].

breaking is introduced by the Higgs potential which is given by:

$$V(\phi) = -\mu^2\phi^\dagger\phi + \frac{\lambda}{2}\left(\phi^\dagger\phi\right)^2, \tag{2.13}$$

with λ and μ being a priori two free parameters. The Higgs potential is Mexican-hat shaped if the parameters are chosen to be $\lambda > 0$ and $\mu^2 > 0$, which is illustrated in Figure 2.1. This shape of the potential results in a non vanishing vacuum expectation value of the newly introduced scalar field

$$|\phi_0| = \frac{1}{\sqrt{2}}\sqrt{\phi_1^2 + \phi_2^2} = \frac{v}{2}, v = \sqrt{\frac{\mu^2}{\lambda}} \tag{2.14}$$

where ϕ_0 denotes the ground state of the field while ϕ_1 and ϕ_2 denote the real and imaginary part of the Higgs field. Thus rendering the Higgs also massive. As a result, the full symmetry of the potential can be explored at high energies, while at low energies the symmetry of the potential is broken. This phenomenon, the symmetry of lower energetic states being less than the symmetry of the physical system is called *spontaneous symmetry breaking*.

Expanding the complex Higgs field around its vacuum expectation value and neglecting higher order terms, the following electroweak fields are obtained:

$$W_\mu^\pm = \frac{1}{\sqrt{2}}\left(W_\mu^1 \mp iW_\mu^2\right), \tag{2.15}$$

$$A_\mu = W_\mu^3 \sin(\theta_W) + B_\mu \cos(\theta_W), \tag{2.16}$$

$$Z_\mu = W_\mu^3 \cos(\theta_W) - B_\mu \sin(\theta_W). \tag{2.17}$$

The mixing of the electromagnetic and the weak interaction is characterized by the Weinberg angle $\theta_W = \tan^{-1}(\frac{g}{g'})$. The masses of the W-boson, Z-boson and photon, A, are: $m_W = \frac{gv}{2}$, $m_Z = \sqrt{g^2 + g'^2}\,\frac{v}{2}$ and $m_A = 0$, with two parameters which have to be measured: θ_W and $e = g\,\sin(\theta_W)$, completing the Standard Model of particle physics.

2.1.1. Particle Content of the Standard Model of Particle Physics

Basically the particles of the Standard Model can be split into two categories according to their spin and consequently to which statistics they obey: *fermions*, carrying half-integer spin, obeying to the *Fermi-Dirac* statistics and *bosons* which obey to the *Bose-Einstein* statistics and carry integer spin. Phrased differently, particles can be grouped into two categories, the first one being the particles which mediate interactions, the *bosons*, and the second one being the other particles which matter is made of, the *fermions*.

Bosons *Bosons* are the "force carriers" of the interactions. They arise in the theory by requiring local gauge invariance. The only exception from this is the Higgs boson which had to be added to the Standard Model to break the $SU(2)_L \otimes U(1)_Y$ symmetry and consequently render the weak bosons and also all charged leptons massive. A summary of the interactions described by the Standard Model of particle physics can be found in Table 2.1.

Table 2.1.: Summary of the interactions described by the Standard Model.

Interaction	Mediator	Coupling to	Mass [GeV]	Relative strength
Strong	8 g(luons)	Color charge	0	1
Electromagnetic	photon (γ)	Electromagnetic	0	10^{-3}
Weak	$W^\pm, Z$ bosons	Weak charge	$80.4, 91.2$	10^{-14}

The weakest of the interactions described by the Standard Model is the *weak interaction*. It is mediated by the massive $W^\pm$ and Z bosons. They obtain their mass via breaking of the $SU(2)_L \otimes U(1)_Y$ symmetry by introducing the complex scalar Higgs field. Since their mass is rather high, their lifetime is rather short and consequently the range of the weak interaction is only about a few atto-meters. Weak bosons also carry weak charge and consequently they are self-interacting. On top of that, the electromagnetically charged $W^\pm$ bosons can also interact with the photon, γ. The photon is the mediator of the *electromagnetic interaction*. Considering its strength it is the "medium" interaction of the three interactions described by the Standard Model. It couples to the electromagnetic

charge and is massless, however it does not carry electric charge. As a result the range of the electromagnetic interaction is infinite, opposed to the *strong interaction* which is, limited in range to a few femto-meters, the size of a nucleus. Strong interactions are mediated by the colored gluons, g. Being color charged, they also self-interact as do the weak bosons. However, opposed to the electromagnetic and the weak interaction the strength of the strong interaction increases with increasing distance, causing the aforementioned limited range of the strong interaction. Therefore colored particles can usually be only observed in bound, color-neutral, states. This effect is called *confinement*.

Fermions Half-integer spin particles are called *fermions*. Simply speaking, fermions are the fundamental building blocks of ordinary matter. They appear in three different families, having the same properties, but different mass. The families are ordered by ascending mass. Since the mass eigenstates of the particles do not coincide with their weak eigenstates, transitions between the families are possible via the weak interaction. Consequently rendering the life-time of particles from the 2nd and 3rd family of fermions finite. Thus only members of the first family are usually observed in nature. The mixing between the mass eigenstates and the weak eigenstates is described by the CKM matrix. So, to be able to study particles from the higher families, they often have to be created at collider experiments. Each family of particles can be further subdivided into two groups, quarks and leptons, depending on whether they carry color charge (quarks) or not (leptons). A summary of fermions is given in Table 2.2.

Table 2.2.: Summary of the fermions described by the Standard Model, the weak isospin, T and the weak hypercharge, Y are related by: $Y = Q - T$, with Q denoting the electromagnetic charge.

	Family			Color charge	Electromagnetic charge	Weak isospin
	1st	2nd	3rd			
Left-chiral						
Quarks	u	c	t	r/g/b	+2/3	+1/2
	d	s	b	r/g/b	-1/3	-1/2
Leptons	e	μ	τ	-	-1	+1/2
	ν_e	ν_μ	ν_τ	-	0	-1/2
Right-chiral						
Quarks	u	c	t	r/g/b	+2/3	0
	d	s	b	r/g/b	-1/3	0
Leptons	e	μ	τ	-	-1	0
	ν_e	ν_μ	ν_τ	Non-interacting if they exist		

Since leptons do not interact via the strong interaction, they are not subject to confinement. Consequently they can exist as free particles. Their only means of interaction are the weak and electromagnetic force. Neutrinos do not carry electromagnetic charge and therefore only interact weakly, making them very hard to detect and study. Until now only upper bounds on the mass of the neutrinos could be provided. However, from

experiments on neutrino oscillations it is know that neutrinos are not massless, but instead at least two of them must be massive. The three charged leptons however are far easier to study, because they also couple to the electromagnetic force. Their masses have been measured to be 0.511 MeV, 106 MeV and 1.78 GeV for the electron, muon and tau respectively.
Quarks however interact via the strong interaction and thus are subject to confinement. Therefore free quarks can usually not be observed. Instead quarks are found in bound states called hadrons. Hadrons are uncolored objects, so quarks have to be combined accordingly. As a consequence only certain types of combinations are possible, namely *Mesons* and *Baryons*[4]. Mesons are bound states of a quark and an anti-quark carrying a specific color and its anti-color respectively, while baryons consist of three quarks which all three carry different colors such that they add up to be white. Studying the mass of the hadrons and comparing it to the mass of its constituents, one will notice a rather huge discrepancy. For example in the case of the proton, the combined mass of its three valance quarks is about $\mathcal{O}(10)$ MeV[5], while its measured mass is about 1 GeV. Hadrons are, as has been already mentioned, compound objects, however they do not only consist of the valance quarks which are responsible for their main physical properties (their quantum numbers like e.g. spin and charge), but also of a "sea" of virtual quarks and gluons which are constantly being created and annihilated in the boundaries of quantum mechanical uncertainty. This "sea" of virtual quarks and gluons carries the remaining mass of the hadron in form of kinetic energy. In case of hadrons consisting of only light quarks (u, d, c) this is close to the total mass of the hadron.

2.1.2. Successes of the Standard Model

The Standard Model of particle physics is unarguably one of the most successful physical theories to date. It is not just able to accurately describe results, but it also made quite a lot of successful predictions in the past. We do not just want to focus on the successful predictions made by the Standard Model as a whole once it was written down in a complete fashion, but also on the success of the building blocks of the Standard Model. The list here is of course very subjective and not exhaustive.

The J/Ψ In 1974 a new, (almost) [7] unexpected, particle was discovered which was independently found by two collaborations. The Brookhaven group named it J [9], while

[4] Just recently the first evidences for tetra and pentaquarks, which are also predicted by QCD, found at LHC, have been published [4, 5].

[5] Quark mass measurements are very difficult. Since quarks are colored, they are subject to the strong force and thus also subject to confinement and only observable as compound objects, consequently rendering direct mass measurements impossible. The only exception from this is the top quark which decays too fast to form a compound object because its mass of 175 GeV is too large and thus its lifetime too short. Quark masses are measured by measuring their impact on hadronic properties and comparing the measurements to theoretical predictions, therefore the predictions are dependent on the theoretical framework used. Nevertheless, recent results are consistent with each other and summarized in the light quark mass listings in [6]. More details about how quark masses can be calculated can be found in the quark masses review found in [6].

the group at SLAC named it Ψ [8], giving the particle its current name J/Ψ. What puzzled people was its unnaturally long lifetime of about $\mathcal{O}(10^{-20})$ seconds, while a lifetime of about $\mathcal{O}(10^{-23})$ seconds was expected because of the particle's heavy mass (about three times the proton mass). The solution to this has however already been proposed many years earlier by Bjorken and Glashow in 1964 [10], because they considered it to be somewhat unnatural that there were four different leptons[6] while only three different quarks had been observed so far. Thus Bjorken and Glashow predicted a whole set of new, charmed, states. Later, in 1970, Glashow, Iliopoulos and Maiani provided an even more appealing technical reason why there should be a fourth quark, namely the *GIM mechanism* [11]. This mechanism was born to account for the low branching fraction of neutral Kaons into a pair of muons. Experimentally it was observed that this fraction is a lot less than expected in the three quark model. To fix this Glashow, Iliopoulos and Maiani introduced the charm quark and therefore a new possible decay channel, reducing the branching fraction into muons. Consequently a zoo of charmed hadrons was predicted by the (four) quark-model of which the J/Ψ was just the first one found.

The tau, the bottom and the top However this joy of two groups of distinct fermions with 4 particles each did not last long. In 1975 a new lepton was discovered, spoiling the symmetrical picture again [12]. Nonetheless, only two years later the first meson carrying a fifth quark, the b-quark, was found, namely the upsilon [13]. Using the same symmetry arguments as Glashow used before, it wasn't hard to predict that a sixth quark should exist, the top-quark. Initial predictions of its mass were obtained from e.g. mixing in the B-meson sector [14, 15], however, since other parameters in the Standard Model were not known with sufficient precision, the predictions fell short of the measured value. Using the electroweak precision data provided by LEP, predictions were gradually improved, e.g. by Ellis et al. [16, 17]. It took about 20 years from the initial proposal of the top-quark until sufficiently high energies could be reached to eventually prove its existence. In 1995 the CDF [18] and D0 [19] collaborations were finally able to announce the discovery of the top-quark, nearly completing the Standard Model of particle physics. Today, the measured mass of the top-quark is about 175 GeV, approximately 40 times the mass of the b-quark.

Prediction of the $W^{\pm}$ and Z bosons While treating the weak interaction as a point-like interaction works extremely well for low energies, it breaks down when going to higher energies and eventually even violates unitarity. This behavior is fixed in the Standard Model by dropping the assumption of a point-like interaction. Instead massive intermediate vector bosons are introduced. As a result of their mass, their lifetime is finite. Predictions of their mass were not possible until the emergence of the electroweak theory of Glashow, Weinberg and Salam [20, 21, 22], because bound states which are mediated by the weak force do not exist. From this it would have been possible to estimate the approximate range of the force and consequently the approximate mass of the mediator. The prediction of the $W^{\pm}$ and Z mass however involves the Standard

[6] The tau had neither been discovered nor been theoretically proposed at that time.

Model parameter θ_W, which had to be measured first [21]. Thus it took until 1982 until a prediction which was precise up to the few GeV level was available. Just one year later, the UA1 collaboration eventually announced the observation of the $W^{\pm}$ and Z bosons at the predicted masses [23, 24].

Prediction of the Higgs boson The unbroken Standard Model of particle physics neither allows the weak bosons, nor the leptons to be massive, because the Standard Model is a gauge theory. The gauge character of the Standard Model is well established, e.g. by measurements of the running of the couplings [25, 26, 27, 6], a feature predicted by gauge theories, which is in very nice agreement with the prediction [28, 29, 30]. Thus, to be able to give mass to all the fermions and to all the weak bosons in the Standard Model, the electroweak $SU(2)_L \otimes U(1)_Y$ symmetry has to be broken. The simplest way to achieve this breaking and to keep the theory consistent in itself was to introduce a complex scalar field into the theory which couples to all massive particles [31, 32, 33, 34]. Calculating the mass of this newly introduced scalar field however is not possible, because it is a parameter of the theory. It can be expressed in terms of other parameters of the Standard Model, but this only shifts the problem towards precision measurements of those parameters. Consequently for quite some time only bounds [35] on and indirect measurements[7] [36] of the Higgs mass were available. It took until 2012 until eventually the final missing part of the Standard Model was discovered, the scalar Higgs field, rendering the Standard Model of particle physics complete.

2.2. Problems of the Standard Model of Particle Physics

Albeit it proofed extremely successful, the Standard Model cannot account for everything. Also some of its features are considered rather unnatural by many physicists. In the following a subjective, non-exhaustive, overview of the current problems of the Standard Model will be given.

2.2.1. Gravity

Gravity is actually the first of the fundamental four forces known today which was discovered and successfully described (at the energies available at that time) by mankind. However, in the Standard Model, gravity is not included. So far every attempt to cast it into a quantum field theory has failed. Compared to the weak force it is 30 orders of magnitude weaker, rendering it impossible to study it on small scales at current accelerators. Simply speaking, in the currently known world of elementary particle physics gravity does not exist up to the Planck scale $M_{\text{Planck}} \sim 10^{19}$ GeV. It cannot be easily included into the Standard Model without breaking it. The mediator of gravity, the *graviton*, needs to be a spin-2 boson, because gravity is described by a second rank tensor. But adding a spin-2 boson to the Standard Model will result in an unrenormalizeable

[7] Indirect measurements of the Higgs mass were made by fitting the Standard Model parameters using the electroweak precision measurements made at LEP, SLAC and TeVatron as input.

[37, 38] theory and thus the model would become uncalculable[8]. In consequence there is currently no (simple) way of incorporating the very successful theory of *general relativity* into the also very successful Standard Model of particle physics.

2.2.2. Unification of Forces

Naively one would not think that unifying the currently known forces is possible, because their couplings are largely different. However, the couplings are not fixed values. Instead they depend on the energy scale. This phenomenon is called running of the renormalization group couplings or just short *running of the couplings* and arises from the renormalization group equations [1]. Sadly in the Standard Model as is, mankind's dream of having a sole explanation for everything will definitely not come true. The explanation in this case being a physical force. While it is possible, even necessary, to unify the electromagnetic and weak force in the Standard Model, it is not possible to unify the electroweak and strong forces without new physics coming into play at some scale beyond the electroweak scale [41]. The couplings of the electroweak and strong interactions cannot be brought into agreement. To illustrate this the running of the couplings of the Standard Model can be found on the left side of Figure 2.2. However, the running of the couplings can change at a given energy scale if new physics come into play, like for example new particles which can be created once the energy is sufficiently high enough. An exemplaric case is illustrated in Figure 2.2 on the right side: new particles have been introduced at the TeV-scale resulting in a kink at around 10 TeV, making the unification of the three forces possible. Consequently new physics is needed to be able to unify the forces described by the Standard Model.

2.2.3. Dark Matter

One of the first hints on *Dark Matter* was already found in 1933. Fritz Zwicky, a swiss physicist, measured the velocities of galaxies in the coma cluster from the Doppler shift of their atomic spectra. From this he calculated the mass of the cluster. Quite surprisingly it turned out that the visible mass and the mass Zwicky calculated do not coincide [43]. Instead the visible mass was more than 100 times less. So most of the cluster's mass is not luminous. Simply speaking it is dark, coining the term *Dark Matter*. In 1939 Babcock measured the rotation curve of stars in the Andromeda nebula. Opposed to expectation the mass-to-light ratio increased with increasing distance from the galaxy's center, but instead of attributing this to Dark Matter , he attributed it to the absorption of light inside the galaxy or to yet unknown dynamics in the outer regions of the galaxy [44]. Vera Rubin and collaborators measured, approximately 40 years after Zwicky's discovery, the rotation curves of about 60 isolated galaxies. These measurements showed extreme deviations from predictions due to Newtonian gravity [45, 46, 47, 48]. An exemplaric measurement of the M33 galaxy can be found in Figure 2.3. Quite obviously the rotation

[8] Actually string theory might come to the rescue here [39, 40], however, as of now, 2016, string theory does not yield any verifyable or falsifyable predictions distinct from other, simpler, extension of the Standard Model. Thus it is only a mind-game which can be played.

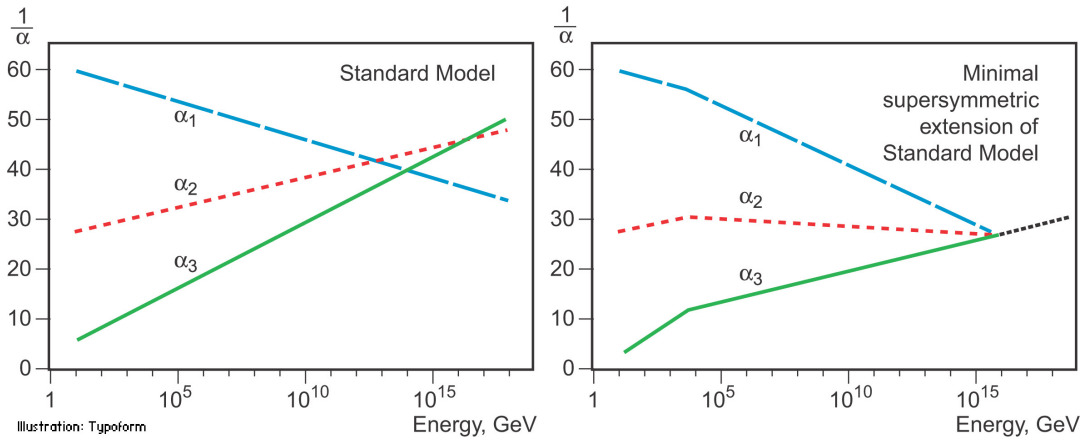

Figure 2.2.: Running of the couplings of the electromagnetic (α_1), weak (α_2) and strong (α_3) interactions. The case of the Standard Model without modifications is depicted on the left. On the right an illustration of the running of the couplings in the minimal supersymmetric extension of the Standard Model is shown where the model parameters have been chosen such that the couplings meet before the Planck scale. Figure from [42].

curve does not follow the shape of the luminous contributions (the stellar disk and the gas), as it should be the case if the mass distribution would closely follow the distribution of luminous matter in the galaxy, but instead it approaches a constant indicating that there is more matter than expected in the outer regions of the galaxies.

Yet another proof that Dark Matter exists was also provided using *gravitational lensing*. According to the theory of general relativity gravity bends space itself. Consequently light passing by a massive object, like e.g. a cluster of stars or Dark Matter, will deviate from its elseways straight path of flight. The massive object behaves like an optical lens, it bends light proportional to the mass of the massive object, coining the name gravitational lens. Using the Chandra X-ray telescope together with Magellan and the Hubble space telescope, the NASA provided the first direct proof that Dark Matter exists in 2006. They measured the distribution of hot gas and that of matter after a collision of two larger galaxy clusters, merging into one big cluster, the *bullet cluster*. In Figure 2.4 the optical image is shown: superimposed in pink is hot gas, while in blueish the distribution of mass is superimposed, measured using gravitational lensing. Clearly, the majority of mass is distributed differently from hot gas. However, most of a galaxy cluster's mass is actually not found in form of stars, but instead in its hot gas. Thus there must have been two different types of matter interacting in the collision which formed the *bullet cluster*. One being the known ordinary matter which was slowed down throughout the collision by a drag force, the other being dark matter which was not subject to the drag force and thus was not slowed down, resulting in the strikingly different distribution of mass and hot gas. An observation which cannot be explained using modified laws of gravity.

Using precision measurements of the cosmic microwave background, a relic from the era

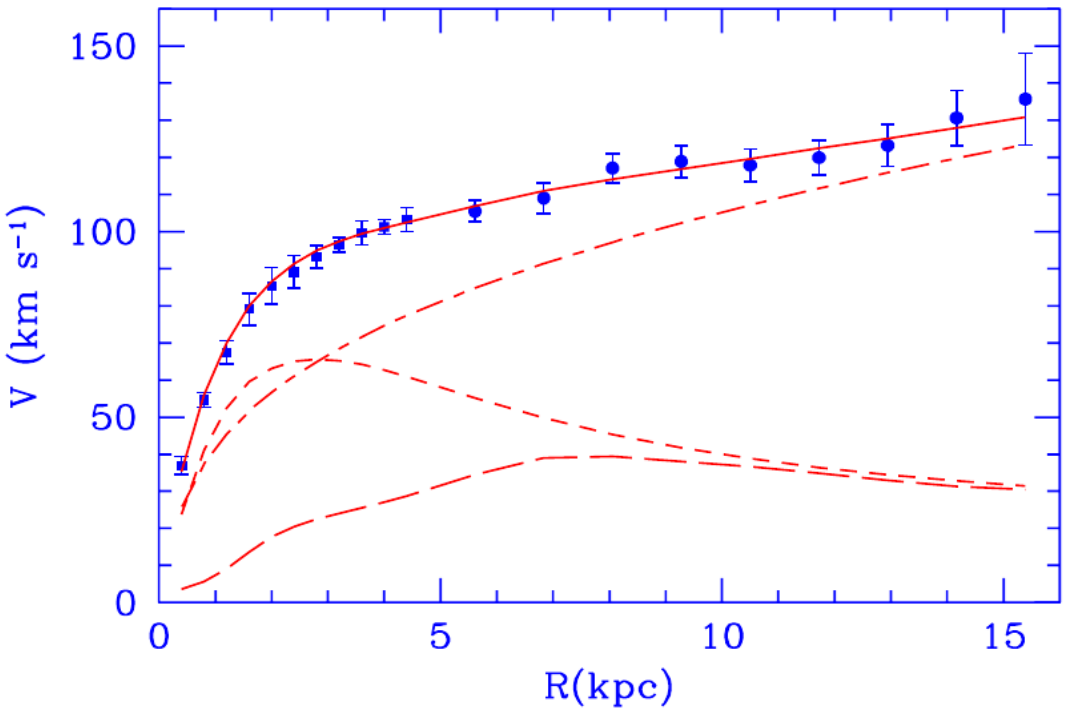

Figure 2.3.: Rotation curve of M33 where the points indicate the actually measured values. The continuous line indicates the best fit model which is a combination of three contributions: the dark halo contribution (dash-dotted line), the stellar disk (short dashed line) and the gas contribution (long dashed line). If dark-matter would not exist, the total rotation curve would be expected to only contain the stellar disk and the gas contributions. Figure from [49].

Figure 2.4.: Optical image of the bullet cluster taken using Magellan and the Hubble Space Telescope. Superimposed in pink is the distribution of hot gas measured using the Chandra telescope. The areas where most of the matter is found is superimposed in blue. The distribution of gravitationally interacting matter has been measured using gravitational lensing. Figure from [50].

of recombination, around $\mathcal{O}(4 \times 10^5)$ years after the Big Bang, the amount of Dark Matter, matter and *Dark Energy* can be inferred. The cosmic microwave background is the thermal radiation left over when the universe cooled down such that its energy does not suffice anymore to break neutral hydrogen atoms into protons and electrons, rendering the universe opaque to it. Simply speaking the cosmic microwave background is a snapshot of the time of recombination. As expected the cosmic microwave background can be characterized by a black body spectrum, nearly uniform in all directions. However it exhibits small residual variations which are caused by interactions of the cosmic microwave background with e.g. gravitational potentials[9]. Measuring these variations precisely a lot of information can be gained, e.g. about the curvature of the universe as well as the matter and dark matter density. It turns out that only approximately 5% of the matter and energy observed in the universe is describable by the Standard Model [51]. 95% of the universe are dark. 26% being Dark Matter, 69% being *Dark Energy*. The question however which could so far not been answered is what is Dark Matter made off? In the Standard Model the only one possible candidate for Dark Matter would be neutrinos. However neutrinos cannot account for the observed cold Dark Matter in the universe, cold referring to the temperature and thus the average velocity of the Dark Matter. Even using current upper bounds on neutrino masses, they are too light to explain the density of cold Dark Matter observed by astronomers. Theoretically neutrinos can only account for warm Dark Matter. So a, Dark Matter wise, good extension of the Standard Model needs to provide at least a new, stable, *weakly interacting massive particle*, sometimes also called wimp to be able to account for Dark Matter.

2.2.4. Neutrino Masses

In the Standard Model neutrinos are strictly massless, because right-handed neutrinos have not been observed yet and consequently only left-handed neutrinos are included in the Standard Model, thus a Yukawa term coupling neutrinos to the Higgs is not possible. However, when measuring the flux of electron neutrinos originating from the sun the first time in 1968, a significant deficit was found. Consequently either modeling of the processes taking place inside the sun had to be wrong or neutrinos were not what people thought them to be. Just a year later Pontecorvo published a possible solution to this problem. He proposed that the neutrino species changes while traveling from sun to earth, violating the per-species lepton number conservation while still conserving the total lepton number. Nowadays this phenomenon is called *neutrino oscillations*. Doing the math just taking electron an muon neutrinos into account[10], one finds that the probability of an electron neutrino to oscillate into a muon neutrino can be written as follows:

[9] If there is a type of matter which already decoupled earlier from the cosmic soup and solely interacts via gravity, it will have clumped together partially at the time of recombination, forming first structures and consequently imprinting them onto the cosmic microwave background via gravitational interactions.

[10] The simple example of a two state system can be found inside [52].

$$P_{\nu_e \to \nu_\mu} = \left[\sin(2\theta) \sin\left(\frac{(m_2^2 - m_1^2)\, c^3}{4\hbar E} z \right) \right], \tag{2.18}$$

θ being the mixing angle, m_2 and m_1 being the masses of the neutrino species, E denoting the initial energy of the neutrino and z the distance the neutrino traveled. For the case of vanishing mixing angle or equal muon and electron neutrino masses this probability would vanish. Thus, in the two-state case, at least one neutrino generation needs to be massive. Generalizing this to three generations yields that at least two of the three need to be massive, proving that the Standard Model, in its current formulation, is not the end.

2.2.5. Matter-Antimatter-Asymmetry

Opposed to expectations, the matter found in today's universe is mostly made out of matter, whereas equal amounts of matter and anti-matter would be expected. Naively it is assumed that matter and antimatter were created in equal amounts in the Big Bang. To date there is no strong evidence that this assumption is false. Instead common belief nowadays is that some reactions distinguish between matter and antimatter, also called CP symmetry violation. CP violation was discovered in 1964 by Christenson, Cronin and Fitch. They studied the decay of neutral, long-lived, K_L^0-mesons. CP conservation would require them to decay into 3 pion final states. The measurement however showed that about 0.2% of the long-lived kaons decayed into two pions, violating CP symmetry. In the decay of the kaons into pions, a s-quark decays into a quark of the first generation, thus the weak interaction had to be involved. Consequently the CP symmetry is not conserved in the weak interaction, while to date the strong and electromagnetic interaction are still considered to conserve CP[11]. The weak interaction distinguishes between matter and antimatter. This property is captured in the so called *CKM matrix*, named after Cabibbo, Kobayashi and Maskawa. It describes the mixing of the mass eigenstates of quarks into the quark eigenstates of the weak interaction. To not violate unitarity, the matrix has to be a unitary matrix, imposing strong constraints on it. In the initially proposed four quark model by Cabibbo, only one real parameter, the mixing angle θ_C, is needed, because the other three real parameters become physically irrelevant due to the unitary requirement. In case of six quarks, corresponding to the Standard Model case, the resulting matrix has three real parameters, the quark mixing angles, and one complex phase which is the source of CP violation in the Standard Model. However, these parameters are not calculable in the Standard Model, they are free parameters which have to be measured. The measured amount of CP violation in the Standard Model nonetheless does not suffice to explain the matter-antimatter asymmetry observed today. Additional processes must have been at play during *baryogenesis*, additional

[11] In case of the strong interaction there is actually no reason why CP should be conserved, the theory of QCD allows for CP violation, however measurements show that strong interactions do not violate CP. Since this requires fine-tuning of parameters in the QCD part of the Lagrangian, this is also referred to as the strong CP problem.

sources of CP violation beyond those in the Standard Model of particle physics are thus needed!

2.2.6. Higgs Mass and Naturalness

The Higgs boson is a scalar field and thus there is no symmetry to prevent it from coupling to other particles such that its mass becomes quadratically divergent. It should be of the order of the highest energy scale involved in the theory, which would be the Planck-scale. However for the vacuum to be stable or at least sufficiently long-lived, it is required that the Higgs mass is of the order of the electroweak scale [53], 16 orders of magnitude smaller. This problem is nowadays named the *naturalness* problem. By renormalizing the theory the Higgs mass can be brought down to the electroweak scale, however this requires extensive fine-tuning. No other known theory requires such an extensive amount of fine-tuning and consequently people named this the *fine-tuning* problem. The corrections to the Higgs mass have the following form:

$$\Delta m_H^2(\text{fermions}) \propto -\frac{|\lambda_f|^2}{8\pi^2}\left[\lambda_{UV}^2 - 3m_f^2 ln\left(\lambda_{UV}^2/m_f^2\right) + ...\right], \tag{2.19}$$

$$\Delta m_H^2(\text{bosons}) \propto \frac{\lambda_B}{16\pi^2}\left[\lambda_{UV}^2 - 2m_B^2 ln\left(\lambda_{UV}^2/m_B^2\right) + ...\right], \tag{2.20}$$

m_f and m_B being the masses of the fermion and the boson, λ_{UV} being the cut-off scale and λ_f and λ_B being the couplings of the fermion and boson to the Higgs. Quite remarkably, they enter with different sign.
Many solutions to aforementioned problems have been developed, here the focus is only on one. Looking at the Higgs mass corrections the question rises: "What if new particles are added?" Assuming all other properties would be exactly the same, adding a partner to each Standard Model field which only differs by 1/2 in spin, the corrections would cancel and the need for fine-tuning would be eliminated. This is the concept of *supersymmetry*.

2.3. Supersymmetry

Supersymmetry is not a theory by itself, it is a concept which introduces a symmetry between fermions and bosons. Not only is it used in particle physics, but also e.g. in nuclear physics when calculating the binding energy of given states [54, 55]. Simply speaking, to each fermionic degree of freedom a bosonic one is associated and vice versa with the only difference being the spin, all other quantum numbers are identical. Applying this to the Standard Model of particle physics and oversimplifying things one could say that the particle content of the Standard Model is being doubled. Superpartners are commonly denoted by the same letters as their Standard Model partners, only adding a tilde on top of them, the t e.g. becomes $\tilde{t}$. The bosonic partners of the Standard Model fermions are named like their counterparts, only a "s" is prefixed, so e.g. the superpartner of the tau is called stau. In case of the Standard Model bosons "-ino" is

suffixed to the name, like e.g. the W becomes the *wino*. However, depending on the actual model, usually the observed *gauginos* are mixtures of the bosinos: four *neutralinos*, $\chi^0_{1,2,3,4}$ and two *charginos*, $\chi^{\pm}_{1,2}$.
If supersymmetry were an exact symmetry, the superpartners would have the same mass as their Standard Model counterparts. Obviously they don't, because no superpartners have been found yet. Consequently supersymmetry is a broken symmetry. The exact mechanism of supersymmetry-breaking is unknown. Many different proposals exists, all have one thing in common: they try to avoid introducing new quadratic divergencies, which is called soft supersymmetry-breaking. The breaking usually occurs in some kind of *hidden sector*, meaning that it is decoupled from the Standard Model particles and their superpartners, the *visible sector*. It is then mediated by *messenger* particles to the visible sector, e.g. by the *gravitino* or by the *gauginos* [12]. In the following, if not stated otherwise, no assumptions about the breaking mechanism will be made, instead focus will be on the implications of supersymmetry at low energy scales compared to the supersymmetry-breaking scale.

R-parity and the proton R-parity is a new quantum number often introduced in supersymmetric extensions of the Standard Model.

$$P_R = (-1)^{3(B-L)+2s}, \tag{2.21}$$

B being the baryon number, L being the lepton number and s being the spin of a particle. Its value is +1 for particles while it is -1 for sparticles. To prevent arbitrary sources of B and L number violation, many supersymmetric extensions of the Standard Model assume R-parity to be conserved. The main implication of R-parity violation would be that the proton would be allowed to decay via sparticles, like shown in the Feynman graph in Figure 2.5. Current measurements however show that the proton is most probably stable. Its lifetime is currently measured to be at least $\mathcal{O}(10^{38}$ s) [6]. Nonetheless R-parity is not strictly required to obtain a proton having a lifetime that long, some possibilities are sketched in [2], however, all models considered in this thesis assume R-parity conservation unless stated otherwise. The main implication of R-parity conservation is that the lightest supersymmetric particle, short lsp, will be stable and thus be created in every decay chain involving supersymmetric particles. In R-parity conserving scenarios supersymmetric particles will always be created in pairs, such that at least two lsps will be created in the subsequent decay chain.

Dark Matter If the lsp is neutral and stable, it will become a natural candidate to explain cold Dark Matter. Its particle nature can be constrained from fits to the Dark Matter relic abundance. Sneutrinos, the superpartners of neutrinos, are expected to annihilate very rapidly in the early universe, resulting in a too low relic density. Lightweight gravitinos, the superpartners of the graviton, have to be classified as hot dark matter. However the large scale structures observed in today's universe are inconsistent with a

[12] More details about supersymmetry-breaking can be found in the following reference: [2].

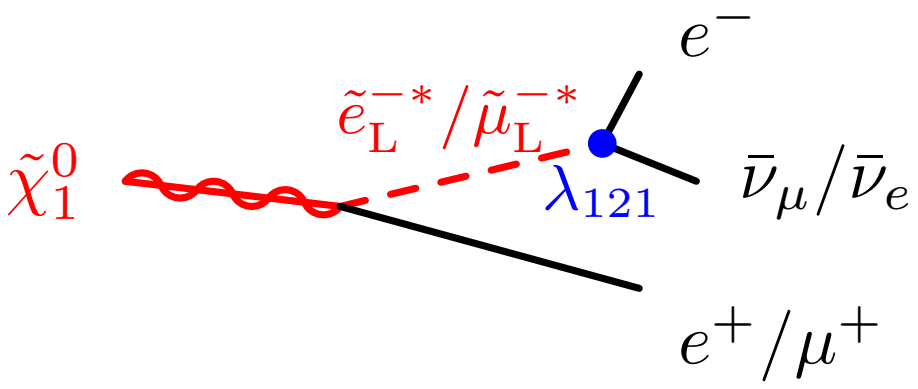

Figure 2.5.: Example of a R-parity violating decay of the lightest neutralino.

hot dark matter universe. Heavy gravitinos on the other hand are hardly detectable since they only interact gravitationally. As a result the only currently viable candidates for detectable cold dark matter are the neutralinos, to be more specific, the lightest one.

Unification of couplings The slope of the renormalization group equations describing the running of the couplings depends on the accessible particle spectrum. Consequently introducing supersymmetry into the Standard Model, the running of the couplings will change. In supersymmetric extensions of the Standard Model the running of the couplings of the three known forces can thus be altered such that they meet with rather high accuracy, as can be seen on the right hand side of Figure 2.2.

Fine-tuning The amount of fine-tuning needed to stabilize the Higgs mass at the electroweak scale naturally vanishes in supersymmetric extensions of the Standard Model, at least mostly. Problems arise if supersymmetry is not exactly conserved, which it isn't. The corrections to the Higgs mass then become proportional to the difference of the masses squared of the particles and their superpartners. Rendering the amount of fine-tuning needed dependent on the energy scale at which the superpartner masses are, the lower the mass of the superpartners the less fine-tuning required. Since a lot of the phase-space below the TeV scale has already been investigated and ruled out, people expect supersymmetry to be found at around the TeV scale.

Parameters, Possible Constraints and Simplifications While the Standard Model already has 18 free parameters which have to be measured, supersymmetry brings in lots of new parameters. The most general supersymmetric *Lagrangian* which is minimal in terms of new fields, the *MSSM*, adds 150 new parameters to the game. If R-parity conservation is at play, 45 parameters become dependent on others and 105 free parameters remain. This is still a lot. Most of these parameters actually stem from supersymmetry-breaking. If one assumes a certain supersymmetry-breaking mechanism, one can actually reduce the number of parameters quite a lot.

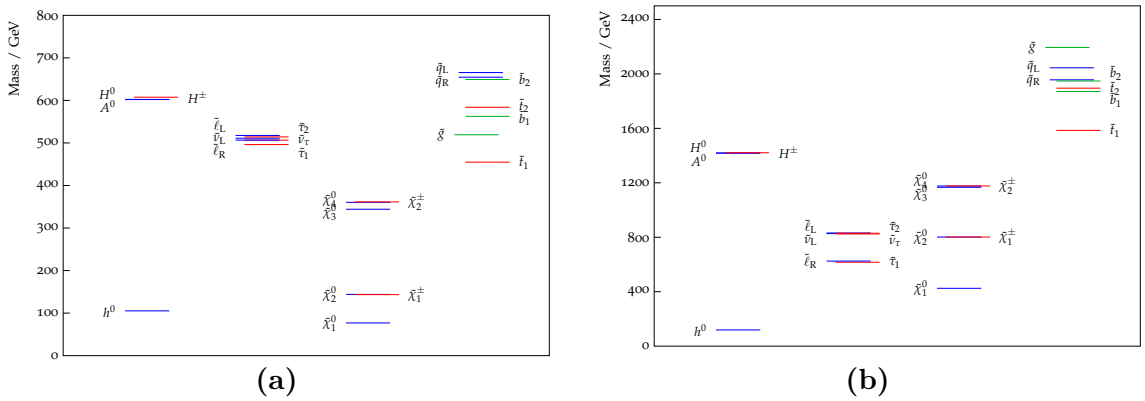

Figure 2.6.: Two mSUGRA mass spectra, the common parameters in both cases are: $\text{sign}(\mu) = 1, \tan\beta = 10, m_0 = 500$ GeV. (a) $m_{1/2} = 200, A_0 = 1000$; (b) $m_{1/2} = 1000, A_0 = 10$. In (a) the sleptons are heavier than all neutralinos and charginos, while in (b) the right handed sleptons are in between the lightest neutralino and the degenerate next-to-lightest neutralino and lightest chargino masses. Spectra generated using [60].

Assuming for example supersymmetry-breaking being mediated via gravity and constructing a realistic, minimal, model for $N = 1$ supergravity, called *mSUGRA*, one ends up with 4 parameters and a sign, being:

- m_0, the common mass of scalars at the GUT scale,
- $m_{1/2}$, the common mass of gauginos and higgsinos at the GUT scale,
- A_0, the common trilinear coupling,
- $\tan\beta$, the ratio of the vacuum expectation value of the two Higgs doublets,
- $\text{sign}(\mu)$, the sign of the higgsino mass parameter.

While having just 4 parameters is very attractive, it of course cannot capture all the phenomenology the full 150 parameter *MSSM* exhibits. Nonetheless it already provides a rich phenomenology to study, as can be seen in Figure 2.6 which shows the mSUGRA particle spectrum for two different parameter-sets. Recent results claim to have shown that most of mSUGRA's parameter space is excluded [56, 57, 58]. However, it can be shown that this is not the case if one actually evaluates the electroweak symmetry breaking at its true scale, the Higgs-vacuum expectation value instead of $\sqrt{m_{\tilde{t_R}} m_{\tilde{t_L}}}$ which is currently commonly in use in mSUGRA particle spectrum generators. The change of scale initially was made to make the one loop corrections negligible, however if one also adds the dominant two loop contributions, one can evaluate the electroweak symmetry breaking at the true electroweak scale [59].
In *gauge-mediated supersymmetry-breaking*, GMSB, the symmetry breaking is mediated from the hidden to the visible sector via the Standard Model's gauge interactions via massive messengers which are charged under the Standard Model's charges. Instead of supersymmetry-breaking occuring at the Planck scale in GMSB it occurs at relatively

low scales [61]. In terms of the number of parameters GMSB scenarios are as attractive as mSUGRA models, 4 parameters and a sign:

- M_{mess}, the overall messenger scale
- N_{mess}, parametrizes the structure of the messenger scale
- Λ, the soft supersymmetry-breaking scale felt by the low-energy sector
- $\tan\beta$, the ratio of the vacuum expectation value of the two Higgs doublets,
- $\text{sign}\,(\mu)$, the sign of the higgsino mass.

Remarkably the gravitino, $\tilde{G}$, is always the lsp in GMSB models, lifting the *next-to-lightest-supersymmetric particle*, nlsp, into the role of being the one to drive the phenomenology of the model:

- *Neutralino nlsp scenario*, $m_{\chi_1^0} < (m_{\tilde{\tau}_1} - m_\tau)$, decay chains will typically end with the decay: $\chi_1^0 \to \tilde{G}\gamma$,
- *Stau nlsp scenario*, $m_{\tilde{\tau}_1} < \text{Min}\left(m_{\chi_1^0},\ m_{\tilde{l}_R}\right) - m_\tau$, featuring mostly $\tilde{\tau}_1 \to \tilde{G}\tau$ decays, as well as kinks in the track of the semi-stable $\tilde{\tau}_1$,
- *Slepton co-nlsp scenario*, $m_{\tilde{l}_R} < \text{Min}\left(m_{\chi_1^0},\ m_{\tilde{\tau}_1} + m_\tau\right)$, $\tilde{l}_R \to \tilde{G}l$ decays become a significant possibility in addition to the already known stau nlsp signatures
- *Neutralino-stau co-nlsp scenario*, $\left|m_{\tilde{\tau}_1} - m_{\tilde{\chi}_1^0}\right| < m_\tau$ and $m_{\tilde{\chi}_1^0} < m_{\tilde{l}_R}$, this scenario allows for both the neutralino nlsp scenario as well as the stau nlsp scenario decay signatures.

This phenomenology is only to be regarded as indicative. Fine-tuned points in the model's phase space can of course exhibit largely different phenomenology, these are just the most 'typical' scenarios as quoted by [61].
Another approach is to constrain the MSSM physically, instead of assuming a specific breaking mechanism. In case of the *phenomenological MSSM*, pMSSM, the following three assumptions are made:

- no new source of CP violation,
- no flavor changing neutral currents,
- first and second generation universality.

These assumptions result in 19 new parameters in the framework of the pMSSM:

- M_1, M_2, M_3, the three gaugino masses,
- m_A, the mass of the pseudoscalar Higgs boson,

- μ, the higgsino mass parameter,
- $\tan\beta$, the ratio of the vacuum expectation value of the two Higgs doublets,
- $m_{\tilde{q}}, m_{\tilde{u}_R}, m_{\tilde{d}_R}, m_{\tilde{l}}, m_{\tilde{e}_R}$, first and second generation squark and slepton masses,
- $m_{\tilde{Q}}, m_{\tilde{t}_R}, m_{\tilde{b}_R}, m_{\tilde{L}}, m_{\tilde{\tau}_R}$, third generation squark and slepton masses,
- A_t, A_b, A_τ, the third generation trilinear couplings.

This is still a huge parameter space making it hard to classify the pMSSM parameter space into groups of similar phenomenology, making the pMSSM parameter space hard to study. Later in this thesis a study will be presented which faces this problem.
Since the supersymmetric parameter space remains huge even after applying several phenomenologically motivated constraints, the dominantly used class of approaches to search for supersymmetry at the LHC are simplified models [62, 63]. As the name suggests these models are simplified a lot. Usually only a small set of supersymmetric particles is assumed to be at or around the TeV scale. The rest of the supersymmetric particle spectrum is assumed to be mostly 'decoupled' by setting their masses to arbitrarily high scales. If the masses of the set of particles at the TeV scale is small and the masses are distinct, meaning that they differ by at more than a few GeV, decay chains are short. However, if several particles are chosen to be at the TeV scale with not so large mass differences (at most a few GeV) several equally likely decay channels open up and thus decay chains become diverse and sometimes rather long. Branching fractions of the superpartners into Standard Model particles are often either assumed to be 100% or only specific decay modes are considered. Thus the remaining 'parameters' of these models are usually just the masses of the sparticles. This makes the models very handy to study, but at a first glance they don't seem very general. However, usually the results of studying those simplified models can be expressed in a rather general way, namely upper limits on the cross section times the branching fraction for a given process. Calculating this quantity in 'real' models, like e.g. the pMSSM, and comparing it to the result from the simplified models, one can often tell whether this model is excluded or not. Later in this thesis results obtained from simplified models will be compared with a study of a larger part of the pMSSM phase space, to investigate the strength of simplified models.

3. Statistical Interpretation

The following is a short summary of the statistical methods and terminology used in the interpretation of results in this thesis. It is inspired by the statistics reviews found in [6] and [64].

Motivation One of the many challenges in finding physics beyond the Standard Model is that it is predicted to be very rare, the Standard Model holds up pretty well so far. Most models do not provide a smoking gun signature. Instead, most models provide signatures which are also expected in the Standard Model, but with different rates, for example the decay of a particle into two taus in the final state together with weakly interacting particles escaping the detector is possible via a neutralino or a Z-boson. Consequently one has to count how many events with a given signature are predicted by an extension of the Standard Model and has to compare this to the Standard Model expectation.
However the question whether a single observed event more than expected by the Standard Model proves new physics or not cannot be generally answered, instead it needs a careful treatment taking into detail the most important sources of uncertainty. In the following a summary of this treatment shall be given[1].
Usually cut-and-count analyses are performed in one or more signal regions. Signal regions use requirements on kinetic and event shape variables to distinguish signal events, meaning events from physics beyond the Standard Model, from Standard Model events. The expected event yield due to Standard Model background is estimated using either simulated samples or data-driven methods, depending on how well the simulated description of the process of interest is performing. The expected event yields for models beyond the Standard Model are obtained form simulated samples. Both expectations are then compared to the data. Simply speaking, the probability for the observed data to be described by the *null hypothesis* (the null hypothesis is the assumption that only the Standard Model is realized in nature) is compared to the probability that the data is described by the extension of the Standard Model under consideration. Depending on that, the extension might be excluded or not and in the best case it might be found to explain the fluctuation observed. This is done using the so-called CL_s method, which needs as inputs the *p-values* and thus the *profile likelihood functions*.

Profile Likelihood Method In case the Standard Model would be the whole truth, the expected number of events would be equal to the number obtained in the background-only case. If the extension of the Standard Model, in the following called signal, is

[1] It shall be noted here, that different viewpoints on the statistical interpretation of results exist. We will only present one here, the one being commonly used by most SUSY searches in ATLAS.

realized, the expected number of events would be the number of expected signal plus background events. To allow for uncertainties in the calculation of the cross section and to make the approach a bit more general, the signal strength μ is introduced as follows:

$$E(n) = \mu s + b, \tag{3.1}$$

where E denotes the expectation value of the number of expected events n, s the number of expected signal events and b the number of background events. Usually the estimate of b is split up, e.g. by splitting it into processes or final states. Thus b is estimated from the individual components as follows:

$$b = \sum_i \tau_i b_i, \tag{3.2}$$

where the b_i denote the individual components and $\tau_i = \frac{\mathcal{L}_i^{\mathrm{MC}}}{\mathcal{L}^{data}}$ is the scaling factor needed to scale the luminosity of the simulated sample to the one of the recorded dataset. The expectation value for each of those background components can be expressed as follows:

$$E(n_i) = \tau_i b_i, \tag{3.3}$$

where E denotes the expectation value of the number of expected events from process i, n_i, and b_i the number of background events from process i. A likelihood function is defined as the probability density $\mathcal{P}$ of a measurement x, given a parameter μ:

$$L(\mu|x) = \mathcal{P}(x|\mu). \tag{3.4}$$

The best estimate of μ is the one which maximizes $L(\mu|x)$. In case of a cut-and-count experiment, the likelihood function can be defined as a product of Poisson probabilities:

$$L(\mu|n, n_i) = \mathcal{P}^{\mathrm{Poiss}}(\mu s + b, n)\Pi_i \mathcal{P}^{\mathrm{Poiss}}(b_i, n_i), \tag{3.5}$$

with

$$\mathcal{P}^{\mathrm{Poiss}}(\lambda, x) = \frac{\lambda^x}{x!} e^{-\lambda}. \tag{3.6}$$

Statistical and systematical uncertainties enter the estimate in form of the so-called nuisance parameters, in the calculation of the likelihood function L. Take for example the integrated luminosity measurement and assume that the measured value is Gaussian distributed around a mean value $\bar{l}$ with width σ_l. It is included in the likelihood by multiplying:

$$L(\mu, l|n) = L(\mu|n)\,\mathcal{G}\left(l|\bar{l}, \sigma_l\right), \tag{3.7}$$

where l is a so-called nuisance parameter used in the calculation of μ. The *profile likelihood ratio* $\lambda(\mu)$ is then used to test a set of values for the parameter μ and is defined as:

$$\lambda(\mu) = \frac{L\left(\mu, \hat{l}'|n\right)}{L\left(\hat{\mu}, \hat{l}|n\right)}, \tag{3.8}$$

where $\hat{l}'$ is the value of l which maximizes L for a given value of μ, while $\hat{\mu}$ and $\hat{l}$ in the denominator are the values maximizing the likelihood function. Thus λ is found to be in the range $0 \leq \lambda \leq 1$. It is often convenient to look at the degree of incompatibility between the data and the proposed value of μ:

$$t_\mu = -2\ln\left(\lambda(\mu)\right). \tag{3.9}$$

So values of t_μ close to 0 indicate the data being described by the hypothesized value of μ well.

p-value The level of disagreement can be quantified using the so-called p-value,

$$p(\mu) = \int_{t_{\mu,\,\mathrm{obs}}}^{\infty} \mathcal{P}\left(t_\mu|\mu\right) dt_\mu. \tag{3.10}$$

Here $t_{\mu,\,\mathrm{obs}}$ denotes the t_μ value obtained from measured data, while $\mathcal{P}\left(t_\mu|\mu\right)$ denotes the probability density function of t_μ given the parameters μ. Useful approximations can be found in [65]. Simply speaking the p-value is the probability of getting the observed result or a result more incompatible with the hypothesis of the given parameter μ, under the assumption that the *null hypothesis* is true. Rephrased this means that the p-value is the probability of obtaining the measured data if the *null hypothesis* is valid.

Significance The p-value and the *significance* Z are related:

$$Z = \phi^{-1}(1-p), \tag{3.11}$$

where ϕ^{-1} is the quantile of the standard Gaussian. It is a measure of how many Gaussian standard deviations away from the mean the measured value is. By convention the p-value of 0.05 is used for excluding a signal hypothesis. It corresponds to a significance of $Z = 1.64$. The quantity significance is quite useful because in the limit of large s and b it can be approximated by $Z = \frac{s}{\sqrt{b}}$, an easy to use formula. If not noted otherwise, the *significance* will be evaluated numerically using the *BinomialExpZ* function from *ROOT*'s *RooStats* framework [66].

CL$_s$ Method While the p-value measures the level of disagreement of a hypothesis with the observed data, the *confidence level* is a measure of the opposite, namely how well the data agrees with the hypothesis. It is the probability, $P\left(t_\mu < t_{\mu,\,\mathrm{obs}}\right)$, that t_μ is less than the observed value and thus related to the p-value by:

$$CL = P\left(t_\mu < t_{\mu,\,\mathrm{obs}}\right) = 1 - p. \tag{3.12}$$

However, using CL values as a mean to exclude a hypothesis is only meaningful if the distributions of both hypotheses are sufficiently well separated. This might e.g. not be the case for models which the experiment is not sensitive to and where thus the signal-plus-background hypothesis and the background-only hypothesis are nearly identical. Consequently at LEP the CL_s method was introduced:

$$\mathrm{CL}_s = \frac{CL_{s+b}}{CL_b} = \frac{p\,(\text{s + b hypothesis})}{1 - p\,(\text{b only hypothesis})}. \tag{3.13}$$

Strictly speaking CL_s is not a confidence level but instead a ratio of a p-value and a confidence level. A hypothesis is excluded if the CL_s value falls below a certain threshold α. Nowadays this value is usually chosen to be $\alpha = 0.05$ in high energy physics. To illustrate the problem and how the CL_smethod solves it: imagine a signal model with tiny cross section compared to an overwhelming background. CL_{s+b} and CL_b will then become approximately equal, because in both cases approximately the same number of events are expected. Now imagine further that the measurement is incompatible with the background such that a CL_{s+b} value of less than a given threshold is reached. Consequently if you only set a limit based on the CL_{s+b} value, you might falsely exclude the signal plus background hypothesis. In case of the CL_s method this is not the case, because CL_s will become one (remember, the background-only and the signal + background hypotheses are near identical) and thus you would not exclude the model yet, saving you from false exclusions in case of models which you are not sensitive to.

4. The LHC and ATLAS

The CERN is located at the border between France and Switzerland, near Geneva. Its name originates from the initial letters of its provisional founding board, the *"Conseil Européen pour la Recherche Nucléaire"*. The laboratory was founded in 1954 with the aim of gaining a better understanding of the structure of particles. Currently it hosts 25 experiments. In the past it hosted several important colliders, amongst them the large-electron-positron collider, LEP. The experiments at the LEP contributed a lot to our understanding of the Standard Model by precisely measuring properties of the Standard Model. Researchers at CERN also discovered the W-, the Z-, as well as the Higgs boson. Not to mention, CERN has always been and still is a major driving force behind many technical advancements, like e.g. the world wide web [67]. Today, CERN hosts the world's currently largest hadron collider, the *Large Hadron Collider*, or short the LHC. The LHC, the ATLAS experiment, one of the experiments at the LHC, as well as CERN's computing facilities, the Grid, will be the focus of this chapter.

4.1. The Large Hadron Collider

Plans for the LHC were already announced four years before the tunnel to host its predecessor, the LEP, was completed at the Lausanne workshop in 1984. Initially the plan was to build a proton-proton collider with a centre-of-mass energy of $\sqrt{s} = 18$ TeV and an instantaneous luminosity of $\mathcal{L} = 10^{33}$ cm^{-2}s^{-1}. At the La Thuille workshop in 1987 however, this was already decreased to $\sqrt{s} = 16$ TeV, just to be decreased again in the first "Conceptual Design Report" to the final value of $\sqrt{s} = 14$ TeV, while the instantaneous design luminosity was raised by one order of magnitude to the final value of $\mathcal{L} = 10^{34}$ cm^{-2}s^{-1} [69]. Additionally plans were made to also use the LHC for heavy-ion physics at $\sqrt{s} = 1000$ TeV with an instantaneous design luminosity of $\mathcal{L} = 10^{27}$ cm^{-2}s^{-1} to e.g. study the quark-gluon plasma.
When the construction started in 1998 the first collisions were scheduled to happen in 2008 at lower energies, followed by a ramp up to the final design energy in the following year. Unfortunately, while the first proton bunches were circulating, a major technical incident happened. After more than a year, in march 2010, eventually the first proton-proton collisions were recorded. One year later the LHC finally started to take data at large scale at half its design center-of-mass energy, at $\sqrt{s} = 7$ TeV, the highest center-of-mass energy reached so far. In 2012 this was increased to $\sqrt{s} = 8$ TeV. Afterwards the LHC entered an extended period of downtime to execute maintenance and to do upgrades of essential parts of the detectors as well as the collider. After the extended shutdown, the LHC resumed operation in 2015 at and a record-breaking center-of-mass

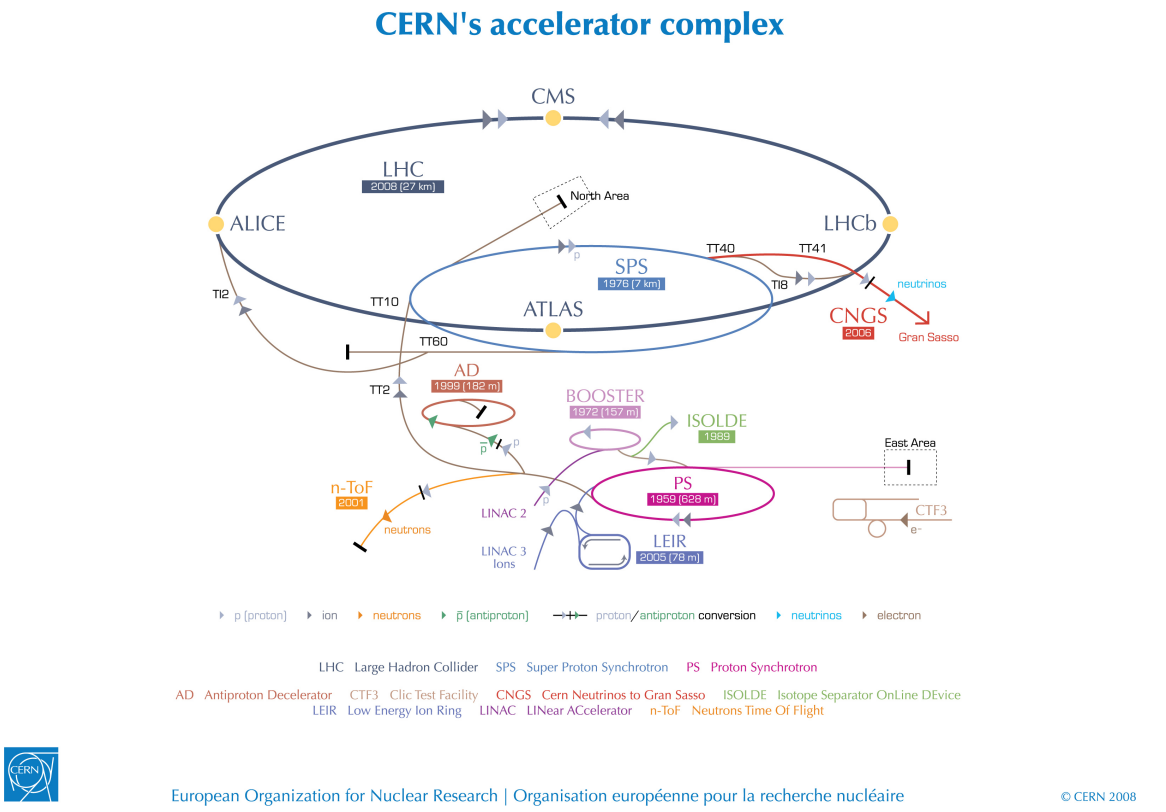

Figure 4.1.: Overview of the CERN accelerator complex and its current experiments as well as its individual accelerators. The years given below the names of the accelerators are the years they started operation. Figure from [68].

energy of $\sqrt{s} = 13$ TeV. The same energy at which it operates in 2016.
At the very beginning of the LHC's acceleration chain is hydrogen which is accelerated by a chain of individual accelerators to increasingly higher energies. A bunch of hydrogen molecules is at first separated into atoms and then stripped of its electrons by using an electric field to obtain protons. These are then injected into the *Linear Accelerator 2* where they are accelerated using radiofrequency cavities in conjunction with cylindrical conductors to about 50 MeV. In the next step protons are injected into the *Proton Synchrotron Booster* where they are accelerated to 1.4 GeV, followed by the *Proton Synchrotron* accelerating the protons to 25 GeV and the *Super Proton Synchrotron* which boosts the energy of the protons to 450 GeV. Eventually the protons are injected into the LHC's two beam pipes, in which the two beams circulate in opposite directions and are being accelerated to their final energy, 3.5/4.0 TeV in Run I (2011, 2012) and 6.5 TeV in Run II (2015, 2016) and eventually it will be risen to the design value of 7.0 TeV. On overview of CERN's current accelerator complex is depicted in Figure 4.1.
Some interesting details [70]:

- it takes 4 minutes and 20 seconds to fill each ring,
- it takes 20 minutes to accelerate the protons to their current maximum energy of 6.5 TeV,
- protons are circulating in the LHC in bunches each containing $\mathcal{O}(10^{11})$ protons,
- the minimal spacing between the bunches has been 50 ns throughout Run I and 25 ns throughout most of Run II.

Actually the LHC is not a perfect circle, but instead consists of 8 different straight sections followed by arcs connecting the different sections. To force the protons on a circular path throughout the arcs, magnetic fields of a strength of about 8.3 T are needed at $\sqrt{s} = 14$ TeV. These are generated by 1232 dipole magnets which make use of superconducting cables which are cooled down to 1.9K, cooler than the universe. Focusing of the bunches is done using 392 quadrupole magnets. The straight sections contain the accelerating cavities, the beam dump mechanism, two cleaning areas as well as four collision points where the main experiments are located [71]:

- A Large Ion Collider Experiment, *ALICE*, a special-purpose detector optimized to reconstruct heavy-ion collisions to study the quark-gluon plasma in more detail.
- LHC beauty, *LHCb*, a special purpose detector to study hadrons containing b-quarks to obtain hints about e.g. additional sources of CP violation.
- Compact Muon Solenoid, *CMS*, a multi purpose detector incorporating a strong solenoid magnet.
- A Toroidal LHC Apparatus, ATLAS, the other multi purpose detector at the LHC, acting as the counterpart of *CMS*. The data presented throughout this thesis is recorded using the ATLAS detector. Thus it will be discussed in more detail in the next section.

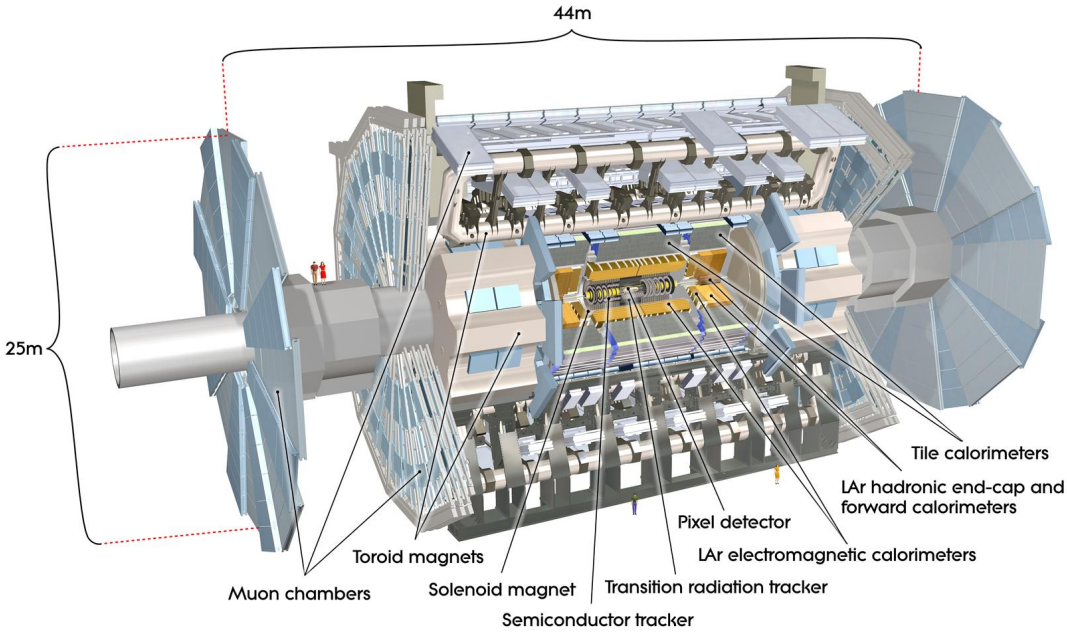

Figure 4.2.: The ATLAS detector and its subsystems. Figure from [74].

Three additional experiments are located at the LHC. They are not located at one of the four collision points, but instead focus on forward particles coming from nearby interaction points.

4.2. The ATLAS detector

The ATLAS detector, depicted in Figure 4.2, has been designed to be a multi purpose detector able to analyse both, proton-proton as well as heavy-ion collisions [72, 73]. It is about 44 meters long, 25 meters tall and weights 7000 tonnes. If one would wrap the ATLAS detector and flood the cavern, it would actually swim opposed to *CMS* which would actually sink.

By convention a right-handed cylindrical coordinate system is used to describe events in the ATLAS detector. The origin is placed in the center of the detector where the bunch crossings are expected to happen, the x-axis points towards the inner of the LHC-ring, the y-axis points up and the z-axis is chosen parallel to the beam axis. If quantities are measured, defined or calculated in the transverse plane, transverse is meant with respect to the beam axis: the $x-y$-plane. The azimuthal angle ϕ is measured in the transverse plane, while the polar angle θ is measured with respect to the z-axis. $\phi = 0$ corresponds to the positive x-axis. Instead of the polar angle the pseudorapidity, η, is used, because

differences in η are invariant under Lorentz-boosts along the z-axis[1]:

$$\eta = -\ln\left(\tan\left(\frac{\theta}{2}\right)\right). \tag{4.1}$$

Since particles usually have a very high energy at the LHC compared to their rest-mass, their energy becomes approximately equal their momentum and thus the pseudorapidity becomes approximately equal to the rapidity y often used in high-energy physics. The distance between two particles, ΔR, in ATLAS is usually expressed in differences in η and ϕ:

$$\Delta R = \sqrt{\Delta\eta^2 + \Delta\phi^2}. \tag{4.2}$$

ATLAS is built cylindrically symmetric to cover the complete solid angle around the interaction point. The different sub-detectors of ATLAS are arranged in an onion-like structure, each specialized for different types of physics. Their aims are:

- cover the whole 4π-range,
- track the path of particles,
- measure their momenta,
- and measure their energy.

4.2.1. Inner Detector

The sub-detector closest to the interaction point is called the *inner detector* or *tracker*. Its outer diameter is 2.3 meters while being 7 meters long and covering the pseudorapidity range up to $|\eta| < 2.5$ [75, 72]. It has been designed to trace the path of charged particles. Since the *tracker* is located inside a strong magnetic field, the curvature of the particles' tracks can be used to determine their momentum. The transverse momentum resolution is $\sigma_{p_\mathrm{T}}/p_\mathrm{T} = 0.0004 \cdot p_\mathrm{T} \oplus 0.02$, where the $\oplus$ symbol indicates a quadratic sum and the p_T is measured in GeV. The ATLAS tracker system was made up of three sub-systems during Run I and is depicted in Figure 4.3.

Pixel Detector The innermost part throughout Run I was the *Pixel Detector*, in radial direction only 5.05 cm away from the interaction point. Roughly 82 million silicon pixels providing a spatial resolution of 12 µm are used, they are 50 µm x 400 µm in size and organized in 3 separate layers.

[1] As long as the particles' masses are negligible, because in that case the pseudorapidity becomes equal to the rapidity used in special-relativity. The assumption of negligible particle masses is usually well justified, because of the high center-of-mass energy which the LHC is operating at.

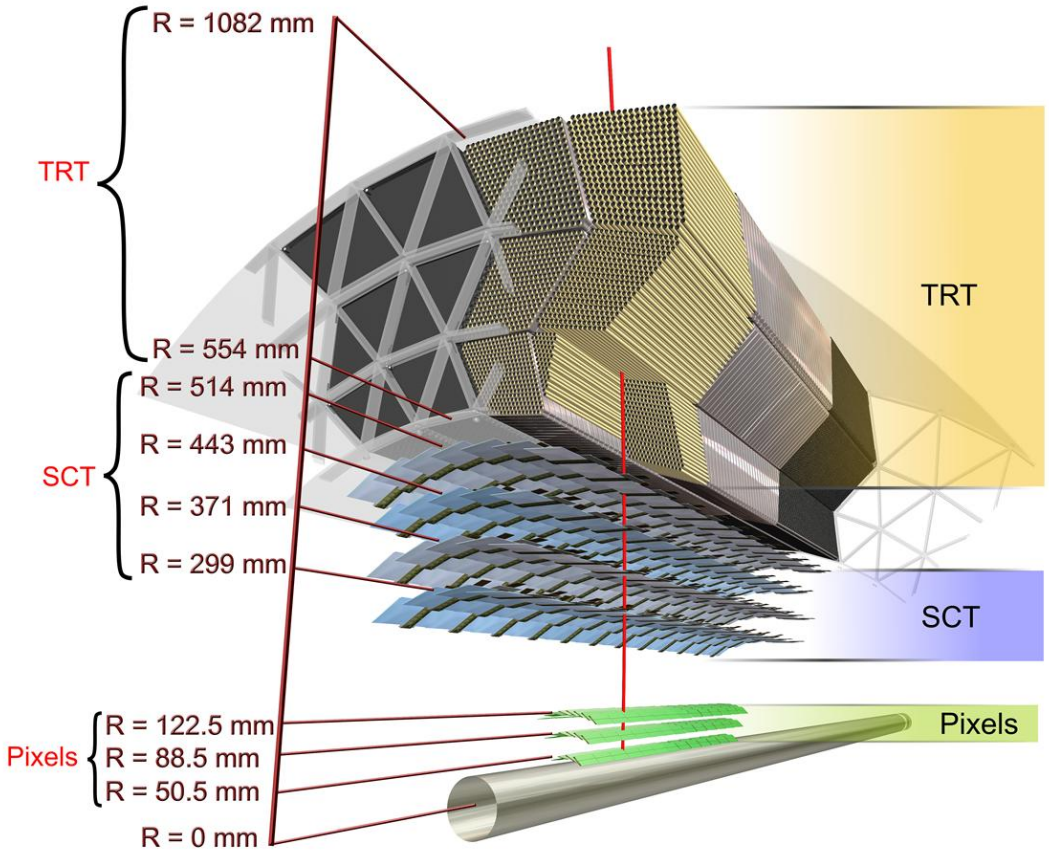

Figure 4.3.: The ATLAS inner detector and its subsystems. Figure from [76].

Semiconductor Tracker The next part is the *Semiconductor Tracker*, located about 30 cm from the interaction point. It consists of four layers of silicon strips. Each strip having a size of 80 µm x 12 cm and a spatial resolution of 17 µm in the direction transverse to the readout strips placed on the silicon, while having a resolution of 580 µm in the z-direction. In the barrel region four layers are installed, while in the end-cap section 9 are installed on each side.

Transition Radiation Tracker Last but not least in the *inner detector* is the *Transition Radiation Tracker*. It starts about 55 cm from the interaction point and contains about 300 000 straw drift tubes made of Kapton filled with a mostly Xenon based gas mixture. Materials with alternating optical density have been used. Charged particles passing through the boundary of two layers of different optical density emit photons proportional to E/m. The photons ionize the gas mixture in the tubes, thus making it possible to distinguish between electrons and hadrons.

IBL and Run II During the long shutdown period between Run I and the start of Run II, a new layer was inserted into the tracking system in between the beampipe and the Pixel Detector, the insertable B-layer, *IBL*. Since the IBL is even closer to the interaction point than the Pixel Detector, new read-out chips and new silicon-based sensor technologies had to be developed to cope with the high radiation as well as the high occupancy. By reducing the size of the pixels an improvement in the physics performance could be achieved. [77].

4.2.2. Calorimeters

Calorimeters are used to measure the energy of incoming particles. Common feature of all calorimeters is that the measurement process is destructive, meaning that after the measurement the particle is fully absorbed, it will not be available for further measurements. The ATLAS calorimeters are depicted in Figure 4.4: the systems "Tile barrel", "Tile extended barrel" as well as the liquid argon (LAr) hadronic end-cap systems make up the hadronic calorimeters, while the liquid argon electromagnetic barrel and the liquid argon electromagnetic end-cap systems make up the electromagnetic calorimeter [78, 79].

Electromagnetic Calorimeters The electromagnetic calorimeters are designed such that electrons and photons will loose all their energy via pair production and bremsstrahlung. Thus the energy deposited by an electron or photon inside the calorimeter will be proportional to the total initial energy of the particle. The electromagnetic calorimeter is divided into two regions, the barrel region, $|\eta| < 1.475$ and the end-cap region, $1.375 < |\eta| < 3.2$. It achieves an energy resolution of $\sigma_E/E = 10\%/\sqrt{E} \oplus 0.7\%$, where E is measured in GeV and the $\oplus$ symbol indicates a quadratic sum [78].
It is made of alternating layers of active and passive material. Lead is used as passive material while liquid argon is used as active material. The passive material is used to

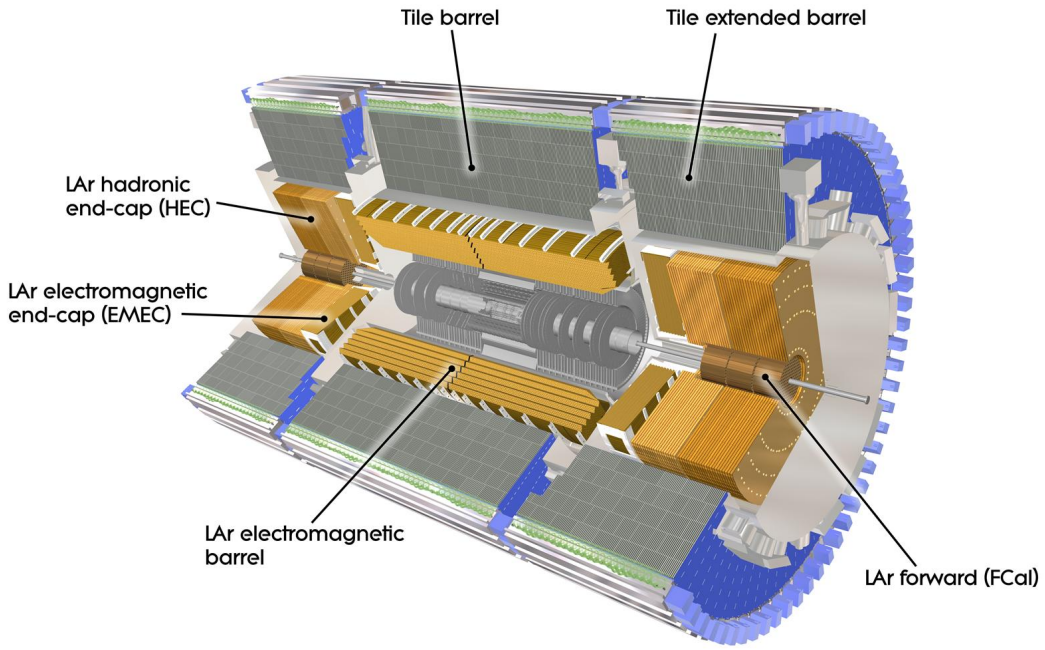

Figure 4.4.: The ATLAS calorimeter systems. Figure from [80].

absorb incoming particles: while passing through the passive material, particles emit bremsstrahlung and electron-positron pairs, which is also called showering. The active material on the other hand is used to measure the energy of the created shower originating form the incoming particle.

Hadronic Calorimeter While hadrons also deposit energy in the electromagnetic calorimeter, they do not deposit all their energy there. Consequently a second calorimeter is needed to measure the energy of hadrons. This feature is used in the reconstruction of leptons and hadrons to distinguish between them. The energy resolution of the *hadronic calorimeter* is $\sigma_E/E = 50\%/\sqrt{E} \oplus 30\%$, where E is measured in GeV and the $\oplus$ symbol indicates a quadratic sum [78, 79]. The layout is similar to the layout of the *electromagnetic calorimeter*, it also uses alternating active and passive materials. To stimulate interactions between the active material and hadrons a cost-efficient material of high-density is chosen. In the barrel region, spanning the pseudorapidity range $|\eta| < 1.7$, iron is used as the active material, while scintillating plastic tiles are used as the passive material, hence the name *Tile Calorimeter*. The end-cap region, $1.5 < |\eta| < 3.2$, of the *hadronic calorimeter* is using copper and liquid argon as active and passive materials respectively.

4.2.3. Muon Spectrometer

The last sub-detector is the *Muon Spectrometer*. Since interactions of leptons in the *electromagnetic calorimeter* scale with the inverse of the particle's mass, muons will not be absorbed by the calorimeter system. This makes it possible to identify muons with high accuracy, because they are the only particles which leave the calorimeters[2]. In ATLAS the muon spectrometer consists of four different sub-systems [72]:

- The *Monitored Drift Tubes* cover the area $|\eta| < 2.7$. They are approximately 3 cm thick and filled with an Argon-CO_2 gas mixture. When muons cross atoms are ionized and drift to the wall of the tube, while the electrons drift towards the central wire.
- *Cathode Strip Chambers* are used to complement the Monitored Drift Tubes in the more forward area of the detector, $2.0 < |\eta| < 2.7$. They are being used in the central area of the end-caps, because they are more stable with respect to higher particle rates. A single chamber consists of crossed anode strips and cathode copper wires. Muons passing through ionize the contained gas. The ion and the electrons then drift towards the cathode and the anode respectively, causing a measureable signal. Since the anode and cathode are crossed, positional information can be extracted.
- *Resistive Plate Chambers* are similar to the *Cathode Strip Chambers*, however instead of the strips and wires, plates are used as electrodes which are placed only 2 mm apart from each other, resulting in a faster response time, making them suitable for triggering events. Resistive Plate Chambers are used in the region $|\eta| < 1.05$.
- *Thin Gap Chambers* again are similar to *Cathode Strip Chambers*, but instead the distance between the wires is smaller than the distance between the wires and the anode. Their response time is also fast and thus they are also suitable to trigger events. Thin Gap Chambers are used in the region $1.05 < |\eta| < 2.4$.

The *muon spectrometer* is depicted in Figure 4.5, it is the outermost sub-detector of the ATLAS detector and thus also the largest. This huge scale makes high precision measurements of the transverse muon momentum possible. The resolution for muons is quite good, it is only about 3% for 100 GeV muons.

4.2.4. Magnets

To extract momenta of charged particles, the bending of their tracks inside magnetic fields is used. However at the LHC particles which are created usually have rather high energies. Consequently also strong magnetic fields are needed to achieve well measurable curvatures of the particles' tracks.

[2]Except for neutrinos of course, however since they only interact weakly, they are not detectable in ATLAS in one way or another.

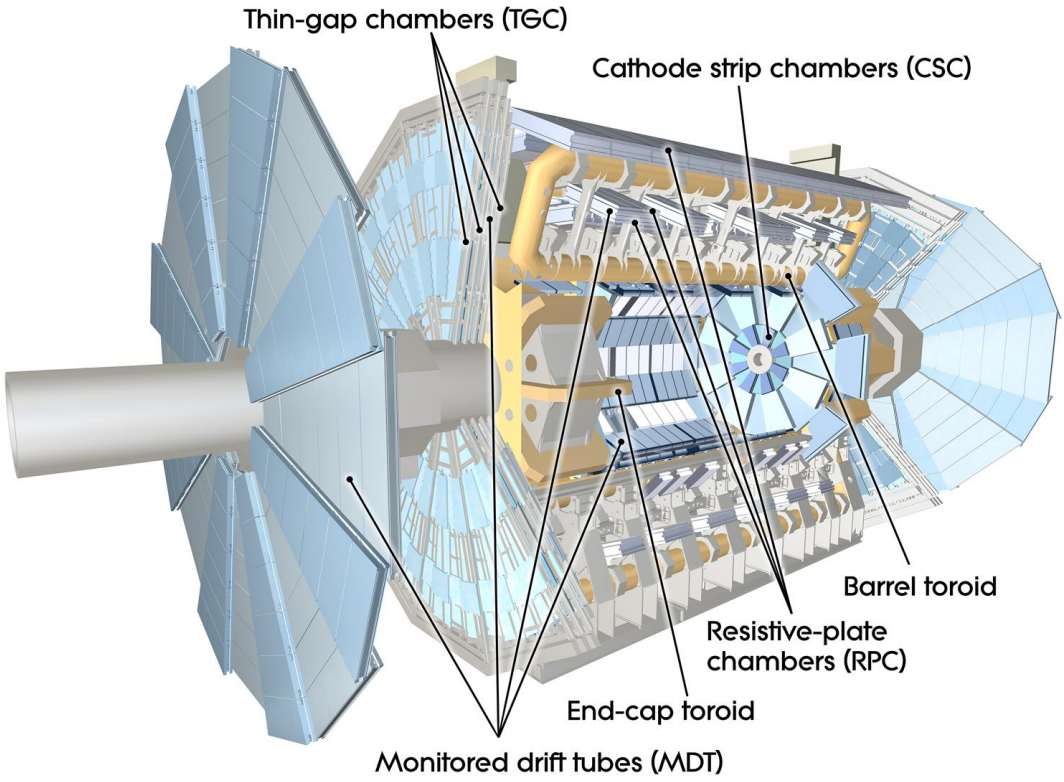

Figure 4.5.: The ATLAS muon systems. Figure from [81].

Superconducting magnets are used to generate the magnetic fields needed. In the inner region of ATLAS detector a solenoid magnet is used to generate a homogeneous field with a bending power of 2.1Tm. The field in the outer detector region, meaning the muon spectrometer, is generated by eight toroid magnets in the barrel region and two end-cap magnets in the end-cap regions, creating fields achieving a bending power of 3Tm in the outer region and 6Tm in the end-cap region.

4.2.5. Forward Detectors

To also cover the forward region, $3.1 < |\eta| < 4.9$, a calorimeter using liquid argon as active material is installed. It is divided into three parts which are distinguished by the passive material used. The first part uses copper and is optimized for electromagnetic measurements, whereas the second and third one use thungsten to predominantly measure the energy from hadrons. In addition, special purpose detectors exist outside the ATLAS cavern, one example being the *Zero Degree Calorimeter*. They are used to study the range $|\eta| > 8.3$. However the forward detectors are not used in the presented analyses.

4.2.6. Trigger and Data Acquisition

At a bunch spacing of 25 ns collisions happen in ATLAS at a rate of 40 MHz. All the data recorded in one event usually takes up approximately 1.5 Mb of disk space. Thus recording each and every event would not just require an enormous bandwidth, but also far too much disk space, approximately one petabyte per second[3]. Consequently, a system to filter events already prior to recording them to disk is been used, the *trigger system*.
The system has been split into three levels during Run I [72, 82] and is being split into two levels in Run II [83, 82] which subsequently filter events. Each level has a given amount of time to determine whether an event is interesting or not. Subsequent levels build on the information of prior levels and extend it by taking into account additional detector systems and computing further derived quantities.
The first level, L1, is implemented completely in hardware, reducing the trigger rate to about 75 kHz. It takes inputs from the calorimeters and the muon spectrometer and defines so called *Regions of Interest*, RoIs, areas in which signatures of particles have been identified. If L1 deems an event to be interesting, it is passed on to the *Read out Drivers*, *RoD*s.
In Run I information from the *RoD*s has been passed on to L2, which has been implemented solely in software, meaning that it is being processed on a computing farm. L2 only reads information within the RoIs to save bandwidth. Using information from all ATLAS subdetectors it examines the RoIs with higher precision, computing more complex, derived, quantities and reducing the event rate to about 3.5 kHz.

[3]Most of the currently available hard disk drives provide about one to five terabyte of space, three orders of magnitude less.

Eventually in Run I the data was processed by the *Event Filter*, EF. The EF trigger level ran algorithms similar to the actually used algorithms in the main physics analysis, making use of the full event information. It reduced the event rate to about 600 Hz and steers the final decision of whether an event is written to disk or not [84].
Quite often lower values are quoted for the L2 and EF rates, namely 2 kHz and 200 Hz respectively. These are the design values. During Run I the data output performed better than had been anticipated, thus the rates could be raised.
Between Run I andRun II the trigger system has been reworked. L2 and the EF have been merged and become the *High Level Trigger*, short HLT. It mostly focuses on the RoIs found by L1. However contrary to the Run I L2, unseeded reconstruction is also possible at the HLT level. In addition new algorithms have been developed. While the available network bandwidth was a major bottleneck throughout Run I, merging of L2 and EF into the HLT improved the situation, because lots of transfers via the network could be changed into in-memory transfers. For Run II the actual rate of the L1 trigger could not yet be pushed close to its to design value of 100 kHz, with a maximum rate of 80 kHz it is still behind expectations due to bandwidth limitations [84, 85], while for the HLT trigger the rates could be pushed to its design value of 1 kHz and beyond [84, 85].

4.3. Computing and the Grid

ATLAS alone records several petabyte of data each year of running. In addition an approximately equal amount of simulated events is needed. Simulating a single event takes several seconds. However to obtain feasible predictions several billion of events are needed: a task which cannot be executed on a few computers alone, but instead involves the coordinated power of several computing farms.
This challenge is addressed by CERN's Grid [86, 87, 88, 89]. It is a global computing infrastructure. It provides scientists around the world and especially the experiments at CERN with the computing resources to store, distribute and analyse the data generated. More than 42 countries are involved, contributing more than 170 computing centres, often called sites, as well as several hundred petabytes of storage.
The Grid is split into different levels of access and importance, called tiers. *Tier-0* is located at CERN and probably the most important tier. It is responsible for recording data, reconstructing and distributing it. *Tier-1* sites are used for permanent storage of data as well as re-processing and analysing it, whereas Monte Carlo simulation and user analysis jobs are being run on *Tier-2* sites. Scientists access the Grid either via their computing farms at their institutes, which are called *Tier-3* sites, or via their own computers, classified as being *Tier-4* sites.

5. Dataset

This chapter will very briefly summarize how the simulation of the Monte Carlo samples works as well as which datasets will be used. Special emphasis will be put on the fast simulation used by the ATLAS experiment, specifically its performance when modeling substructure observables. A complete list of simulated datasets and the generators used to simulate them can be found in section A.1 of the appendix.

5.1. Simulation of Datasets

Simulation of events in high energy physics is a science on its own. Many different processes need to be taken into account. Lots of different interactions need to be accounted for. Everything needs to be treated in one way or another.
The first step in the simulation chain is to calculate the involved matrix elements for the hard scattering process as well as the subsequent decays [90, 91]. Phrasing it differently: the Feynman graph is being drawn and evaluated. Afterwards the parton shower is being generated. It is the cascade of colored particles which is being created by colored particles in the final and initial state by emitting additional gluons and quarks until they eventually reach a (semi-)stable state by forming hadrons. Already at this stage going through the whole framework of particle physics would take far too much time and is not feasible anymore, because the problem becomes too complex. Thus simpler models are used as approximations. Next the *underlying event* or *pile-up* is being added: since single particles cannot be brought into collision easily, bunches of particles are being collided, consequently not only one pair of protons interacts, but several. Additionally, the proton itself is a composite object and thus several partons might interact[1]. As a result, not just one, but several, superimposed events are observed in the detector. The one with the highest sum of transverse momenta is usually considered to be the one of interest to the analysis. The *underlying event* is added to the hard-scatter event either by adding minimum bias events on top of the hard-scatter event or by superimposing additional simulated events on the simulated hard-scatter event. Afterwards hadronization takes place, meaning that the colored (semi-)stable particles form hadrons. Not much is known about the process of hadronization so this is again being modeled by approximate models. However hadrons do not necessarily need to be stable. Eventually the decay of hadrons is being simulated.

[1] Recently the fraction of events arising from double-parton interactions in the production of W bosons in association with two jets has been measured. It was found to be 0.08 ± 0.01 (stat.) ± 0.02 (sys.) [92]. In four-jet events it was found to be $0.092^{+0.005}_{-0.011}$ (stat.)$^{+0.033}_{-0.037}$ (sys.) [93].

After hadronization the particles are handed over to programs simulating the interaction of the particles with the detector material. The ATLAS collaboration uses two different simulation chains to simulate the response of the detector to the passing particles, the *Full Detector Simulation* and the *Fast Detector Simulation*. However they both differ only in the treatment of the calorimeters. The propagation of the particles through the rest of the detector is handled by *GEANT4*, a toolkit for the simulation of the passage of particles through matter [94]. In the end the simulated detector response is written to disk and digitized similarly to the real experimental data.

5.1.1. Calorimeter Simulation

In case of the *Full Detector Simulation GEANT4* [94] is used to simulate the propagation of the particles through the calorimeters. This is rather costly, because the particle track will be broken down into many smaller steps. At each step individual processes are applied which may alter the particle's properties as well as the properties of the surrounding material, the direction of the particle might for example be changed or it may deposit energy in the material, even new particles might be created by e.g. bremsstrahlung. Using Monte Carlo methods the stochastic nature of showering in the calorimeters is thus well captured.
The fast calorimeter simulation instead uses a custom, self-written, calorimeter simulation called *FastCaloSim* [95, 96]. Instead of operating at the same level of granularity as *GEANT4*, *FastCaloSim* uses averaged, parametrized, shower shapes [95]. Thus the interaction with the material is not simulated, but instead it is obtained from a parametrized template. The advantage is that far less computing power is need and thus more Monte Carlo events can be generated. However the downside is that it is less accurate since everything is averaged out. Especially the tails of variables sensitive to the substructure of showers, like e.g. the lateral extension of a shower, will be mismodeled, because fluctuations are essentially missing in this approach. However the parametrization and the shower shapes have been tuned such that they model observables on the physical level, like e.g. the transverse momentum of a particle, well.
This can be seen in Figure 5.1, which shows the p_{T} as well as ϕ distributions of pions in a simulated particle gun experiment using 50 GeV pions. In a particle gun experiment particles are initialized with fixed conditions, instead of simulating a complete collision. In this case only a single pion has been used. In order to obtain a clean comparison of the two different calorimeter simulations, pile-up is not included in the simulation of the samples.

5.1.2. Performance of Substructure Observables in Fast Simulation

While *FastCaloSim* has been tuned to get observables on the physical level right, it could not be tuned to get substructure related variables right. The problem is that the approach used by *FastCaloSim*, namely to use parametrized templates, inherently lacks the stochastic part of the processes which are taking place. If quantum mechanics would

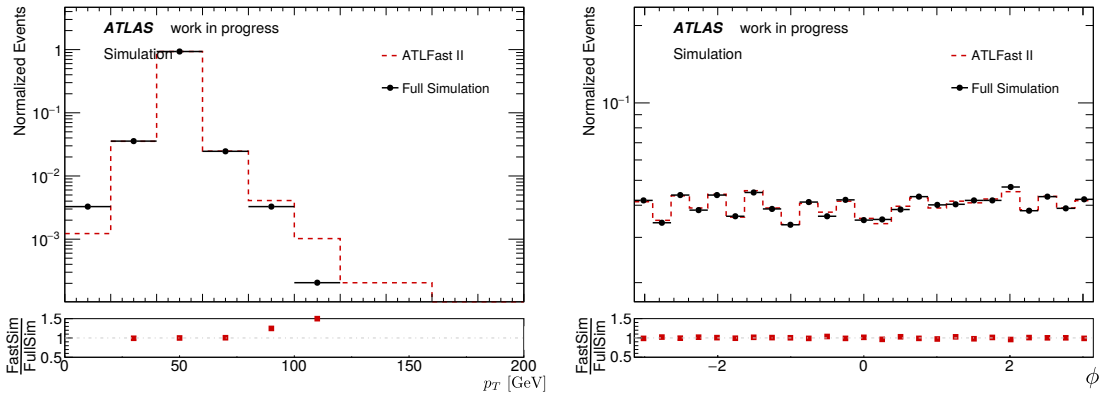

(a) p_{T} [GeV] **(b)** ϕ

Figure 5.1.: The (a) p_{T} and (b) ϕ distributions of 50 GeV pions injected into ATLAS in a simulated particle gun experiment to compare the performance of the full simulation, black dots, versus the fast simulation, red dashed line. Both perform rather similar, because the fast simulation has been tuned to reproduce the full simulation on the physical observable level.

be deterministic there would not be a stochastic part and thus both methods should yield qualitatively the same results.
Energy deposits in the calorimeter are usually grouped into groups of close-by deposits, called clusters. By analyzing these clusters, grouping those and adding information from the inner detector as well as the muon spectrometer, particles are identified. Looking at the transverse and lateral extensions of the clusters associated to the pions from the aforementioned particle gun experiment in Figure 5.2, it can be inferred that full and fast simulation do not agree well anymore. This is a result of the missing fluctuations in *FastCaloSim*.
However one has to remark here, that the comparison shown is not the complete truth. We compare one simulation to another. Both use approximations to obtain results. Thus it can only be judged whether full and fast simulation perform similar, but a final conclusion which simulation performs better cannot be drawn. To be able to tell which simulation performs better both have to be compared to data. This is left for future studies.

5.2. Data Taken Using ATLAS

The data which will be analyzed in the following has been recorded using the ATLAS detector during 2012 and 2015 at a center-of-mass energy of $\sqrt{s} = 8$ TeV and $\sqrt{s} = 13$ TeV respectively. To filter events where the detector was not working correctly, a *good runs list*, GRL, has been used. A total of 20.3 fb^{-1} of usable data has been collected in 2012, a total of 3.5 fb^{-1} in 2015. While the complete 2012 data was recorded using a 50 ns bunch spacing, most of the 2015 data has been recorded using a 25 ns bunch spacing.

Since however the Monte Carlo datasets used in this analysis for the 2015 data were simulated using a 25 ns bunch spacing, the effectively usable amount of data from the 2015 data reduces to about 3.2 fb^{-1}.

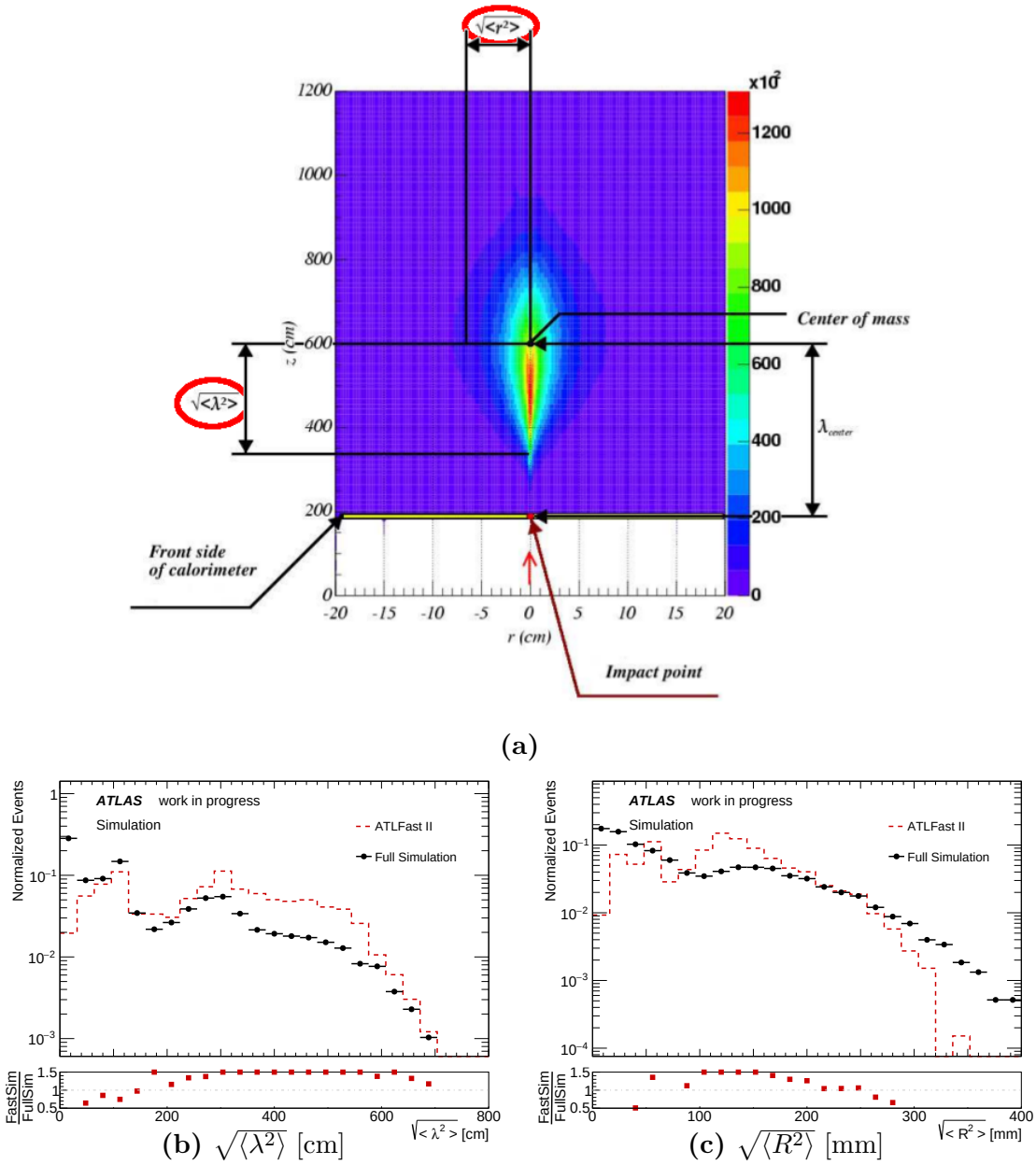

Figure 5.2.: (a) Exemplaric illustration of a shower in the calorimeter. $\sqrt{\langle R^2 \rangle}$ is the square-root of the energy weighted mean of the squared distance of all energy deposits associated with the particle with respect to the shower's center of mass in the *transverse* direction. It is a measure of the transverse extension of a shower. $\sqrt{\langle \lambda^2 \rangle}$ is the square-root of the energy weighted mean of the squared distance of all energy deposits associated with the particle with respect to the shower's center of mass in the *longitudinal* direction. It is a measure of the longitudinal extension of a shower. The (a) $\sqrt{\langle \lambda^2 \rangle}$ and (b) $\sqrt{\langle R^2 \rangle}$ distributions of 50 GeV pions injected into ATLAS in a simulated particle gun experiment to compare the performance of the full simulation, black dots, versus the fast simulation, red dashed line. On the substructure level fast and full simulation do not agree well anymore, because fluctuations are essentially missing in fast simulation.

6. Object Definitions and Discriminating Variables

The data being recorded by the ATLAS detector and in Monte Carlo simulations is the response of the detector to particles. Before being able to identify the objects of interest, the detector response needs to be translated into meaningful quantities like the measured deposited charge, the measured light and similar. This step is called digitization. Afterwards this information is connected to build higher level information like tracks and to identify energy deposits. Eventually, the actual reconstruction algorithms are run, using the previously generated information to identify particle candidates.
However in any case all information about an event cannot be recorded, thus it is not possible to reproduce the complete decay chain. As an additional complication not just one but several interactions take place during one bunch crossing. As a result, several events are superimposed, detector signals from different particles might overlap. Consequently the reconstruction algorithms need to work very precisely. Each particle passing through the detector leaves its footprint, because its interaction with the detector subsystems depends highly on the particles properties, like its mass or its quantum numbers. Shower shapes in the calorimeter will be quite different for e.g. electrons, muons and jets. This is being exploited in the reconstruction, by training the reconstruction algorithms on simulated data sets, where all information about the decay, the so-called truth information, is available: one exactly knows what happened. The following aims to provide a brief overview of how reconstruction algorithms define particles. Additionally the procedure to remove overlaps between particle candidates is explained, followed by the selection applied to events to ensure that all parts of the detector are working correctly. In the end, observables like the transverse mass will be defined. The main analyses presented in this thesis are photon agnostic, so photons will not be discussed in the following.

6.1. Primary Vertex and Pile-up

At particle accelerators bunches of particles are brought to collision, several particles might interact throughout one bunch-crossing at different locations in the detector. The location where a collision occurred in the detector is called a *collision vertex*. Collision vertices can be reconstructed by reconstructing all inner detector particle tracks and extrapolating them to $r = 0$. They have to fulfill requirements on the number of hits in the silicon tracker as well as have a transverse momentum of at least 400 MeV. In Run I the primary vertex candidates had to have at least 3 associated tracks, while

in Run II this requirement was lowered to two. The candidates were sorted by the sum of the squared transverse momenta over the associated tracks. The one with the highest sum becomes the *primary vertex* [97]. All other collision vertices in the same event are considered to be *pile-up*. In the analyses presented in this thesis pile-up vertices are only used to apply corrections to the measured particle energies[1]. Usually 20 to 40 simultaneous interactions are happening throughout one bunch crossing at the LHC. The definition of pile-up phrased differently: pile-up collisions are secondary interactions happening throughout one bunch-crossing, they aren't considered to be of physical interest, because the energy-exchange is lower than in case of the primary vertex, however they have to be used to correct particle energies.

6.2. Electrons

In the region $|\eta| < 2.5$ electron candidates are first of all identified using the inner detector and the electromagnetic calorimeter [98]. Since electrons are electrically charged, they leave tracks in the inner detector. An electron candidate is identified by a cluster in the electromagnetic calorimeter having $E_T > 3$ GeV and a track from the inner detector matched to it within $|\Delta\eta| < 0.05$ and $|\Delta\Phi| < 0.10$. Additionally the momentum of the inner detector track may not exceed ten times the energy of the cluster inside the electromagnetic calorimeter. Since the inner detector only extends up to $|\eta| < 2.5$, electron candidates in the region of $2.5 < |\eta| < 3.7$ are identified using the electromagnetic calorimeter only. Thus the efficiency of electron reconstruction in that region is not as high as in the more central region, except if specific processes are investigated, e.g. the decay of heavy particles which constrain the invariant mass, therefore they are not used in the presented analyses.
However jets will also leave tracks in the inner detector and they will also deposit energy in the electromagnetic calorimeter. Consequently electron candidates are further grouped into categories depending on quality criteria on the shower shape, track quality and the track cluster matching, to account for the different needs of different analyses. The tighter these criteria, the more electron candidates will be rejected, while the remaining electron candidates become more likely to be real electrons. Cut-based, as well as likelihood based, criteria were available [98] in Run I, however, only the cut-based criteria will be used in the presented Run I analysis and thus the likelihood based ones will not be discussed. Throughout Run I the available quality criteria were:

- *loose++*: $|\eta| < 2.47$, limited leakage into hadronic calorimeter, constrained shower shape in the second layer of the electromagnetic calorimeter
- *medium++*: *loose++* criteria, constrain shower shape in the first layer of the

[1] Showers created by particles from pile-up vertices might overlap with showers from particles originating from the primary vertex and thus the showers might get merged, although they were originally two distinct particles, causing the measured energy of the reconstructed particle to be higher than it should. To compensate for this corrections are applied to the reconstructed particles. Details about the corrections can be found in the references for each of the particles.

electromagnetic calorimeter, require hits in the pixel detector and scilicon tracker, constrain transverse impact parameter $|d_0| < 1$ mm

- *tight++*: *medium++* criteria, require isolation, meaning the transverse energy around the candidate in a $\Delta R < 0.2$ cone has to fulfill requirements with respect to the candidates total transverse energy, at least one hit in the vertexing layer is required, hits in the transition radiation tracker are required, matching between clusters and tracks is narrowed

In Run II the electron identification changed. Instead of the cut-based approach to identify electrons, a likelihood-based identification has been developed. The reconstruction, the initial selection of the electron candidates, however remained the same. Also the set of variables used to identify electrons remained mostly the same [99, 98]. The likelihood-based selection criteria have been re-optimized yielding signal efficiencies of approximately $\sim 95\%, 90\%$ and 80% for the *loose, medium* and *tight* working points respectively [100], the corresponding background efficiencies ranging between: 0.8% and 0.3% [100].
For Run I and Run II, correction factors have been obtained by the ATLAS egamma combined performance group to account for mismodeling of the trigger system in simulation as well as different identification efficiencies observed between data and simulation. The presented Run I analysis uses electrons identified by the *medium++* quality criteria, while the Run II one uses the *loose* quality criteria.

6.3. Muons

Muon candidates are being grouped into three different categories, depending on which detector subsystems they use and depending on how they use these informations [101, 102, 103]. As in the case of electrons, scale factors need to be applied for muons. These have been obtained by the ATLAS muon combined performance group. Muons stemming from cosmic processes are discussed in section 6.8.

Standalone Muons *Standalone* muons are identified using the muon system alone. It extends up to $|\eta| < 2.7$. Tracks are reconstructed by extrapolating the track obtained in the muon system back to the origin. However this mode is not suitable for rather soft muons, because they might be stopped before reaching the muon system. The momentum of the muons is corrected for energy loss in the calorimeter.

Combined Muons Identification of *combined* muons uses information from the muon system as well as the inner detector. Full tracks from the inner detector are matched against full tracks in the muon system[2]. Different algorithms exist to do the combination of inner detector tracks and muon spectrometer tracks. The one which will be used in

[2]The inner detector as well as the muon system consist of several layers. A track is called a full or complete track if there is a hit in each layer associated with this track.

this analysis is the *staco* algorithm [104, 102, 105]. If they can be successfully combined, the impact parameter of the muon with respect to the primary vertex is calculated from the inner detector track.

Segment/Calorimeter Tagged Muons *Tagged* muons make use of information coming from the inner detector, the muon chambers, as well as the calorimeters. If a track from the inner detector can be matched to an energy deposit in the calorimeters compatible with a minimum-ionizing particle, it is called a *calorimeter-tagged* muon. If however the track can be extrapolated to a track in the muon chambers which is not complete, it is called a *segment-tagged* muon.

Differences Between Run I and Run II While in Run I the track from the inner detector and the one from the muon spectrometer have been usually combined using the so called *staco* algorithm, as mentioned before, in Run II an additional global fit is performed. The quality of this fit is used in the identification step of the muons to define different levels of selection criteria to address the needs of different physics analyses [103], which were not available in Run I. Four categories have been defined, three inclusive ones plus an additional category targeting analyses requiring high transverse momentum muons: *loose, medium, tight* and *high-*p_{T}.

- *loose*: specifically optimized to identify Higgs-boson candidates in the four lepton final state. All muon types are included.

- *medium*: the default criteria used in ATLAS. Designed to minimize systematic uncertainties. Only combined and standalone muons are used. Requirements on the hits in the muon chambers are imposed. Loose criteria on the compatibility between the inner detector and muon spectrometer momentum measurements are imposed, suppressing hadrons misidentified as muons. The charge to momentum significance is required to be less than seven.

- *tight*: the same criteria as for *medium* muons are applied. Additionally only combined tracks are considered and further requirements on the tracks as well as on the normalized χ^2 of the global fit of the combined track are applied.

- $high-p_{\mathrm{T}}$: a selection optimized to maximize the momentum resolution for tracks with high transverse momenta, specifically targeting W' and Z' analyses. Combined muons are used with additional requirements on the number of hits in the muon chambers. Regions where the alignment of the muon chambers is not optimal are vetoed.

In the Run I analysis segment tagged muons are used, while in the Run II analysis muons passing the *medium* quality criteria are used.

6.4. Taus

Taus are tricky objects to reconstruct. Their lifetime is only about $\mathcal{O}(10^{-13}$ s) [6], thus they decay before reaching the inner detector, inside the beam-pipe. Thus taus cannot be observed directly, but instead only via their decay products. However, the leptonic decay channels of the tau cannot easily be separated from other light leptons originating from the main interaction. Instead one has to use the hadronic decay channel of the tau. Several pions are usually created in hadronic tau decays. They are grouped by the number of charged pions which are created. To make up for the initial charge of the tau, the charged pions have to be created in odd numbers. Thus hadronically decaying taus are said to be *1-prong* taus if only one charged pion is created, analogously they are called *3-prong* taus if three charged pions are created. These decay modes can be distinguished by counting the number of tracks in the inner detector associated with the hadronically decaying tau.
The tau reconstruction is seeded by jets [106], defined in the next section. A tau candidate's jet has to have a transverse momentum of at least 10 GeV. Since information from the inner detector is used it also needs to be in the central region of the detector, $|\eta| < 2.47$. Tracks within a $\Delta R = \sqrt{(\Delta\eta)^2 + (\Delta\phi)^2} = 0.2$ cone and a transverse momentum of at least 1 GeV are associated to the tau candidate. Furthermore requirements on the number of hits in the pixel detector and the silicon tracker are imposed. To reject taus from pile-up, cuts on the impact parameter with respect to the tau vertex are also applied. Simply speaking, the tau vertex is the interaction vertex which the tracks of the tau are pointing to. For higher-p_{T} objects this is most often the primary vertex as defined later.
Due to the difference in the decay of taus with respect to jets originating from a quark or a gluon in the hard-scattering event, taus are corrected to the tau energy scale. It is calibrated independently of the *Jet Energy Scale*. A Monte Carlo based procedure is used which derives corrections by comparing the true and the reconstructed energy in simulated events. Additional corrections are applied on top which have been derived using a data-driven method [106].
These requirements however do not allow for an efficient discrimination of taus against jets. Consequently a separate identification step is needed. Discriminating variables based on the tracks and the clusters associated to the tau candidate are used. Separate boosted decision trees have been trained based on these variables for 1-prong and 3-prong taus. The 5-prong channel is heavily suppressed, the many particles involved render the possible phase-space small [6], therefore there hasn't been a separate training for 5-prong taus. Three different working points have been defined, *loose*, *medium* and *tight*, to yield a flat signal efficiency for 1/3-prong taus of approximately: 70%/55%, 60%/40% and 40%/30%.
1-prong taus are also likely to be faked by electrons, thus additional discrimination against electrons is provided using an *electron veto*, exploiting the fine differences between electrons and 1-prong taus.

- Transition radiation is more likely to be emitted by an electron and thus their hits

in the transition radiation tracker usually trigger an even higher threshold than hadronically decaying taus do.

- The angular distance of the associated track to the direction of the shower in the calorimeter.
- The ratio of energy deposited in the electromagnetic and hadronic calorimeters, which should be lower for electrons.
- The amount of energy leaking into the hadronic calorimeter, because electrons should be mostly confined to the electromagnetic calorimeter.
- The ratio of the energy in the $0.1 < \Delta R < 0.2$ cone to the energy in the total core region $\Delta R < 0.2$, because showers caused by electrons are more constrained.

These are again fed into a separately trained boosted decision tree whose decision is used to veto potential 1-prong tau candidates stemming from prompt electrons.
Muons are already well rejected by removing any tau candidate which overlaps with a muon candidate, because hadronically decaying taus are unlikely to reach the muon spectrometer. The remaining contamination from muons is removed using the *muon veto* which compares the measured momentum and the measured energy of the candidate. For high energetic muons which are being stopped in the calorimeter the fraction of energy deposited in the electromagnetic calorimeter is low and the track-p_{T}-to-E_T ratio is large, while for low p_{T} muons which do not reach the muon spectrometer it is the opposite way around, the fraction of energy deposited in the electromagnetic calorimeter is large and thus the p_{T}-to-E_T ratio low. Simple cuts based on the track-p_{T}-to-E_T ratio and the fraction of energy in the electromagnetic calorimeter are used to reduce the muon contamination.
For Run II the tau reconstruction has been reoptimized [107]. The identification step as well as the rejection against jets have been developed along the same lines as for Run I. Mostly the same input variables have been used to train the boosted decision trees used to distinguish between jets and taus and to identify taus. One of the major differences being that a harmonization between the jet rejection on trigger and on analysis level took place. The changes to the input list can be found in [107]. A dedicated muon veto is not used anymore.
While the boosted decision tree classifier used to reject jets did not change considerably compared to Run I, the electron veto changed a lot, making use of the updates to the electron reconstruction. The electron reconstruction has been specifically optimized to distinguish charged pions from electrons. Since taus decay mostly to charged pions, the decision was made for Run II to change the electron rejection step in the tau identification to a simple overlap removal. Taus which can be matched to an electron candidate with $p_{\mathrm{T}} > 5$ GeV and a large likelihood score within a $\Delta R = \sqrt{(\Delta\eta)^2 + (\Delta\phi)^2} < 0.4$ cone are rejected.
The calibration of the energy of the taus has also changed slightly. While the energy scale is still corrected for by a simulation-based approach similar to the one used in Run

I, data-driven corrections are not available yet. Both presented analyses make use of taus passing at least the loose quality criterion.

6.5. Jets

Since the force between colored objects becomes stronger with increasing distance, opposed to the electroweak force where it is exactly the opposite, colored objects cannot exist freely. Thus they hadronize and form hadrons. Usually if a quark or gluon is created in the hard scattering event not just one, but several hadrons emerge due to conservation laws and the decay of unstable particles. Calorimeters can currently not be built fine-grained enough to resolve each single hadron. Instead the resolution of the calorimeters usually only allows for detection of several hadrons as a cluster. These clusters of hadrons are called *jets*.

Definition *Jets* are cone-shaped groups of hadrons and other particles [3]. In ATLAS the default algorithm to identify jets is the anti-k$_t$ algorithm [108]. It uses topological calorimeter clusters as input. Topological clusters are constructed by taking a *seed* cell from the calorimeter. The energy deposited in this cell has to be at least four times the noise level[4]. All neighboring cells which posses a signal to noise ratio of at least 2 will be added to the cluster seed. Eventually all cells neighboring the aforementioned cells will be added [109], independent of their signal to noise ratio.
Once all cluster candidates have been identified, they are being merged according to their distance. The distance between two clusters i and j or a cluster i and the beam axis B are defined as:

$$d_{ij} = \min\left(\frac{1}{k_{Ti}^2}, \frac{1}{k_{Tj}^2}\right)\frac{\Delta_{ij}^2}{R^2}, \tag{6.1}$$

$$d_{iB} = \frac{1}{k_{Ti}^2}. \tag{6.2}$$

Here k_{Ti} denotes the transverse momentum of particle i, $\Delta_{ij}^2 = (y_i - y_j)^2 + (\phi_i + \phi_j)^2$ denotes the distance between the particles in the $y - \phi$-plane, y being the rapidity $y = \frac{1}{2}\ln\left(\frac{E+p_z}{E-p_z}\right)$, while R is the distance parameter of the algorithm. In ATLAS, as well as in this thesis, jets are defined using a distance parameter of 0.4. For all clusters i the distances to all other clusters j and to the beam axis are calculated. If the distance of one of the clusters to the beam axis is smaller then all other distances, the cluster i is defined as a jet and removed from the list of available clusters. If not, the cluster i is merged with the cluster j which yields the smallest d_{ij} and another iteration starts. The advantage of this algorithm is that soft particles tend to cluster with hard particles

[3] Hadrons might also decay leptonically and thus leptons might be found inside a cone emerging from a colored object.

[4] The noise level is measured by computing the RMS of the energy distribution measured in events triggered at random bunch crossings [109].

stemming from the prompt interaction, making the algorithm robust against noise and pile-up.

Calibration and Resolution The problem with the aforementioned soft radiation is that it is highly possible that it does not stem from the original hard-scattering event, but instead from pile-up. Thus energy will be attributed to the jet which does not belong to it. To account for the additional energy of jets caused by pile-up a calibration procedure is introduced. *Jets* are calibrated to the so called *Jet Energy Scale*, *JES*. It is derived mainly from simulated samples and consists of an offset correction of E_T, based on the number of primary vertex candidates, giving an estimate of how much pile-up to expect inside the event, on the pseudorapidity, as well as the bunch spacing. In addition the direction of the jet is being corrected to originate from the primary vertex. Eventually a correction of the jet energy is applied which is based on the ratio of the truth jet energy to the reconstructed jet energy obtained from simulated samples [109]. The *Jet Energy Resolution*, *JER*, can be measured in-situ, exploiting the transverse momentum balance in events containing high p_{T} jets [110].

Pile-up Rejection In Run I a quantity called the *Jet Vertex Fraction*, *JVF*, has been used to distinguish between jets from the primary vertex and pile-up. From the tracks associated with the jet the transverse momentum stemming from the primary vertex has been computed and divided by the transverse momentum of all tracks associated with the jet [111]. If no tracks can be matched to the jet, the *JVF* will be set to a value of -1. A cut on this value of 0.64 is being used to suppress jets from pile-up. However, this introduces a strong dependence of jet-reconstruction on pile-up, because the more simultaneous interactions happen throughout one bunch-crossing the higher the probability that tracks from pile-up vertices are matched to a jet which originated from the primary vertex.
Thus in Run II the method changed. A new tool called the *Jet Vertex Tagger* has been developed [112]. It is a multivariate discriminant using two variables as input, the corrected jet vertex fraction, corrJVF, and R_{pT}, the ratio of the scalar sum of the tracks that are associated with the jet and originate from the primary vertex over the calibrated jet p_{T}. The corrected jet vertex fraction is computed similar to the jet vertex fraction, the only difference being that the transverse momenta of the jets stemming from pile-up are divided by a factor kn_{trk}^{PU}, where k is chosen to be 0.01 and n_{trk}^{PU} is the number of tracks associated with pile-up. The discrimination power of corrJVF between jets from pile-up and from the primary vertex is independent of the actual choice of k [112]. Both variables have been combined in a 2-dimensional likelihood function. The output of the likelihood function is flat with respect to the number of pile-up vertices, the efficiencies of the jet vertex tagger are compatible within 1% between a measurement in data and Monte Carlo prediction and the fake rates for given signal efficiencies could be lowered from $1.3\%, 2.2\%$ and 4% to $0.4\%, 1.0\%$ and 3% for signal efficiencies of $80\%, 90\%$ and 95%, respectively [112].

b-tagging Hadrons containing a b-quark, just like taus, do not decay instantly, instead they have a sufficiently long enough lifetime to decay typically well separated from the primary vertex, but still inside the beam-pipe, making it possible to distinguish between jets initiated by b-quarks, called b-jets, and other jets. b-tagging algorithms exploit the finite lifetime of B-hadrons, by reconstructing the decay vertex of the B-hadron and investigating its properties, like the large impact parameter with respect to the primary vertex, the large B-hadron mass or its long lifetime.
Throughout Run I the ATLAS collaboration used as default a combination of three different b-tagging algorithms as input to a neural network, called *MV1*, to tag b-jets [113, 114]. The neural network has been trained on simulated samples of b-jets as signal and light-flavor jets as background. Light-flavor jets are jets which contain only u, d or s quarks. The inputs used by *MV1* are:

- *IP3D* [115] which uses a likelihood ratio based approach to analyze the impact parameter significances d_0/σ_{d_0} and z_0/σ_{z_0}.
- *SV1* [115] using *SV0* (which mainly uses the three dimensional decay-length significance L/σ_L as input) in combination with the invariant mass of all tracks associated to the secondary vertex, the number of vertices with at least two tracks and the energy ratio of the tracks associated to the secondary vertex to the sum over the tracks associated to the jet.
- *JetFitterCombNN* [115] is based on the *JetFitter* algorithm which tries to reconstruct the whole decay chain of the B-hadron [115]. In addition, the *JetFitterCombNN* algorithm uses the *IP3D* algorithm as input and combines both algorithms in a neural network.

The final decision of the *MV1* algorithm is computed using a likelihood ratio based approach taking the output from *MV1*'s neural network as input [115].
For Run II the algorithm has been reoptimized and retuned, leading to *MV2c20* [116]. It still uses the the same three aforementioned taggers as input, however instead of training a neural network, a boosted decision tree is trained, causing a notable performance gain in terms of computing resources. Additionally it also uses kinematic information of the jet as input, namely its p_{T} as well as its pseudo-rapidity. Furthermore the composition of the training sample changed. While for *MV1* b-jets have been used as signal and light flavor jets as background, the background has been changed to consist of 80% light flavor jets and 20% c-jets when training *MV2c20*.
It has been observed that b-tagging performs differently for simulation and data and thus scale factors have been derived by the corresponding ATLAS performance group separately for Run I and Run II.

Central and Forward Jets The analysis based on the Run I data further divides jets into three categories: b-jets, central light jets and forward jets. b-jets are defined by the aforementioned b-tagging algorithm. Central light jets are required to be found in the central region of the detector $|\eta| < 2.4$, to not be identified as b-jets and to have at least

one track with a transverse momentum larger than 400 MeV, if its transverse momentum is less than 50 GeV. Forward jets are jets which are found in the region $2.4 < |\eta| < 4.5$.

6.6. Missing Transverse Energy

While particles interacting electromagnetically or strongly are directly detectable within ATLAS, particles which only interact weakly or even gravitationally are not. They escape the detector undetected. However since in the initial state energy and momentum in the transverse plane are zero, the energy missing due to undetectable particles can be estimated by imposing energy conservation in the transverse plane:

$$0 = E_x^{miss} + \sum E_x^{i,visible}, \tag{6.3}$$

$$0 = E_y^{miss} + \sum E_y^{i,visible}, \tag{6.4}$$

where the sum extends over all detected particles. Consequently the missing transverse energy can be computed as follows:

$$\not{E}_{\mathrm{T}} = \sqrt{\left(E_x^{miss}\right)^2 + \left(E_y^{miss}\right)^2} \tag{6.5}$$

The individual contributions to the missing transverse energy, or phrased differently, the undetectable particles, can not be inferred.

6.7. Overlap Removal Procedure

Particle candidates reconstructed by different algorithms might share the same input information, like for example tracks in the inner detector or energy deposits in the calorimeter, consequently double counting might occur. To remove these ambiguities a so-called *overlap-removal* procedure is applied which is slightly different between the Run I and Run II analyses presented in this thesis. Prior to the beginning of Run II the overlap removal had been re-optimized and synchronized between the different ATLAS analyses. However, it turned out that this overlap removal procedure not optimal for all analyses, so some Run II analyses deviated from the official recommendations. The subsequent steps used in the presented analyses are found in Table 6.1 for Run I and Run II.

6.8. Event Cleaning Procedure

To make sure that only events in which all detector systems were working correctly during data taking are used, *event cleaning* criteria are applied. These changed only slightly between Run I and Run II.

Run I	Object removed	Object compared against	Condition
1.	baseline electron	baseline electron	$\Delta R < 0.05$
2.	jet	baseline electron	$\Delta R < 0.2$
3.	jet	baseline tau	$\Delta R < 0.2$
4.	loose tau	baseline electron	$\Delta R < 0.2$
5.	loose tau	baseline muon	$\Delta R < 0.2$
6.	baseline muon	jet	$\Delta R < 0.4$
7.	baseline electron	jet	$0.2 < \Delta R < 0.4$
8.	baseline electron and baseline muon	baseline muon	$\Delta R < 0.1$
9.	both baseline muons	baseline muon	$\Delta R < 0.05$
10.	baseline electron and baseline muon	baseline muon	$m_{e\mu}^{inv} < 12$ GeV
Run II	**Object removed**	**Object compared against**	**Condition**
1.	loose tau	baseline electron	$\Delta R < 0.2$
2.	loose tau	baseline muon	$\Delta R < 0.2$
3.	baseline electron	baseline muon	shared ID track
4.	jet	baseline electron	$\Delta R < 0.2$
5.	baseline electron	jet	$\Delta R < 0.4$
6.	baseline muon	jet	$\Delta R < 0.4$
7.	jet	loose tau	$\Delta R < 0.2$

Table 6.1.: Overview of the subsequent steps in the overlap removal used in the two analyses presented here.

Run I Events are filtered using the following criteria:

- Skip events in which not all sub-detectors were working properly.
- Reject events where particles point to regions of the calorimeter currently suffering from noise bursts.
- Consider only events where the information about the detector is complete.
- Events not containing a primary vertex with at least 5 tracks are skipped.
- Do not take into account events containing badly reconstructed muons. One speaks of badly reconstructed muons if: $\sigma\left(\frac{q}{p}\right) / \frac{q}{p} > 0.2$, where q denotes the charge of the muon and p the momentum.
- Reject events containing cosmic muons. Cosmic muons are identified by requiring $\left|z_0^{PV}\right| > 1.0$ mm and $\left|d_0^{PV}\right| > 0.2$ mm for the longitudinal and transverse impact parameters with respect to the primary vertex respectively.

Run II The selection is basically the same like in Run I, except for the requirement on the primary vertex being lowered to require only two tracks instead of 5 and the cosmic muon veto being removed.

6.9. Discriminating Variables

This section will define all the discriminating variables which will be used throughout the following chapters.

- $N(Bx)$: the number of b-jets with a transverse momentum of at least x GeV,
- $N(Fx)$: the number of forward jets with a transverse momentum of at least x GeV
- $N(Lx)$: the number of central light jets with a transverse momentum of at least x GeV
- N_{jet}: the number of jets with transverse momentum of at least 20 GeV
- $N_{b-\text{jet}}$: the number of b-jets with transverse momentum of at least 20 GeV
- $m_T = \sqrt{2 p_{\text{T}} \not{E}_{\text{T}} \left(1 - \cos\Delta\phi\left(object, \vec{\not{E}}_{\text{T}}\right)\right)}$
- $\not{E}_{\text{T}}$ the missing transverse energy
- $m_{\text{eff}} = \not{E}_{\text{T}} + p_{\text{T}}^{\tau_1} + p_{\text{T}}^{\tau_2}$
- $\Delta R\left(\tau,\tau\right)^2 = \Delta\eta\left(\tau,\tau\right)^2 + \Delta\phi\left(\tau,\tau\right)^2$, computed using the leading tau pair
- $H_{\text{T}} = \sum_i p_{\text{T}}^{\tau_i} + \sum_j p_{\text{T}}^{jet_j}$
- $m_T^{12} = m_T^{\tau_1} + m_T^{\tau_2}$
- $m_{\text{Tsum}} = m_T^{12} + \sum_i m_T^{jet_i}$

Stransverse mass, m_{T2} The *stransverse mass* is a variable specifically designed to search for pair production of new particles and can be regarded as a generalization of the transverse mass, which was used in the search for the W boson, from a single parent particle to two [117]. It assumes that initially two parent particles of same mass are created which eventually decay into two invisible particles. A generalization to the case of unequal masses is possible [118], but not discussed here. Although this seems a bit unnatural at first, imposing such a strong constraint, it is rather natural in some of the extensions of the Standard Model. In case of R-parity conserving supersymmetry, for example, supersymmetric particles are created in pairs, and if the lsp is stable, it is the perfect candidate for the invisible particle. Throughout the decay chain several visible particles are created, however no assumptions are made about the exact topology of the decay chain or the actual nature of the particles created. If more than one visible particle

is created the matching of particles to the corresponding decay branches becomes crucial. For the sake of understanding however, the most simple case has been chosen.
Assuming that the parent particle which is created, $\tilde{A}$, decays in one step into a Standard Model particle, s, as well as an invisible particle $\tilde{\chi}$, its mass is calculated as follows:

$$m_{\tilde{A}}^2 = m_s^2 + m_{\tilde{\chi}}^2 + 2\left(E_{Ts}E_{T\tilde{\chi}}\cosh\left(\Delta\eta\right) - \vec{p}_{Ts}\vec{p}_{T\tilde{\chi}}\right), \tag{6.6}$$

where $\vec{p}_{Ts}/E_{Ts}$ and $\vec{p}_{T\tilde{\chi}}/E_{T\tilde{\chi}}$ are the transverse momenta/energies of the Standard Model particle and the invisible particle respectively, while $\Delta\eta$ denotes the difference in rapidity between the invisible particle and the Standard Model one. Since the cosine-hyperbole is always ≥ 1, one can also rewrite the equation as an inequality:

$$m_{\tilde{A}}^2 \geq m_{\mathrm{T}}^2\left(\vec{p}_{Ts}, \vec{p}_{T\tilde{\chi}}\right) \equiv m_s^2 + m_{\tilde{\chi}}^2 + 2\left(E_{Ts}E_{T\tilde{\chi}} - \vec{p}_{Ts}\vec{p}_{T\tilde{\chi}}\right). \tag{6.7}$$

In our case, however, not just one, but two parent particles and thus not one but two invisible particles are created. The missing transverse momentum however cannot be independently determined for each of the invisible particles, instead only the sum can be measured:

$$\vec{\not{p}}_{\mathrm{T}} = \vec{\not{p}}_{\mathrm{T}\tilde{\chi}_a} + \vec{\not{p}}_{\mathrm{T}\tilde{\chi}_b}, \tag{6.8}$$

where the missing transverse momentum, $\vec{\not{p}}_{\mathrm{T}}$, is defined in the same way as the missing transverse energy in section 6.6, with the energy being exchanged by the transverse momentum. Consequently the best estimate for the mass of the parent particle is:

$$m_{\tilde{A}} \geq m_{\mathrm{T2}}^2 \equiv \min_{\not{p}_{\mathrm{T}}=\not{p}_{\mathrm{T}\tilde{\chi}a}+\not{p}_{\mathrm{T}\tilde{\chi}_b}} \left[\max\left(m_{\mathrm{T}}^2\left(\vec{p}_T^{\,s_1}, \not{p}_{\mathrm{T}\tilde{\chi}a}\right), m_{\mathrm{T}}^2\left(\vec{p}_T^{\,s_2}, \not{p}_{\mathrm{T}\tilde{\chi}_b}\right)\right)\right], \tag{6.9}$$

where the unknown missing transverse momenta $\not{p}_{\mathrm{T}\tilde{\chi}_{a,b}}$ are minimized under the condition of Equation 6.8, $\not{p}_{\mathrm{T}}$ being the measured missing transverse momentum. As in the case of the transverse mass, m_{T2} has a kinematic endpoint at the true mass of the parent particle $m_{\tilde{A}}$. In case of W-pair production for example, its endpoint corresponds to the mass of the W.
In the following, m_{T2} will also be computed for events which might contain more than two visible particles. In those cases m_{T2} is computed amongst all possible particle pairs, assuming that the additional particles stem from secondary interactions. The combination which yields the largest value is selected.

7. Searching for Electroweak Production of Supersymmetric Particles at $\sqrt{s} = 8$ TeV

In the following, 20.3 fb^{-1} of data collected with the ATLAS detector in 2012 at a center-of-mass energy of 8 TeV will be analyzed. An analysis will be presented specifically targeting final states containing two hadronically decaying taus and missing transverse energy. Jets will be vetoed, because scenarios characterized by the electroweak production of supersymmetric particles will be considered, thus no jets are expected in the final states. No significant excess over the Standard Model expectation is found. The results are interpreted in simplified models, as well as pMSSM scenarios. This thesis specifically focuses on the validation of the diboson background, the optimization of the channel where one tau decays hadronically and the other leptonically (*the tau + light lepton channel*) and the combination of the tau + plus light lepton channel with the channel where both taus decay hadronically (the di-tau channel). Eventually the sensitivity at a center-of-mass energy of 13 TeV is estimated to investigate whether the analysis will be able to improve its reach using the data collected in 2015. The analysis is published in [119].

7.1. Targeted Signal Processes and Models

As explained in chapter 2, a plethora of different supersymmetric extensions of the Standard Model as well as a plethora of different phenomenologies exist. To simplify life, analyses in high energy physics are usually split into final states instead of models, allowing to focus on the features of a specific final state. Depending on the final state an analysis targets, the strategy to estimate the background might change considerably, because the background composition changes considerably. While nowadays our understanding of the Standard Model is rather good and often well modeled in Monte Carlo, the description of misidentified particles is not so well modeled and thus different strategies usually need to be employed to estimate backgrounds from so-called fakes.
The presented analysis [119] focuses on scenarios characterized by light charginos, next-to-lightest neutralinos, relatively light sleptons and the lightest neutralino being the lightest supersymmetric particle. To be more exact, the supersymmetric partner of the tau lepton, the stau, $\tilde{\tau}$, and its neutrino are considered to be the only light sleptons. A phenomenology which can be observed in the framework of the pMSSM [120, 121, 122]. Corresponding final states commonly include hadronically decaying taus, as well as a

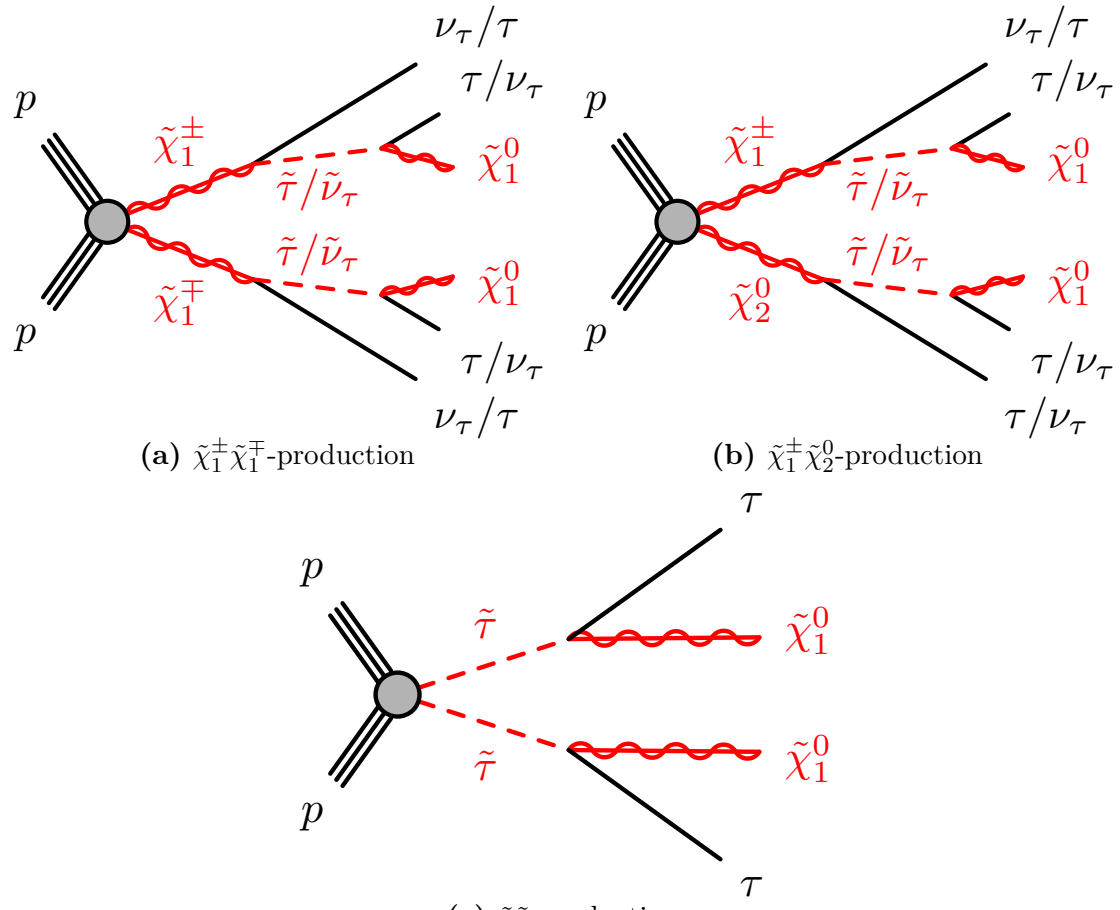

(a) $\tilde{\chi}_1^{\pm}\tilde{\chi}_1^{\mp}$-production **(b)** $\tilde{\chi}_1^{\pm}\tilde{\chi}_2^0$-production

(c) $\tilde{\tau}\tilde{\tau}$-production

Figure 7.1.: Diagrams characterizing the three processes the analysis presented here focuses on. (a) The production of a pair of lightest charginos decaying via a pair of intermediate staus or tau-sneutrinos to a pair of neutralinos, a pair of tau neutrinos as well as a pair of taus. (b) The production of a lightest chargino togetwher with a next-to-lightest neutralino. Both decaying via intermediate staus or tau sneutrinos to a pair of neutralinos and three taus plus a tau neutrino or three tau neutrinos plus a tau. (c) Direct production of a stau pair decaying to two taus as well as a pair of neutralinos.

lot of missing transverse energy due to the tau neutrinos and the neutralinos escaping the detector undetected. Three exemplaric processes will be considered in this thesis, pair production of the lightest chargino, associated production of a lightest chargino and a next-to-lightest neutralino as well as the direct production of a stau pair. The corresponding Feynman diagrams can be found in Figure 7.1. Two simplified models, as well as three different pMSSM models are investigated.

One of the simplified models targets $\tilde{\chi}_1^{\pm}\tilde{\chi}_1^{\mp}$ production, the other one $\tilde{\chi}_1^{\pm}\tilde{\chi}_2^0$ production. In both models all sparticles except for the $\tilde{\chi}_1^{\pm}$, the $\tilde{\chi}_2^0$, the $\tilde{\chi}_1^0$, the $\tilde{\tau}$ partner of the

left-handed τ[1] and the tau sneutrino are assumed to have masses of the order of 2 TeV. Thus the heavier next-to-lightest neutralino and the lightest chargino exclusively decay via intermediate staus or tau sneutrinos which are assumed to be mass degenerate. A situation favored by pMSSM scenarios with large mass splitting between the lightest chargino and the lightest neutralino. The mass of the left-handed stau and its sneutrino are set to be halfway between the lightest chargino and neutralino. To achieve a maximal coupling to the left handed stau the $\tilde{\chi}_1^{\pm}$ and the $\tilde{\chi}_2^0$ are assumed to be purely wino and additionally degenerate in mass. The $\tilde{\chi}_1^0$ on the other hand is assumed to be purely bino. In both models the parameters being varied are the mass of the lightest chargino, as well as the mass of the lightest neutralino, the first in the range between 100 and 500 GeV, the latter in the range between zero and 350 GeV. The resulting cross section of supersymmetric particles in both models ranges from 0.01 to 2 pb.

One of the pMSSM models is focusing on direct-stau pair production. It incorporates the spartners of the left-handed as well as the right-handed taus, but no tau sneutrinos. All sparticle masses are set to 2.5 TeV, except for the staus and the lightest neutralino. The staus are not set to be mass degenerate, instead the right-handed stau is set to be the lightest one. Model points with stau masses in the range from 90 to 300 GeV have been generated. The lightest neutralino is bino-like and its mass is varied in the range from zero to 200 GeV. In this model the direct-stau pair production cross section solely depends on the stau mass and decreases from 176 to 1.4 fb for the left-handed stau and from 70 to 0.6 fb for the right-handed stau in the aforementioned stau mass range.

The remaining two pMSSM models are both characterized by a large value of $\tan\beta = 50$ and masses of all squarks, gluinos and sleptons, other than the spartner of the of the right-handed tau, being set to 3 TeV. The parameter M_1 is set to 50 GeV in the first model, while it is being set to 75 GeV in the second one. The right-handed stau is considered to be the lighter one and its mass is set to 95 GeV in the first model and to $(\tilde{\chi}_2^0 + \tilde{\chi}_1^0)/2$ in case of the second. M_2 and μ are being varied between 100 GeV and 500 (600) GeV in the first (second) case. Depending on the values of M_2 and μ the dominant processes change. In the first model this can either be the associated production of the lightest chargino together with the next-to-lightest neutralino or the pair production of lightest charginos or of staus. Since the two chosen parameters only change the gaugino and higgsino masses, the cross section of direct-stau pair production is constant for all models: 163 fb. The cross section for the associated production of a next-to-lightest neutralino and a chargino varies from 5×10^{-3} to 40 pb, in case of the chargino pair production it varies from 0.01 to 16 pb. Due to the varying stau mass in the second model, the dominant processes are either the pair production of charginos or the associated production of the next-to-lightest neutralino and a lightest chargino. The direct-stau production cross section varies from 0.4 to 42 fb, the chargino pair production cross section varies from 8×10^{-4} to 0.9 pb while the chargino neutralino associated production cross section varies from 5×10^{-4} to 1.2 pb.

[1] Although this is physically not correct, it will be, for the sake of simplicity, in the following be abbreviated as the left-handed stau, the supersymmetric partner of the right-handed τ as right-handed stau.

Three reference points are being defined. They have been chosen to illustrate typical features of the three different processes studied, found in Figure 7.1.

- *Reference point 1*: simplified model for $\tilde{\chi}_1^{\pm}\tilde{\chi}_2^0$ production with mass of $\tilde{\chi}_1^{\pm}/\tilde{\chi}_1^0$ equal to 250/100 GeV,
- *Reference point 2*: simplified model for $\tilde{\chi}_1^{\pm}\tilde{\chi}_1^{\mp}$ production with mass of $\tilde{\chi}_1^{\pm}/\tilde{\chi}_1^0$ equal to 250/50 GeV,
- *Reference point 3*: pMSSM model targeting direct-stau production with mass of the right/left-handed $\tilde{\tau}$ equal to 127/129 GeV and massless $\tilde{\chi}_1^0$.

7.2. Event Selection

When events are selected for analysis, they are first of all required to pass the *event cleaning* procedure as outlined in section 6.8. The trigger used to select events requires two hadronically decaying taus, having a transverse momentum at trigger level of 29/20 GeV in case of the first/second one. To ensure that the trigger operates in its efficiency plateau, meaning the region at which it starts to operate at constant efficiency independently of the properties of the triggering objects, the transverse momentum of the more/less energetic tau is further constrained to be at least 40/25 GeV [123]. One of the taus is required to pass the tight tau quality criteria, while the other one only has to pass the medium criterion, to maintain a reasonable signal efficiency while rejecting most of the multi-jet background. Di-tau pairs from low mass resonances are removed by requiring the invariant mass of any oppositely charged (also called opposite-sign or short OS) tau pair to be larger than 12 GeV. Since supersymmetric particles are rather heavy, this cut has a negligible effect on the studied signal. Except for the background estimate, events containing additional light leptons are vetoed, to allow for statistical combination with ATLAS searches targeting final states including light leptons [124, 125].
To separate the supersymmetric signal from the known Standard Model processes, further requirements are applied to define so-called signal regions. A priori the targeted final states do not contain any jets, thus a jet veto would be a viable option. However jets from initial state radiation as well as pile-up might end up in our selection. Compared to jets from the decay of a top-quark, these are rather soft and do not contain b-jets. Consequently three different types of jet-based vetoes have been developed:

- b-jet veto: rejects events containing b-jets with a transverse momentum of at least 20 GeV,
- jet veto: requires $N(B20) + N(L30) + N(F30) = 0$,
- looser jet veto: $N(B20) + N(L50) + N(F30) = 0$.

Also Z bosons are not expected in the targeted final states. To veto events containing a Z boson, events where at least one of the oppositely charged tau pairs has an invariant

mass within 10 GeV of the visible Z boson mass, 81 GeV, are vetoed. It is crucial to note here that the visible Z boson mass in the di-tau final state is not equal to the true Z boson mass, because in the decay of the tau momentum is carried by the undetected neutrinos. The visible Z mass has been obtained by fitting the invariant mass distribution of oppositely charged tau pairs in simulated $Z \to \tau\tau$ events.
In total four signal regions have been defined to search for electroweakly produced supersymmetric particles in final states containing two hadronically decaying taus. The aforementioned jet and Z vetoes have been used to suppress Standard Model processes containing high energetic jets or events containing a Z boson. Additionally the missing transverse energy, $\not{E}_{\mathrm{T}}$, the stransverse mass, m_{T2}, the sum of the transverse masses of the two taus, $m_{\mathrm{T}}^{\tau_1} + m_{\mathrm{T}}^{\tau_2}$, the effective mass, m_{eff}, as well as the separation between the taus, $\Delta R(\tau, \tau)$ have been used to define the signal regions. m_{T2} actually has a rather good discrimination power between signal and background processes and is thus used in all four signal regions, which are not designed to be exclusive.

SR-C1N2 This signal region has been specifically optimized for the simplified model targeting associated $\tilde{\chi}_1^{\pm}\tilde{\chi}_2^0$ production. The corresponding diagram is depicted in Figure 7.1 (b). Even though three hadronically decaying taus are expected in the final state, only two are actually required, because the reconstruction efficiency for taus is only about 40% for 1-prong taus passing the tight quality criterion and only about 60% for 1-prong taus passing the medium criterion [106]. For 3-prong taus the situation is even worse. Since at least three invisible particles are expected, a moderate cut on the missing transverse energy of 40 GeV as well as a high cut on the stransverse mass of 100 GeV are applied. These two cuts already reject most of the Standard Model background, because neither a lot of missing transverse energy is expected in those events, nor are high energetic taus expected which might also cause a high m_{T2} value. To veto events which contain top-quarks, a b-jet veto is additionally applied.

SR-C1C1 SR-C1C1 has been optimized to target pair production of the lightest chargino. In the simplest possible decay chain involving staus, depicted in Figure 7.1 (a), only two taus are created. Consequently exactly two taus are required. To reject multijet events, a jet veto is applied. Other Standard Model processes are vetoed using a cut on m_{T2} of at least 30 GeV, as well as on the sum of the transverse masses of the taus of at least 250 GeV. Processes taking place in the Standard Model do not predict such large transverse masses for taus.

SR-DS-highMass and SR-DS-lowMass If staus are pair produced they are usually boosted, because the sum of their masses is larger than the mass of any known Standard Model boson, requiring the Standard Model boson to have a rather large transverse momentum. Consequently the distance between them is usually less than in the case of a particle at rest decaying into two particles. Thus for both direct-stau signal regions $\Delta R(\tau, \tau) < 3.0$ is required. When optimizing the cuts to define the direct-stau signal regions, it turned out that the looser jet veto yields a better signal acceptance than

SR-C1N2	SR-C1C1	SR-DS-highMass	SR-DS-lowMass
≥ 2 OS taus	2 OS taus	≥ 2 OS taus	≥ 2 OS taus
b-jet veto	jet veto	looser jet veto	looser jet veto
Z veto			
		$\Delta R(\tau,\tau) < 3.0$	$\Delta R(\tau,\tau) < 3.0$
$\not{E}_{\mathrm{T}} > 40$ GeV	$m_{\mathrm{T2}} > 30$ GeV	$m_{\mathrm{T2}} > 60$ GeV	$m_{\mathrm{T2}} > 30$ GeV
$m_{\mathrm{T2}} > 100$ GeV	$m_{\mathrm{T}}^{\tau_1} + m_{\mathrm{T}}^{\tau_2} > 250$ GeV	$m_{\mathrm{eff}} > 230$ GeV	$m_{\mathrm{eff}} > 260$ GeV

Table 7.1.: Signal region definitions used in the presented analysis. A mnemonic naming convention has been used, denoting $\tilde{\chi}_1^{\pm}$ with C1, $\tilde{\chi}_2^0$ with N2 and direct-stau production with DS. Table from [119].

the jet veto. To investigate direct-stau pair production two different signal regions have been defined, one targeting the high-mass and one the lower-mass region, both cutting on the same variables, m_{T2} and m_{eff}. The high-mass signal region, SR-DS-highMass, cuts harder on m_{T2}, since it is a measure for the mass of the parent particles, namely at 60 GeV, while the low mass signal region only cuts at 30 GeV. The cut on the effective mass, m_{eff}, is 230 GeV in case of SR-DS-highMass and 260 GeV in case of SR-DS-lowMass. Both variables suppress Standard Model backgrounds well, because Standard Model process tend to lower values for both.
The signal region definitions are summarized in Table 7.1.

7.3. Background Estimate

In the following the methods to obtain estimates for the Standard Model processes in the signal regions will be described. The list of datasets used for each process can be found in the appendix. The main processes contributing to the considered final states are multi-jet, W+jets and diboson events. While the tau candidates picked up in diboson events are usually real taus, meaning that they have been correctly identified, in W+jets events one of the tau candidates is usually a fake, while in multi-jet events both taus are fakes, meaning that they originate from misidentified jets or misidentified light leptons. The most notable difference between true and fake-taus is that the latter is not as well understood as the first. True taus are modeled well in Monte Carlo and thus events containing two true taus can be solely estimated based on simulated data. To estimate backgrounds containing fake-taus more elaborate, data-driven, methods have to be used or they have to be suppressed well using cuts.
In the signal regions, the contribution from the Standard Model Higgs boson decaying to two taus is negligible, less than 0.1%, and thus not considered. Contributions from processes involving top-quarks, the Z boson or two Standard Model bosons are estimated solely from Monte Carlo, because either they involve two real taus or are considered to be negligible. The multi-jet contribution is estimated from data using the so-called ABCD method. An estimate for the W+jets process is obtained using a dedicated control region to normalize the estimate from Monte Carlo. Eventually a simultaneous profile

likelihood based fit, including uncertainties, is performed for each signal region to obtain the event yields of the W+jets and the multi-jet background in the corresponding signal regions.

7.3.1. Multi-jet Estimate

Although the probability to fake a tau is at most 1% [126], multi-jet events are still one of the dominant backgrounds in the signal regions, because at LHC the cross section for the production of multi-jet events is huge. The estimate is obtained using the so-called ABCD method which defines four exclusive regions in a two-dimensional plane of two uncorrelated variables, meaning that the ratio of the number of events can be factorized into two independent functions each depending only on one of the variables:

$$r_{A/B}\left(v_1, v_2\right) = N_A\left(v_1, v_2\right) / N_B\left(v_1, v_2\right) = f\left(v_1\right) g\left(v_2\right), \tag{7.1}$$

$v_{1,2}$ denoting the two uncorrelated variables, $N_{A,B}$ denoting the number of events in region A and B while f/g are two functions depending solely on v_1/v_2. If region D is the signal region, the number of events in the signal region can be computed by computing a transfer factor from two of the regions, say C and B, and applying it to the third one, A:

$$N_D = N_A T, \tag{7.2}$$
$$T = N_C / N_B. \tag{7.3}$$

It is not expected for taus to behave significantly different when requiring different identification quality criteria, thus the identification quality requirement of taus is assumed to be uncorrelated with other variables and thus has been chosen as one of the two variables used in the ABCD estimate. The other one depends on the signal region: m_{T2} for SR-C1N2, $m_{\mathrm{T}}^{\tau_1} + m_{\mathrm{T}}^{\tau_2}$ for SR-C1C1 and m_{eff} for the direct-stau signal regions. Region D is defined in the same way as the corresponding signal regions, while region A is also defined in the same way except that all taus must satisfy the loose, but fail the tight tau quality criterion to be exclusive with respect to the signal region which requires at least one tightly identified tau. Control regions B and C share the same tau-identification criteria as regions A and D with the requirements on the kinematic variables being changed, leaving enough phase-space to define validation regions called E and F. Regions E and F are used to validate the method and to estimate systematic uncertainties. The control region definitions of region A, B and C are found in Table 7.2, while the kinematic cut values for the validation regions E and F can be found in Table 7.3. A schematic sketch of the method can be found in Figure 7.2.
To obtain a multi-jet estimate cleaned from contaminations of other Standard Model processes, Standard Model processes are estimated from Monte Carlo and subtracted. Results obtained in the validation regions are summarized in Table 7.4. The agreement between data and the Standard Model estimate is well within errors. The results of the

Regions	A	B	C
CR-C1N2	$m_{\mathrm{T2}} > 100$ GeV ≥ 2 loose taus tight tau veto	$m_{\mathrm{T2}} < 40$ GeV ≥ 2 loose taus tight tau veto	$m_{\mathrm{T2}} < 40$ GeV ≥ 1 medium tau ≥ 1 tight tau
CR-C1C1	$m_{\mathrm{T}}^{\tau_1} + m_{\mathrm{T}}^{\tau_2} > 250$ GeV ≥ 2 loose taus tight tau veto	$80 < m_{\mathrm{T}}^{\tau_1} + m_{\mathrm{T}}^{\tau_2} < 150$ GeV ≥ 2 loose taus tight tau veto	$80 < m_{\mathrm{T}}^{\tau_1} + m_{\mathrm{T}}^{\tau_2} < 150$ GeV ≥ 1 medium tau ≥ 1 tight tau
CR-DS-highMass	$m_{\mathrm{eff}} > 230$ GeV ≥ 2 loose taus tight tau veto	$130 < m_{\mathrm{eff}} < 150$ GeV ≥ 2 loose taus tight tau veto	$130 < m_{\mathrm{eff}} < 150$ GeV ≥ 1 medium tau ≥ 1 tight tau
CR-DS-lowMass	$m_{\mathrm{eff}} > 260$ GeV ≥ 2 loose taus tight tau veto	$100 < m_{\mathrm{eff}} < 150$ GeV ≥ 2 loose taus tight tau veto	$100 < m_{\mathrm{eff}} < 150$ GeV ≥ 1 medium tau ≥ 1 tight tau

Table 7.2.: The multi-jet control region definitions. Only those requirements that are different in the control regions with respect to the signal regions are listed. Table from [119].

Regions	E/F
VR-C1N2	40 GeV $< m_{\mathrm{T2}} <$ 100 GeV
VR-C1C1	150 GeV $< m_{\mathrm{T}}^{\tau_1} + m_{\mathrm{T}}^{\tau_2} <$ 250 GeV
VR-DS-highMass	150 GeV $< m_{\mathrm{eff}} <$ 230 GeV
VR-DS-lowMass	150 GeV $< m_{\mathrm{eff}} <$ 260 GeV

Table 7.3.: The requirement on the kinematic variables used to define the validation regions E and F. Only those requirements that are different with respect to the corresponding control and signal regions are given. Table from [119].

multi-jet estimate in all control regions as well as the obtained estimate in the signal regions are summarized in Table 7.5.

7.3.2. W+Jets Estimate

Another important background in the signal regions is the production of W bosons in association with jets where one of those jets is misidentified as a tau. Although one of the two taus required in the analysis has to pass the tight tau-identification criteria to suppress contributions from fake-tau backgrounds, the other one does not have to pass these. Consequently W+jets events entering our selection are usually events in which the W decays into a tau and a jet is misidentified as a tau, the real tau being the one passing the tight identification criteria.
A semi-data-driven method is employed to estimate the contribution of W+jets events in the signal region: a control region is defined to normalize the Monte Carlo expectation to data. The expectation is that, since one real tau is still present in W+jets events passing our signal region selection, the kinematics are modeled at an acceptable level while only the production cross section for the final state is off. However, defining a control region enriched in W+jets events in the two hadronically decaying tau final state is not possible, because the contamination from multi-jet events is too large and cannot

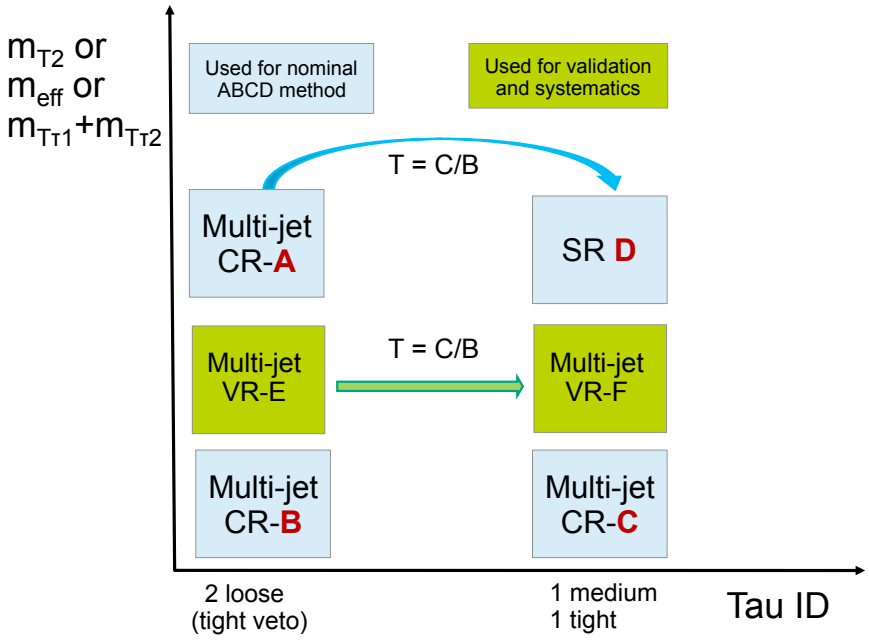

Figure 7.2.: Illustration of the ABCD method for the multi-jet background determination. The control regions A, B, C, and signal region D for the ABCD method described in the text (labelled as Multi-jet CR-A/B/C and SR D) are drawn as light blue boxes. Shown in green and labelled as Multi-jet-VR are the regions E and F, which are used to validate the ABCD method and to estimate the systematic uncertainties, as will be described in the next section. The transfer factor T is calculated from the event counts in regions C and B and applied to the event count in region A to obtain an estimate in the signal region. To obtain an estimate in region F the transfer factor is applied to validation region E. Figure from [119].

be reduced without cutting away too many events, making the statistical errors on the estimate large. Consequently, the decision has been made to instead design a control region requiring a muon and a hadronically decaying tau. Muons have been chosen instead of electrons, because the rate for jets to fake muons is less than to fake electrons, reducing the multi-jet contribution, and because the statistics is higher, as can be seen in Table 7.7, because of the higher identification efficiency for muons. Electrons are thus used to define the corresponding validation region. This choice of control and validation regions reduces the multi-jet contamination in the estimate of the normalization factor. The selected signal leptons are required to have opposite electrical charge, as in the signal region. To veto events containing a Z boson, $m_{T\tau} + m_{T\mu} > 80$ GeV is required, where $m_{T\tau}/m_{T\mu}$ are the transverse mass of the tau and the muon. Additionally, Z events are rejected by requiring the invariant mass of the muon and the tau, $m_{\tau,\mu}$, to be outside the Z mass window, which is different from the two tau channel, because if a pair of a tau and muon stems from a Z it must either be new physics or a tau pair where one tau decays hadronically and the other one into a muon. This involves an additional neutrino and thus further smears the Z peak comparing to the two tau channel, resulting in a Z mass window of: 40 GeV $< m_Z^{\tau,\mu} <$ 100 GeV. As in the two tau channel, low mass resonances

Sample	VR-C1N2	VR-C1C1	VR-DS-highMass	VR-DS-lowMass
Data	5585	1846	163	764
SM total	5840 ± 340	1870 ± 87	170 ± 24	860 ± 110
Multi-jet	5370 ± 320	1570 ± 61	120 ± 19	670 ± 100
W+jets	320 ± 93	240 ± 60	37 ± 15	130 ± 42
Z+jets	97 ± 39	34 ± 12	5.6 ± 2.9	36 ± 14
Diboson	27 ± 8	15.1 ± 5.4	5.1 ± 1.5	12.9 ± 3.6
Top	24 ± 10	5.0 ± 2.1	3.6 ± 1.7	9.5 ± 3.3

Table 7.4.: Number of events in the multi-jet validation regions F, including both statistical and systematic uncertainties. The Standard Model Monte Carlo backgrounds are normalized to the integrated luminosity of the corresponding data, 20.3 fb^{-1}. The multi-jet contribution is estimated from data using the ABCD method. Table from [119].

are vetoed by $m_{\tau,\mu} > 12$ GeV. Events containing top-quarks are vetoed by applying a b-jet veto, while multi-jet events and Z+jets events are further suppressed by asking for moderate missing transverse energy, $\not{E}_{\mathrm{T}} > 40$ GeV, as well as requiring that the leptons are not back-to-back, $|\Delta\phi(\tau,\mu)| < 2.7$ and $|\Delta\eta(\tau,\mu)| < 2.0$. The corresponding validation region is defined in exactly the same way with the only difference being that instead of muons electrons are required. The definition of the W control and validation region can be found in Table 7.6.

Multi-jet events are estimated differently in the W control and validation regions than in the signal regions, namely using the OS-SS method. It relies on the assumption that the ratio of same charged to oppositely charged events is close to unity in case of multi-jet events which in turn implicitly assumes that the fake rate of jets to taus does not depend on their charge. To obtain the multi-jet estimate, the number of events with same charged leptons is computed in data, n_{ss}^{data}, ss indicating the same sign of the charged leptons. The number of same charged events stemming from Standard Model processes other than multi-jet production are estimated from Monte Carlo, n_{ss}^{mc}. Finally, the multi-jet estimate in the opposite-sign region, $n_{os}^{multi-jet}$, is computed by subtracting all Standard Model processes in the same sign region from the number of events in data in the same sign region: $n_{os}^{multi-jet} = n_{ss}^{data} = n_{ss}^{mc}$.

The event yields in the W+jets control and validation regions can be found in Table 7.7. The purity is above 75% in both regions, the agreement between the predictions and data can be considered good. Distributions of kinematic variables in the control region as well as in the validation region can be found in Figure 7.3. No strong systematic mis-modeling is observed.

7.3.3. The Diboson Background

Amongst the possible diboson processes contributing to the final signal region selection the largest contributions stem from $WW \to \tau\nu\tau\nu$ and $ZZ \to \tau\tau\nu\nu$ events. All other processes include either more or less than two taus and usually do not end up in the

	Sample	Region A	Region B	Region C	T = C/B	Multi-jet in SR (D)
C1N2	**Data**	**6**	**36907**	**24601**	0.55 ± 0.03	2.3 ± 1.4
	Z+jets	0.28 ± 0.16	730 ± 260	3980 ± 1060		
	W+jets	1.0 ± 0.4	250 ± 82	590 ± 180		
	diboson	0.51 ± 0.26	14.6 ± 4.8	72 ± 20		
	top	0.10 ± 0.06	17.3 ± 6.1	68 ± 22		
	multi-jet	*4.1 ± 2.5*	*35900 ± 330*	*19890 ± 1090*		
	Ref. point 1	1.9 ± 0.9	1.4 ± 0.7	17.8 ± 6.2		
C1C1	**Data**	**18**	**8479**	**4551**	0.51 ± 0.01	5.8 ± 2.3
	Z+jets	0.06 ± 0.06	21 ± 10	80 ± 25		
	W+jets	5.6 ± 1.2	71 ± 32	160 ± 46		
	diboson	0.9 ± 0.4	1.2 ± 0.6	5.4 ± 2.2		
	top	0.11 ± 0.06	0.0 ± 1.0	0.6 ± 0.5		
	multi-jet	*11.3 ± 4.4*	*8390 ± 98*	*4300 ± 85*		
	Ref. point 2	3.9 ± 1.0	0.13 ± 0.09	1.4 ± 0.4		
DS-highMass	**Data**	**5**	**500**	**268**	0.50 ± 0.05	$0.9^{+1.2}_{-0.9}$
	Z+jets	0.24 ± 0.18	1.0 ± 0.7	1.7 ± 1.0		
	W+jets	2.2 ± 0.7	12.3 ± 6.6	20.6 ± 9.6		
	diboson	0.7 ± 0.4	0.2 ± 0.1	0.6 ± 0.3		
	top	0.06 ± 0.03	0.0 ± 1.0	0.8 ± 0.6		
	multi-jet	*1.8 ± 2.4*	*487 ± 23*	*244 ± 19*		
	Ref. point 3	0.9 ± 0.4	0.0 ± 1.0	0.20 ± 0.13		
DS-lowMass	**Data**	**8**	**13419**	**7632**	0.54 ± 0.01	2.8 ± 1.7
	Z+jets	0.14 ± 0.09	57 ± 26	180 ± 49		
	W+jets	2.3 ± 0.7	140 ± 51	290 ± 75		
	diboson	0.40 ± 0.24	3.1 ± 1.4	10.7 ± 3.6		
	top	0.09 ± 0.05	0.1 ± 0.1	3.8 ± 1.9		
	multi-jet	*5.1 ± 2.9*	*13220 ± 130*	*7150 ± 130*		
	Ref. point 3	1.4 ± 0.5	0.11 ± 0.11	1.3 ± 0.4		

Table 7.5.: The predicted backgrounds in the multi-jet control regions, including both the statistical and systematic uncertainties. Except for the multi-jet contribution, in italics, all backgrounds have been obtained from Monte Carlo. The expected multi-jet contribution, has been obtained by subtracting the total Monte Carlo contributions from observed data, in bold. Predicted event yields for the reference points are also shown. The estimated multi-jet contribution in the signal region is given in the last column. The high uncertainty on the multi-jet estimate for DS-highMass is caused by the low statistics in the corresponding Region A. If the prediction yields 0 events for a given process, the corresponding error is set to 1 event to be conservative in the estimate. It is expected that at least a small fraction of events should contribute to each of the defined regions and thus the simulated statistics is too low if 0 events are predicted. The details of the systematic uncertainties reported here are discussed in the next section. Table from [119].

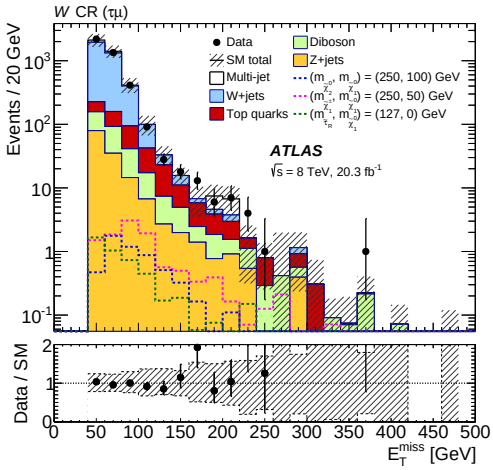

(a) W-CR: $\not{E}_{\mathrm{T}}$ [GeV]

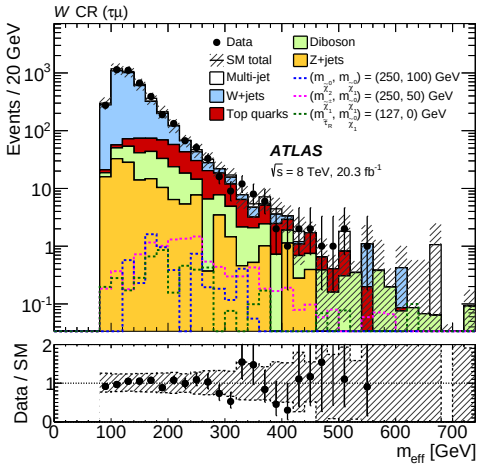

(b) W-CR: m_{eff} [GeV]

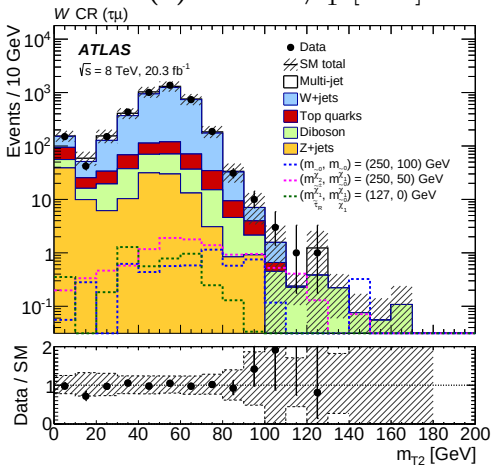

(c) W-CR: m_{T2} [GeV]

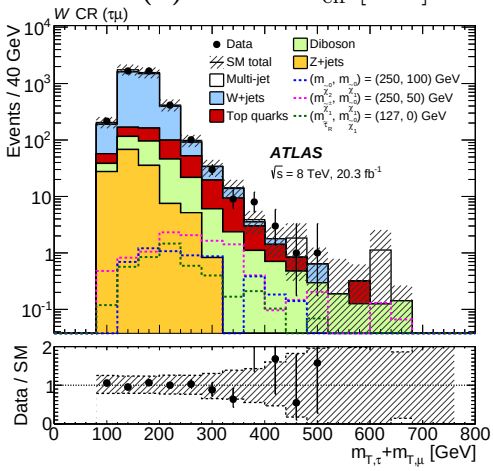

(d) W-CR: $m_{\mathrm{T}}^{\tau} + m_{\mathrm{T}}^{\mu}$ [GeV]

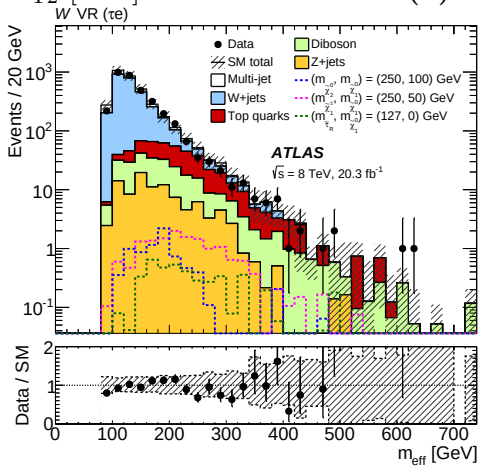

(e) W-VR: m_{eff} [GeV]

Figure 7.3.: (a-d) Distributions in the W+jets control region of the kinematic variables which are used in the signal region definition. (e) An examplaric distribution in the W+jets validation region, m_{eff} is shown. The Standard Model backgrounds other than multi-jet production are estimated from Monte Carlo simulation and normalised to 20.3 fb^{-1}. The multi-jet contribution is estimated from data using the OS-SS method, as explained in the text. The hatched bands represent the combined statistical and systematic uncertainties on the total Standard Model background. For illustration, the distributions of the reference points are also shown as dashed lines. The lower panels show the ratio of data to the Standard Model background estimate. Figure from [119].

Control Region	Validation Region
1 tight tau	
1 isolated muon	1 isolated electron
opposite charge	
b-jet veto	
$\lvert\Delta\phi(\tau,\mu)\rvert < 2.7$	$\lvert\Delta\phi(\tau,e)\rvert < 2.7$
$\lvert\Delta\eta(\tau,\mu)\rvert < 2.0$	$\lvert\Delta\eta(\tau,e)\rvert < 2.0$
$\not{E}_{\mathrm{T}} > 40$ GeV	
$m_{T\tau} + m_{T\mu} > 80$ GeV	$m_{T\tau} + m_{Te} > 80$ GeV
$m_{\tau,\mu} > 12$ GeV	$m_{\tau,e} > 12$ GeV
$m_{\tau,\mu} < 40$ GeV or $m_{\tau,\mu} > 100$ GeV	$m_{\tau,e} < 40$ GeV or $m_{\tau,e} > 100$ GeV

Table 7.6.: Definition of the W+jets control and validation regions. Table from [119].

Sample	W CR	W VR
Data	4120	3420
SM total	4100 ± 900	3500 ± 600
W+jets	3300 ± 800	2600 ± 500
Top	250 ± 80	240 ± 70
Diboson	180 ± 50	170 ± 40
Z+jets	140 ± 40	99 ± 31
Multi-jet	250 ± 250	400 ± 200

Table 7.7.: Event yields in the W+jets control and validation regions. The SM backgrounds other than multi-jet production are estimated from MC simulation and normalised to 20.3 fb^{-1}. The multi-jet contribution is estimated using the OS-SS method as explained in the text. The quoted uncertainty is the sum in quadrature of statistical and systematic uncertainties. Table from [119].

selection. To validate the modeling and normalization of the WW process, events with one electron and one muon are used to define validation regions. Events with two hadronically decaying taus are dominated by the large irreducible QCD background. Similarly, when requiring one muon and one tau and large MET the W+jets process largely dominates over WW. In the following the diboson backgrounds are split into three different categories: WW events, ZV events and other VV events, V denoting any electroweak Standard Model boson except for the Higgs.
Events with one opposite-sign electron and muon pair are selected. To keep the phase space as close to the main analysis as possible, the leading-p_{T} lepton is required to have a p_{T} larger than 40 GeV, whereas the sub-leading lepton is required to have at least 25 GeV. The requirements on kinematic variables were chosen such as to be orthogonal to the signal regions while still being as close as possible. Therefore the same Z-veto as in the main event selection is applied, meaning events with $|m_{ll} - 81\ \mathrm{GeV}| < 10$ GeV are rejected. In all WW validation regions the jet veto, as defined earlier, has been used to suppress the top backgrounds. The WW validation regions are listed in Table 7.8

	Signal region	Validation region (VR)
SR-C1N2	at least two taus at least 1 OS tau pair b-jet veto Z-veto $\not{E}_{\mathrm{T}} > 40$ GeV $m_{\mathrm{T2}} > 100$ GeV	exactly one OS emu pair jet veto Z-veto $\not{E}_{\mathrm{T}} > 40$ GeV $50 < m_{\mathrm{T2}} < 100$ GeV
SR-C1C1	exactly two taus at least 1 OS tau pair jet veto Z-veto $m_{\mathrm{T2}} > 30$ GeV $m_{T\tau 1} + m_{T\tau 2} > 250$ GeV	exactly one OS emu pair jet veto Z-veto $m_{\mathrm{T2}} > 30$ GeV $150 < m_{Te} + m_{T\mu} < 250$ GeV
SR-DS-highMass	at least two taus at least 1 OS tau pair looser jet veto Z-veto $\Delta R(\tau, \tau) < 3.0$ $m_{\mathrm{T2}} > 60$ GeV $M_{eff} > 230$ GeV	exactly one OS emu pair jet veto Z-veto $\Delta R(e, \mu) < 3.0$ $m_{\mathrm{T2}} > 60$ GeV $150 < M_{eff} < 230$ GeV
SR-DS-lowMass	at least two taus at least 1 OS tau pair looser jet veto Z-veto $\Delta R(\tau, \tau) < 3.0$ $m_{\mathrm{T2}} > 30$ GeV $M_{eff} > 260$ GeV	exactly one OS emu pair jet veto Z-veto $\Delta R(e, \mu) < 3.0$ $m_{\mathrm{T2}} > 30$ GeV $150 < M_{eff} < 260$ GeV

Table 7.8.: Comparison of the WW validation region definition to the signal region definition.

together with their corresponding signal regions.

Relevant distributions of the kinematic variables used to define each validation region can be found in Figure 7.4. For all kinematic distributions there is good agreement between data and the Standard Model prediction. No systematic mismodeling of the WW background is observed. The rather distinct spikes in the Z+jets and W+jets distributions are due to the low statistics in the used samples.

In Table 7.9 the composition of the backgrounds in each of the validation regions is shown, while in Table 7.10 the event yields in each validation region are shown. The fraction of WW events is always above 70%. If the jet veto were loosened, the contribution from the top backgrounds would increase and thus decrease the purity of WW events. Since the data-over-Standard Model ratios for the leading and sub-leading jet p_{T} distribution, as well as the signal-jet multiplicity are flat, as shown in Figure 7.5, it

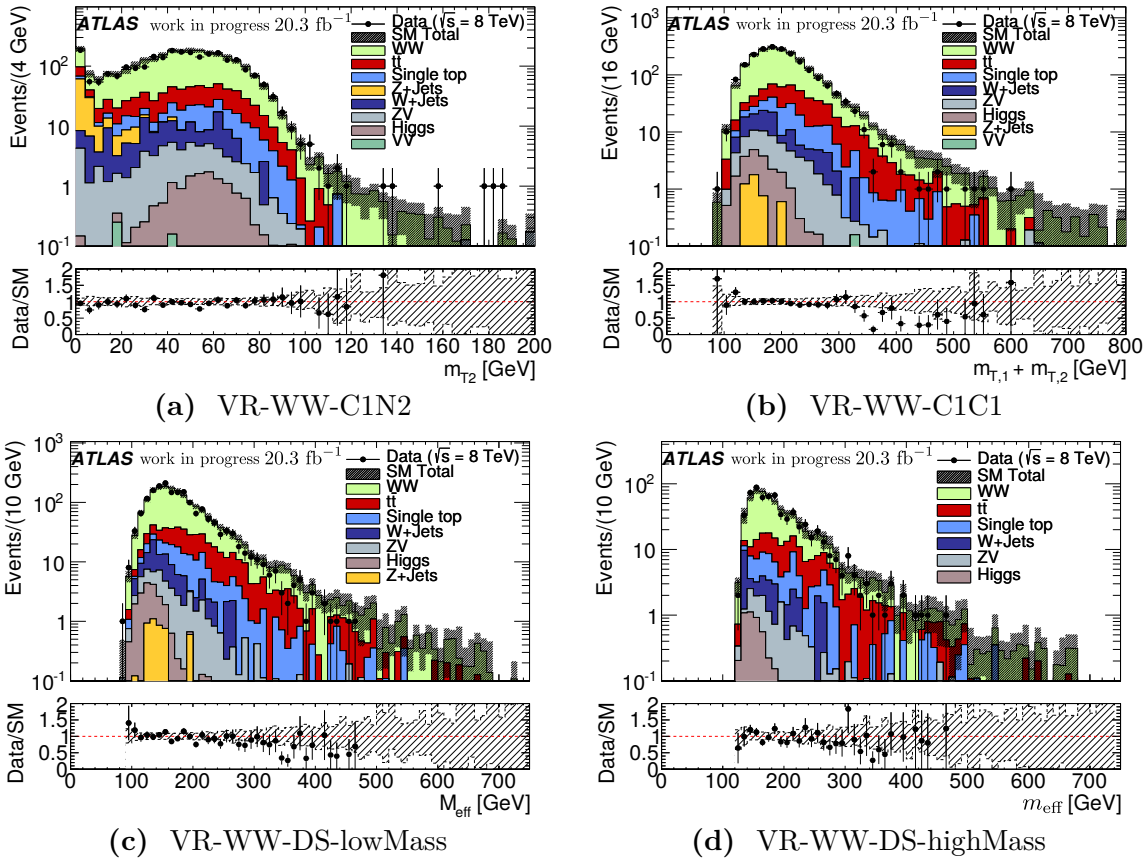

(a) VR-WW-C1N2 **(b)** VR-WW-C1C1

(c) VR-WW-DS-lowMass **(d)** VR-WW-DS-highMass

Figure 7.4.: The distributions one of the cut variables for each validation region before cutting on them: m_{T2} in VR-WW-C1N2 (a) $m_{Te} + m_{T\mu}$ in VR-WW-C1C1 (b) and M_{eff} in VR-WW-DS-lowMass (c) and VR-WW-DS-highMass (d). The depicted uncertainty band is a combination of the statistical and systematic error. All backgrounds are estimated from MC.

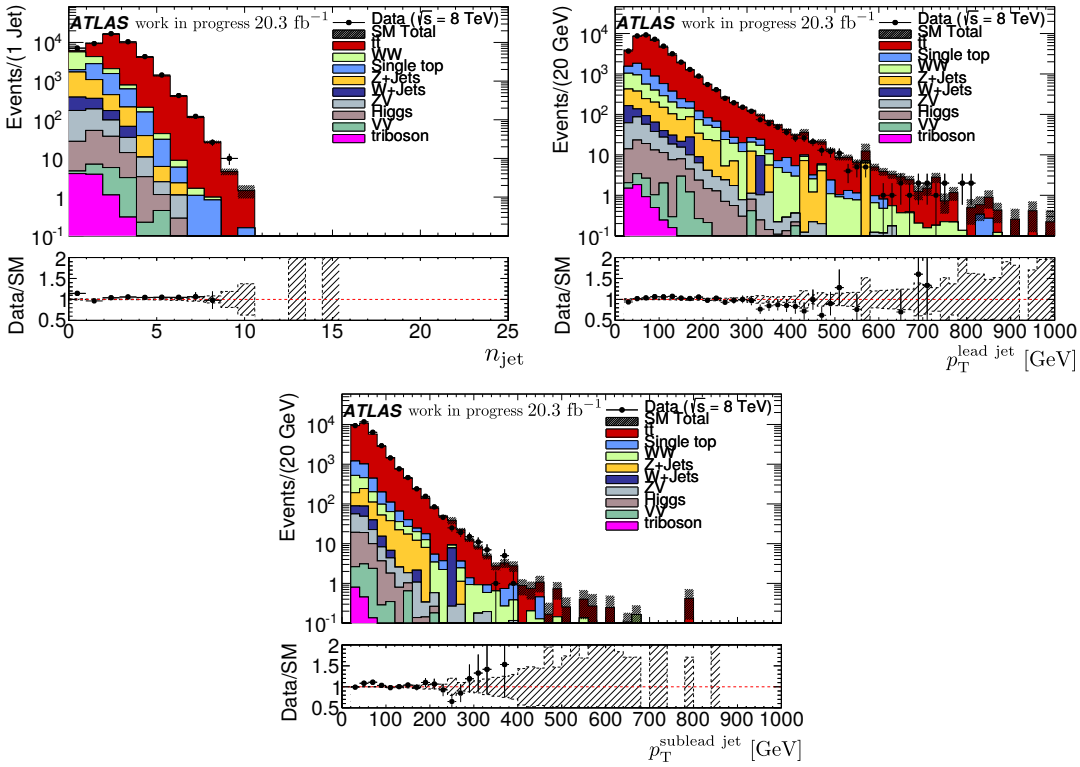

Figure 7.5.: From left to right: the signal jet multiplicity, the p_{T} of the leading jet and the p_{T} of the sub-leading jet before the jet veto cut. The uncertainty bands depict the combined statistical and systematic uncertainty.

VR	WW-C1N2	WW-C1C1	WW-DS-highMass	WW-DS-lowMass
WW	71 ±9	77 ±9	72 ±10	72 ±9
VV	0.0 ±1.0	0.0 ±1.0	0.0 ±1.0	0.0 ±1.0
ZV	1.7 ±0.4	2.0 ±0.6	1.7 ±0.4	1.7 ±0.5
$t\bar{t}$	15.8 ±2.0	11.7 ±1.5	15.4 ±2.1	15.4 ±2.2
Single Top	7.8 ±1.2	6.0 ±0.9	7.2 ±1.2	7.8 ±1.5
Higgs	0.77 ±0.08	0.66 ±0.07	0.242 ±0.033	0.51 ±0.07
Z+Jets	0.0 ±1.0	0.19 ±0.10	0.13 ±0.10	0.0 ±1.0
W+Jets	2.8 ±1.0	2.9 ±0.9	2.8 ±0.7	2.9 ±1.1

Table 7.9.: Contribution of each process (in percent) to the validation regions (VR). The uncertainties are the combined statistical and systematic uncertainties. Due to rounding the contributions do not necessarily add up to 100 percent. The diboson backgrounds are split into three different categories: WW events, ZV events and other VV events, V denoting any electroweak Standard Model boson, except for the Higgs.

is not expected that a tightening of the jet veto will impact the results.
To judge the need for additional normalization factors for the WW backgrounds, the normalization of the WW background estimate with respect to data in the validation regions is computed. Contributions from other Standard Model processes are subtracted using estimates from Monte Carlo. The normalization factors in each validation region are calculated according to the following formula:

$$SF(VR) = \frac{N_d - \sum_{\text{all processes except WW}} N_p}{N_{WW}}, \tag{7.4}$$

where N_d is the number of events observed in data and N_p is the number of expected events for the process, obtained from Monte Carlo. The resulting normalization factors can be found in Table 7.11. For all validation regions, the normalization factors are compatible with 1. Their deviation from 1 is within the error on the WW cross section (5%), and the total systematic uncertainty is significantly larger than the deviation of the normalization factors from 1. It is assumed that the di-tau channel and the electron + muon channel are equally well modeled in the WW samples, because in both cases both leptons are real, only misidentified leptons are expected to be modeled badly. Therefore no normalization factor is needed in the di-tau channel as well.

7.3.4. Remaining Backgrounds

The remaining backgrounds are mainly the Z+jets background as well as backgrounds containing top-quarks or Drell-Yan processes. They are estimated solely from Monte Carlo. To check the modeling of the Z+jets and the top-quark pair production backgrounds, two additional validation regions are defined.
The Z+jets validation region is defined requiring one tight tau and an isolated muon or electron. The pair of selected leptons has to be oppositely charged and its invari-

VR	WW-C1N2	WW-C1C1	WW-DS-highMass	WW-DS-lowMass
WW	800 ± 60	1170 ± 80	790 ± 60	295 ± 21
VV	0.0 ± 1.0	0.0 ± 1.0	0.0 ± 1.0	0.0 ± 1.0
ZV	19 ± 4	30 ± 7	18.6 ± 3.5	7.0 ± 1.5
$t\bar{t}$	179 ± 13	178 ± 13	168 ± 12	63 ± 5
Single Top	88 ± 9	92 ± 10	78 ± 8	32 ± 4
Higgs	8.7 ± 0.4	10.1 ± 0.5	2.63 ± 0.21	2.10 ± 0.18
Z+Jets	0.0 ± 1.0	3.0 ± 1.4	1.4 ± 1.0	0.0 ± 1.0
W+Jets	31 ± 10	45 ± 11	30 ± 6	12 ± 4
SM	1130 ± 60	1530 ± 80	1090 ± 60	411 ± 22
data	1071	1503	1055	403

Table 7.10.: Event yields in the validation regions. The luminosity of the Monte Carlo samples has been normalized to 20.3 fb^{-1}. The errors are the combined statistical and systematic uncertainty. The diboson backgrounds are split into three different categories: WW events, ZV events and other VV events, V denoting any electroweak Standard Model boson.

ant mass has to be within the tightened Z-window of 40 GeV $< m_{\tau,\mathrm{l}} <$ 75 GeV, to increase purity in Z+jets events. Events containing top-quarks are vetoed using a b-jet veto, while other Standard Model contributions are suppressed by requiring $m_{T\tau} + m_{T\mu} < 80$ GeV and $|\Delta\phi(\tau, \mu)| > 2.4$. Contributions from multi-jet events in the Z+jets validation region are estimated in the same manner as in the W+jets control and validation region, namely using the OS-SS method.
The top-quark validation region is defined requiring at least two tau candidates, where one of them needs to pass the tight tau-identification criteria and at least one tau pair has to be oppositely charged. Standard Model backgrounds are suppressed by requiring a non vanishing $\not{E}_{\mathrm{T}}$, 50 GeV $< \not{E}_{\mathrm{T}} <$ 100 GeV and $m_{\mathrm{T}}^{\tau_1} + m_{\mathrm{T}}^{\tau_2} > 80$ GeV. To obtain mostly events containing top-quarks, two b-jets are required and the events are required to be top tagged using the cotransverse mass, m_{CT} [127]. The bounds used in tagging events containing top-quarks are described in [128]. Last but not least, the scalar sum of the p_{T} of the two taus and of at least one combination of two jets has to exceed 100 GeV. A summary of the definition of the Z+jets and top-validation regions can be found in Table 7.12. In the Z+jetsas well as in the top-validation regions the purity which could be achieved is above 80%. Data and the Standard Model expectation are in good

VR-WW-C1N2	0.94 $\pm$0.10
VR-WW-C1C1	0.99 $\pm$0.08
VR-WW-DS-highMass	0.97 $\pm$0.10
VR-WW-DS-lowMass	0.98 $\pm$0.13

Table 7.11.: Normalization factors and their combined statistical and systematic error for each WW validation region.

Z+jets	top
1 tight tau	
1 isolated μ or e	at least one add. tau
opposite charge	
b-jet veto	2 b-jets
$\lvert\Delta\phi(\tau, l)\rvert > 2.4$	-
$m_{T\tau} + m_{Tl} < 80$ GeV	$m_{\mathrm{T}}^{\tau_1} + m_{\mathrm{T}}^{\tau_2} > 80$ GeV
-	50 GeV $< \not{E}_{\mathrm{T}} < 100$ GeV
-	$p_{\mathrm{T}}(\tau_1) + p_{\mathrm{T}}(\tau_2) + p_{\mathrm{T}}(j_1) + p_{\mathrm{T}}(j_2) > 100$ GeV
40 GeV $< m_{\tau,l} < 75$ GeV	top tagged using m_{CT} [128]

Table 7.12.: Definition of the Z+jets and the top validation region.

agreement as can be seen in Figure 7.6 showing relevant kinematic variables.

7.3.5. Fitting Procedure

To incorporate correlations between the background estimates, a simultaneous fit is performed based on a profile likelihood method [65] to obtain the final background estimate. The background estimates are simultaneously normalized in the control regions and the nuisance parameters are obtained. For each control region the number of events is assumed to be described by a Poisson distribution with the mean being the sum of the expected contributions from all background sources. Systematic uncertainties are taken into account as nuisance parameters, assumed to be Gaussian distributed, as explained in chapter 3. The transfer factors used in the multi-jet estimate are calculated prior to fitting and are used as inputs to the fit. Further input parameters to the fit are: the number of observed events in the multi-jet control region A, the corresponding non-multi-jet and multi-jet contribution, the number of observed events in the W+jets control region and the corresponding non-W+jets as well as W+jets contributions. The free parameters in the fit are the normalizations of the W+jets and multi-jet backgrounds. As detailed in chapter 3, the fit parameters are obtained by maximizing the likelihood functions.

7.4. Uncertainties

Backgrounds Estimated from Monte Carlo Systematic uncertainties on the backgrounds estimated from Monte Carlo are split into two larger categories, the experimental and the theoretical uncertainties. The first group encompasses all uncertainties which are related to the actual measurement, like e.g. resolution effects, the later group contains all uncertainties related to the modeling of physics, like e.g. the cross section calculation. In the following a summary of the uncertainties taken into account will be given. Further details can be found in [119] and the references therein.
Experimental systematic uncertainties on these quantities are considered:

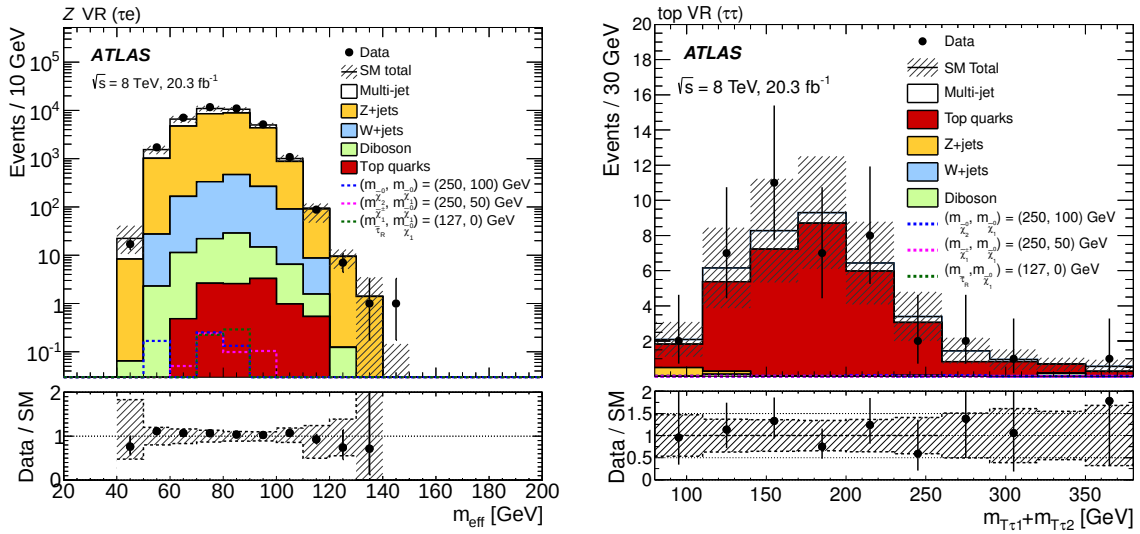

(a) m_{eff} [GeV] **(b)** $m_{\text{T}}^{\tau_1} + m_{\text{T}}^{\tau_2}$ [GeV]

Figure 7.6.: Distributions in the (a) Z+jets and (b) top validation regions of relevant variables: m_{T2} in the Z+jets validation region and $m_{\text{T}}^{\tau_1} + m_{\text{T}}^{\tau_2}$ in the top validation region. The Standard Model backgrounds other than multi-jet production are estimated from Monte Carlo simulation and normalised to 20.3 fb^{-1}. The multi-jet contribution is estimated from data using the OS-SS method, as explained in the text. The hatched bands represent the combined statistical and systematic uncertainties on the total Standard Model background. For illustration, the distributions of the reference points are also shown as dashed lines. The lower panels show the ratio of data to the Standard Model background estimate. Figure from [119].

Source	W+jets	Diboson	Z+jets	Top
MC statistics	16–36%	15–28%	44–80%	23–50%
Theoretical uncertainty	17–30%	17–27%	25–30%	10–20%
Tau ID and trigger	10–18%	20–21%	10–20%	22–28%
Tau Energy Scale	12–20%	3–13%	4–12%	2–7%
Others	1–10%	3–9%	5–10%	10–20%
Total	34–48%	35–44%	58–85%	43–62%

Table 7.13.: Summary of the various sources of uncertainty for the backgrounds estimated from Monte Carlo. The first row shows the uncertainty due to the limited statistics in the simulated samples. The second row shows the total systematic uncertainty from theory. The main experimental systematic uncertainties are given in the rows labelled with "Tau ID and trigger" and "Tau Energy scale", while the row "Others" shows the contribution from the remaining sources of experimental systematic uncertainty as described in the text. The "Total" uncertainty is the sum in quadrature of each source. Table is taken from [119].

- jet energy scale and resolution,
- $\not{E}_{\mathrm{T}}$ energy scale and resolution,
- b-tagging efficiency and mis-identification rate,
- tau-identification, trigger efficiency and energy scale,
- luminosity.

Theoretical uncertainties on these quantities are considered:

- simulation of pile-up,
- renormalization and factorization scales,
- parton density function,
- parton jet matching,
- parton shower modeling,
- cross section,
- ISR modeling (found to be negligible).

The dominant uncertainties are the tau-related uncertainties, namely the uncertainty on the tau-identification, the tau trigger efficiency, as well as the tau energy scale. A summary of the most important uncertainties can be found in table Table 7.13.

Systematic Source	SR-C1N2	SR-C1C1	SR-DS-highMass	SR-DS-lowMass
Correlation	4.9%	1.6%	8.0%	14%
Monte Carlo systematics in Region A	8.0%	12%	21%	13%
Monte Carlo systematics in Region B	1.0%	0.4%	1.2%	0.5%
Monte Carlo systematics in Region C	2.7%	1.4%	3.6%	2.0%
Statistics in Region A	61%	38%	133%	57%
Statistics in Regions C and B	1.0%	2.0%	8.4%	1.5%
Total	62%	40%	135%	60%

Table 7.14.: Summary of the systematic uncertainties for the multi-jet background estimation. The total uncertainty is the sum in quadrature of each source. Table extracted from [119].

Multi-jet The systematic uncertainties on the multi-jet estimate can be roughly grouped into the three following categories: *correlation*, *systematic errors in the estimate of other processes* and *statistical errors*. The *correlation* between the kinematic variable used in the ABCD estimate and the tau-identification is estimated by comparing the transfer factor computed from regions B and C to that computed from regions E and F. *Systematical uncertainties* in the multi-jet estimate are estimated by considering the systematic uncertainty of the Standard Model processes in their Monte Carlo estimates. *Statistical errors* are considered analogously to the systematical ones, additionally taking the error on the obtained event yield from data into account. A summary of the uncertainties on the multi-jet background estimate can be found in Table 7.14. The dominant uncertainty clearly is the limited statistics in region A.

7.5. Results

The results obtained from the fit described in section 7.3.5 can be found in Table 7.15. Signal contamination in the control regions is neglected. They can be summarized in one sentence: no significant excess above the Standard Model expectation has been found. In all signal regions except for SR-C1C1, the observed number of events is well in agreement with the Standard Model prediction, a downwards fluctuation is observed in SR-C1C1.
The background contributions are extracted from the fit. The normalization factors obtained by the fit do not deviate from unity by more than one percent. The error on the multi-jet estimate is, looking at Table 7.14, clearly dominated by statistics, so to reduce it, a new method needs to be developed to estimate the multi-jet contribution or more data needs to be collected. However the total uncertainty is well under control and always about or less than 30%.
The p_0 value, giving the probability of the background-only hypothesis to fluctuate to the observed number of events or higher, as described in chapter 3, has also been computed and is given for each signal region in Table 7.15. For technical reasons, it is clamped at a value of 0.5. Additionally, the expected and observed upper limits on the

SM process	SR-C1N2	SR-C1C1	SR-DS-highMass	SR-DS-lowMass
Top	0.30 ± 0.19	0.7 ± 0.4	0.9 ± 0.4	1.3 ± 0.6
Z+jets	0.9 ± 0.5	0.20 ± 0.17	0.6 ± 0.4	0.40 ± 0.27
W+jets	2.2 ± 0.8	11.2 ± 2.8	2.7 ± 0.9	4.1 ± 1.2
Diboson	2.2 ± 0.9	3.8 ± 1.4	2.5 ± 1.0	2.9 ± 1.0
Multi-jet	2.3 ± 2.0	5.8 ± 3.3	0.9 ± 1.2	2.8 ± 2.3
SM total	7.9 ± 2.4	22 ± 5	7.5 ± 1.9	11.5 ± 2.9
Observed	11	12	7	15
Ref. point 1	11.3 ± 2.8	8.5 ± 2.2	10.2 ± 2.6	7.5 ± 2.0
Ref. point 2	9.2 ± 2.1	20 ± 4	12.4 ± 2.8	12.8 ± 2.7
Ref. point 3	0.8 ± 0.5	7.6 ± 1.9	3.8 ± 1.0	5.2 ± 1.3
p_0	0.20	0.50	0.50	0.21
Expected σ^{95}_{vis} (fb)	$< 0.42^{+0.19}_{-0.11}$	$< 0.56^{+0.25}_{-0.14}$	$< 0.37^{+0.17}_{-0.10}$	$< 0.51^{+0.18}_{-0.15}$
Observed σ^{95}_{vis} (fb)	< 0.59	< 0.37	< 0.37	< 0.66

Table 7.15.: Observed and expected numbers of events in the signal regions for 20.3 fb^{-1}. The contributions of multi-jet and W+jets events were scaled with the normalisation factors obtained from the fit described in section 7.3.5. The shown uncertainties are the sum in quadrature of statistical and systematic uncertainties. The correlation of systematic uncertainties among control regions and background processes is fully taken into account and, as a result, the numbers given here may be different from those in Table 7.5 and Table 7.13. Expected event yields for the SUSY reference points (see section 7.1) are also shown. The one-sided p_0-values and the observed and expected 95% CL upper limits on the visible non-SM cross section (σ^{95}_{vis}), obtained from the fit described in section 7.5, are given. Values of $p_0 > 0.5$ are truncated to $p_0 = 0.5$. Table extracted from [119].

visible non Standard Model cross section at 95% confidence level using the CL$_s$ prescription as described in chapter 3 are given. The visible cross section is the product of the acceptance of events times the reconstruction efficiency times the production cross section, so it should not be confused with the production cross section. Figure 7.7 shows distributions of relevant kinematic variables and compares data, the Standard Model prediction as well as the benchmark models. The agreement between data and the Standard Model prediction is good. Background estimates are obtained as explained in section 7.3.

7.6. Interpretation

Since no significant excess over the Standard Model background expectation has been observed, model-dependent exclusion limits are derived. The limits are calculated at 95% confidence level using the CL$_s$ method as used to compute the limits on the visible cross sections in section 7.5 and, as explained in chapter 3, the only difference being that signal contamination in the control regions is now taken into account. Since the signal regions were not defined to be exclusive, but instead optimized for specific processes,

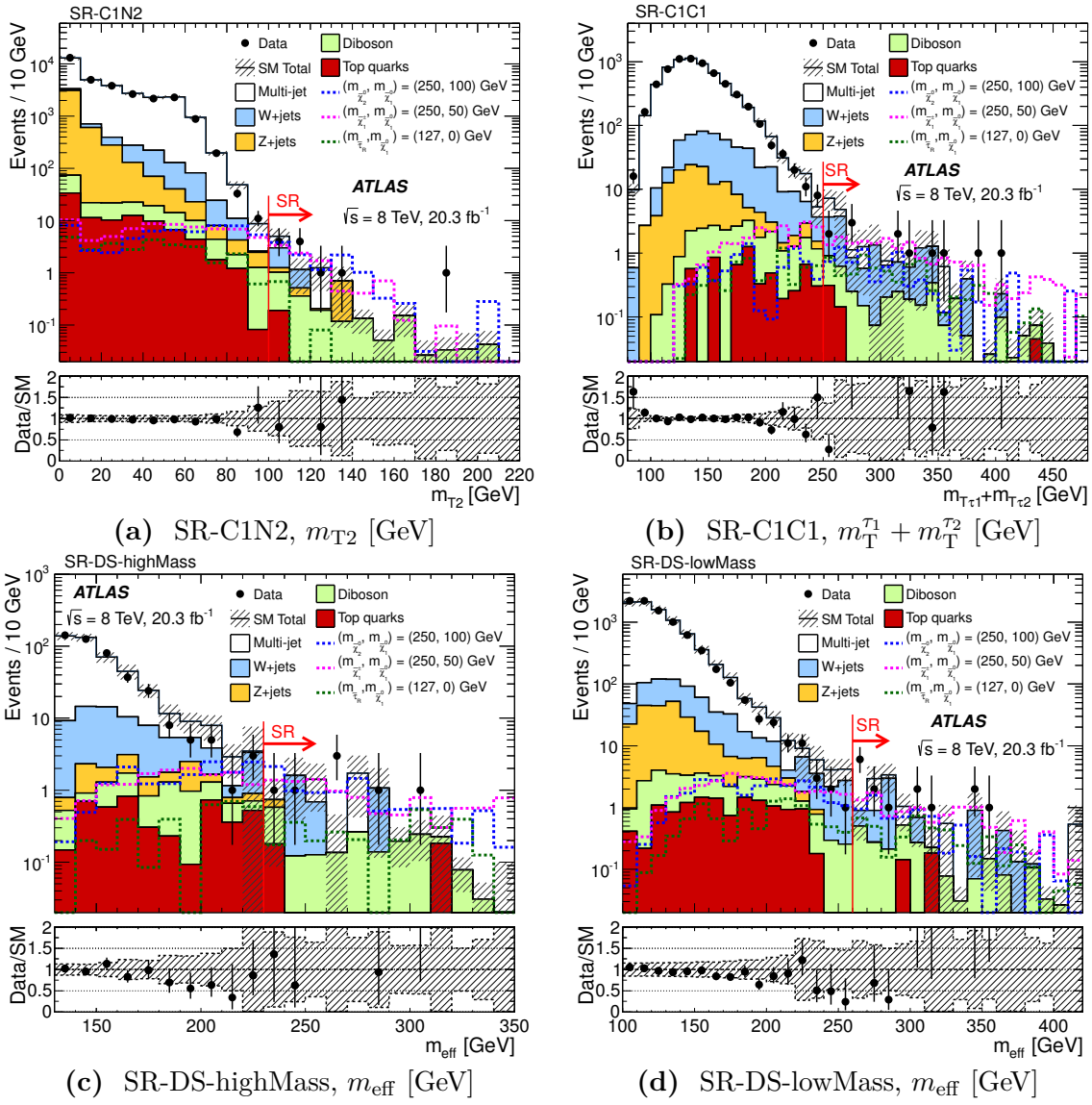

(a) SR-C1N2, m_{T2} [GeV] **(b)** SR-C1C1, $m_{\mathrm{T}}^{\tau 1} + m_{\mathrm{T}}^{\tau 2}$ [GeV]

(c) SR-DS-highMass, m_{eff} [GeV] **(d)** SR-DS-lowMass, m_{eff} [GeV]

Figure 7.7.: Distributions of relevant kinematic variables before the requirement on the given variable is applied: (a) m_{T2} for SR-C1N2, (b) $m_{\mathrm{T}}^{\tau 1} + m_{\mathrm{T}}^{\tau 2}$ for SR-C1C1, (c) m_{eff} for SR-DS-highMass, and (d) m_{eff} for SR-DS-lowMass. The stacked histograms show the expected SM backgrounds normalised to 20.3 fb^{-1}. The multi-jet contribution is estimated from data using the ABCD method. The hatched bands represent the sum in quadrature of systematic and statistical uncertainties on the total SM background. The lower panels show the ratio of data to the total SM background estimate. Figures extracted from [119].

a simple statistical combination of the signal regions cannot be done. Instead for each specific point in the model parameter space, the signal region which yields the best expected limit is chosen. This does not necessarily coincide with the observed limit and also does not imply that the observed limit will also always be the best, however in order to avoid to bias the analysis by looking at the observed limit and data first, this approach was chosen.
The exclusion plots, shown in the following, show the observed and expected exclusion contours as solid and dashed lines, respectively. The yellow band around the expected limit shows the $\pm 1\sigma$ variations including all uncertainties except the one on the signal cross section. That is indicated by the dotted lines around the observed limit. To give a conservative limit, all observed limits in the following will be reduced by 1σ of the signal cross section.

7.6.1. Simplified Models

The exclusion limits for the simplified models introduced in section 7.1 are shown in Figure 7.8. They are targeting chargino pair production, $\tilde{\chi}_1^{\pm}\tilde{\chi}_1^{\mp}$, as well as associated chargino-neutralino production $\tilde{\chi}_1^{\pm}\tilde{\chi}_2^0$. For sake of comparability to the results published by the ATLAS three-lepton analaysis [125], Figure 7.8 (a) shows the limit obtained when considering chargino pair production and associated chargino-neutralino production simultaneously.
In the case of simultaneous $\tilde{\chi}_1^{\pm}\tilde{\chi}_1^{\mp}$ and $\tilde{\chi}_1^{\pm}\tilde{\chi}_2^0$ production, $\tilde{\chi}_1^{\pm}/\tilde{\chi}_1^0$ masses of up to 410/140 GeV can be excluded, while in the case of $\tilde{\chi}_1^{\pm}$ pair production alone, chargino/neutralino masses of up to 345/90 GeV can be excluded. A clear improvement compared to the ATLAS three-lepton analysis [125], depicted as solid blue line in Figure 7.8 (a). Since however the three-lepton analysis does not have noticeable sensitivity to two lepton final states, as in the case of $\tilde{\chi}_1^{\pm}$ pair production, there is no comparable limit from the three-lepton analysis in Figure 7.8. It is interesting to note that in case of high chargino masses in both cases SR-DS-highMass performs best in both scenarios, whilst in case of low chargino masses the signal regions developed with the corresponding production process in mind perform best, SR-C1C1 for $\tilde{\chi}_1^{\pm}\tilde{\chi}_1^{\mp}$ production and SR-C1N2 for $\tilde{\chi}_1^{\pm}\tilde{\chi}_2^0$ production, as can be seen in Figure 7.8 (c) and (d).

7.6.2. Direct-Stau Production

Since the cross section for the direct production of stau pairs is generally lower compared to $\tilde{\chi}_1^{\pm}\tilde{\chi}_1^{\mp}$ and $\tilde{\chi}_1^{\pm}\tilde{\chi}_2^0$ production (see section 7.1), the sensitivity of this analysis to direct-stau production is lower. As a result, only one of the simulated model points can be excluded. Consequently upper limits on the cross section were derived and are shown in Figure 7.9. The limits are shown separately for the production of right-handed stau pairs on the left and for left-handed stau pairs on the right. Interestingly for low stau masses, SR-C1C1 yields the best expected exclusion limit, resulting in an even stronger observed limit than expected, because a downwards fluctuation is observed in SR-C1C1. In case of higher stau masses SR-DS-highMass provides the best upper limits.

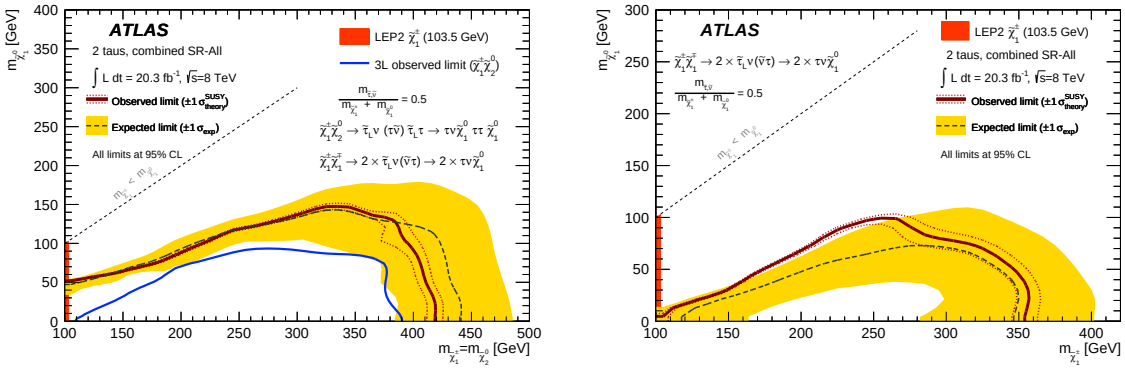

(a) $\tilde{\chi}_1^{\pm}\tilde{\chi}_1^{\mp}$ and $\tilde{\chi}_1^{\pm}\tilde{\chi}_2^0$ production

(b) $\tilde{\chi}_1^{\pm}\tilde{\chi}_1^{\mp}$ production

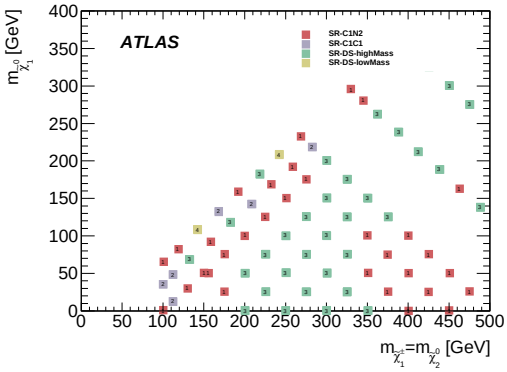

(c) $\tilde{\chi}_1^{\pm}\tilde{\chi}_1^{\mp}$ and $\tilde{\chi}_1^{\pm}\tilde{\chi}_2^0$ production

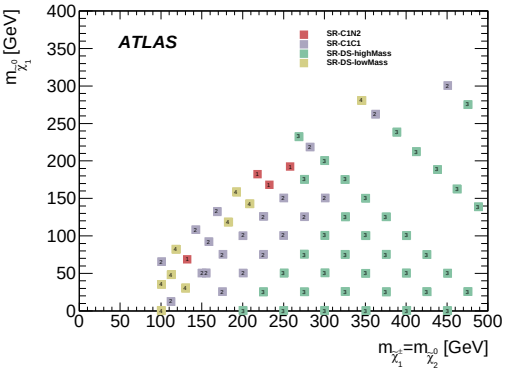

(d) $\tilde{\chi}_1^{\pm}\tilde{\chi}_1^{\mp}$ production

Figure 7.8.: (a, b) 95% CL exclusion limits for simplified models with (a) a combination of chargino–neutralino and chargino–chargino production and (b) chargino–chargino production only. See text for details of exclusion curves and uncertainty bands. Also shown is the LEP limit [129] on the mass of the chargino. The blue contour in (a) corresponds to the observed limit from the ATLAS three-lepton analysis [125], where only $\tilde{\chi}_1^{\pm}\tilde{\chi}_2^0$ production was considered. (c, d) Signal region with best expected p_0-value for each point in the simplified model with (a) associated chargino-neutralino and chargino-chargino production and (b) chargino pair production only. SR-C1N2 is indicated with 1, SR-C1C1 with 2, SR-DS-highMass with 3 and SR-DS-lowMass is indicated with 4. Figure from [119].

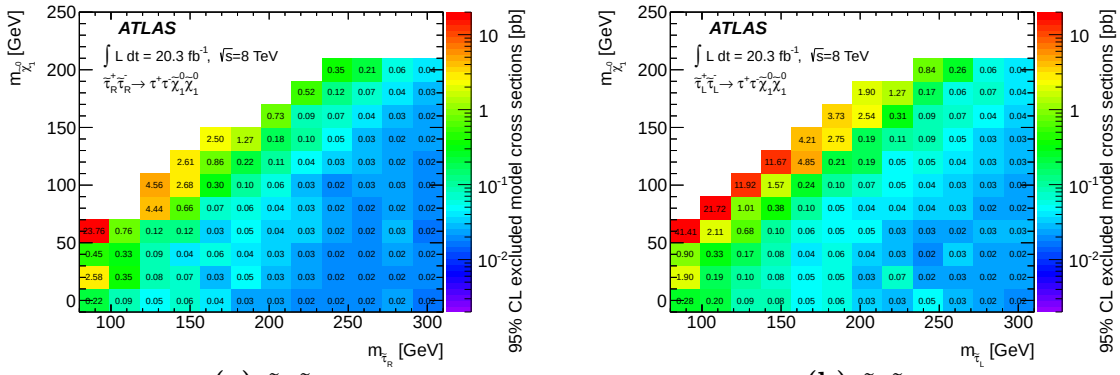

(a) $\tilde{\tau}_R\tilde{\tau}_R$ **(b)** $\tilde{\tau}_L\tilde{\tau}_L$

Figure 7.9.: Upper limits on the cross section for production of only (a) $\tilde{\tau}_R\tilde{\tau}_R$ or (b) $\tilde{\tau}_L\tilde{\tau}_L$ pairs. Figure from [119].

Limits on the signal strength have been computed for the associated production of pairs of the spartners of the right-handed and left-handed tau. The signal strength is defined as the ratio of the excluded cross section of the model at 95% confidence level to the theoretical cross section. It is shown as a function of the right handed stau mass for different lsp masses in Figure 7.10. The best observed upper limit is found for a mass of about 90 GeV for the staus and massless lsp. However the point can barely be excluded, only in case of the combined production of right handed and left handed stau pairs the signal strength get lower than 1, 0.95 to be exact.

7.6.3. pMSSM

For the two parameter planes chosen within the pMSSM framework, limits are set on the M_2 and μ parameters and can be found in Figure 7.11. In case of the model with fixed stau mass, Figure 7.11 (a), the region at low M_2 can in general not be excluded using this analysis, because the mass of the stau is fixed to 95 GeV and thus for low values of M_2 the chargino and neutralino would become lighter than the stau and thus the production of staus in the final state becomes disfavored. Since the direct-stau production in this model is constant while the production cross section of charginos and neutralinos varies with M_2 and μ, the direct-stau production becomes the dominant process at large values of M_2 and μ and thus dominates in the remaining allowed region.
The case of variable stau mass is shown in Figure 7.11 (b). It behaves similarly. For both models similar chargino mass ranges are excluded, namely approximately $100-350$ GeV, as can be inferred from the grey iso-mass lines depicted in the exclusion plots. Going to larger values of μ while keeping M_2 in the range of $100-350$ GeV, it is expected that the limits behave similar, because the masses and couplings of the involved particles do not change much, as can also be inferred from the grey iso-mass lines. The same holds true for the case of going to larger values of M_2 while keeping μ in the range of $100-350$ GeV.
SR-DS-highMass provides the best exclusion at high μ and M_2 for the model with fixed

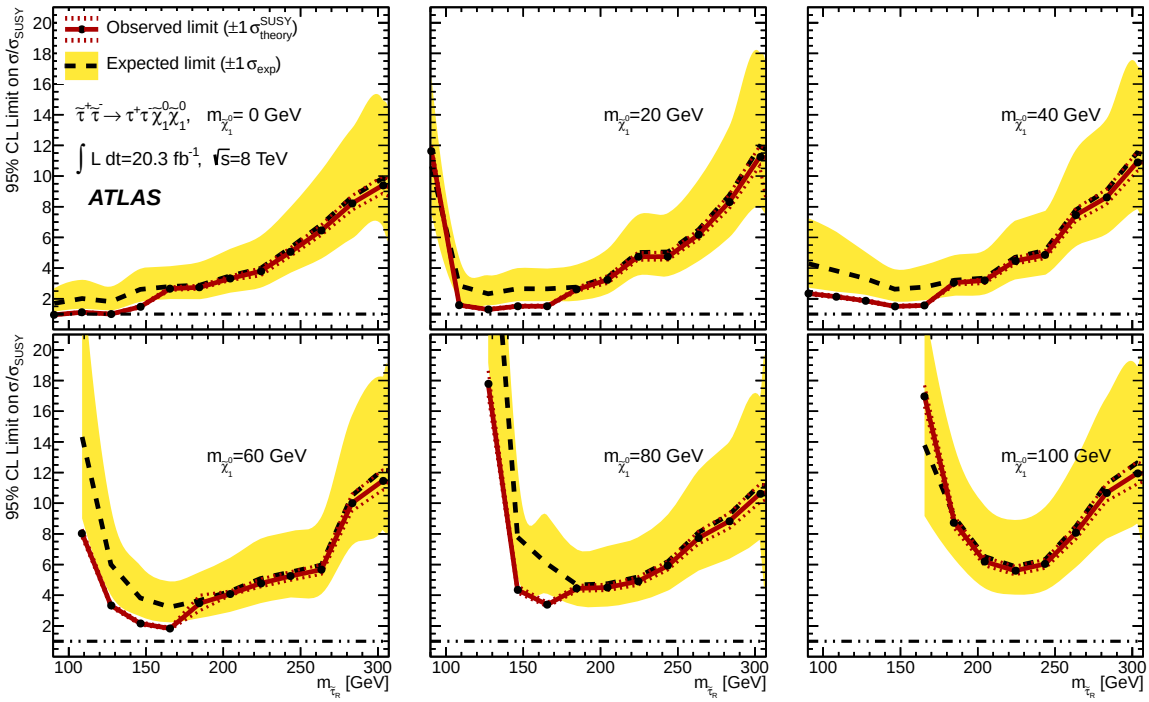

Figure 7.10.: Upper limit on the signal strength for the associated production of $\tilde{\tau}_R\tilde{\tau}_R$ and $\tilde{\tau}_L\tilde{\tau}_L$, for different lightest neutralino masses and as a function of the $\tilde{\tau}_R$ mass. See text for details of exclusion curves and uncertainty bands. Figure from [119].

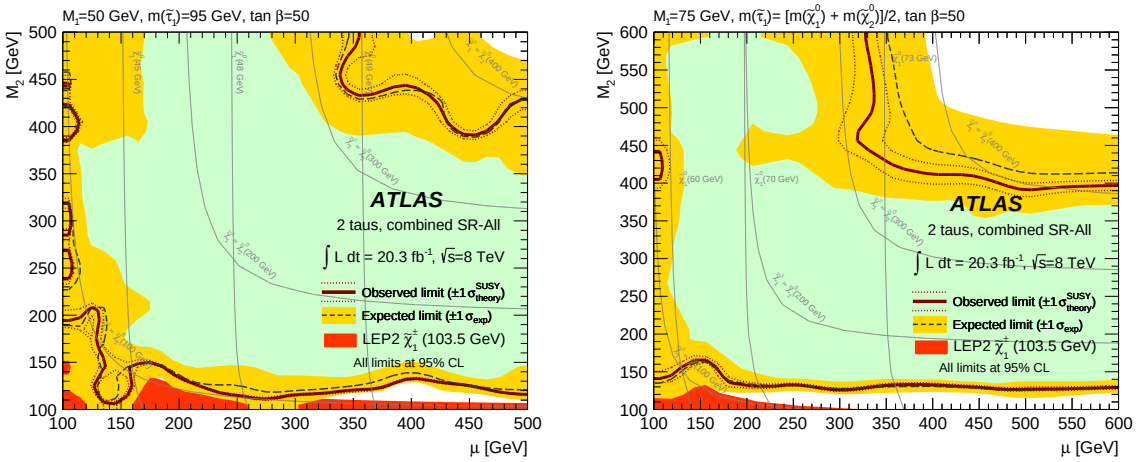

(a) pMSSM model (fixed stau mass) **(b)** pMSSM model (variable stau mass)

Figure 7.11.: 95% CL exclusion limits in the μ–M_2 mass plane for the pMSSM models with (a) fixed and (b) variable stau mass. See text for details of exclusion curves and uncertainty bands. The areas excluded by the -1σ expected limit are shown in green. The LEP limit [129] on the mass of the chargino is also shown in red. Figure from [119].

stau mass, while at lower values SR-C1N2 and SR-C1C1 provide better limits. For the other model SR-C1N2 and SR-DS-highMass compete for the best sensitivity over the whole parameter space studied.

7.7. Tau + Light Lepton Channels

The previously presented analysis addresses final states where both taus decay hadronically, in the following also called di-tau channel. In this section, final states with one tau decaying hadronically and one tau decaying into a light lepton, i.e. an electron or muon, will be considered. By convention these final states will be called after their detector signature in the following, namely a tau-tagged jet and a light lepton, the corresponding channels will be referred to as $\tau + e$ and $\tau + \mu$ channels.

The modeling of the Standard Model backgrounds taken from Monte Carlo, especially of the relevant kinematic distributions, will not be studied here. Instead the modeling has been studied in [130]. The bottom line is that the event yields in the tau + light lepton channels are significantly overestimated by the Monte Carlo in parts of the phase space where the contribution of W+jets production is dominant. However, this does not depend on the event kinematics, instead it is an overall offset in the production cross section of the final states considered. This can be taken into account by introducing appropriate scale factors [130] to re-weight the different types of backgrounds which are affected (0.414 for W+jets, 1.339 for Z+jets, 0.826 for $t\bar{t}$). Good agreement between distributions found in data and Monte Carlo could be achieved. However, to be independent from the aforementioned mis-modeling in the Monte Carlo simulation, for the studies presented in this section, the approach of assuming that there is no SUSY signal

in the data is adopted. A small subset (here: 5 fb^{-1}) of data is used as background estimation.
In the following, a short overview of the tau + light lepton analysis is given. The sensitivity has been studied using a cut-and-count-based approach.

7.7.1. Motivation

In the following the sensitivity of the $\tau + e$ and $\tau + \mu$ channels compared to the di-tau channel will be studied. Taus decay with a probability of approximately 1/6 into an electron and with about the same probability into a muon, whereas they decay with a probability of approximately 4/6 into hadrons. As a result, when considering final states with two taus, an equal amount of events is expected in the combined tau + light lepton channels and the di-tau channel, as illustrated in Figure 7.12 (a): the number of events with two hadronically decaying taus (indicated by the yellow area) is the same as the number of events with one hadronically and one leptonically decaying tau (indicated by the green area). The latter are shared in equal parts between the $\tau + e$ and $\tau + \mu$ channels.
For reasons of orthogonality to other ATLAS analyses the focus is on chargino-chargino production where exactly two taus are expected in the final state, as shown in Figure 7.12 (b), and thus constrain to final states containing exactly one hadronically decaying tau and exactly one leptonically decaying tau. The impact of this rather strict requirement will be investigated later on. The pMSSM model with direct stau pair production also has final states with two taus, however, as explained before, the production cross section is far lower, causing the sensitivity in the di-tau channel also to be rather low and leaving a lot of room for improvement. Results on the direct stau pair production model are presented in section 7.7.3.

Trigger In both channels, the $\tau + e$ and the $\tau + \mu$ channel, the corresponding lowest-threshold unprescaled tau + light-lepton trigger is used. The triggers use considerably lower thresholds than the di-tau trigger. The threshold cut used to ensure that the trigger is operating in the efficiency plateau of its tau leg can be lowered to about 25 GeV while the cuts on the electron- and muon-trigger leg are only about 20 GeV. These significantly lower thresholds should result in more signal events being selected.
However, in contrast to the di-tau channel, an additional light lepton neutrino is created in the decay chain of the tau + light lepton channel (cf. Figure 7.12, (b)). Thus in total, instead of 6 invisible particles, as in the di-tau channel, 7 invisible particles are created in the tau + light lepton channels. This in particular softens the visible p_{T} spectrum of the reconstructed objects as can be seen in Figure 7.13 (b). The visible p_{T} refers to the measured p_{T} of the object. It does not contain any information about the neutrino, because it leaves the detector undetected. From the visible p_{T} spectra the loss on the expected significance is not negligible, since the light leptons become much softer due to the additional lepton neutrino than a second hadronically decaying tau would be.
The left plot in Figure 7.13 shows the true visible p_{T} spectrum of the two taus coming from the SUSY decay chain or their decay products. The p_{T} shown in this plot is the

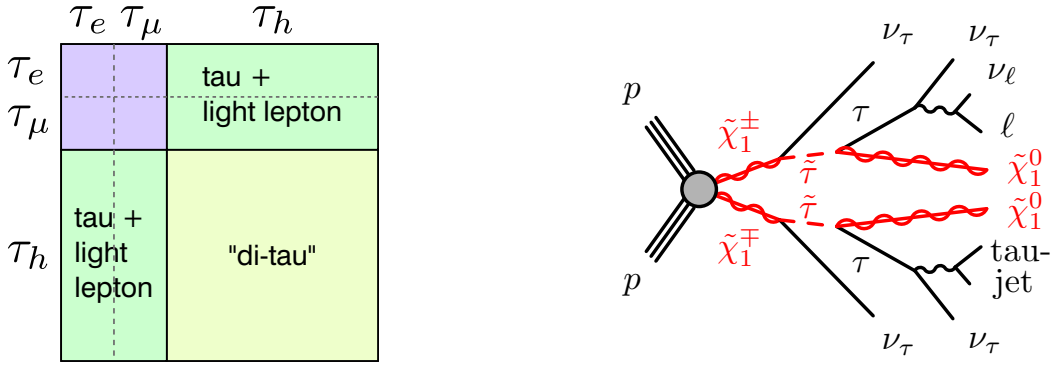

(a) Two τ decays **(b)** tau + light lepton final state

Figure 7.12.: Left: Illustration of the combinatorics arising from the branching ratios of a tau into light leptons ($\Gamma_e/\Gamma = 17.9\%$, $\Gamma_\mu/\Gamma = 17.4\%$) or hadrons (rest). The size of the colored areas is proportional to the number of events expected for different final states. Right: Decay chain including tau decays in the tau + light lepton channels, exhibiting 7 invisible particles in total.

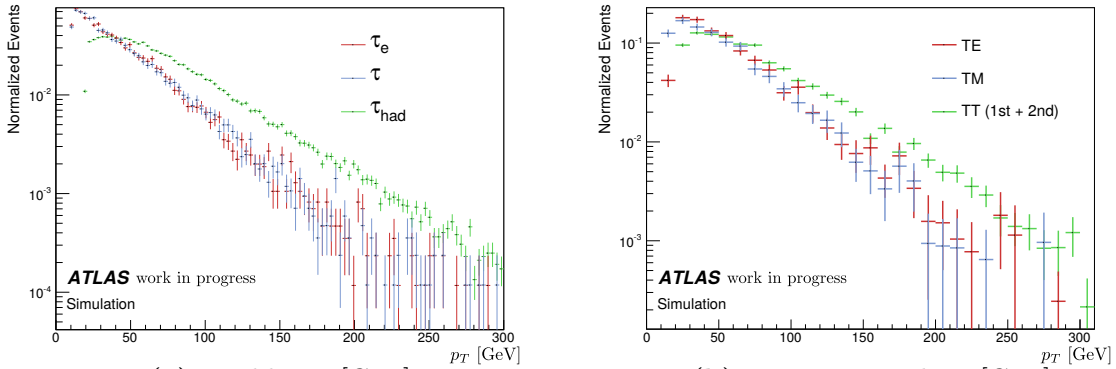

(a) Visible p_{T} [GeV] **(b)** Reconstructed p_{T} [GeV]

Figure 7.13.: True visible p_{T} spectrum (a) and reconstructed p_{T} spectrum (b) of the taus or their decay products, respectively, in the 3 different channels. For these plots the $\tilde{\chi}_1^{\pm}\tilde{\chi}_1^{\mp}$ grid point with $m(\tilde{\chi}_1^{\pm}) = 325$ GeV, $m(\tilde{\chi}_1^0) = 75$ GeV has been used.

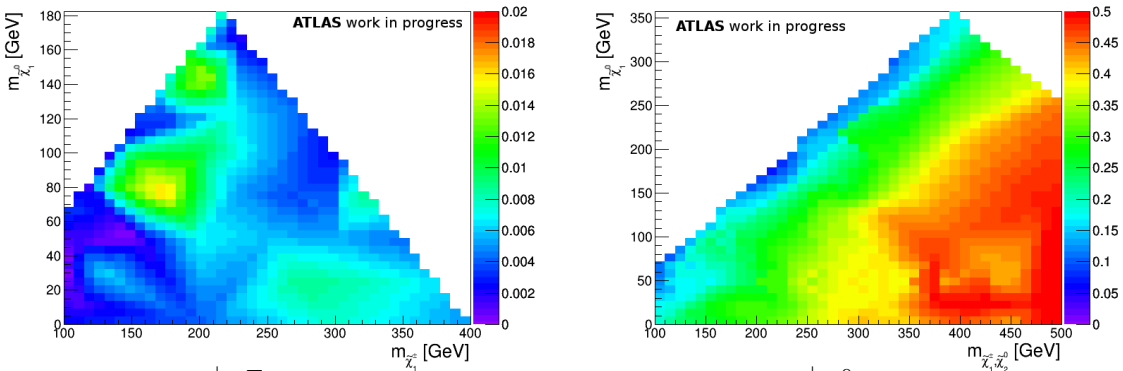

(a) $\tilde{\chi}_1^\pm \tilde{\chi}_1^\mp$ production **(b)** $\tilde{\chi}_1^\pm \tilde{\chi}_2^0$ production

Figure 7.14.: Signal gain in the $\tau + e$ channel when allowing for additional taus while still vetoing additional light leptons for the simplified model targeting $\tilde{\chi}_1^\pm \tilde{\chi}_1^\mp$ production (a) and the simplified model targeting associated $\tilde{\chi}_1^\pm \tilde{\chi}_2^0$ production (b). The $\tau + \mu$ channel yields very similar results.

p_{T} of the tau minus the p_{T} of the tau neutrino for a hadronically decaying tau, or the p_{T} of the electron or muon into which the tau decays otherwise, extracted from the Monte Carlo truth information. It can be seen that the impact of the additional ν_e or ν_μ is quite substantial, and moves the peak of the distribution from around 40 GeV to about 20 GeV. This unfortunately pretty much nullifies the gain from using lower trigger thresholds. The right plot in Figure 7.13 shows the reconstructed p_{T} spectra, measured for the two selected signal leptons corresponding to each channel. It is very similar to the left plot, showing that the p_{T} of the selected signal leptons behaves the same as the true p_{T} spectra. For these plots the $\tilde{\chi}_1^\pm \tilde{\chi}_1^\mp$ grid point with $m(\tilde{\chi}_1^\pm) = 325$ GeV, $m(\tilde{\chi}_1^0) = 75$ GeV has been used.

Impact of Orthogonality Requirement To be able to combine the results with the di-tau analysis and the three-lepton analysis, additional taus and light leptons have to be vetoed. The impact of the additional tau veto can be seen in Figure 7.14, which shows the signal gain in percent in the $\tau + e$ channel when allowing for additional hadronically decaying taus. On the left side of Figure 7.14 the signal gain in the simplified model describing $\tilde{\chi}_1^\pm \tilde{\chi}_1^\mp$ production is shown. The gain by loosening the additional lepton veto is negligible $\mathcal{O}(1\%)$, because additional leptons are not expected. However, for the simplified model targeting associated $\tilde{\chi}_1^\pm \tilde{\chi}_2^0$ production (right side of of Figure 7.14), the events with more than one tau and one light lepton are $\mathcal{O}(20 - 50\%)$, which is expected, because in this model one expects three taus in the final state. In the following the focus will be on the simplified model targeting $\tilde{\chi}_1^\pm \tilde{\chi}_1^\mp$ production, because it targets two tau final states and thus it better fits this analysis.

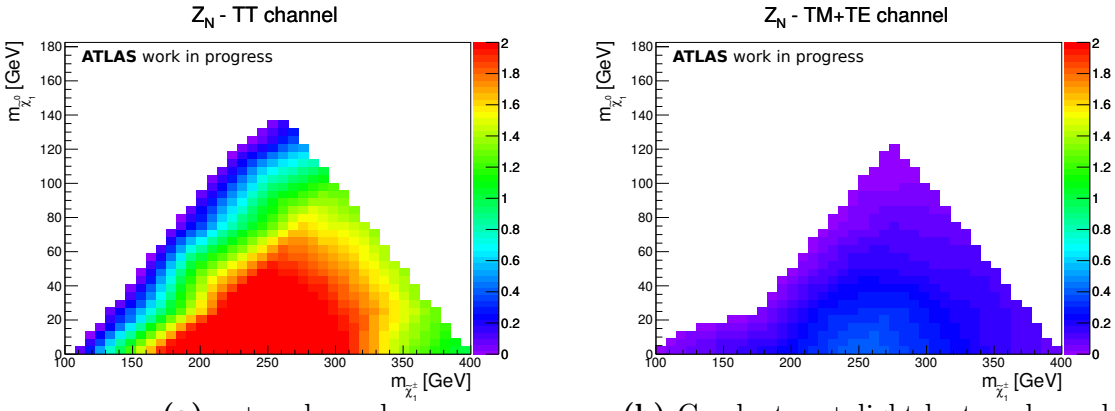

(a) $\tau + \tau$ channel **(b)** Comb. tau + light lepton channel

Figure 7.15.: The expected significance Z_N scaled to a luminosity of 20.3 fb^{-1} in the simplified model targeting $\tilde{\chi}_1^{\pm}\tilde{\chi}_1^{\mp}$ production for the $\tau+\tau$ channel (a) and the combination of the $\tau+e$ and $\tau+\mu$ channels (b), using a modified SR-C1N2, as explained in the text. An error of 30% on the background estimate has been assumed when calculating Z_N. The background has been estimated from 5 fb^{-1} of data, assuming that there is no SUSY signal in data.

7.7.2. Expected Significance Using Di-Tau SR

In Figure 7.15 the expected significances Z_N in the $\tilde{\chi}_1^{\pm}\tilde{\chi}_1^{\mp}$ simplified model, scaled to a luminosity of 20.3 fb^{-1}, for the $\tau+\tau$ channel and the combined $\tau+e$ and $\tau+\mu$ channel are shown using a slightly modified SR-C1N2: in each of the channels exactly one tau + exactly one electron, muon or tau are required. The expected significance in the combined tau + light lepton channel is not of the same order as the significance of the $\tau+\tau$ channel, as expected by the combinatorics depicted in Figure 7.12, it is significantly smaller. The significances for each grid point of the $\tau+e$ and $\tau+\mu$ channels have been combined, assuming statistical independence, as follows:

$$Z_N = \sqrt{(Z_N^{\mathrm{TE}})^2 + (Z_N^{\mathrm{TM}})^2}, \tag{7.5}$$

where Z_N^{TE} denotes the significance in the $\tau+e$ channel, Z_N^{TM} the significance in the $\tau+\mu$ channel and Z_N the combined significance of both channels.

The problem is rooted in different shapes of the distributions. In the tau + light lepton channels the signal is buried under the background, at least in case of the variables which have been used to define SR-C1N2, the visible tau p_{T} spectrum, Figure 7.13, already hinted at this. This is caused by the additional lepton neutrino in the leptonic decay of the tau. Its effect can be seen in Figure 7.17, showing the $\not{E}_{\mathrm{T}}$ distribution on the left and the m_{T2} on the right after requiring at least two taus and applying the Z veto for, from top to bottom, the $\tau+e$, the $\tau+\mu$ and the di-tau channel. The dotted lines show exemplaric signal points: they are more distinct from the Standard Model background in the case of the di-tau channel. Consequently the signal acceptance is lower, as can be seen in Figure 7.16. Therefore, an optimization in the tau + light

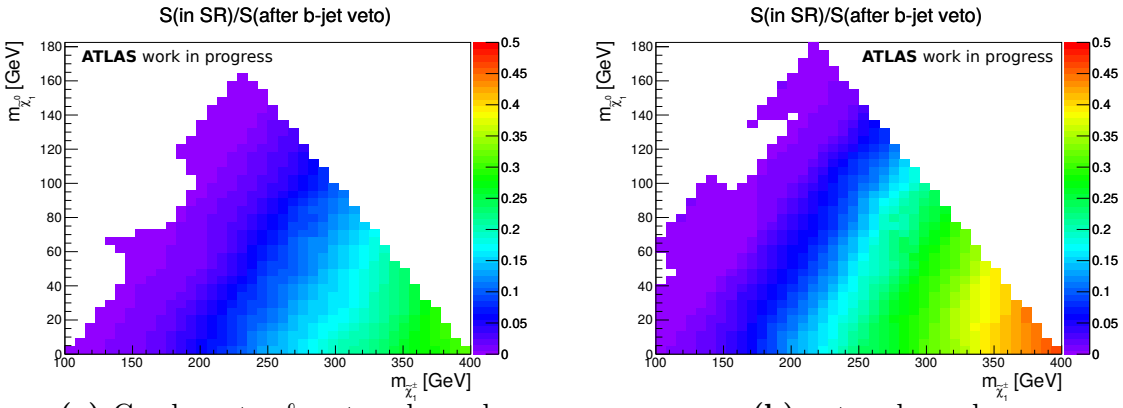

(a) Comb. $\tau + e$ & $\tau + \mu$ channel **(b)** $\tau + \tau$ channel

Figure 7.16.: Signal acceptance in the combined tau + light lepton channel on the left compared to the signal acceptance in the di-tau channel on the right. The signal acceptance in these plots is defined as being the ratio of the number of Monte Carlo events in SR-C1N2 over the number of Monte Carlo events after event cleaning, the requirement of 2 OS signal leptons and the b-jet veto.

lepton channels is needed to obtain a better background rejection.

7.7.3. Cut and Count Based Optimization

The following section summarizes the cut and count based analysis performed to optimize the significance for the tau + light lepton channels in the $\tilde{\chi}_1^{\pm}\tilde{\chi}_1^{\mp}$ model, as well as for the pMSSM model targeting direct-stau pair production (see section 7.1). More details can be found in the appendix, section A.2.1. The improvement when combining all three channels, the impact of the signal-jet veto, replacing the Z-veto by a cut on m_{T2}, as well as alternate definitions of m_{T2} have also been studied. To simplify the analysis, the error in the calculation of Z_N has always been assumed to be 30% instead of calculating the full systematics.

$\tilde{\chi}_1^{\pm}\tilde{\chi}_1^{\mp}$ Production To find a set variables with good discrimination power between background and signal, the correlation of potential cut variables has been studied. The correlation between variables a and b has been calculated as follows:

$$\chi_{TE} = \frac{\langle ab \rangle - \langle a \rangle \langle b \rangle}{\sqrt{(\langle a^2 \rangle - \langle a \rangle^2)(\langle b^2 \rangle - \langle b \rangle^2)}}, \tag{7.6}$$

where the index TE denotes the $\tau + e$ channel and the averages run over all events which belong to this channel, without any kinematic cuts applied except for the event cleaning as described in section 6.8 and the trigger cuts.
The correlations between different event variables are shown in Figure 7.18 for different processes: a $\tilde{\chi}_1^{\pm}$ pair production signal benchmark point is shown in Figure 7.18

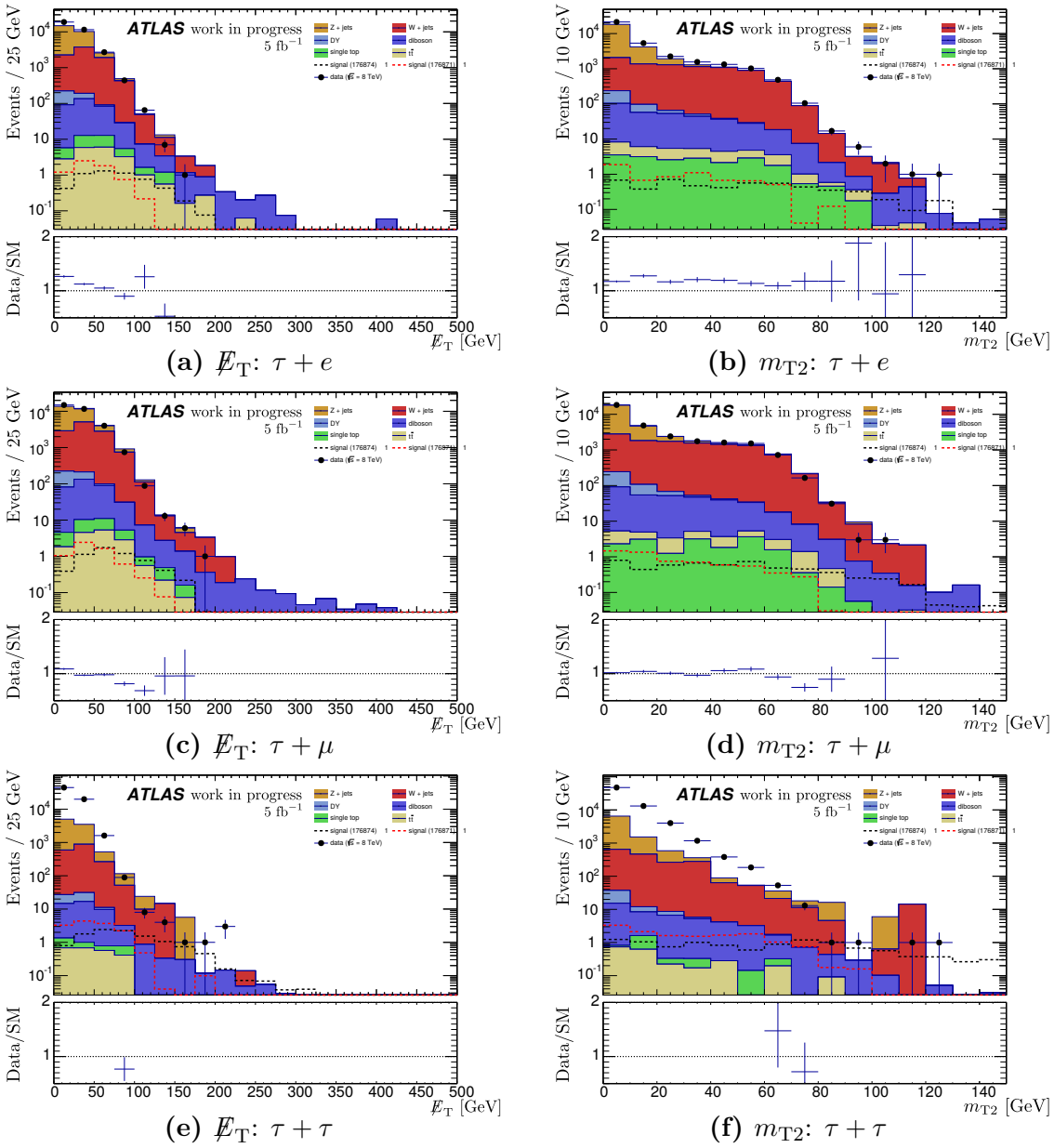

(a) $\not{E}_T$: $\tau + e$ (b) m_{T2}: $\tau + e$

(c) $\not{E}_T$: $\tau + \mu$ (d) m_{T2}: $\tau + \mu$

(e) $\not{E}_T$: $\tau + \tau$ (f) m_{T2}: $\tau + \tau$

Figure 7.17.: Distributions of $\not{E}_T$ (left) and m_{T2} (right). The $\tau + e$, $\tau + \mu$ and $\tau + \tau$ channels (from top to bottom) are shown. The QCD estimate is missing, and this explains the discrepancy between data and SM predictions in the $\tau + \tau$ channel.

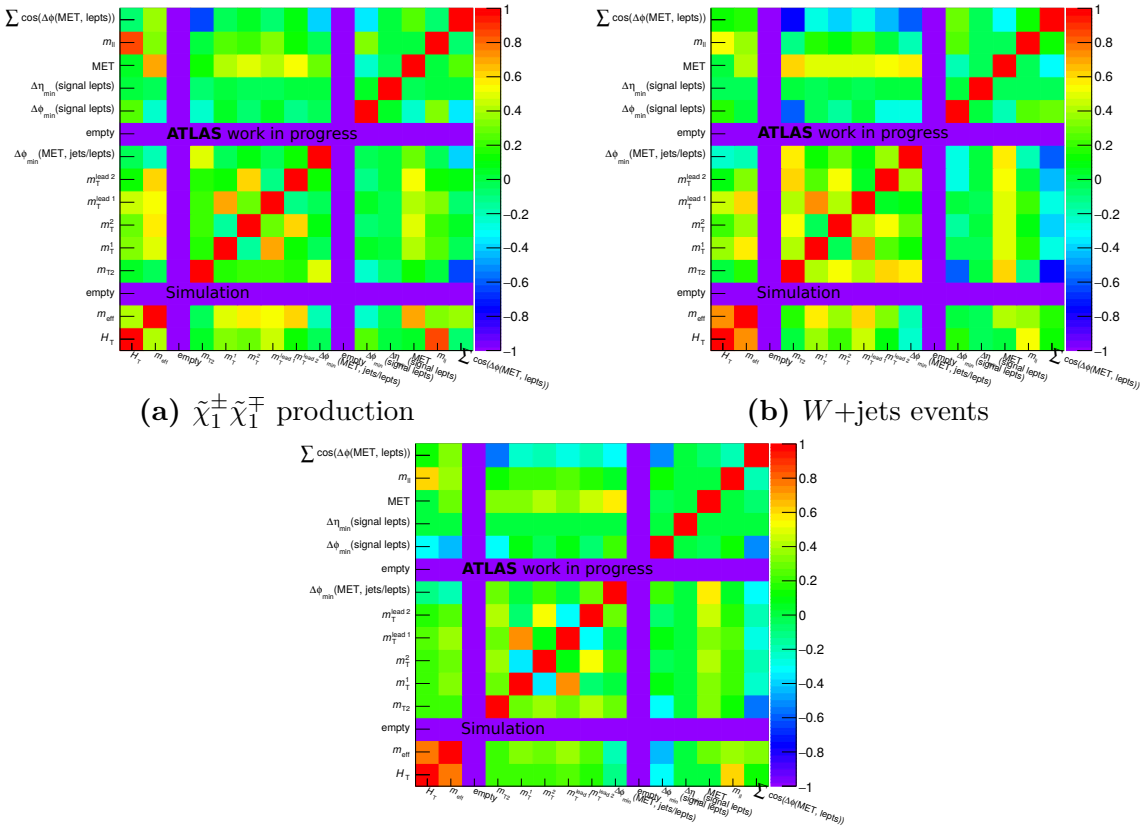

(a) $\tilde{\chi}_1^{\pm}\tilde{\chi}_1^{\mp}$ production

(b) W+jets events

(c) Z+jets events

Figure 7.18.: Correlations as defined in the text, for one grid point of the $\tilde{\chi}_1^{\pm}\tilde{\chi}_1^{\mp}$ signal sample (a), a simulated $W \to \tau\nu$ + jets (b) and a simulated $Z \to \tau\tau$ + jets sample (c). All three plots are ATLAS work in progress.

(a), while, for the sake of comparison, the correlations in simulated W+jets events, Figure 7.18 (b), and in simulated Z+jets events, Figure 7.18 (c) are also shown. As expected, the correlations between the observables are different for different processes. For example, the missing transverse energy in W+jets events is correlated stronger with the transverse masses than in case of Z+jets events, because missing transverse energy is not expected in Z+jets events, whereas it is expected in W+jets events, because of the neutrino created in the W decay.

Cut variables are picked which are mostly uncorrelated in case of the $\tilde{\chi}_1^{\pm}$ pair production benchmark point: the stransverse mass m_{T2}, the transverse mass of the leading p_{T} lepton, the transverse mass of the sub-leading lepton p_{T}, the missing transverse energy $\not{E}_{\mathrm{T}}$, the effective mass m_{eff} and H_{T}. In addition, also a set of commonly used variables will be studied: the transverse momentum p_{T} of the leading signal lepton, as well as the difference in pseudorapidity η and the angle ϕ in the transverse plane between the selected leptons.

To reduce the set of variables further, the power of each variable to discriminate signal from background is estimated by investigating the signal-over-background-ratio when cutting on these variables. The complete set of signal-over-background-ratio plots can be found in the appendix in section A.2.1 for a set of exemplaric signal points. In summary: for all variables under investigation it is impossible to find cut values yielding a signal-over-background-ratio larger than 1, instead the signal-over-background-ratio usually stays way below 1. The signal-over-background-ratio does not improve much when using $\Delta\eta$ or $\Delta\phi$. The spread in the values at which the signal-over-background distributions reach a value close to 0 is too large for the p_{T} of the leading signal lepton and H_{T}, meaning that for different signal points different cut-values are optimal. For the purpose of further optimization, the list of variables has been slimmed to include m_{T2}, the transerve mass of the leading-p_{T} lepton, m_{eff} and $\not{E}_{\mathrm{T}}$.

A combination of variables is needed to achieve a better significance. To decide which variables to use for further optimization, two criteria were considered: on the one hand the deviation of the end points of the signal-over-background distributions for different signal points, because the background should be rejected equally well throughout the whole parameter space and on the other hand the maximum signal-over-background-ratio so decent statistics can be retained after cutting, i.e. $\mathcal{O}(10)$ events or more.

To reduce the processing power needed[2] to perform the optimization, only one m_{T} definition is being used. The detailed comparison of the different m_{T} definitions, including also the sum of the transverse masses, can be found in the appendix, section A.2.3. In summary: the transverse mass of the leading p_{T} lepton has been chosen as the transverse mass of interest, because its power to discriminate between signal and background becomes better with increasing mass of supersymmetric particles, because the m_{T} spectrum becomes harder.

After a brute-force optimization, trying different combinations of at most three variables, two signal regions are defined to cover the low and high mass region and another one

[2]The computation time needed to try all possible combinations of variables increases exponentially with the number of variables tried.

specifically optimized for the di-tau channel for the sake of comparison:

- SR-TL-lowMass: b-jet veto, Z-veto, $H_{\mathrm{T}} > 275$ GeV, $m_{\mathrm{T}} > 140$ GeV and $\not{E}_{\mathrm{T}} > 80$ GeV;
- SR-TL-highMass: b-jet veto, Z-veto, $m_{\mathrm{T2}} > 100$ GeV and $\not{E}_{\mathrm{T}} > 40$ GeV;
- SR-TT: b-jet veto, Z-veto, $m_{\mathrm{T}} > 140$ GeV and $\not{E}_{\mathrm{T}} > 100$ GeV.

In SR-TL-highMass (for high mass charginos), the optimization did not yield a large improvement. The significance stays below one, as can be seen in Figure 7.19 (a). Interestingly, this signal region was already quite optimized with respect to the high sparticle mass region. However, for the low sparticle mass region, cuts were found which performed better in the tau + light lepton channels, namely using the transverse mass of the leading p_{T} lepton and H_{T} as cut variables instead of m_{T2}: SR-TL-lowMass. The resulting significance has been depicted in Figure 7.19 (b). In this region, the combined tau + light lepton channel outperforms the di-tau channel, as can be seen when comparing (b) and (c) of Figure 7.19. However, when optimizing for the di-tau channel independently of the tau + light lepton channel, it is possible to find signal regions which outperform the tau + light lepton channels in SR-TL-lowMass. This can be seen by comparing (b) and (d) in Figure 7.19. In Figure 7.19 (d) the cuts have been optimized for the di-tau channel: SR-TT.

pMSSM DStau For the cut and count analysis in the direct stau pMSSM model it has been assumed that the correlations between the observables do not differ significantly from those observed in the $\tilde{\chi}_1^{\pm}\tilde{\chi}_1^{\mp}$ production model. Consequently the same variables as before are used as a starting point, with the exception that the sum of the transverse masses, $m_{\mathrm{T}}^{12} = m_{\mathrm{T}}^{1} + m_{\mathrm{T}}^{2}$, was added to the list of cut variables, as well as the p_{T} of the sub-leading lepton to the list of cut-variable candidates. The detailed results can again be found in the appendix, section A.2.1.
The optimization of the tau + light lepton channel for the pMSSM model focusing on direct stau pair production however sadly suffers from the same problem as before: it is impossible to find suitable cuts to reach a signal-over-background-ratio larger than 1. Consequently again a set of variables which perform best (according to the same criteria as before) is selected and combined to achieve a better significance. After optimization two signal regions are defined:

- SR-TL-DS: Jet50-jet veto, Z-veto, $H_{\mathrm{T}} > 175$ GeV, $\not{E}_{\mathrm{T}} > 80$ GeV and $m_{\mathrm{T}}^{12} > 350$ GeV.
- SR-TL-DS-TT: Jet50-jet veto, Z-veto, $H_{\mathrm{T}} > 175$ GeV, $\not{E}_{\mathrm{T}} > 80$ GeV, $m_{\mathrm{T}}^{12} > 280$ GeV and $m_{T2} > 20$ GeV.

The resulting significances can be found in Figure 7.21 (a) and (b). In SR-TL-DS, both channels are approximately equally strong. However, as can be seen by comparing the

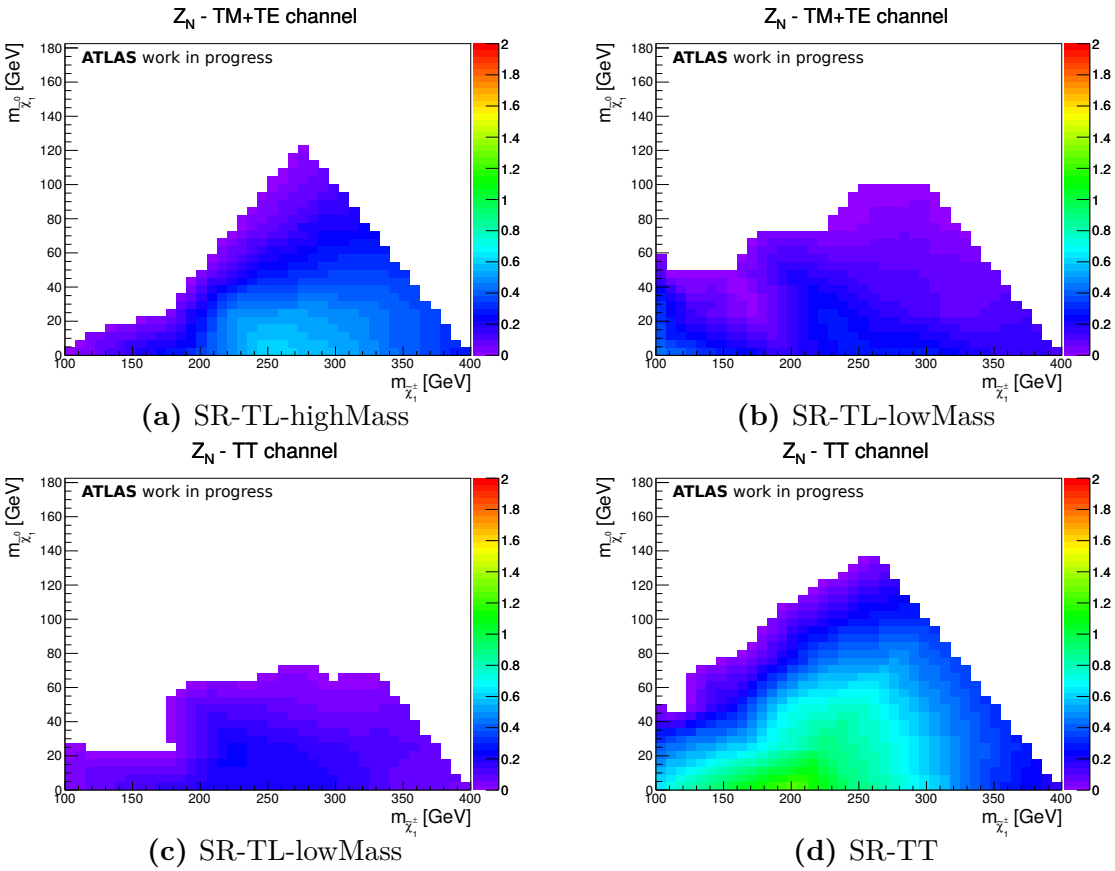

(a) SR-TL-highMass **(b)** SR-TL-lowMass

(c) SR-TL-lowMass **(d)** SR-TT

Figure 7.19.: Significance in the combined tau + light lepton channels after optimization for SR-TL-highMass (a) and SR-TL-lowMass (b). For comparison the bottom plot shows the significance in the di-tau channel only for the SR-TL-lowMass (c) and following cuts (d): b-jet veto, Z-veto, $m_{\mathrm{T}} > 140$ GeV and $\not{E}_{\mathrm{T}} > 100$ GeV. These cuts have been optimized for the di-tau channel. The background estimate is computed from 5 fb^{-1} of data assuming that there are no supersymmetric events in data. The channel is given in the caption of each plot.

upper and the lower plots, the cut values in the SR-TL-DS signal region are not optimized for the di-tau channel. When optimizing with respect to the di-tau channel, obtaining SR-TL-DS-TT, one is able to achieve a better significance than in the combined tau + light lepton channel, as can be seen in Figure 7.21 (c).
A few more ways to increase the sensitivity of the tau + light lepton channels have been tried, and are presented in section A.2.4 (a jet-veto has been compared to a b-jet veto, m_{T2} cut to replace the Z-veto, asymmetric m_{T2}). However, no significant improvement has been found.

7.7.4. Improvement When Combining all Three Channels

To improve the analysis, the statistical combination of all three channels, as done for the tau + light lepton channels in Equation 7.5, is studied in the following. As a reference the sensitivity of the channel performing better in the considered signal region is chosen: the di-tau channel is chosen as reference in the SR-TL-highMass signal region and the combined tau + light lepton channel as reference in the SR-TL-lowMass. The improvement in sensitivity when combining the tau + light lepton with the di-tau channel is shown in Figure 7.20 (the strong improvement seen along the diagonal is a computational artifact). In SR-TL-highMass the significance does not improve much when combining all three channels, because the significance in the combined tau + light lepton channels is always lower than in the di-tau channel. In the tau + light lepton channels it is harder to discriminate the signal from the background than in the di-tau channel, because of the additional neutrino which softens the spectrum of the lighter signal lepton, as seen in Figure 7.13. In SR-TL-lowMass one could gain up to 20% or more in Z_N when combining all three channels. The combination of all three channels, however, gives significant improvement only in regions where the overall significance of both channels is approximately equal. Looking at Equation 7.5, it can be inferred that the maximum gain in sensitivity when statistically combining the three channels is $\sqrt{3}$ if all three regions perform equally well. Since the di-tau analysis found also for the low sparticle mass region a signal region (namely SR-C1C1) which is far more sensitive than the signal region proposed here, a statistical combination of all three channels is not expedient.

7.8. Estimating the Sensitivity at $\sqrt{s} = 13$ TeV

The data used so far was collected by the ATLAS experiment at the LHC at a center-of-mass energy of $\sqrt{s} = 8$ TeV throughout 2012. In 2015 the LHC resumed operations at a center-of-mass energy of $\sqrt{s} = 13$ TeV. Initial predictions of the amount of data to be collected were of the order of 10 fb^{-1}, while eventually only 3.2 fb^{-1} were collected, significantly less than in 2012 (about 20 fb^{-1}). Consequently an estimate is needed whether the analysis presented in the preceding sections is worthwhile pursuing using the data collected in 2015: on the one hand, the production cross sections increase proportionally to the mass of the particles produced when raising the center-of-mass energy, consequently especially for higher-mass signal points a higher increase in the

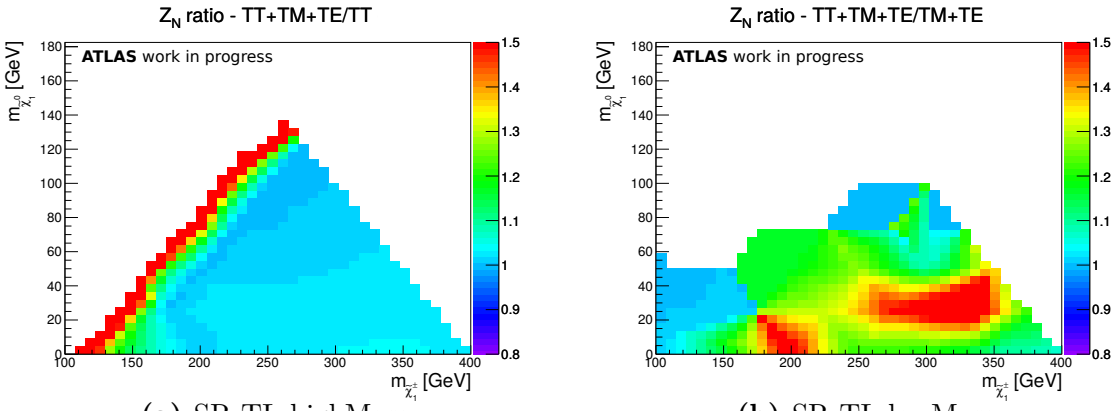

(a) SR-TL-highMass **(b)** SR-TL-lowMass

Figure 7.20.: Comparison of the significance of all three channels combined: for SR-TL-highMass, (a), and for SR-TL-lowMass, (b): the ratio of the significances when statistically combining all three channels over only using the stronger channel is shown, i.e. the di-tau for SR-TL-highMass and the combined tau + light lepton channel for SR-TL-lowMass. The improvement seen along the diagonal in SR-TL-highMass is an artifact of a division by zero. The individual significances can be found in Figure A.3.

production cross section is expected than for Standard Model backgrounds, on the other hand less data is available.

Background Estimate To estimate the Standard Model background in the signal regions it is assumed that the event kinematics do not change when going to a higher center-of-mass energy, instead it is assumed that only the production cross sections will change due to the change in the parton density function when going to a higher center-of-mass energy. As a result, the data sets used in the preceding sections, simulated at $\sqrt{s} = 8$ TeV, can be re-used to obtain an estimate of the Standard Model background event yields and the signal event yields at $\sqrt{s} = 13$ TeV.
The package LHAPDF [131] is used to re-weight the Monte Carlo datasets simulated at $\sqrt{s} = 8$ TeV to 13 TeV by using the energy of the interacting partons as input. The probability to encounter partons with the given energy is computed at a center-of-mass energy of 8 TeV and 13 TeV. Eventually the event is weighted to 13 TeV by applying the re-weighting factor:

$$w = \frac{p(x_1, 13\text{ TeV})p(x_2, 13\text{ TeV})}{p(x_1, 8\text{ TeV})p(x_2, 8\text{ TeV})}, \tag{7.7}$$

where $p(x_1, 13\text{ TeV})$ is the parton density function, the first parameter, x_i, denotes the energy fraction of the i-th parton, while the second parameter denotes the center-of-mass energy at which the parton density is evaluated. The same is done for signal samples. The multi-jet contribution, however, has to be estimated differently, because no information about the interacting partons is available in recorded data. It is estimated

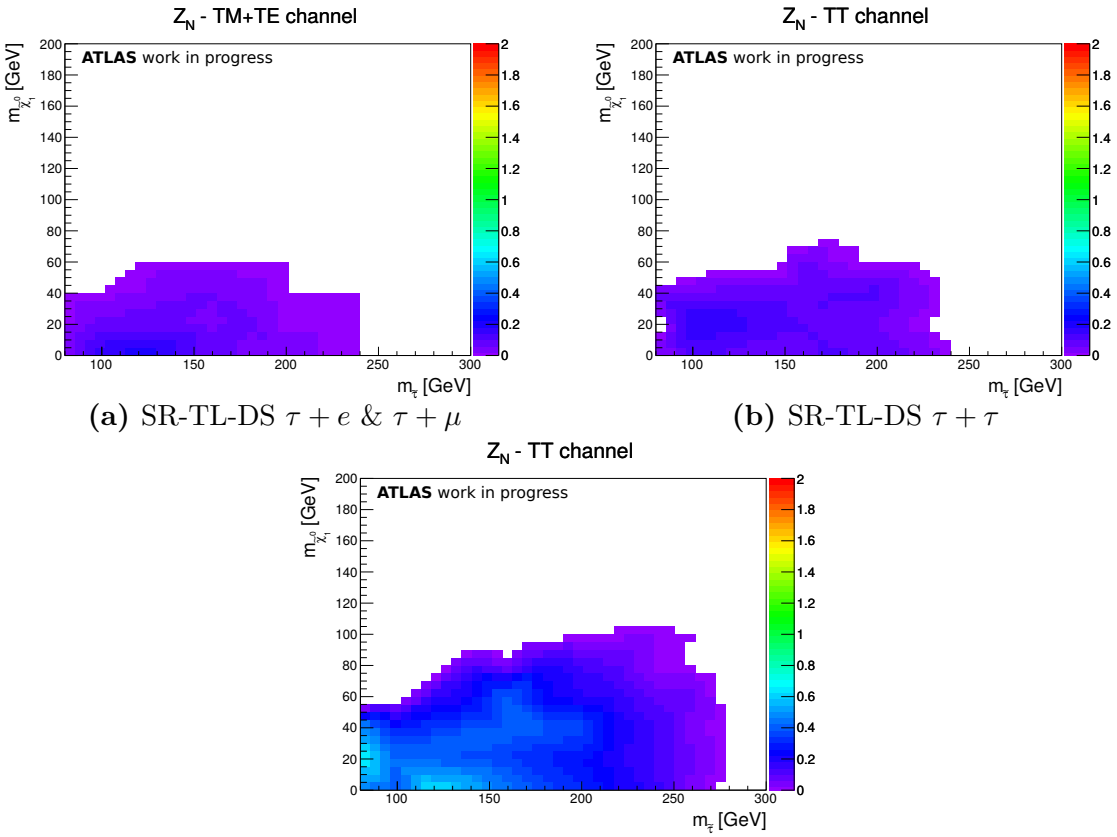

(a) SR-TL-DS $\tau + e$ & $\tau + \mu$

(b) SR-TL-DS $\tau + \tau$

(c) SR-TL-DS-TT $\tau + \tau$

Figure 7.21.: Significance for SR-TL-DS after optimization in the combined tau + light lepton channels (a) and the di-tau channel (b). The bottom plot, (c), shows SR-TL-DS-TT which is better optimized for the di-tau channel. The tau + light lepton does not show any significance in the SR-TL-DS-TT signal region and thus a combination is not feasible.

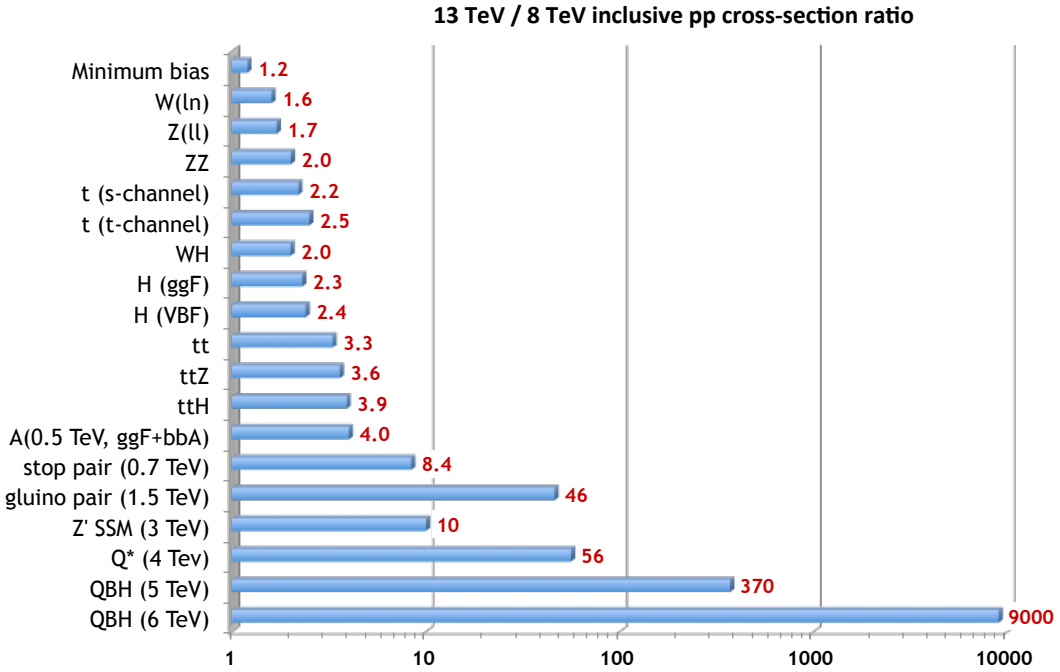

Figure 7.22.: Ratio of the inclusive cross section at 13 TeV at the LHC over the inclusive cross section at 8 TeV at the LHC for different processes. The increase in the cross section for multi-jet events is of the same order as for minimum bias events. Figure from [132].

by using the prediction from Run I and scaling it up. A factor of 2.8 has been chosen for the main results to emulate a worst-case scenario[3], while the expected increase in the production cross section of multi-jet events is only about 20%, as can be seen in Figure 7.22.

Validation of Background Estimate To validate the initially made assumption, namely that the event kinematics are not changed when going to a higher center-of-mass energy, normalized distributions of the transverse momenta of the leading and sub-leading tau are compared in Figure 7.23 for a sample from the pMSSM model tuned for the direct production of staus. The unweighted sample simulated at a center-of-mass energy of 8 TeV is depicted in green, the re-weighted sample is depicted in black and the sample simulated at a center-of-mass energy of 13 TeV is depicted in red. The ratios of the re-weighted sample and the sample simulated at a center-of-mass energy of 13 TeV to the unweighted sample, depicted in the lower panels of Figure 7.23, are flat within statistical errors. A nice agreement is found and thus a sensible prediction can be made using this technique.

[3]The expected exclusion contours for different multi-jet scaling factors are compared in section A.3 using SR-C1C1 and an expected luminosity of 5 fb^{-1}.

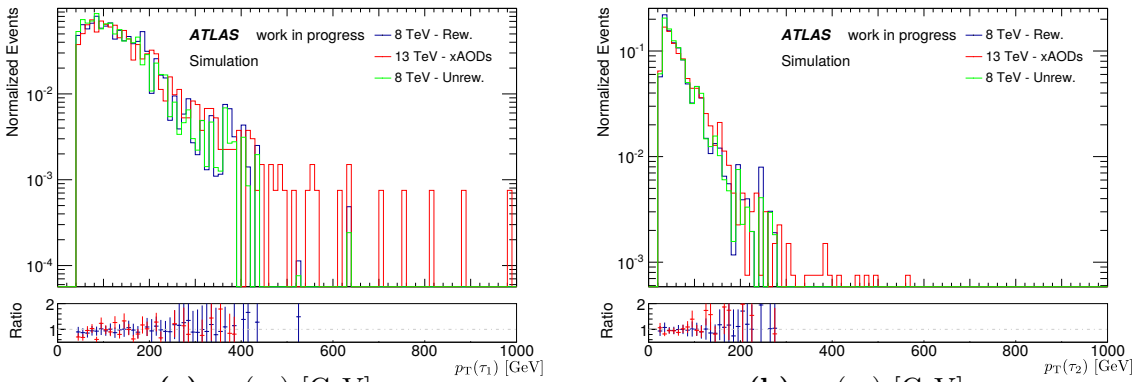

(a) $p_{\mathrm{T}}(\tau_1)$ [GeV] **(b)** $p_{\mathrm{T}}(\tau_2)$ [GeV]

Figure 7.23.: Upper panels show the normalized distributions of the transverse momenta of the (a) leading tau and (b) the sub-leading tau in p_{T}. A sample from the pMSSM model tuned for the direct production of staus is used with $m_{\tilde{\tau}} = 200$ GeV and $m_{\tilde{\chi}_1^0} = 0$ GeV. Depicted in green is the unweighted sample simulated at a center-of-mass energy of 8 TeV, in black the same sample reweighted to a center-of-mass energy of 13 TeV and in red the sample simulated at a center-of-mass energy of 13 TeV. The lower panels show the ratio of the re-weighted (black) sample and the sample simulated at a center-of-mass energy of 13 TeV (red) to the unweighted sample simulated at a center-of-mass energy of 8 TeV. The uncertainties depicted in the lower panels are statistical uncertainties. The agreement is remarkably well, as expected there is no difference in the event kinematics.

Sensitivity at $\sqrt{s} = 13$ TeV The expected significance at a center-of-mass energy of $\sqrt{s} = 13$ TeV is shown in Figure 7.24 for three different integrated luminosities as well as the unweighted samples corresponding to the analysis at a center-of-mass energy of $\sqrt{s} = 8$ TeV. About 10 fb^{-1} are needed to achieve a similar exclusion limit to the analysis using the 2012 dataset, as can be seen by comparing Figure 7.24 (c) and (d). The comparable level of sensitivity makes a statistical combination of both datasets worthwhile, see Figure 7.24 (e): the exclusion limits can be pushed beyond the limits of the available signal points, while the limits for claiming evidence can be pushed from about 250 GeV in the lightest chargino mass to about 350 GeV. While this prospect is highly encouraging, the actual amount of data collected by ATLAS in 2015 was less than needed, only 3.2 fb^{-1} were collected. Consequently one cannot expect to achieve a comparable sensitivity to the Run I analysis using the 2015 data, consequently, also a statistical combination becomes unfavorable, resulting in the decision to target final states additionally containing jets when analyzing the 2015 data in chapter 9.

7.9. Summary

An analysis has been presented searching for electroweak production of supersymmetric particles in events with at least two hadronically decaying taus, missing transverse energy and low jet activity, where 20.3 fb^{-1} of proton-proton collision data taken by the

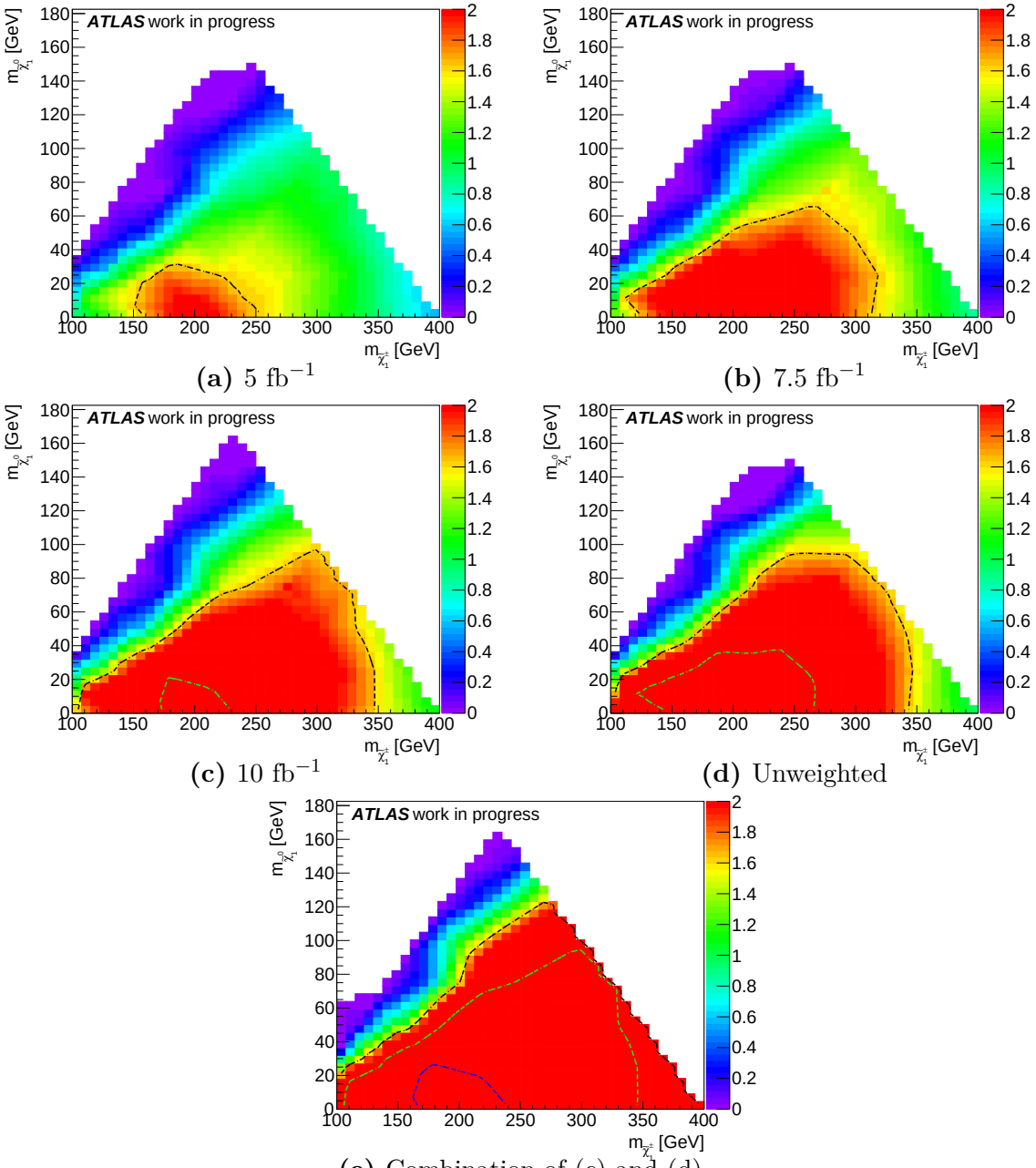

(a) 5 fb^{-1} **(b)** 7.5 fb^{-1}

(c) 10 fb^{-1} **(d)** Unweighted

(e) Combination of (c) and (d)

Figure 7.24.: Expected significance obtained by weighting the Standard Model backgrounds taken from Monte Carlo to a center-of-mass energy of 13 TeV and using the multi-jet estimate from Run I multiplied by a factor of 2.8 for different expected integrated luminosities: (a) 5 fb^{-1}, (b) 7.5 fb^{-1} and (c) 10 fb^{-1}. In (d) the expected significance using the unweighted samples is shown, corresponding to the 2012 analysis. Sub-figure (e) depicts the statistical combination of (c) and (d), the estimated significance when combining the 2012 and expected 2015 data. The black-dashed line corresponds to the region which can potentially be excluded, while the green-dashed line corresponds to the region where one can potentially claim evidence for supersymmetry and the blue-dashed line corresponds to the region where one can claim discovery of supersymmetry if it exists within that region. To achieve a comparable sensitivity to the Run I analysis, about 10 fb^{-1} are needed.

ATLAS experiment throughout 2012 at $\sqrt{s} = 8$ TeV have been used. To estimate the multi-jet background, the data-driven ABCD method has been used. All other Standard Model backgrounds have been taken from Monte Carlo, control regions have been used to correct for potential errors in the cross section calculation and validation regions have been used to investigate the quality of the extrapolation of the estimates from the control to the signal regions. Four signal regions have been defined targeting different final states. No excess over the Standard Model expectation has been found, instead only a downwards fluctuation has been observed and consequently limits were set in simplified models, a pMSSM model targeting direct-stau pair production, as well as two further pMSSM parameter planes, one with fixed stau mass, the other with the stau mass set to $(m_{\tilde{\chi}_1^0} + m_{co})/2$.
Compared to the results presented by the three-lepton analysis [125], the limits could be improved by approximately 50 GeV in the lightest chargino mass and between 10 GeV to 50 GeV in the next-to-lightest neutralino mass. In the case of simultaneous $\tilde{\chi}_1^{\pm}\tilde{\chi}_1^{\mp}$ and $\tilde{\chi}_1^{\pm}\tilde{\chi}_2^0$ production, $\tilde{\chi}_1^{\pm}/\tilde{\chi}_1^0$ masses of up to 410/140 GeV can be excluded, while in the case of $\tilde{\chi}_1^{\pm}$ pair production alone, chargino/neutralino masses of up to 345/90 GeV can be excluded. Due to the small cross section, the analysis presented here is not yet sensitive to large parts of the phase-space of the pMSSM model targeting direct-stau pair production. In the other two pMSSM parameter planes with $\tan\beta = 50$, where in one case the stau mass is fixed and in the other it is set halfway between lightest neutralino and the lightest chargino, similar lightest chargino mass ranges can be excluded, namely approximately 100 GeV $-$ 350 GeV. The obtained model independent observed upper limit on the visible cross section, $\langle\sigma_{\text{vis}}\rangle_{\text{obs}}^{95}$, is 0.37 fb.
From the combinatorics alone, see Figure 7.12, a combination with the tau + light lepton channel looks promising at first, but it does not improve the results significantly. Only a minor gain is observed while the analysis is complicated significantly by: introducing new systematics, introducing the need to validate the modeling of the background prediction in the tau + light lepton channels and also by the need to ensure that there is no overlap between the tau + light lepton control/signal/validation regions and the W control and validation regions, because this would make a simple statistical combination impossible. The reduced sensitivity of the light lepton channels is caused by the additional neutrino created in the leptonic decay of the tau. It makes the light leptons softer and thus more Standard Model like, making the distinction from the Standard Model background processes harder than in the di-tau channel.
Under the assumption that only the production cross sections, not the event kinematics, change when raising the center-of-mass energy from 8 TeV to 13 TeV, the sensitivity of the presented analysis at $\sqrt{s} = 13$ TeV was studied by re-weighting simulated 8 TeV events to 13 TeV using the LHAPDF package. An estimate of the multi-jet contribution has been obtained by scaling the estimate obtained from the 2012 data by a worst case factor of 2.8. It turns out that about 10 fb^{-1} are needed for the analysis to become approximately as sensitive as when using the 2012 data, making a statistical combination feasible. Since only 3.2 fb^{-1} of data were collected in 2015 by the ATLAS experiment, the decision was made to search for strong production of supersymmetric particles in the 2015 data and thus to include jets in the final states.

8. ATLAS Results on the Search for Supersymmetry After Run I and the pMSSM Summary Paper

For a selection of analyses the excluded mass ranges at 95% confidence level, using the CL_s prescription, are shown in Figure 8.1. These limits have been obtained by the ATLAS collaboration using the data collected throughout Run I of the LHC. Most of the analyses are carried out using simplified models. If more general models are used, like e.g. mSUGRA, most of the parameters are fixed such that the final state of interest is observed more frequently, usually leaving only two free parameters to study. Consequently one always has to take these limits with a grain of salt, because supersymmetry might not manifest itself by single distinct signatures, which the parameters of those models are optimized for, but instead allow for a plethora of different decay chains to take place, significantly lowering the probability to encounter specific processes and thus rendering the limits considerably weaker.
The pMSSM summary paper [134] is an attempt to investigate the effect of aforementioned simplifications by reinterpreting ATLAS searches in the framework of the pMSSM, applying physics constraints from other sources like e.g. observations in astrophysics or flavor physics. In total 22 ATLAS searches were taken into account, amongst them is the search for electroweak production of supersymmetric particles with two hadronically decaying taus in the final state which will be presented in chapter 7. In the following the idea of the analysis will be briefly summarized, assuming the reader is familiar with the basic concepts of a cut-and-count analysis in high energy physics. The focus is on the comparison of the results to the aforementioned limits obtained by studying simpler models and simplified models.

8.1. Idea of the Analysis

Instead of trying to investigate the behavior of a small number of kinematically accessible sparticles, decoupling all others under the assumption that they do not play a role, the complex interplay between competing processes is studied by not fixing any of the parameters of the pMSSM. The set of parameter values studied however has been constrained by requiring the points in the pMSSM phase-space to fulfill constraints from e.g. astrophysics or flavor physics. Additionally the sparticles are required to have masses below 4 TeV. The complete list of constraints is given in chapter 3 of [134]. Using the constraints to filter the pMSSM phase-space one is still left with about 300.000 different

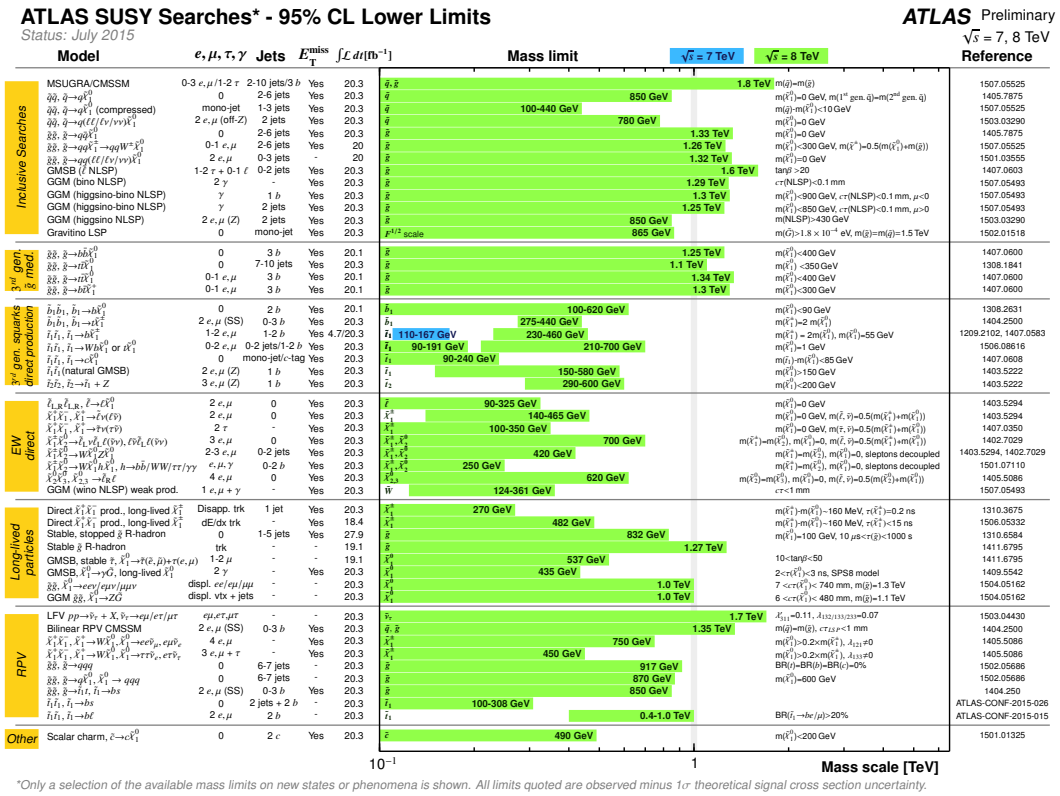

Figure 8.1.: Selection of analyses by the ATLAS collaboration searching for the production of supersymmetric particles. Targeted models, final states and the amount of data used are indicated in the first column. The excluded mass ranges at 95% confidence level are indicated by the bars in the second column. References to the corresponding publications are given in the last column. Analyses are performed using data taken with the ATLAS detector at $\sqrt{s} = 7$ TeV (turquoise) and $\sqrt{s} = 8$ TeV (light green). Figure from [133].

sets of parameters to study. Each parameter set will be referred to as a model in the following. Running each model through a full detector simulation is not feasible, because it would require enormous computing resources. Instead only the hard-scattering event is generated for most of the models: information about which particles are being created in the interaction of the protons and information about the particles which they decay into, the so-called *truth-information*. The *detector response*[1] is not simulated.
In measured data, however, truth-information is not available, only the detector response is available. The detector response is highly specific to the considered final state, because the reconstruction and identification efficiencies of different particle types differ considerably as can be seen in chapter 6. Therefore each analysis group developed a program which uses the truth-information as input, emulates the detector response and from the emulated detector response estimates of the number of events in their signal regions[2]. These estimates are compared to the Standard Model estimates obtained by each of the analyses and afterwards confidence levels are computed. The models are then grouped into three categories: the ones which can certainly be excluded, the ones which certainly cannot be excluded and the ones where one is uncertain about the exclusion. Models ending up in the latter category were fed into the fast detector simulation chain and then analyzed in more detail to see whether they can or cannot be excluded.

8.2. Results

The main result from [134] is Figure 8.2. It shows the fraction of models excluded versus the mass of the sparticles. Models with gluinos below a mass of 1 TeV can almost certainly be excluded, as well as models with squark masses below 500 GeV. However, this is not the case for neutralinos, charginos and sleptons: although quite some analyses in Figure 8.1 claim strong limits on the mass of neutralinos and charginos, the fraction of pMSSM models excluded draws a different picture: only a fraction of models with light neutralinos and light charginos can be excluded when interpreting the analyses in the context of the pMSSM. This is caused by the competition of different production processes as well as the competition of different decay possibilities. Thus there is still plenty of phase-space for supersymmetry to hide at the LHC even though results obtained using simplified models, shown in Figure 8.1, might suggest otherwise.

[1] Particles traveling through the detector interact with it and thereby cause signals which can be measured, like e.g. ionization or Cherenkov light. These signals are the detector response.

[2] A lot of work in collaboration with Luis Escobar Sawa and Alexander Mann has been put into developing the program used to emulate the detector response for the analysis presented in chapter 7. The results of this work have been published in the Master Thesis of Luis Escobar Sawa.

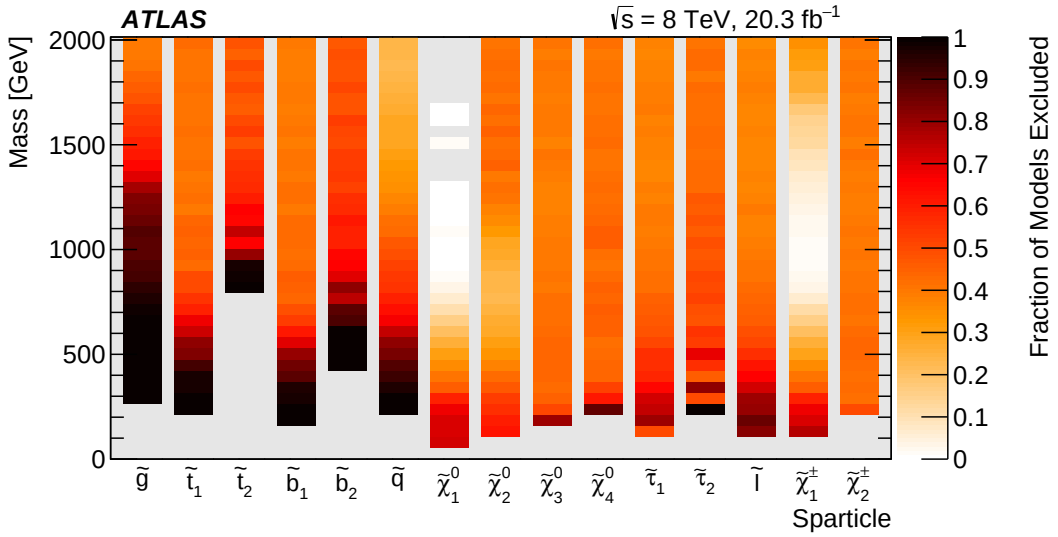

Figure 8.2.: Fraction of models excluded versus the mass of the sparticles. Interestingly for quite some particles the fraction of models which can be excluded is not yet above 90%, although some of the analyses "claimed" that some of those sparticles with masses up to 1 TeV can be excluded, see Figure 8.1. Figure from [134].

9. Searching for Strong Production of Supersymmetric Particles at $\sqrt{s} = 13$ TeV

In the following, 3.2 fb^{-1} of data collected with the ATLAS detector in 2015 at a center-of-mass energy of 13 TeV will be analyzed. An analysis will be presented specifically targeting final states containing two or more hadronically decaying taus, jets and missing transverse energy. Opposed to the analysis presented in chapter 7, this analysis will focus on the production of supersymmetric particles via the strong interaction, thus motivating the requirement of jets. The decision to study the strong production of supersymmetric particles in the 2015 datasets instead of the electroweak production was made, because the collected amount of data does not suffice to improve the limits over the ones presented in section 7.6, as has been shown in section 7.8. The following specifically focuses on the development of the compressed signal region and the multi-jet estimate. An excess over the Standard Model expectation could not be found, thus the results are interpreted in a GMSB model as well as in a simplified model. The analysis presented in the following is published in [135], it is an update of [136] and [137], but only focuses on final states containing at least two taus.

9.1. Targeted Signal Processes and Models

The presented analysis [135] focuses on scenarios characterized by the presence of light gluinos, light squarks, a stable and neutral lsp, light charginos, next-to-lightest neutralinos as well as a light stau and tau sneutrino. Models including light staus are of particular interest in searches for supersymmetry, because light sleptons could play an important role in the co-annihilation of neutralinos in the early universe, specifically models with light scalar taus are consistent with dark-matter searches [138]. Like the previously presented analysis, final states include hadronically decaying taus, as well as missing transverse energy due to the tau neutrinos and the neutralinos escaping the detector undetected. In addition final states also contain jets, setting it apart from the previously presented analysis (see section 7.1).

The search strategy presented in the following is based on two exemplaric processes, first, the pair production of squarks decaying via intermediate neutralinos and staus into final

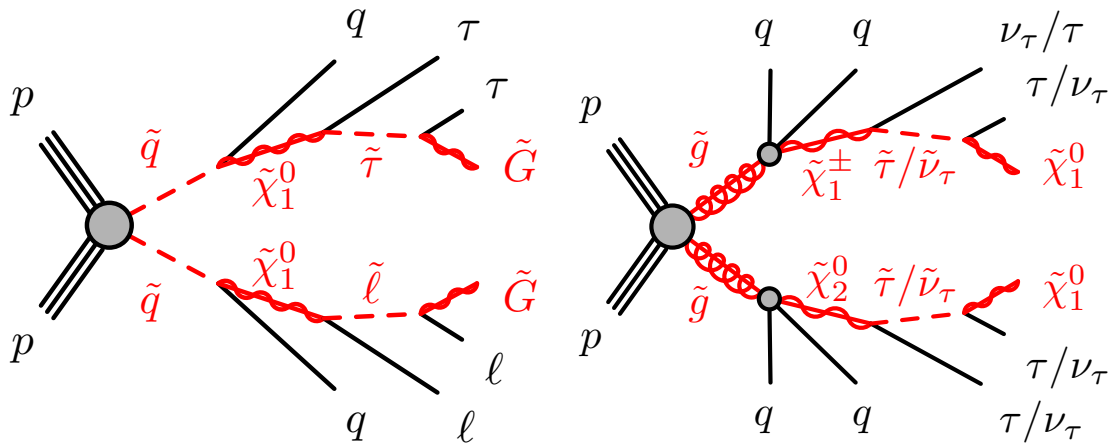

(a) GMSB **(b)** Simplified Model

Figure 9.1.: Diagrams characterizing the two processes which the presented search strategy is based on. (a) The production of a pair of squarks decaying via intermediate neutralinos and staus/sleptons to a pair of gravitinos, a pair of quarks and up to four taus or a pair of taus plus a pair of leptons, typical in GMSB scenarios. (b) The production of a pair of gluinos decaying asymmetrically via a lightest chargino and a next-to-lightest neutralino and via staus or tau sneutrinos into quarks, neutrinos and a pair of lightest neutralinos.

states containing jets, taus, maybe leptons[1], as well as a pair of gravitinos and second, the pair production of gluinos decaying asymmetrically via a lightest chargino and a next-to-lightest neutralino and via staus into jets, taus, neutrinos and a pair of lightest neutralinos. The first process is typical in the framework of gauge-mediated-symmetry-breaking, GMSB, while the second one is often present in more generic models, like the pMSSM. Both frameworks have been discussed in section 2.3. The diagrams depicting the studied processes can be found in Figure 9.1. The second process will be investigated using a simplified model [139], while the first one will be investigated in the framework of GMSB.

In the GMSB model studied the messenger mass scale M_{mess} has been chosen to be larger than the supersymmetry-breaking scale Λ to avoid tachyonic messengers as well as charge- and color-breaking vacua. To suppress additional sources of flavor violation, M_{mess} has additionally been chosen to be less than the Planck mass: it is set to $M_{mess} = 250$ TeV. The number of messenger multiplets is set to $N_5 = 3$, the gravitino-mass-scale parameter has been chosen to be $C_{grav} = 1$ and the sign of the higgsino mass parameter is chosen to be positive. The model is then probed using the two remaining free parameters Λ and $\tan\beta$ denoting the supersymmetry-breaking scale as well as the ratio of the

[1] This actually depends on the mass of the selectron and the smuon. In the models considered in the following, the stau is always the lightest slepton. Depending on the model used and its parameters,the difference between the stau mass and the selectron and smuon masses varies. For small mass-differences the selectron and smuon might be produced, while for large mass-differences the production of selectrons and smuons becomes highly suppressed.

Higgs-vaccum-expectation-values at the electroweak scale. This choice of parameters renders the lightest stau the next-to-lightest supersymmetric particle for large values of $\tan\beta$. For low values of $\tan\beta$ the lightest stau is almost mass-degenerate with the supersymmetric partners of the right-handed electron and muon. A high value of Λ favors the squark-antiquark production mechanism as depicted in Figure 9.1 (a). Since the parameter C_{grav}, which controls the decay rate of the next-to-lightest supersymmetric particle into the lightest, has been chosen to be one, the nlsp decays promptly. The region of small Λ and large $\tan\beta$ is considered unphysical, because it results in tachyonic states. The simplified model is inspired by parts of the pMSSM phase-space where R-parity is conserved, gluino pair production dominant, the stau light and the lsp a neutralino [139]. In the studied scenario gluinos are assumed to undergo a two-step decay resulting in tau- as well as jet-rich states, as depicted in Figure 9.1 (b). The stau and its sneutrino are assumed to be mass-degenerate, as well as the next-to-lightest neutralino and the lightest chargino. Masses of the chargino and the stau are computed as follows:

$$m_{\tilde{\chi}_1^\pm} = m_{\tilde{\chi}_2^0} = \frac{1}{2}\left(m_{\tilde{g}} + m_{\tilde{\chi}_1^\pm}\right), m_{\tilde{\tau}_1} = m_{\tilde{\nu}_\tau} = \frac{1}{2}\left(m_{\tilde{\chi}_1^\pm} + m_{\tilde{\chi}_1^0}\right). \tag{9.1}$$

All other sparticles are kinematically decoupled, leaving us with the mass of the gluino and the mass of the lsp as the two remaining free parameters of the model. Gluinos are assumed to decay with equal branching ratio either into $\tilde{\chi}_1^\pm q\bar{q}'$ or $\tilde{\chi}_2^0 q\bar{q}$. Decays into third generation quarks are not allowed, they are considered in separate models [139] which are not discussed here[2], thus q and q' denote quarks from either the first or the second generation. Since the stau and its sneutrino are assumed to be mass-degenerate, the $\tilde{\chi}_2^0$ decays either to $\tilde{\tau}\tau$ or to $\tilde{\nu}_\tau\nu_\tau$ with equal probability, while the $\tilde{\chi}_1^\pm$ decays with equal probability either into $\tilde{\tau}\nu_\tau$ or $\tilde{\nu}_\tau\tau$. The last step in the decay chain is always the stau or the sneutrino decaying into the lsp plus a tau or a neutrino.

9.2. Event Selection

Events are selected by first of all requiring them to pass the *event cleaning* procedure for Run II as outlined in section 6.8. Ambiguities between objects are removed by applying the Run II overlap removal as outlined in section 6.7. To trigger events the lowest-threshold $\not{E}_{\mathrm{T}}$ trigger that was in place throughout the whole 2015 data-taking period is used, triggering at $\not{E}_{\mathrm{T}} > 80$ GeV. By requiring $\not{E}_{\mathrm{T}} > 180$ GeV and a jet with $p_{\mathrm{T}} > 120$ GeV the trigger is ensured to work in a region of constant efficiency. The efficiency of the trigger, as well as the aforementioned, so-called *plateau cuts*, were obtained by studying events triggered by the uncorrelated jet triggers in data. Since at least two jets are expected in the final states (see Figure 9.1), at least two jets are required. Multi-jet events are rejected by requiring the two leading jets and the $\not{E}_{\mathrm{T}}$ to

[2]This split is motivated by the large Yukawa coupling of the top compared to the first and second generation quarks. This allows for significant mass-splittings between the stop and the first and second generation squarks. Consequently, the resulting final states are quite different, they contain top quarks, whereas this is not the case in the models studied here.

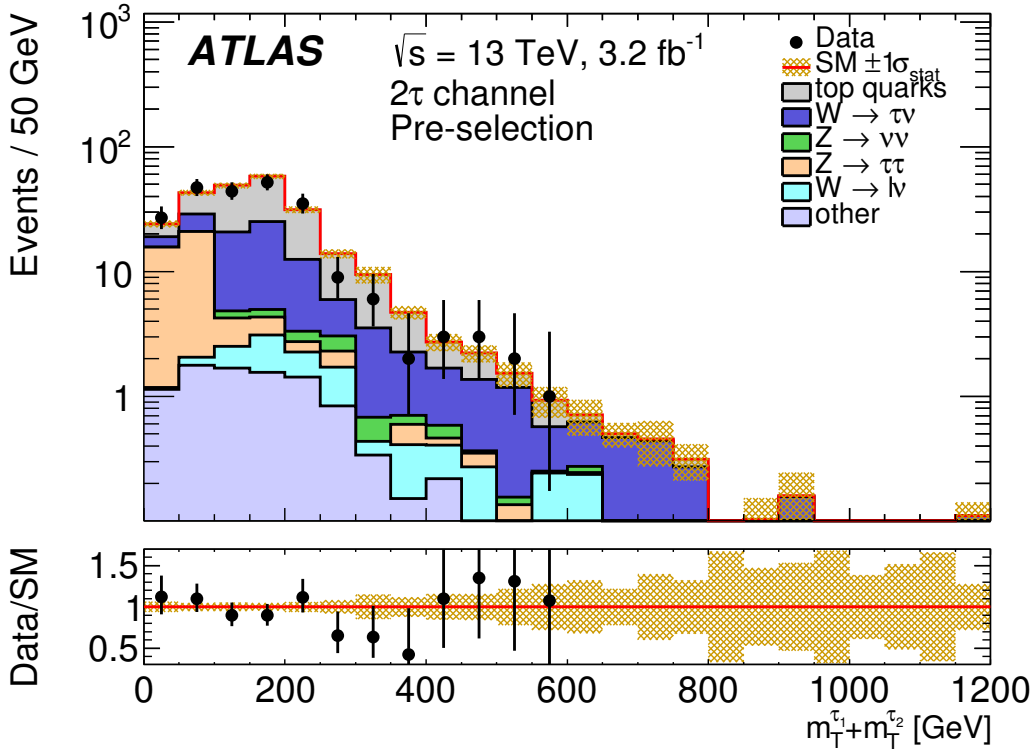

Figure 9.2.: Distribution after applying the pre-selection cuts. The last bin includes overflow events. The shaded bands indicate the statistical uncertainties in the background predictions. The contribution labeled as "other" includes diboson events and the V+jets processes not explicitly listed in the legend. Figure from [135].

be well separated in the transverse plane, because it is expected that $\not{E}_{\mathrm{T}}$ in multi-jet events mostly stem from the mis-measurement of jets and thus $\not{E}_{\mathrm{T}}$ is likely to be aligned with a high-p_{T} jet in multi-jet events. The pre-selection is completed requiring at least two loose taus while not vetoing light leptons, because a lepton veto would considerably impact the ability to select GMSB events.
In Figure 9.2 the sum of the transverse masses, $m_{\mathrm{T}}^{\tau_1}+m_{\mathrm{T}}^{\tau_2}$, of the two leading taus is shown after pre-selection. Since the individual components of the $\not{E}_{\mathrm{T}}$, e.g. the neutrinos from the tau decay, cannot be reconstructed, the transverse mass of the taus is computed from the transverse momentum of the taus and the full $\not{E}_{\mathrm{T}}$. As a result, the $m_{\mathrm{T}}^{\tau_1}+m_{\mathrm{T}}^{\tau_2}$ distribution extends to rather high values. Within uncertainties the data is nicely described by the Standard Model prediction, however the uncertainties are rather large due to low statistics. The low statistics is the result of the high $\not{E}_{\mathrm{T}}$ pre-selection, making it hard to define signal, control and validation regions with high statistics. The dominant backgrounds after applying the pre-selection are: events containing top-quarks, W+jets events as well as Z+jets events, as can be seen in Figure 9.2. Multi-jet and diboson backgrounds do not contribute significantly.
To discriminate between signal and background, three signal regions are defined using different means to suppress Standard Model backgrounds. Two signal regions are defined

targeting the simplified model. One to cover smaller mass-splittings (< 900 GeV) and the other to target larger mass-splittings (> 1200 GeV), the intermediate region is covered by both. The last signal region is defined to target the GMSB scenario. The signal regions are summarized in Table 9.1.

High-Mass Signal Region The High-Mass signal region exploits the fact that the number of jets is usually larger in cases where the gluino-gluino production mechanism dominates over the squark-anti-squark production mechanism by requiring an additional jet compared to the pre-selection. H_{T} is used to exploit the harder p_{T} spectrum of the jets compared to Standard Model backgrounds, because the energy available for the jets increases with increasing gluino mass. Lastly the High-Mass signal region uses the sum of the transverse masses of the leading taus, $m_{\mathrm{T}}^{\tau_1} + m_{\mathrm{T}}^{\tau_2}$, to suppress Z+jets, W+jets, di- and semi-leptonic $t\bar{t}$ events. Z+jets events passing the pre-selection usually exhibit rather low values of $m_{\mathrm{T}}^{\tau_1} + m_{\mathrm{T}}^{\tau_2}$, because the trigger plateau cuts primarliy select boosted Z+jets event topologies where the selected high-p_{T} jet recoils against the Z-boson. If the Z-boson is boosted, also its decay products become boosted and thus the emerging tau leptons are usually not well separated in the transverse plane from the neutrinos resulting in low values of $m_{\mathrm{T}}^{\tau_1} + m_{\mathrm{T}}^{\tau_2}$. Larger values are expected for W+jets, di- and semi-leptonic $t\bar{t}$ backgrounds, either because the genuine $\not{E}_{\mathrm{T}}$ is expected to be higher (di-leptonic $t\bar{t}$) or because one of the taus has to be a mis-identified jet (W+jets and semi-leptonic $t\bar{t}$ events).

Compressed Signal Region While in the GMSB model with its massless lsp the mass-splitting between initially produced and final state particles is generally large, in the simplified model scenarios with heavy lsp and about equally heavy next-to-lightest supersymmetric paricle, hence small mass-splittings, are included. Scenarios where the splitting between initially produced and final state particles is small are called compressed. Since the previously presented high mass selection proved less efficient in compressed regions, an optimization is performed in the following.
Compressed scenarios are often characterized by long decay chains, resulting in many soft decay products. This makes discriminating variables which rely on the properties of single objects, like e.g. the transverse momentum of the leading tau, less powerful to distinguish the Standard Model background from the signal. Instead variables which also take into account properties of other objects, like e.g. the missing transverse energy, H_{T} or m_{Tsum} (the definitions can be found in section 6.9), are more powerful, since high object multiplicities are not expected in Standard Model processes except for top backgrounds.
The requirement of large $\not{E}_{\mathrm{T}}$ coming from the trigger plateau cut and the requirement of two tau candidates already poses a strong rejection for multi-jet events which can be seen in Figure 9.3 (a) which shows the $\not{E}_{\mathrm{T}}$ distribution after pre-selection. Other Standard Model backgrounds, especially Z+jets events, are efficiently suppressed by cutting on m_{T2}, as can be seen in Figure 9.3 (b). Signal events usually prefer higher m_{T2} values, because the initial particles in the decay chain, namely the charginos and

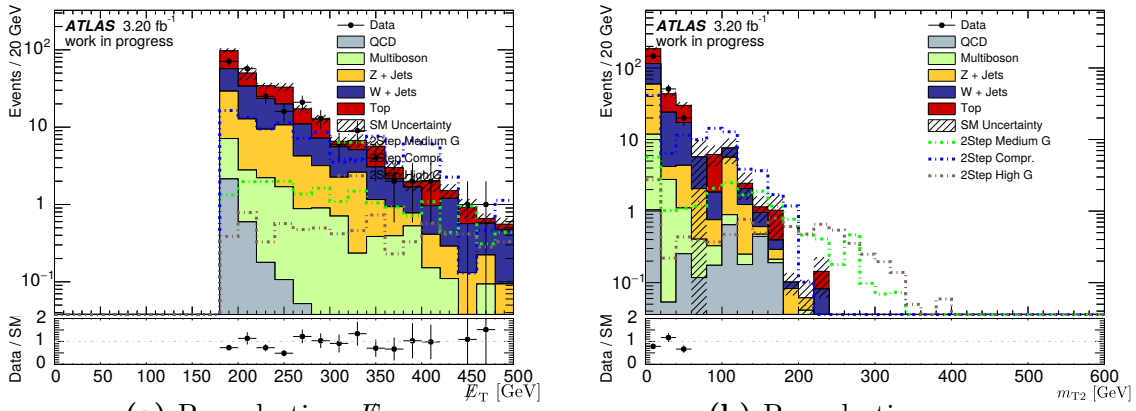

(a) Pre-selection, $\not{E}_{\mathrm{T}}$ **(b)** Pre-selection, m_{T2}

Figure 9.3.: Distributions of $\not{E}_{\mathrm{T}}$ and m_{T2} after pre-selection. Only statistical uncertainties are depicted.

neutralinos, are heavier than Standard Model bosons and m_{T2} yields as a kinematic endpoint the mass of the initially produces particles. A cut of at least 60 GeV will be used to discriminate signal from background.

Starting from this, several different observables have been investigated whose definitions can be found in section 6.9. Specifically variables built from multiple objects like H_{T}, m_{eff}, m_{Tsum} and others were investigated. It turned out that on top of the previous selection the two variables yielding the best results are m_{Tsum} and N_{jet}. While a cut on N_{jet} explicitly exploits the decay topology of the studied simplified model (each gluino decays into to two quarks and either a chargino or a neutralino, see section 9.1), m_{Tsum} does so implicitly, because the sum over the transverse masses of the jets in m_{Tsum} extends over all jets and thus scales with the number of jets.

The final selection has been determined by an optimization based on the Asimov discovery significance [65]. Uncertainties due to limited Monte Carlo statistics have been evaluated bin by bin. Additionally, a constant uncertainty of 30% has been assumed and added in quadrature to the statistic uncertainty to estimate systematic uncertainties. When optimizing the main attention was given to maximizing the Asimov significance, while keeping at least 3 expected background events.

The "N-1" plots and the significance scan on N_{jet} and m_{Tsum} after applying the pre-selection and requiring $m_{\mathrm{T2}} > 60$ GeV can be found in Figure 9.4. In case of the jet-multiplicity, Figure 9.4 (a), a cut of $N_{\mathrm{jet}} > 4$ is obtained, defining SR-nJets, while in case of m_{Tsum}, Figure 9.4 (b), a cut of $m_{\mathrm{Tsum}} > 1400$ GeV is obtained, defining SR-mTSum. Both signal regions apply the pre-selection and cut on $m_{\mathrm{T2}} > 60$ GeV in addition.

Comparing the exclusion power of both signal regions by looking at the respective exclusion contours[3], see Figure 9.5, one can see that they behave rather similar. The exclusion contours in Figure 9.5 have been computed using a simplified setup compared to the full fit setup used later in section 9.3.3: the background normalizations as well as the nui-

[3] As defined in section 7.6

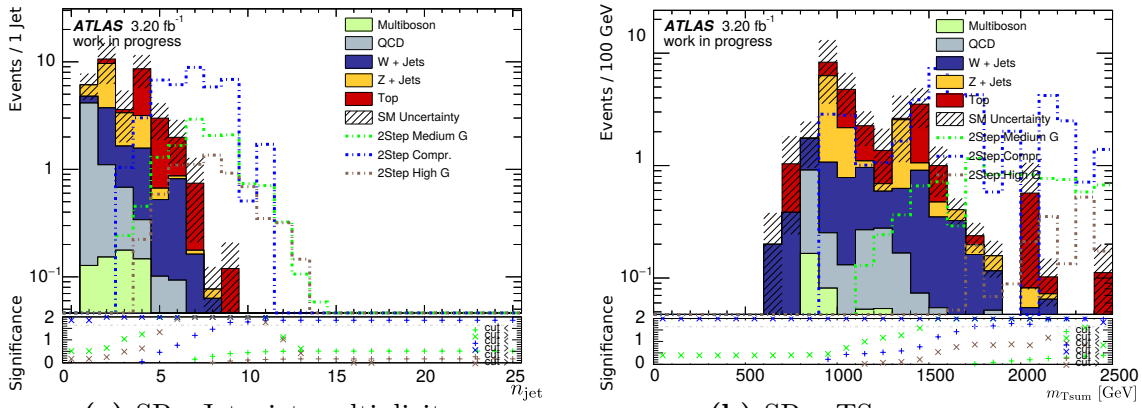

(a) SR-nJets, jet multiplicity **(b)** SR-mTSum, m_{Tsum}

Figure 9.4.: N-1 distributions and significance scans of the jet multiplicity and m_{Tsum} for SR-nJets and SR-mTSum. The upper part of each plot shows the kinematic distribution, while the lower part shows the significance scans. In the calculation of the significance, the statistical as well as an additional constant uncertainty of 30% have been taken into account. The significance has been calculated using the Asimov method [65].

sance parameters have been fixed to one. Since high jet multiplicities are not expected to be modeled well in Monte Carlo samples, SR-nJets is dropped and the m_{Tsum} based signal region will be referred to as the "Compressed" SR in the following.

GMSB Signal Region In case of the GMSB signal region the same variables as in case of the High-Mass one have been used, except for the number of jets. In the GMSB signal region no additional jet is required, because in events triggered by squark-anti-squark production the expected jet multiplicity is not as high. H_{T} and $m_{\text{T}}^{\tau_1} + m_{\text{T}}^{\tau_2}$ still yield remarkably large discrimination power in the GMSB model, because the same features are basically present as in the high-mass region of the simplified model. In case of the GMSB model the decay chains might become even longer and the particle p_{T} spectra might become even harder due to the low mass of the gravitino leaving more energy to other particles.

Different Trigger Strategies The gain of using different triggers has been studied, specifically the gain of using a di-tau trigger has been studied in more detail. As it turned out, the thresholds of the di-tau trigger are too high, consequently nullifying the gain of using a non-$\not{E}_{\text{T}}$ based trigger, because a rather strict cut of at least 100 GeV on $\not{E}_{\text{T}}$ is still needed to efficiently suppress the multi-jet background. All other triggers studied suffered from the very same problems: the $\not{E}_{\text{T}}$ cut required to efficiently suppress multi-jet events is too hard, while the requirement on the separation between the $\not{E}_{\text{T}}$ and jets does not suppress multi-jet events well enough. No other suitable alternative to suppress multi-jet events could yet be developed. Nevertheless, the insights gained led to the development of the compressed signal region: using the sum of the transverse masses as a signal region defining variable to implicitly exploit the signal decay topology.

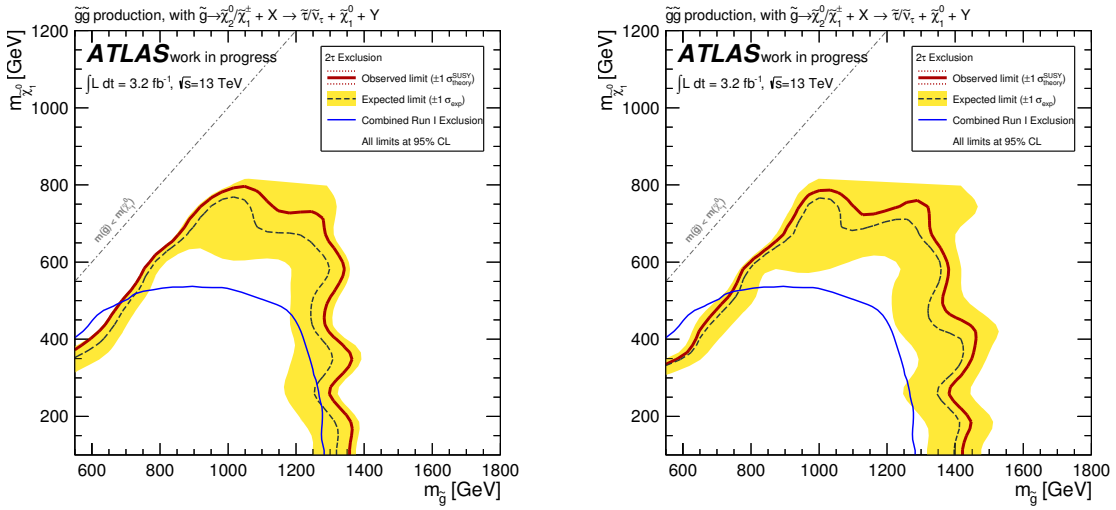

(a) SR-nJets, jet multiplicity

(b) SR-mTSum, m_{Tsum}

Figure 9.5.: Exclusion plots for SR-nJets on the left and SR-mTSum on the right considering only statistical uncertainties. A simpler fit setup has been used than in section 9.3.3: the background normalizations as well as the nuisance parameters have been fixed. Figure from [140].

9.3. Background Estimate

Figure 9.2 and Figure 9.3 show example kinematic distributions after pre-selection without applying normalization factors: the data is described well by the simulated datasets. Consequently the assumption is made that all discrepancies can be absorbed in overall normalization factors. Similar to the analysis presented in the previous chapter, the dominant backgrounds are normalized using control regions which are simultaneously fitted using HistFitter [141]. Control regions are designed to be as pure as possible in one process while keeping the cuts as close as possible to the signal regions and while leaving enough phase-space to define validation regions. The validation regions are used to validate how well the extrapolation of the normalization factors performs. Only multi-jet events are treated differently, they are estimated using a fake-rate approach and validated using the OS-SS method to be of negligible impact.

9.3.1. Vector-Boson and Top-Quark Backgrounds

As can be inferred from Figure 9.2, already after pre-selection the dominant backgrounds are not multi-jet events, but instead Standard Model events either containing vector bosons in association with jets or events containing top-quarks. For the W+jets and the top-quark backgrounds the control regions are split into three categories: true, fake and kinematic, while for Z+jets events only one control region will be defined. The true tau-lepton control regions are used to correct for theoretical uncertainties in the cross section computations, experimental uncertainties in the estimation of the integrated luminosity and to account for potential differences in the reconstruction and identification

	Compressed SR	High-Mass SR	GMSB SR
Trigger plateau	$\not{E}_{\mathrm{T}} > 180$ GeV, $p_{\mathrm{T}}^{\mathrm{jet}_1} > 120$ GeV		
Tau leptons	$N_{\tau}^{\mathrm{loose}} \geq 2$, $p_{\mathrm{T}}^{\tau} > 20$ GeV		
Multi-jet rejection	$\Delta\phi(\mathrm{jet}_{1,2}, \not{E}_{\mathrm{T}}) \geq 0.4$		
$m_{\mathrm{T}}^{\tau_1} + m_{\mathrm{T}}^{\tau_2}$	–	> 350 GeV	> 150 GeV
H_{T}	–	> 800 GeV	> 1700 GeV
N_{jet}	≥ 2	≥ 3	≥ 2
$m_{\mathrm{T2}}^{\tau\tau}$	> 60 GeV	–	–
m_{Tsum}	> 1400 GeV	–	–

Table 9.1.: Selection criteria for the signal regions. Extracted from [135].

efficiencies between data and simulation for tau leptons. Effects absorbed in the normalization factor obtained from the fake tau-lepton control regions are uncertainties in the modeling and simulation of jets: the shower shapes, the hadronization model and the quark/gluon composition. Lastly, the mis-modeling of event kinematics, like e.g. a potential mis-modeling of $\not{E}_{\mathrm{T}}$ or H_{T}, is incorporated into a separate kinematic normalization factor. While the kinematic effects account for mis-modeling on a per-event basis, the fake- and true-tau normalization factors account for a mis-modeling on a per-particle basis. Consequently the kinematic normalization factor is only applied once per-event while the true- and fake-normalization factors need to be applied on a per-tau basis.

W+jets Events and Top-Quark Backgrounds Control regions for W+jets events and events containing top-quarks are defined similarly to the signal regions, however instead of requiring two taus, at least one of the taus is replaced either by requiring a muon or a jet. The distinction between W+jets events and top-quark backgrounds is made by vetoing or respectively requiring events containing b-jets.
To obtain the true-tau normalization factor a loosely identified tau, as well as an additional jet compared to the pre-selection are required. The additional jet takes the role of the second tau so the basic requirement on the object multiplicity is kept the same as in the signal region, thus keeping also the topology as close as possible. To additionally suppress contributions from fake-taus, the transverse mass of the selected tau is required to be less than 80 GeV, because in case of fake taus it is usually larger, because the taus are better separated from the $\not{E}_{\mathrm{T}}$.
The fake-tau control regions are defined requiring one loosely identified tau as well as exactly one muon[4]. Since the reconstruction and identification efficiencies are much higher in case of muons and their fake rate is much less, it is expected that usually the

[4]To increase statistics it has also been tried to select one loosely identified tau as well as exactly either a muon or an electron. However, the electron channel is swamped by multi-jet events as shown in the next subsection.

muon will be the real lepton stemming from either a top-quark-decay or a W-decay. Di-leptonic $t\bar{t}$ decays, where one of the tops decays into a muon and the other into a tau are vetoed by requiring the transverse mass of the muon to be less than 100 GeV.
To be independent from the modeling of tau kinematics, the kinematic control regions are defined vetoing taus and requiring exactly one muon and one additional jet compared to the pre-selection. Opposed to the other two types of signal regions, no additional cut is required to suppress fake or true-tau backgrounds.
All three types of control regions have a upper bound of $H_{\mathrm{T}} < 1200$ GeV in common and an extended multi-jet rejection cut of $0.4 < \Delta\phi\left(\mathrm{jet}_{1,2}, \not{E}_{\mathrm{T}}\right)$ to keep the phase space close to the signal region but not exactly like the signal region and to veto multi-jet events respectively.

Z+jets Events The Z+jets background stands out a bit from the aforementioned two, because it was not possible to apply the same procedure. Not many events which contain a true and a fake tau are compatible with the Z-boson mass, because this constraint requires a strong correlation between the two particles whereas real and fake taus are usually uncorrelated. As a result only a single control region has been defined to estimate the normalization of Z+jets events, but this is perfectly valid since the only remarkable contribution is actually coming from $Z \to \tau\tau$ events. In the Z control region exactly two loosely identified taus with opposite charge are required. b-jets are vetoed. The same multi-jet rejection cut is used as in the signal regions. To avoid any overlap with the signal regions, H_{T} is required to be less than 800 GeV and $m_{\mathrm{T}}^{\tau_1} + m_{\mathrm{T}}^{\tau_2}$ is required to be less than 150 GeV.

Validation Regions Validation regions are defined using two taus to validate also the extrapolation in the particle type. Z+jets events used for validation are selected by keeping the upper bound on $m_{\mathrm{T}}^{\tau_1} + m_{\mathrm{T}}^{\tau_2}$, effectively selecting Z+jets events. The extrapolation in H_{T} is tested by inverting the cut on H_{T}. In the top and W+jets validation regions Z+jets events are suppressed by inverting the $m_{\mathrm{T}}^{\tau_1} + m_{\mathrm{T}}^{\tau_2}$ cut used in the Z+jets validation region. To avoid overlap with the Z control region H_{T} is required to be less than 800 GeV in the W+jets and top validation regions. Events which might appear in the compressed signal region are vetoed by inverting the compressed signal region's cut on m_{T2}. A distinction between the top and W+jets validation regions is made by requiring or vetoing b-jets respectively. Multi-jet events are vetoed as in the signal regions, by requiring the separation between the jets and the $\not{E}_{\mathrm{T}}$ in the transverse plane to be larger than 0.4.
The defined control regions can be found in Table 9.2 and the validation regions in Table 9.3. In Figure 9.6 (a) and (b) the H_{T} distribution is shown for the top fake-tau control region and the Z control region respectively. Overall the agreement between data and the Standard Model prediction is nice, which in turn suggests that the multi-jet background is negligible. The number of observed and predicted events in the validation regions after fitting the control regions are compared in Figure 9.7, only the last three bins of this plots are of relevance to this analysis. The agreement is not as good as in

	Kinematic CR		Fake tau CR		True tau CR		
	W+jets	Top	W+jets	Top	W+jets	Top	Z+jets
Trigger plateau	$\not{E}_{\mathrm{T}} > 180$ GeV, $p_{\mathrm{T}}^{\mathrm{jet}_1} > 120$ GeV						
Tau leptons	$N_\tau^{\mathrm{loose}} = 0$		$N_\tau^{\mathrm{loose}} = 1$				$N_\tau^{\mathrm{loose}} = 2$ opposite charge
Light leptons	$N_\mu = 1$				$N_\mu = 0$		–
N_{jet}	≥ 3		≥ 2		≥ 3		≥ 2
$N_{b-\mathrm{jet}}$	$= 0$	≥ 1	$= 0$	≥ 1	$= 0$	≥ 1	$= 0$
Multi-jet rejection	$0.4 < \Delta\phi(\mathrm{jet}_{1,2}, \not{E}_{\mathrm{T}}) < 2.9$						$\Delta\phi(\mathrm{jet}_{1,2}, \not{E}_{\mathrm{T}}) > 0.4$
CR selection	$H_{\mathrm{T}} < 1200$ GeV						$H_{\mathrm{T}} < 800$ GeV
	–		$m_{\mathrm{T}}^{\mu} < 100$ GeV		$m_{\mathrm{T}}^{\tau} < 80$ GeV		$m_{\mathrm{T}}^{\tau_1} + m_{\mathrm{T}}^{\tau_2} < 150$ GeV

Table 9.2.: Overview of the control regions used. Table extracted from [135].

	VR W+jets	VR Top	VR Z+jets
Trigger plateau	$\not{E}_{\mathrm{T}} > 180$ GeV, $p_{\mathrm{T}}^{\mathrm{jet}_1} > 120$ GeV		
Tau leptons	$N_\tau^{\mathrm{loose}} \geq 2$		
N_{jet}	≥ 2		
$N_{b-\mathrm{jet}}$	$= 0$	≥ 1	$= 0$
Multi-jet rejection	$\Delta\phi(\mathrm{jet}_{1,2}, \not{E}_{\mathrm{T}}) \geq 0.4$		
VR selection	$H_{\mathrm{T}} < 800$ GeV $m_{\mathrm{T}}^{\tau_1} + m_{\mathrm{T}}^{\tau_2} > 150$ GeV $m_{\mathrm{T2}}^{\tau\tau} < 60$ GeV		$H_{\mathrm{T}} > 800$ GeV $m_{\mathrm{T}}^{\tau_1} + m_{\mathrm{T}}^{\tau_2} < 150$ GeV –

Table 9.3.: Overview of the validation regions defined. Table from [135]

the control regions, but still mostly within one standard deviation. To verify that the multi-jet background is negligible, it will be estimated in the following.

9.3.2. Multi-jet Estimate

Three different methods to estimate QCD in events containing two hadronically decaying taus as well as at least two jets have been studied: the JetSmearing technique as described in section A.4.1, the OS-SS method which has already been used in the Run Ianalysis presented earlier, and a fake-rate based method. In addition, the contribution of multi-jet events to the signal regions will be discussed.

JetSmearing It turned out that JetSmearing is not usable in practice in final states containing two hadronically decaying taus. The idea behind the JetSmearing method is to select multi-jet events and smear the jets according to their response functions, meaning the ratio of their observed p_{T} to their true p_{T}. This is based on the assumption that $\not{E}_{\mathrm{T}}$ in multi-jet events solely stems from mis-measured jets (a more detailed explanation of the method can be found in section A.4.1). The probability of a multi-jet event to

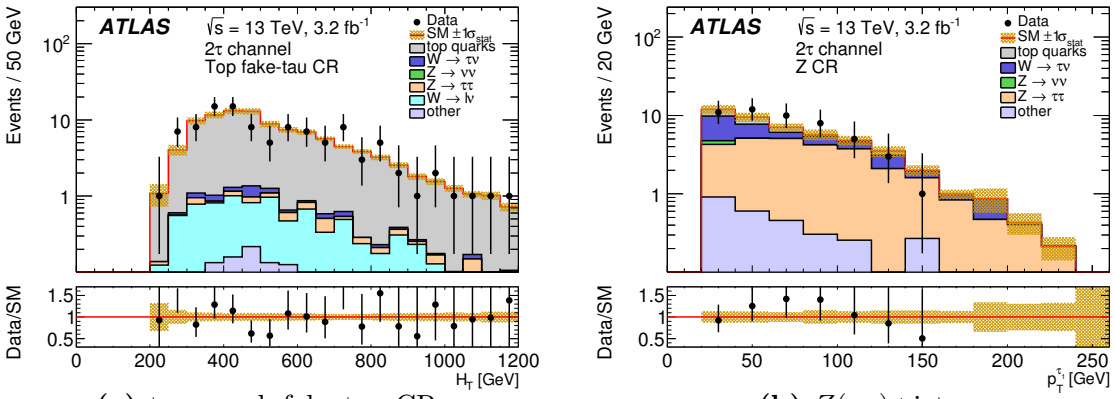

(a) top-quark fake-tau CR **(b)** $Z(\tau\tau)$+jets

Figure 9.6.: H_{T} distribution in the top-quark fake-tau CR and transverse momentum of the leading tau lepton in the $Z(\tau\tau)$+jets CR of the channel after the fit, illustrating the overall background modelling in the control regions. By construction, the total fitted background is equal to the number of observed events in each CR. The last bin includes overflow events. The shaded bands indicate the statistical uncertainties in the background predictions. Figure extracted from [135].

contain two jets faking taus is rather low, it is $\mathcal{O}\left(10^{-4}\right)$ [126]. Furthermore, most of the triggers used to collect the multi-jet sample are heavily pre-scaled, meaning that if they fire, the event is only written to disk every n-th time the trigger fired, this is needed, because the rate of observing events containing low p_{T} jets is enormous. Consequently the statistics is very limited, causing a non uniform sampling of event kinematics resulting in spiky behavior in relevant distributions. Additional details are documented in section A.4.1.

Multi-jet Enriched Control Region Independent of the method used, a control region was defined to validate predictions. In the main signal regions a $\not{E}_{\mathrm{T}}$ trigger is used which requires a rather high cut on $\not{E}_{\mathrm{T}}$ to ensure that it is operating in its efficiency plateau. This cuts away approximately all multi-jet events, as could be seen in Figure 9.2, showing relevant distributions after pre-selection which includes the trigger plateau cuts. Consequently a different trigger strategy was needed to define a multi-jet enriched control region. Instead of triggering on the missing transverse energy in the event, events are triggered by requiring two hadronically decaying taus with a transverse momentum of at least 45 GeV and 35 GeV respectively to ensure the trigger is working in its plateau region. In case the trigger is not available it is emulated by only applying the trigger plateau cuts. To avoid any overlap with the signal regions the cut on the missing transverse energy, m_{Tsum} and m_{T2} are inverted. A cut on the transverse momentum of the leading jet of at least 120 GeV is applied to ensure consistency. The multi-jet control region definition can be found in Table 9.4.

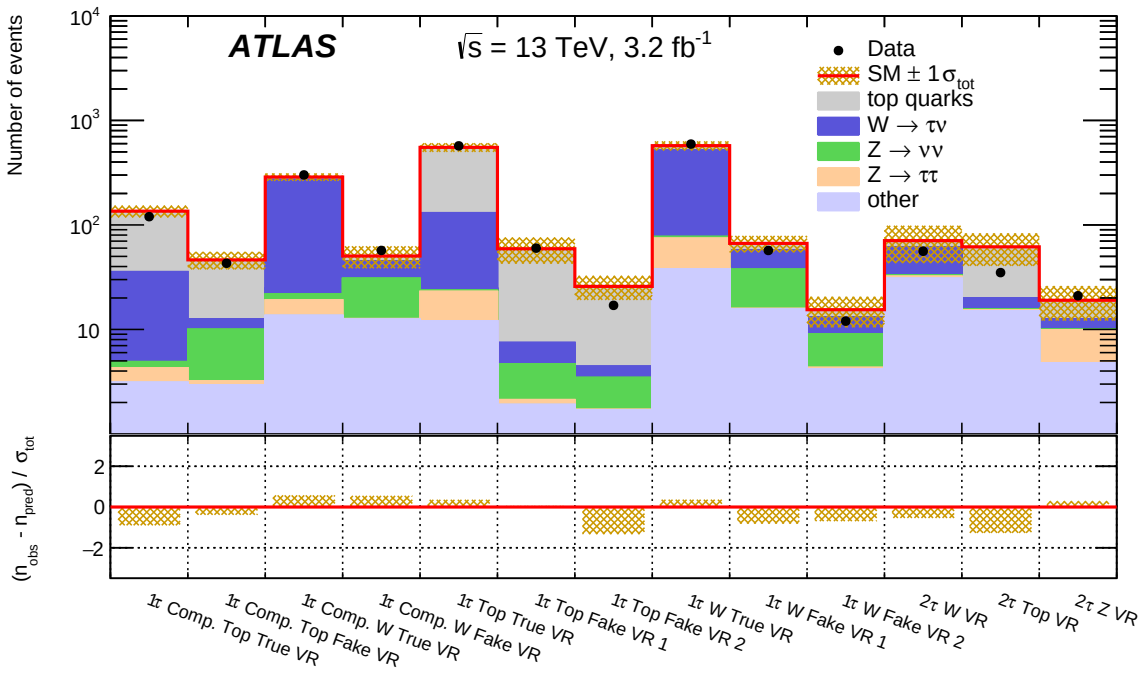

Figure 9.7.: Number of observed events, n_{obs}, and predicted background yields after the fit, n_{pred}, in the validation regions of the 1τ and 2τ channels. Here, only the 2τ channel is discussed, so only the last three bins are of importance. The background predictions are scaled using normalization factors derived in the control regions. The shaded bands indicate the statistical uncertainties in the background predictions, and correspond to the σ_{tot} uncertainties used in the lower part of the figure. Figure extracted from [135].

Jet-fake method The limiting factor of the JetSmearing method is statistics which cannot be easily improved, because the seed events used are taken from data measured with the ATLAS detector to avoid any simulation-introduced bias. The limited statistics resulted in a non-representative sample of the phase-space of multi-jet events containing two taus and thus a spiky behavior of distributions, as can be seen in section A.4.1. To get a more representative sample of the phase-space, events are selected which trigger any of the single jet triggers, taus are not required. A combination of all available single jet triggers is used to obtain an unbiased sample of the phase-space. Pre-scales of the triggers are taken into account by weighting events accordingly. In addition at least two jets are required to be present in the event. One of the jets in the event will be randomly selected and treated as being a lepton, while being removed from the list of available jets. This is based on the assumption that leptons in multi-jet events are mostly misidentified jets and therefore share the same kinematic properties.

However, the probability of a jet to fake a lepton largely depends on the jet's kinematic properties, especially the p_{T}, because it is directly related to the resolution of the ATLAS calorimeters. Without taking the fake probability into account, one will overestimate the number of multi-jet events. Hence, every event is weighted by the probability

	Multi-jet CR
Trigger plateau	$N_\tau \geq 2, p_{\mathrm{T}}^{\tau_1} > 45$ GeV, $p_{\mathrm{T}}^{\tau_2} > 35$ GeV
N_{jet}	≥ 2
Inverted SR	$m_{\mathrm{Tsum}} < 1.4$ TeV
	$m_{\mathrm{T2}} < 60$ GeV
Boosted regime	$p_{\mathrm{T}}^{\mathrm{jet}_1} > 120$ GeV
Multi-jet requirement	$\not{E}_{\mathrm{T}} < 180$ GeV

Table 9.4.: Multi-jet control region definition

of the selected jet to fake a lepton, defined as:

$$w_F^{QCD}(p_{\mathrm{T}}) = \frac{N_\ell(p_{\mathrm{T}})}{N_\ell(p_{\mathrm{T}}) + N_{\mathrm{jets}}(p_{\mathrm{T}})}, \tag{9.2}$$

where N_ℓ and N_{jets} are the number of leptons and jets respectively. This quantity highly depends on the lepton type and is measured for each lepton type individually.
$w_F^{QCD}(p_{\mathrm{T}})$ has been computed in multi-jet Monte Carlo by selecting all events which contain at least one jet. For taus, electrons and muons the fake-rates are depicted in Figure 9.8. In the high p_{T} region the statistics are rare, thus the fake-rates have been fitted:

- τ: $a * (x * 0.001)^b + c + d * \exp(e - f * x)$, with $a = 7.0104 * 10^{-2}$, $b = -9.5367 * 10^{-1}$, $c = 0.125 * 10^{-3}$, $d = 10^{-3}$, $e = 20$, $f = 7 * 10^{-4}$,
- e: $\exp(a + b * x)$, with $a = -8.9$, $b = 2.25 * 10^{-6}$,
- μ: $2 * 10^{-5}$.

The fitting functions have been chosen by educated guessing, looking at the fake-rate distributions using different axis scales. The parameters were then chosen to be conservative in a sense that it will overestimate the fake-rate most of the time, leading to an overestimation of the multi-jet contribution. Statistics were taken into account, so the parameters have been chosen such that an overestimation is ensured in the high statistic bins. The errors obtained from the initial fit are on the percent level for taus and of the order of 10-20 percent for electrons, while for muons it is hard to quote a number since a constant fit function has been chosen.
Which object is faked depends on the region which is investigated. In case the region contains at least one tau, the candidate jet will become a tau, otherwise it will become either an electron or a muon with equal probability, but using the corresponding fake-factors. This splits the dataset into two equal halves, which is accounted for by applying an additional factor two to the probability of the jet to fake the electron or muon. Consequently, in the control regions taus are faked, except for the kinematic control regions, where electrons and muons are faked.

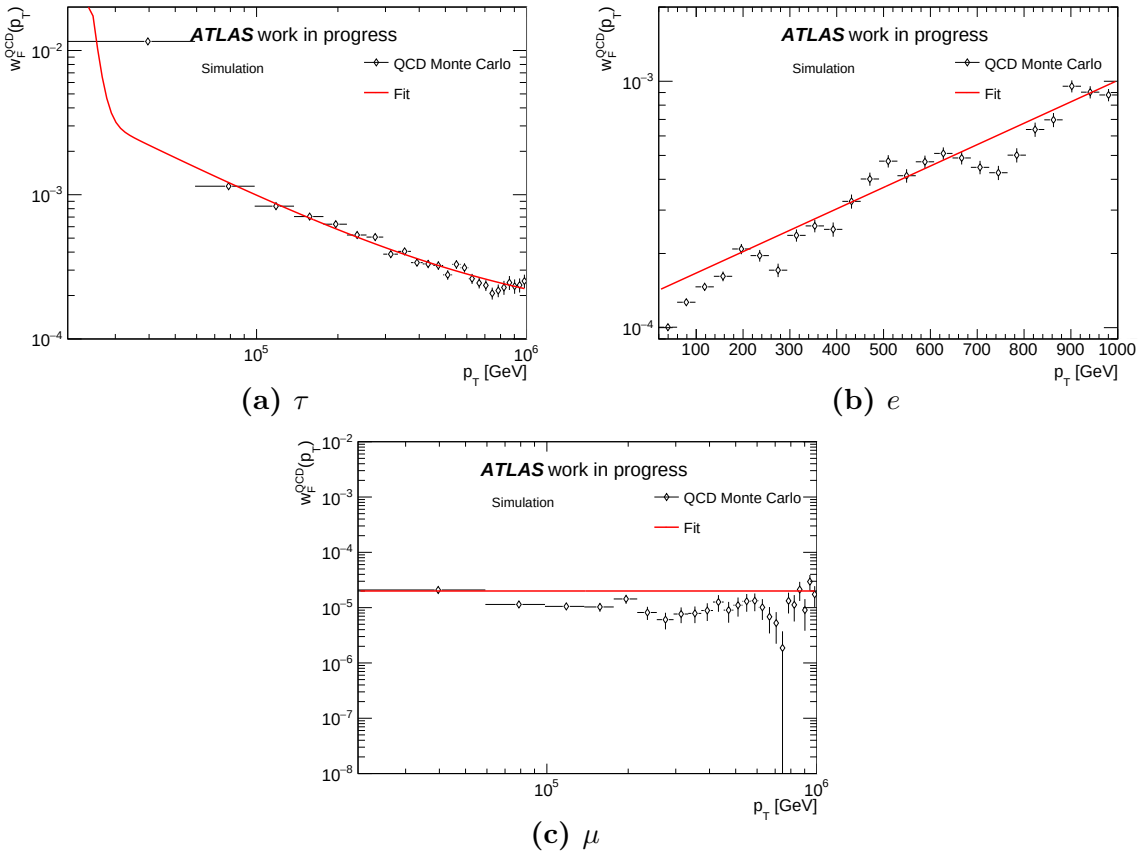

(a) τ **(b)** e

(c) μ

Figure 9.8.: Distribution of the jet reweighting factor, $w_F^{QCD}(p_\mathrm{T})$, for (a) taus (in log-log scale), (b) electrons (in log-scale) and for (c) muons (log-log scale). Obtained from multi-jet Monte Carlo. This is used to correct for the dependence of the fake-rate on the p_T of the jet.

Using this technique results in much larger statistics than using the JetSmearing technique. After applying the trigger and the at least one tau and at least one jet requirements about 150000 events remain, approximately a factor 1000 more than when applying the JetSmearing technique to two tau final states. It is assumed that the multi-jet Monte Carlo samples describe the fake-rate of jets to leptons, thus, by construction, no additional multi-jet control region is needed to normalize the sample. Instead the proposed multi-jet enriched region will be employed to validate the estimate from the jet-smearing method.
Figure 9.9 (a) and (b) show the $\not{E}_{\mathrm{T}}$ and the m_{Tsum} distributions in the multi-jet enriched region, further plots can be found in the appendix in Figure A.14. All of them are in reasonable agreement with data.

OS-SS method To validate the predictions of the jet-fake method, the OS-SS method is used. It has already been used in the Run I analysis presented previously. This method relies on the assumption that the jet-to-tau fake-rate is independent of the charge of the jet. Thus, looking at multi-jet events containing two fake taus, one would expect as many oppositely charged tau pairs as like-sign pairs. This is exploited in the OS-SS method by dividing the selected events into two categories, one with an oppositely charged tau pair (**OS**) and the other with an equally charged tau pair (**SS**). For the sake of simplicity only the leading p_{T} tau pair is considered.
The multi-jet estimate in a signal/control/validation region is calculated from events in the SS channel. All known Standard Model processes are estimated from Monte Carlo and subtracted. Negative values in the prediction of the multi-jet contribution are truncated to zero. To ensure that there is no overlap with the region of interest an additional OS cut needs to be applied. The multi-jet contribution estimated from the SS channel is eventually added on top of all the other backgrounds in the OS channel.
Figure 9.9 shows the overall performance of the OS-SS method for two relevant variables, $\not{E}_{\mathrm{T}}$ and m_{T2}. Further plots can be found in the appendix in Figure A.15. The agreement between data and the Standard Model estimate is comparable to that of the jet-fake method.
The downside of the OS-SS method is that it will cut away parts of our signal in models containing three or more taus. Considering the case of three taus, two will always have the same charge. The leading tau p_{T} pair will be either of equal or opposite charge with same probability. Assuming that there is no correlation between the charge of the taus and their p_{T}, effectively half of the signal events will be cut away. The signal efficiency cannot be recovered, because all modifications to the selection of the tau pair would introduce a bias incompatible with the initial assumption. This renders the method unusable in the main analysis. Nevertheless, the OS-SS method can be used to validate the multi-jet estimate obtained from the jet-fake method.

Comparison Both methods are well in agreement with data in the multi-jet enriched control region, hence they must also be in nice agreement with each other. Comparing them "side by side", see Figure 9.9 (a) and (c) for $\not{E}_{\mathrm{T}}$ and (b) and (d) for m_{T2}, indeed a

Signal Region	Contribution [%]	Stat. Error [%]
Compressed	7.90	4.37
HighMass	2.37	0.61
GMSB	2.36	0.75

Table 9.5.: Relative multi-jet contribution to the signal regions and their statistical errors estimated using the jet-fake method.

Signal Region	Contribution [%]	Stat. Error [%]
Compressed	0	0
HighMass	0	0
GMSB	0	0

Table 9.6.: Relative multi-jet contribution to the signal regions and their statistical errors estimated using the OS-SS method.

rather nice agreement between both estimates is observed. To disentangle the multi-jet estimates from the the Standard Model Monte Carlo estimates, solely the multi-jet contributions are compared in Figure 9.9 (e) and (f) for $\not{E}_{\mathrm{T}}$ and m_{T2} respectively. Additional comparisons can be found in section A.4.2. Both estimates are well in agreement with each other within statistical uncertainties. Thus the jet-fake method can be considered safe to use to estimate the multi-jet contribution in the signal and control regions.

Multi-Jet Contribution in the Signal Regions Using the jet-fake method the contribution of multi-jet events to the signal regions is found to be always below 10%, as can be seen in Table 9.5[5]. Multi-jet events will therefore be considered a negligible contribution to the signal regions.
This has been verified using the OS-SS method; the corresponding contributions can be found in Table 9.5[6]. Quite remarkably, the multi-jet event yield predicted by the OS-SS method is always 0, which can be understood by looking at the expected background yields in the signal regions. They are of the order of just a few events, so one does not expect many events in data in the signal regions as can be seen in Table 9.10. Consequently, the OS-SS method will not yield sensible results, because the OS-SS multi-jet estimate is directly estimated from data.

Multi-Jet Contribution in the Control Regions The multi-jet contribution in the control regions is estimated using the jet-fake method, except for the Z control region which, by construction, is more suited for the OS-SS method due to the opposite sign cut applied to select Z events. To investigate whether the statistics can be increased, instead of requiring exactly one muon, exactly one muon or one electron is selected. The

[5]The detailed background composition for the different signal regions can be found in tables A.1, A.2, and A.3 for the compressed, the high mass and the GMSB signal regions respectively.
[6]While the corresponding background compositions can be found in tables A.10, A.11, and A.12 for the compressed, the high mass and the GMSB signal regions respectively..

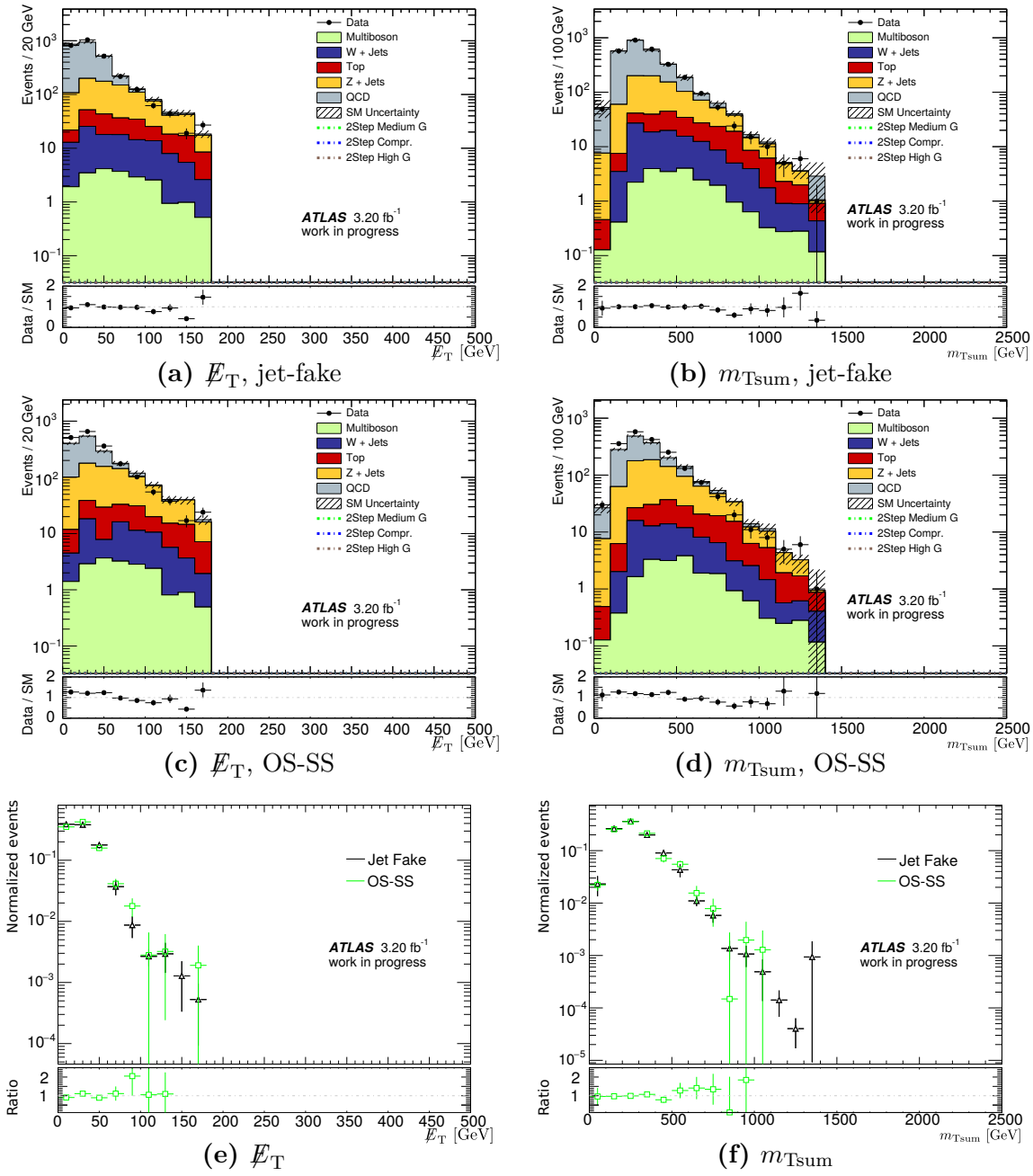

(a) $\not{E}_T$, jet-fake (b) m_{Tsum}, jet-fake

(c) $\not{E}_T$, OS-SS (d) m_{Tsum}, OS-SS

(e) $\not{E}_T$ (f) m_{Tsum}

Figure 9.9.: Distributions of relevant kinematic variables to investigate the performance of the multi-jet estimates and to compare the methods "side-by-side": jet-fake method (upper) and the OS-SS method (middle), $\not{E}_T$ (left) and m_{Tsum} (right) in the multi-jet enriched two-tau control region. The lower panel in the aforementioned plots shows the data to Standard Model ratio. The lower two plots show a normalized comparison of the multi-jet estimates obtained using the jet-fake method (black) and the OS-SS method (green) for (e) $\not{E}_T$ and (f) m_{Tsum} respectively. In the last two plots the ratio of the OS-SS method to the jet-fake method is shown. Only statistical uncertainties are depicted.

Control Region	Contrib. [%]	Stat. Error [%]	Contrib.[%]	Stat. Error[%]
	W CR		Top CR	
True	0.81	0.06	0.99	0.07
Fake	17.00	0.81	12.71	0.74
Kinematic	0.02	0.00	0.02	0.00

Table 9.7.: Multi-jet contribution in percent to the W and top control regions and their statistical errors estimated using the jet-fake method.

Control Region	Contrib. [%]	Stat. Error [%]	Contrib.[%]	Stat. Error[%]
	W CR		Top CR	
Fake + μ channel	5.41	0.68	6.01	0.72
Fake + e channel	26.78	1.38	18.99	1.26

Table 9.8.: Multi-jet contribution in percent to the W and top fake control regions and the corresponding statistical error when selecting a fake tau plus either a muon or an electron estimated using the jet-fake method.

resulting multi-jet contribution to each of the W and top control regions can be found in Table 9.7[7], the multi-jet contribution in the Z control region is about $6.49 \pm 8.06\%$, the error only including the statistical uncertainty. For all regions, except for the fake tau control regions, the QCD contribution to the control regions is always below 10%. For the true tau and kinetic control regions it is even below the percent level and thus definitely negligible. The multi-jet contribution in the fake tau control region, however, is higher, 17% in case of the W fake tau control region and 13% in case of the top fake tau control region. This is expected because hadronically decaying taus are reconstructed and consequently the most likely cause for a fake tau is a jet, which multi-jet events contain many.
To shed more light on this the fake tau control region is split into an electron and a muon channel. In Table 9.8 the resulting multi-jet contributions to the fake tau control regions can be found[8]. In the muon channel the multi-jet contribution is notably lower, because the probability for jets to fake muons is rather low, jets are usually already stopped inside the calorimeter and do not reach the outer muon chambers. As a result only the muon channel will be used to estimate multi-jet events in the fake tau control regions.

Summary of Multi-Jet Estimates As shown above, multi-jet events are a negligible contribution in all signal regions. There is however a non-negligible contibution to some CRs, given electrons are used, hence only muon based control regions are considered to

[7]The background composition for the different control regions can be found in tables Table A.4, Table A.5, Table A.6 and Table A.7 for the true tau, kinetic, fake tau and Z control regions, respectively.

[8]The corresponding background composition tables for the fake control regions can be found in Table A.8 and Table A.9 for the electron and muon channel, respectively.

limit the multi-jet contribution.

9.3.3. Fitting Procedure

The procedure used to incorporate correlations between the background estimates is basically the same as in section 7.3.5: a simultaneous fit is performed based on a profile likelihood method [65] to obtain the final background estimate. The background estimates are also assumed to be Poisson distributed and simultaneously normalized in control regions. Systematic uncertainties are again assumed to be Gaussian distributed. Opposed to the previously presented analysis, contributions from multi-jet events are negligible and therefore not taken into account in the fit. The input parameters to the fit are the number of observed events in all control regions and the contributions from the process of interest to the control regions as well as the contaminating processes respectively. The free parameters in the fit are the normalizations of the backgrounds. As detailed in chapter 3, the fit parameters are obtained by maximizing the likelihood functions.

9.4. Uncertainties

As in section 7.4 uncertainties can be split into two larger groups, namely the experimental and the theoretical ones. Experimental uncertainties refer to all uncertainties related to the actual measurement, like e.g. identification, reconstruction and calibration uncertainties. The later ones include the cross section uncertainties as well as the generator modeling uncertainties.
Uncertainties considered are basically the same as before; experimental uncertainties on the following quantities are considered:

- jet energy scale and resolution,
- $\not{E}_{\mathrm{T}}$ energy scale and resolution,
- b-tagging efficiency and mis-identification rate,
- tau identification, trigger efficiency and energy scale,
- luminosity.

Theoretical uncertainties on the following quantities are considered:

- simulation of pile-up,
- renormalization and factorization scales,
- parton density function,
- parton jet matching,

Source of uncertainty	Compressed SR	High-Mass SR	GMSB SR
Top generator modeling	60	23	22
V+jets generator modeling	4.2	6.3	4.3
Jet energy scale	14	2.0	6.0
Jet energy resolution	8.1	1.2	4.3
b-tagging efficiencies	8.8	5.1	7.7
Tau energy scale	19	13	8.5
Total	72	36	35

Table 9.9.: Dominant systematic uncertainties in the total background predictions, in percent. The total systematic uncertainty accounts for other minor contributions not listed in this table, as well as correlations between the uncertainties. Table extracted from [135]

- parton shower modeling,
- cross section,
- ISR modeling.

Further details can be found in [135]. The most important contributions to the total uncertainty can be found in Table 9.9, given in percent. The total uncertainty in Table 9.9 contains all uncertainties not just the ones shown in the table. Of all uncertainties the top generator modeling is always the top contributor to the total uncertainty followed by the tau energy scale. All other contributions are usually significantly lower. Total uncertainties range from 72% in the compressed region to about 35% in the High-Mass and GMSB signal regions.

9.5. Results

The results can be found in Table 9.10. They have been obtained from the fit as described in section 9.3.3. Signal contaminations in the control regions were neglected. As in section 7.5, the results can be summarized in one sentence: no significant excess above the Standard Model expectation has been found.
The expected and observed upper limits on the number of non Standard Model events, $\langle\sigma_{\text{vis}}\rangle^{95}_{\text{obs}}$ and $\langle\sigma_{\text{vis}}\rangle^{95}_{\text{exp}}$, at the 95% confidence level using the CL_s prescription, as described in chapter 3, are given in the lower part of Table 9.10. Additionally, the upper limit on the visible cross section, $\langle\sigma_{\text{vis}}\rangle^{95}_{\text{obs}}$, which is defined as the product of the acceptance of events times the reconstruction efficiency times the production cross section, is given as well as the confidence level for the background-only hypothesis, CL_b. Figure 9.10 shows distributions of relevant kinematic variables and compares data, the Standard Model prediction as well as benchmark models. The agreement between data and the Standard Model prediction is within statistical uncertainties. Background estimates are obtained as explained in section 9.3.

	Compressed SR	High-Mass SR	GMSB SR
Data	4	0	0
Total background	4.2 ± 3.0	3.2 ± 1.2	0.69 ± 0.24
Top	$2.5^{+2.9}_{-2.5}$	0.87 ± 0.78	0.20 ± 0.20
$W(\tau\nu)$+jets	0.51 ± 0.38	1.75 ± 0.65	0.31 ± 0.14
$Z(\tau\tau)$+jets	0.04 ± 0.02	0.13 ± 0.06	0.04 ± 0.02
$Z(\nu\nu)$+jets	0.28 ± 0.12	0.07 ± 0.03	0.02 ± 0.01
$W(\ell\nu)$+jets	0.37 ± 0.34	0.12 ± 0.07	0.02 ± 0.01
Diboson	0.25 ± 0.10	0.21 ± 0.08	0.06 ± 0.02
Multi-jet	0.21 ± 0.21	0.07 ± 0.07	0.06 ± 0.06
S^{95}_{obs} (S^{95}_{exp})	8.2 ($8.0^{+2.1}_{-2.0}$)	3.4 ($4.8^{+1.4}_{-1.0}$)	3.4 ($3.7^{+0.5}_{-0.2}$)
$\langle\sigma_{\mathrm{vis}}\rangle^{95}_{\mathrm{obs}}$ [fb]	2.55	1.07	1.07
$\mathrm{CL_b}$	0.53	0.12	0.53

Table 9.10.: Number of observed events and predicted background yields in the three signal regions. The background prediction is scaled using normalization factors derived in the control regions. All systematic and statistical uncertainties are included in the quoted uncertainties. The bottom part of the table shows the observed and expected model-independent upper limits at the 95% CL on the number of signal events, S^{95}_{obs} and S^{95}_{exp}, respectively, the corresponding observed upper limit on the visible cross section, $\langle\sigma_{\mathrm{vis}}\rangle^{95}_{\mathrm{obs}}$, and the $\mathrm{CL_b}$ value, i.e. the confidence level observed for the background-only hypothesis. Table extracted from [135].

9.6. Interpretation

Since no significant excess over the Standard Model background expectation has been observed, model-dependent exclusion limits are placed, as in section 7.6. The limits are calculated at 95% confidence level using the CL_s method, as before, the only difference is that the signal contamination in the control regions is now taken into account. A simple statistical combination of the signal regions cannot be done, because they were not defined to be exclusive, instead the signal region yielding the lowest CL_s is chosen for each specific model point. Keep in mind, that this does not necessarily coincide with the observed limit and also does not imply that the observed limit will also always be the best. This approach has been chosen in order to avoid any bias the analysis.
The exclusion plots, shown in the following, show the observed and expected exclusion contours as solid and dashed lines respectively, just like in section 7.6. The yellow band around the expected limit shows the $\pm 1\sigma$ variations including all uncertainties, except the one on the signal cross section. That is indicated by the dotted lines around the observed limit. To give a conservative limit, all observed limits in the following will be reduced by 1σ of the signal cross section.
The results are interpreted in context of the previously introduced simplified model and the GMSB model, see section 9.1 (a) and (b) respectively. For sake of comparison the limit obtained by the Run I version of this analysis is indicated by the gray colored area [139, 137]. Stronger limits could be achieved!

Quite interestingly, the observed limit in the simplified model is always stronger than the expected in case of gluino masses above 1.3 TeV, see Figure 9.11 (a). This is caused by the strong under-fluctuation in the High-Mass signal region (see Table 9.10), which is in this regime the strongest expected signal region. In case of the GMSB model, see Figure 9.11 (b), the same effect is observed: an under-fluctuation in the GMSB signal region is causing a stronger observed than expected limit.

9.7. Summary

An analysis has been presented searching for squarks, gluinos and staus in events with at least two hadronically decaying tau leptons, jets and missing transverse momentum. About 3.2 fb^{-1} of proton-proton collision data collected with the ATLAS detector in 2015 at a center-of-mass energy of 13 TeV have been analyzed. All Standard Model backgrounds were taken from Monte Carlo, except for multi-jet events. Dedicated control regions have been developed to correct for a mis-modeling of kinematic effects, a mis-modeling of the tau fake rates, as well as for the true tau normalization. Contributions from multi-jet events were estimated using a fake-rate approach. The rates for jets to be mis-identified as taus, electrons or muons have been measured in simulated di-jet events. The method has been validated against the OS-SS method, a nice agreement was found. Multi-jet contributions to the control and signal regions have been found to be negligible and were therefore neglected in the background estimate of the signal regions.
The analysis was optimized for two models, one being a simplified model of gluino pair production with subsequent decays via a chargino, a next-to-lightest neutralino and staus or tau sneutrinos into final states containing jets, taus, neutrinos and lightest neutralinos, the other being a GMSB model with fixed parameters except for $\tan\beta$ and Λ. Two dedicated signal regions have been developed to target the simplified model. One focusing on the high gluino mass region, one focusing on the region of small mass-splittings. Both fulfill their duties well. A third signal region has been developed to specifically target final states observed in the GMSB model. However, no excess over the Standard Model expectation has been found. Instead two under-fluctuations have been observed and limits have been calculated. The limits are stronger than in Run I [136, 137] over the whole accessible phase-space. In the simplified model the limit in the gluino mass could be improved by about 300 GeV from 1250 GeV to 1550 GeV, while the limit on the neutralino mass could be pushed from about 500 GeV to approximately 750 GeV for gluino masses larger than 1 TeV. For the GMSB model gluino masses up to 2.2 TeV can be excluded for large values of $\tan\beta$. The obtained model independent observed upper limit on the visible cross section, $\langle\sigma_{\text{vis}}\rangle^{95}_{\text{obs}}$, is 1.07 fb.
The main trigger used in the analysis requires a harsh cut on $\not{E}_{\text{T}}$ of at least 180 GeV, thus it was also tried to use different triggers without a $\not{E}_{\text{T}}$ requirement, however, optimizing for different trigger topologies did not yield sensible improvements, mainly because a rather harsh $\not{E}_{\text{T}}$ cut is needed to suppress the multi-jet background efficiently.

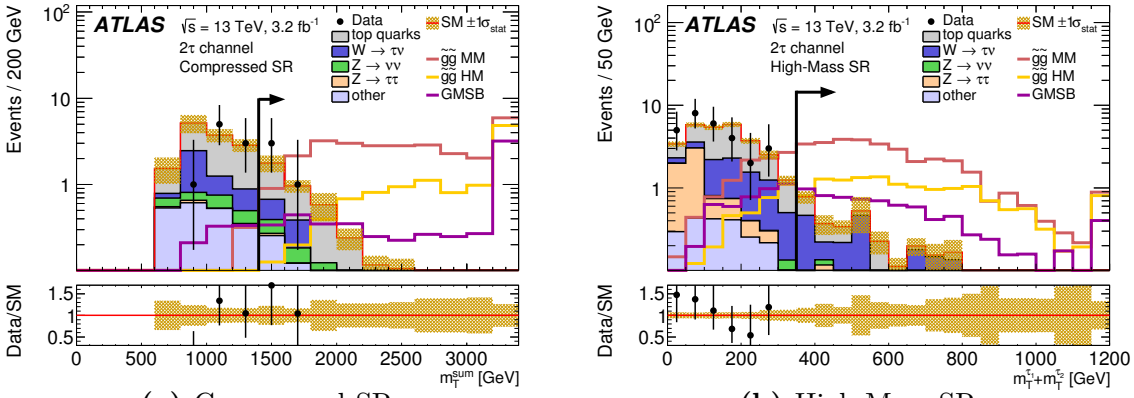

(a) Compressed SR **(b)** High-Mass SR

(c) GMSB SR

Figure 9.10.: Kinematic distributions for (a) m_{Tsum} in the Compressed SR selection without the $m_{\mathrm{Tsum}} > 1400$ GeV requirement, (b) $m_{\mathrm{T}}^{\tau_1} + m_{\mathrm{T}}^{\tau_2}$ in the High-Mass SR selection without the $m_{\mathrm{T}}^{\tau_1} + m_{\mathrm{T}}^{\tau_2} > 350$ GeV requirement, and (c) H_{T} in the GMSB SR selection without the $H_{\mathrm{T}} > 1700$ GeV requirement. The last bin includes overflow events. The shaded bands indicate the statistical uncertainties in the background predictions. The signal region is indicated by the black arrow. Signal predictions are overlaid for several benchmark models, normalized to their predicted cross sections. For the simplified model, "MM" refers to a medium mass-splitting, with $m_{\tilde{g}} = 1145$ GeV and $m_{\tilde{\chi}_1^0} = 265$ GeV; "HM" denotes a high mass-splitting scenario, with $m_{\tilde{g}} = 1305$ GeV and $m_{\tilde{\chi}_1^0} = 105$ GeV. The GMSB benchmark model corresponds to $\Lambda = 90$ TeV and $\tan\beta = 40$. Figures extracted from [135].

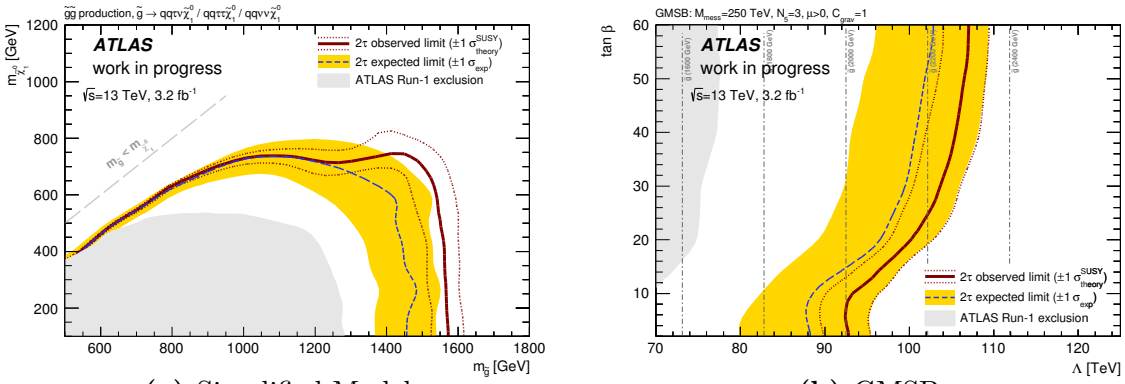

(a) Simplified Model **(b)** GMSB

Figure 9.11.: (a) Exclusion contours computed for the Simplified Model grid for the combination of the Compressed signal region and the high mass signal region. The combination is performed by selecting the signal region with the best expected significance for each point of the signal grid. (b) Exclusion contours computed for the GMSB grid for the GMSB signal region. The gray-shaded area corresponds to the limits obtained by the Run I iteration of this analysis [139, 137]. Figure from [140].

10. Conclusions and Summary

Despite its remarkable successes, the Standard Model, as introduced in chapter 2, has weaknesses: for example, it neither can explain dark matter nor neutrino masses. Consequently physics beyond the Standard Model must exist.
Supersymmetric extensions of the Standard Model are currently amongst the most promising candidates for physics beyond the Standard Model: by introducing an additional symmetry between fermions and bosons, lots of problems of the Standard Model can be solved. However, so far no supersymmetric particles have been observed and thus supersymmetry must be broken. Supersymmetry at the TeV-scale is a favorable option, because, for example, it can solve the *fine-tuning* problem and if the lightest supersymmetric particle is neutral and stable, it is a good candidate for cold dark matter.
This thesis presented two analyses searching for supersymmetry at the TeV-scale. Both target final states containing two hadronically decaying taus and large missing transverse momentum. One analysis targets the electroweak production of supersymmetric particles, the other targets the strong production of supersymmetric particles. The production mechanism determines whether jets are expected in the final state or not. In case of the electroweak production of supersymmetric particles no jets are expected, while in case of the strong production lots of jets are expected.
The analysis targeting the electroweak production of supersymmetric particles was carried out using the full 2012 dataset collected by the ATLAS detector at the LHC at $\sqrt{s} = 8$ TeV. Except for multi-jet events, all backgrounds were estimated from Monte Carlo. The W+jets background was normalized in a separate control region. The contribution from multi-jet events was estimated using the data-driven ABCD method. The background estimates were validated using validation regions. Four signal regions were defined, one targeting the production of a pair of lightest charginos, one targeting the associated production of a lightest chargino and a next-to-lightest neutralino and the third targeting direct production of stau pairs. No excess over the Standard Model expectation was found, instead model dependent, as well as model independent limits were set at 95% confidence level using the CL_s method. To optimize the analysis, a combination of the di-tau channel with the tau + light lepton channel was investigated, however, as it turns out, it is not feasible, because the additional neutrino in the decay chain smears the spectra of the light leptons such that they become far too Standard Model like. With the changed conditions in Run II however this option might become feasible again, because trigger thresholds for the tau triggers will rise to cope with the increased activity. Thus, triggering on e.g. light leptons and an additional tau might aid in improving the sensitivity of the analysis. Additionally, the main analysis needs to be re-optimized to cope with the changed conditions at $\sqrt{s} = 13$ TeV in Run II: especially

estimates of the multi-jet and W+jets backgrounds need a revision, because they are amongst the main sources of uncertainty. However, this is left for further study.
The analysis targeting the strong production of supersymmetric particles is using the full 2015 dataset collected by the ATLAS detector at the LHC at $\sqrt{s} = 13$ TeV with a bunch spacing of 25 ns. Except for the contribution from multi-jet events, all backgrounds are taken from Standard Model Monte Carlo. A major update compared to the Run I analysis was the development of a fake-rate based approach to estimate the multi-jet contribution in the signal, as well as control regions. It was validated using the OS-SS method which has also been used in the presented analysis of the 2012 data. Three signal regions were defined: two targeting a simplified model of gluino pair production decaying into staus, the other targeting a GMSB model. No excess over the Standard Model expectation was found, instead model dependent limits were calculated at 95% confidence level using the CL_s method. Model independent limits were calculated as well. The improvement in the limits is remarkable in case of the simplified model, as well as in the case of the GMSB model. Already at trigger level a rather harsh cut on the missing transverse energy has to be applied to ensure that the trigger is working in its efficiency plateau. This cuts away nearly all multi-jet events in the signal, as well as control regions, as has been verified by employing a fake-rate based approach. As it turns out, both work rather well, the limiting factor in both cases is only statistics.
However, in both cases, one has to be careful regarding the limits. Limits have been set on simplified models or on models under very constrained conditions. As has been shown in section 8.2, limits obtained from simplified models or models assuming specific breaking mechanisms have to be taken with a grain of salt. In supersymmetric models a strong competition between different production and decay processes is a-priori not excluded and thus the assumption of pure branching fractions might be invalid. Thus, there is still plenty of room for supersymmetry to hide at the TeV-scale, so new methods need to be developed to target also scenarios where there is strong competition between different decay- and production-processes.

Appendix

A. Appendix

A.1. Datasets Used

A.1.1. Run I Analysis

The following information is an excerpt from [119].

All Standard Model background processes have been simulated using the full detector simulation [142, 143], all signal samples using the fast calorimeter simulation [96], as explained in section 5.1.1.

The diboson samples are generated with SHERPA v1.4.1 [144], with additional gluon–gluon contributions simulated with gg2WW v3.1.2 [145]. The production of top quark pairs is also simulated with the SHERPA v1.4.1 generator. Samples of $t\bar{t}+V$ ($V = W, Z$) are generated with the leading-order (LO) generator MadGraph 5 v1.3.33 [146] interfaced to PYTHIA v8.165 [147, 148]. Single-top production is simulated with MC@NLO v4.06 (Wt- and s-channel) [149, 150, 151] and AcerMC v3.8 (t-channel) [152]. In all samples the top quark mass is set to 172.5 GeV. Events with $Z/\gamma^* \to \ell\ell$ and $W \to \ell\nu$ produced with accompanying jets (including light and heavy flavours) are generated with ALPGEN v2.14 [153] interfaced to PYTHIA 6. The gluon fusion and vector-boson fusion production modes of the SM Higgs are simulated with POWHEG-BOX v1.0 [154], and the associated production (WH and ZH) with PYTHIA v8.165.

The simulation parameters are tuned to describe the soft component of the hadronic final state [155, 156]. The next-to-leading-order (NLO) CT10 [157] parton distribution function (PDF) set is used for SHERPA and MC@NLO. The CTEQ6L1 [158] set is used for MadGraph, AcerMC, PYTHIA, and ALPGEN.

All SM background production cross sections are normalised to the results of higher-order calculations when available. The inclusive W and Z production cross sections are calculated to next-to-next-to-leading order (NNLO) in the strong coupling constant with DYNNLO [159] using the MSTW2008NNLO PDF set [160]. The $t\bar{t}$ cross section is normalised to a NNLO calculation including resummation of next-to-next-to-leading logarithmic (NNLL) soft gluon terms obtained with Top++ v2.0 [161]. The diboson production cross section is normalised to NLO using MCFM v6.2 [162, 163]. The production of $t\bar{t}$ in association with W/Z is normalised to the NLO cross section [164, 165].

Simulated signal samples are generated with Herwig++ v2.5.2 [166] and the CTEQ6L1 PDF set. Signal production cross sections are calculated to NLO using PROSPINO2 [167]. They are in agreement with the NLO calculations matched to resummation at the next-to-leading-logarithmic accuracy (NLO+NLL) within ∼2% [168, 169, 170].

A.1.2. Run II Analysis

The following information is an excerpt from [135].
All simulated samples have been generated at $\sqrt{s} = 13$ TeV. Pile-up has been included in the simulation using Pythia 8.186 [171] with the A2 [172] parameter set and the MSTW2008LO [173] parton density function. Simulated events are reweighted such that the average number of interactions per bunch crossing are the same in data and simulation. All Standard Model background processes have been simulated using the full detector simulation [142, 143], all signal samples using the fast calorimeter simulation [96], as explained in section 5.1.1.
The W+jets and Z+jets processes are simulated with the Sherpa 2.1.1 [174] generator. Matrix elements (ME) are calculated for up to two partons at next-to-leading order (NLO) and up to four additional partons at leading order (LO) in perturbative QCD using the OpenLoops [175] and Comix [176] matrix element generators, respectively. The polarisation of tau leptons in $W(\tau\nu)$+jets and $Z(\tau\tau)$+jets events is handled by the TauSpinner [177] program. The phase-space merging between the Sherpa parton shower (PS) [178] and matrix elements follows the ME+PS@NLO prescription [179]. The CT10 [180] PDF set is used in conjunction with dedicated parton-shower tuning. Simulated samples are generated in bins of the transverse momentum (p_{T}) of the vector boson. The inclusive cross sections are normalised to a next-to-next-to-leading-order (NNLO) calculation [159] in perturbative QCD based on the FEWZ program [181].
For the simulation of $t\bar{t}$ and single-top-quark production in the Wt- and s-channels, the Powheg-Box v2 [182] generator is used with the CT10 PDF set for the matrix elements calculation. Electroweak t-channel single-top-quark events are generated using the Powheg-Box v1 generator. This generator uses the four-flavour scheme for the NLO matrix element calculation together with the fixed four-flavour CT10f4 PDF set. For all top quark processes, top quark spin correlations are taken into account (for t-channel production, top quarks are decayed using MadSpin [183]). The parton shower, hadronisation, and underlying event are simulated using Pythia 6.428 [184] with the CTEQ6L1 [185] PDF set and the corresponding Perugia 2012 tune [156]. Cross sections are calculated at NNLO in perturbative QCD with resummation of next-to-next-to-leading logarithmic (NNLL) soft gluon terms using the Top++ 2.0 program [161].
Diboson production is simulated using the Sherpa 2.1.1 generator with the CT10 PDF set. Processes with fully leptonic final states are calculated with up to one (4ℓ, $2\ell + 2\nu$) or no partons ($3\ell + 1\nu$) at NLO and up to three additional partons at LO. Diboson processes with one of the bosons decaying hadronically and the other leptonically are simulated with up to 1 (ZZ) or 0 (WW, WZ) partons at NLO and up to 3 additional partons at LO. The generator cross sections are used for these samples.
The simplified-model signal samples are generated using MG5_aMC@NLO v2.2.3 [186] interfaced to Pythia 8.186 with the A14 tune [187] for the modelling of the parton shower, hadronisation and underlying event. The ME calculation is performed at tree level and includes the emission of up to two additional partons. The PDF set used for the generation is NNPDF23LO [188]. The ME–PS matching is done using the CKKW-L prescription [189], with a matching scale set to one quarter of the gluino mass. The

GMSB signal samples are generated with the HERWIG++ 2.7.1 [166] generator, with CTEQ6L1 PDFs and the UE-EE-5-CTEQ6L1 tune [190], using input files generated in the SLHA format with the SPHENO v3.1.12 [191] program. The parton shower evolution is performed using an algorithm described in Refs. [166, 192, 193, 194]. Signal cross sections are calculated at NLO in the strong coupling constant, adding the resummation of soft gluon emission at next-to-leading-logarithm accuracy [195, 196, 197, 198, 199]. The nominal cross section and the uncertainty are taken from an envelope of cross section predictions using different PDF sets and factorisation and renormalisation scales, as described in Ref. [200].

A.2. Tau + Light Lepton Channels

A.2.1. Signal-over-Background-Ratios

To reduce the set of uncorrelated variables used in the optimization in section 7.7.3, the power of each variable to discriminate signal from background has been investigated using the signal-over-background-ratio.

$\tilde{\chi}_1^{\pm}\tilde{\chi}_1^{\mp}$ Production

The signal-over-background-ratios for the studied set of variables: $\Delta\eta$, $\Delta\Phi$, H_{T}, $\not{E}_{\mathrm{T}}$, m_{T} of the leading p_{T} lepton, m_{T} of the sub-leading p_{T} lepton, the p_{T} of the leading lepton and m_{eff}, are shown in Figure A.1. As explained in the main text, in no case the signal-over-background-ratio yields a value above 1.
The signal-over-background-ratio in case of $\Delta\eta$ and $\Delta\phi$ is mostly flat and signal as well as background perform similarly. The spread in the values at which the signal-over-background distributions reach a value close to 0 is too large for the p_{T} of the leading signal lepton and H_{T}, meaning that for different signal points different cut-values are optimal. Consequently, for the purpose of further optimization, the list has been slimmed to: m_{T2}, the transverse mass of the leading lepton, $m_{\mathrm{eff}}$and $\not{E}_{\mathrm{T}}$.

pMSSM Direct Stau Production

The signal-over-background-ratios for the studied set of variables: $\Delta\eta$, $\Delta\Phi$, H_{T}, $\not{E}_{\mathrm{T}}$, m_{T} of the leading p_{T} lepton, m_{T} of the sub-leading p_{T} lepton, the p_{T} of the leading lepton, m_{eff}, m_{T}^{12} and the p_{T} of the sub-leading lepton, are shown in Figure A.2. As explained in the main text, in no case the signal-over-background-ratio yields a value above 1.
As in the previous case, the signal-over-background-ratio in case of $\Delta\eta$ and $\Delta\phi$ is mostly flat and signal as well as background perform similarly. The spread in the values at which the signal-over-background distributions reach a value close to 0 is too large for the p_{T} of the leading signal lepton and H_{T}, meaning that for different signal points different cut-values are optimal. Consequently, for the purpose of further optimization, the list has been slimmed to: m_{T2}, the transverse mass of the leading lepton, $m_{\mathrm{eff}}$and $\not{E}_{\mathrm{T}}$.

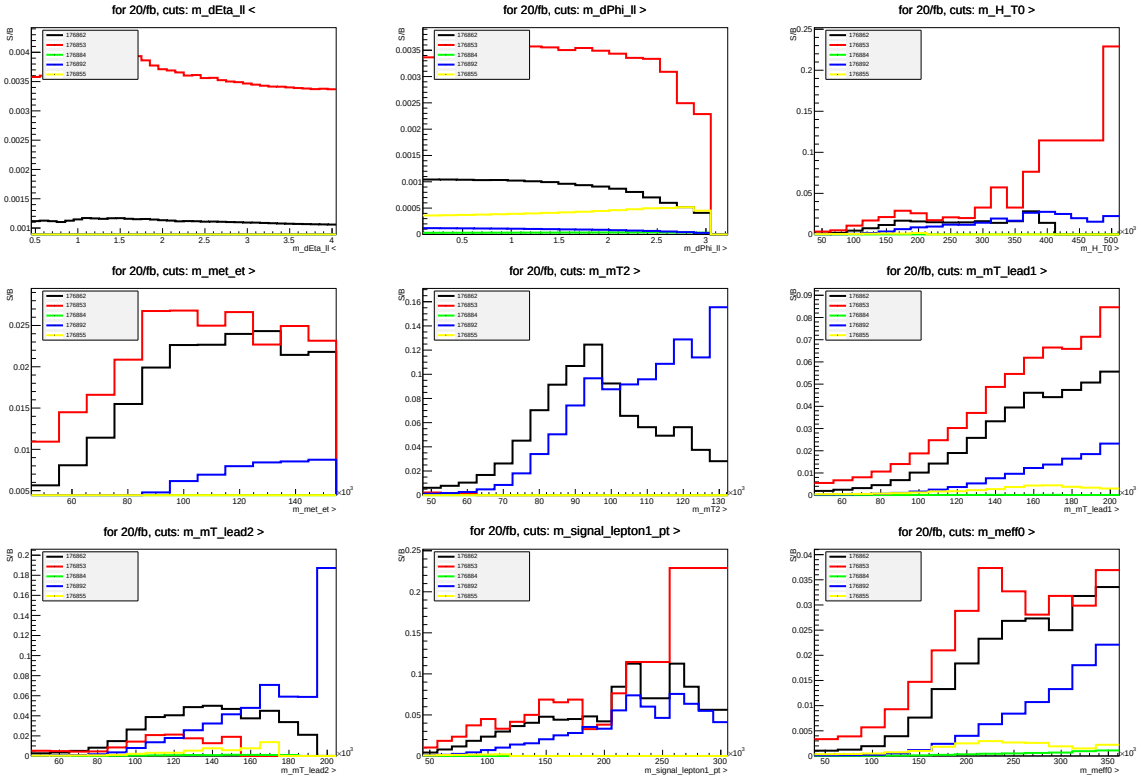

Figure A.1.: Signal-over-background-ratio in the $\tau + e$ channel when cutting on different variables for different signal grid points in the simplified model targeting $\tilde{\chi}_1^{\pm}$ pair production. The number of expected signal events has been scaled to the number of events expected in 20.3 fb^{-1}. The number of background events has been estimated from a small subset, 5 fb^{-1} of the data collected during Run I, assuming that no SUSY signal is in this set of data. The plots show (from left to right and top to bottom): $\Delta\eta$, $\Delta\Phi$, H_{T}, $\not{E}_{\mathrm{T}}$, m_{T} of the leading p_{T} lepton, m_{T} of the sub-leading p_{T} lepton, the p_{T} of the leading lepton, m_{eff}. *All plots are to be considered ATLAS work in progress.*

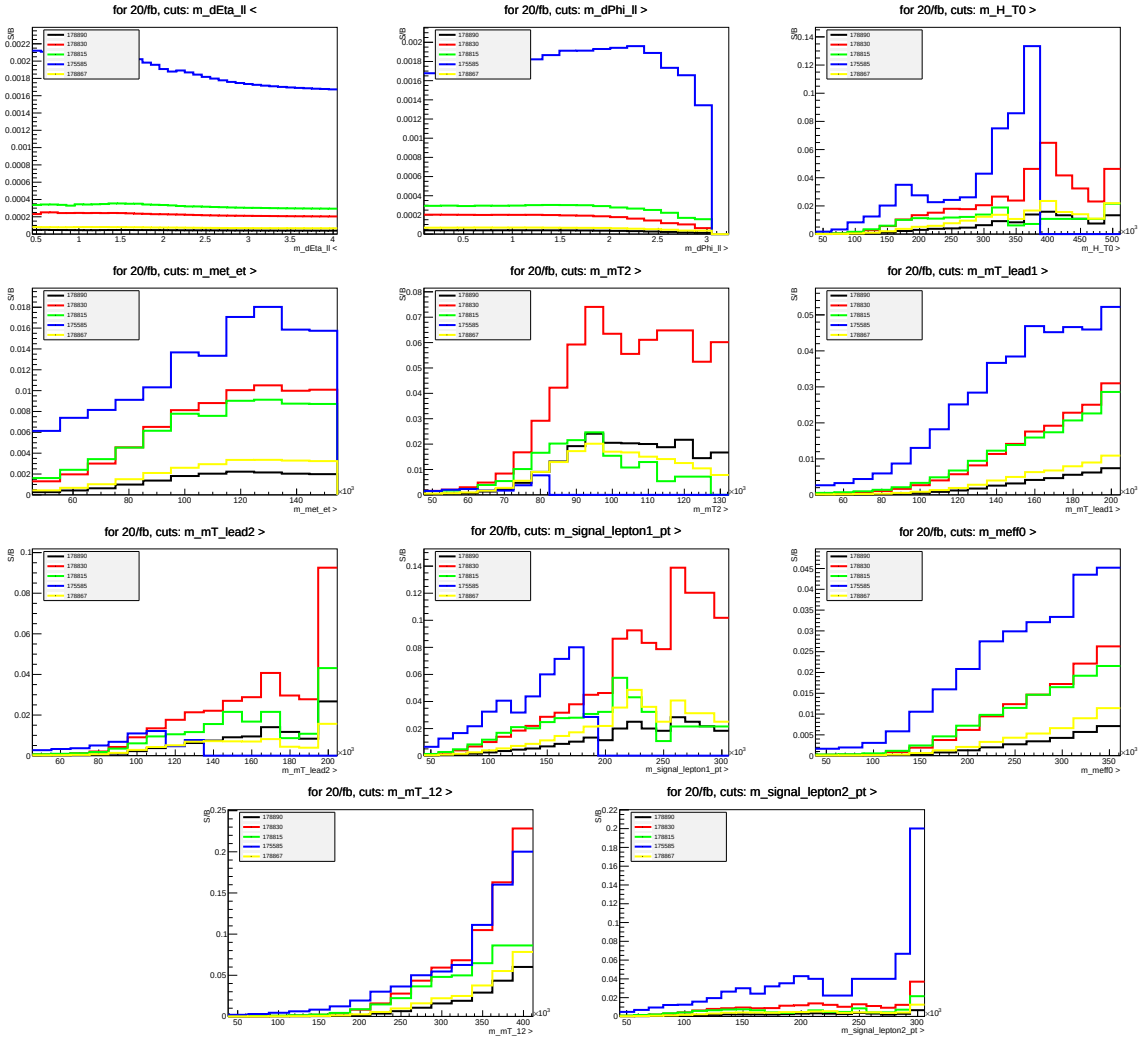

Figure A.2.: Signal-over-background-ratio in the $\tau + e$ channel when cutting on different variables for different signal grid points in the pMSSM model focussing on direct stau pair production. The number of expected signal events has been scaled to the number of events expected in 20.3 fb^{-1}. The plots show (from left to right and top to bottom): $\Delta\eta$, $\Delta\Phi$, H_{T}, $\not{E}_{\mathrm{T}}$, m_{T} of the leading p_{T} lepton, m_{T} of the sub-leading p_{T} lepton, the p_{T} of the leading lepton, m_{eff}, m_{T}^{12}, the p_{T} of the sub-leading lepton. *All plots are to be considered ATLAS work in progress.*

A.2.2. Combination of all Three Channels

Figure A.3 shows a more detailed comparison of the significances obtained when combining all three channels as explained in the text. The significances of the di-tau channel are compared to the significances when all three channels are combined. Due to the squared combination of the significances the gain is only noticeable if the significances are of the same order of magnitude. The maximum gain is, as can be inferred from Equation 7.5, a factor of $\sqrt{3}$ if all three channels perform equally well.

A.2.3. The Choice of the Transverse Mass Variable

To reduce the processing power needed to perform the optimization, only one of the available m_{T} definitions will be used. In Figure A.4 the normalized distributions of different ways to define m_{T} are compared for a set of selected low mass and high mass points, as well as for data. The discrimination power between signal and background suffers from high neutralino masses in all cases. The transverse mass of the leading p_{T} signal lepton (second row in Figure A.4) performs best, because its spectrum is on average harder for signal than for data. In higher mass regions the transverse mass of the light lepton, as well as the transverse mass of the sub-leading lepton are also viable options (left plots of the lower two rows of Figure A.4). However, since they do not perform equally well in case of the lower mass signal points, the transverse mass of the leading p_{T} lepton is used as cut variable.
In addition also the sum of the transverse masses of the two signal leptons, $m_{\mathrm{T}}^1 + m_{\mathrm{T}}^2$, has been investigated. For higher mass points, this is also a viable cut variable, as can be seen on the left hand side of Figure A.5. However, for lower sparticle masses it only shows a weak discrimination between signal and background, as can be seen on the right hand side of Figure A.5. Consequently the sum of the transverse masses of the two signal leptons will not be used.

A.2.4. Further Optimizations Investigated

Effect of using a Signal-Jet Veto instead of a *b*-Jet Veto

The impact of a signal-jet veto (veto also on light quark jets) instead of a b-jet veto is studied. In Figure A.6 the significance when using a b-jet veto in SR-TL-highMass is compared to the case when a signal-jet veto in SR-TL-highMass is used, by computing the ratio of the significances: Z_N(b-jet veto)/Z_N(signal-jet veto). When combining all three channels (left side of Figure A.6), the gain is of the order of a few percent, while when combining the tau + light lepton channels (right side of Figure A.6), it is larger. However, the problem is that the statistics is low for the tau + light lepton channels and already minor changes in the number of signal events passing the cuts have a large impact on the significance. Nevertheless, the b-jet veto is the best choice for the tau + light lepton channels.

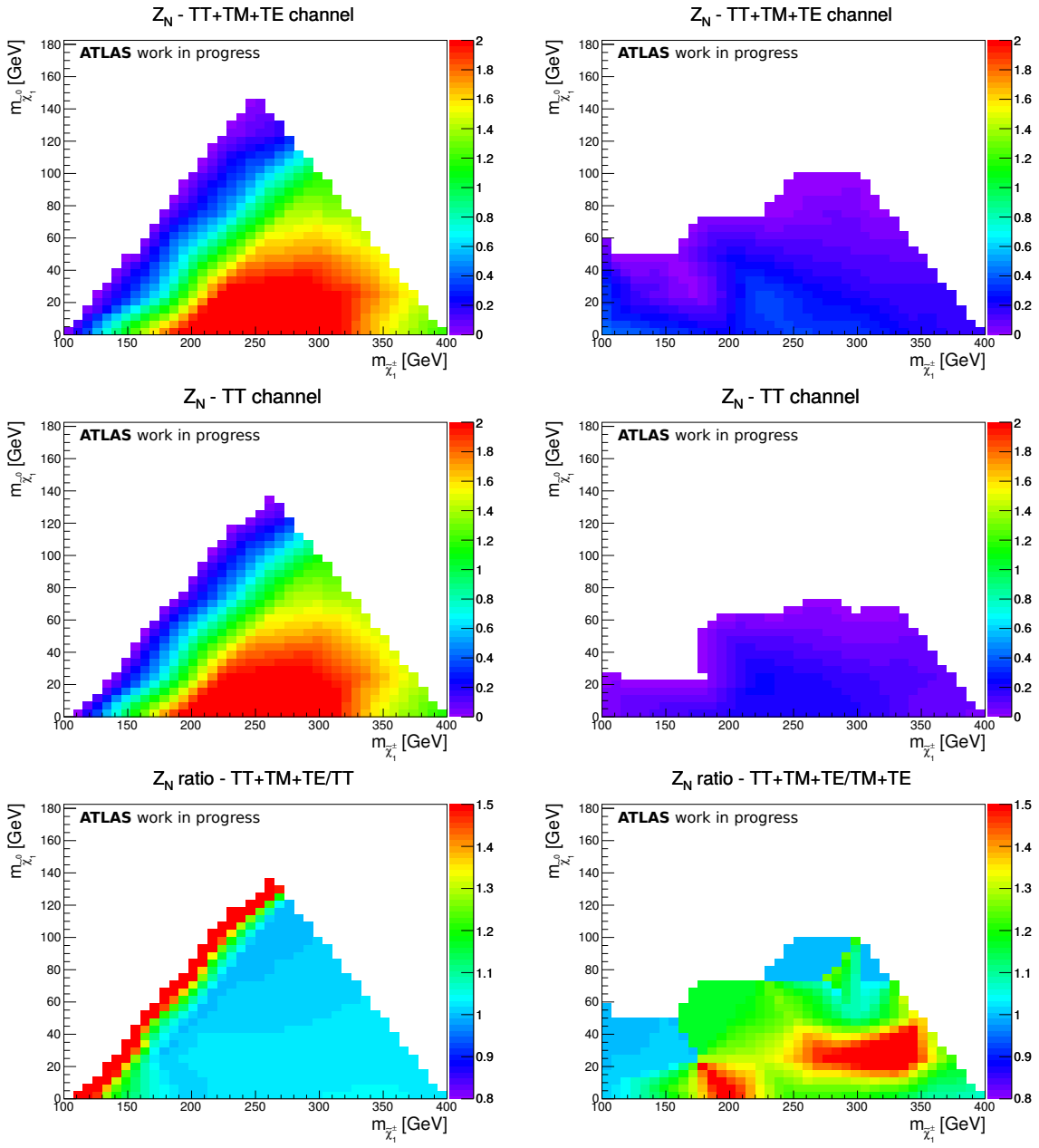

Figure A.3.: Detailed comparison of the significance of all three channels combined (top) and the significance of di-tau channel standalone (middle), in the left column for SR-TL-highMass and in the right for SR-TL-lowMass. The bottom plots show the ratio of the significances when statistically combining all three channels over only using the stronger channel, i.e. the di-tau for SR-TL-highMass and the combined tau + light lepton channel for SR-TL-lowMass. The improvement seen along the diagonal in SR-TL-highMass is an artifact of a division by zero.

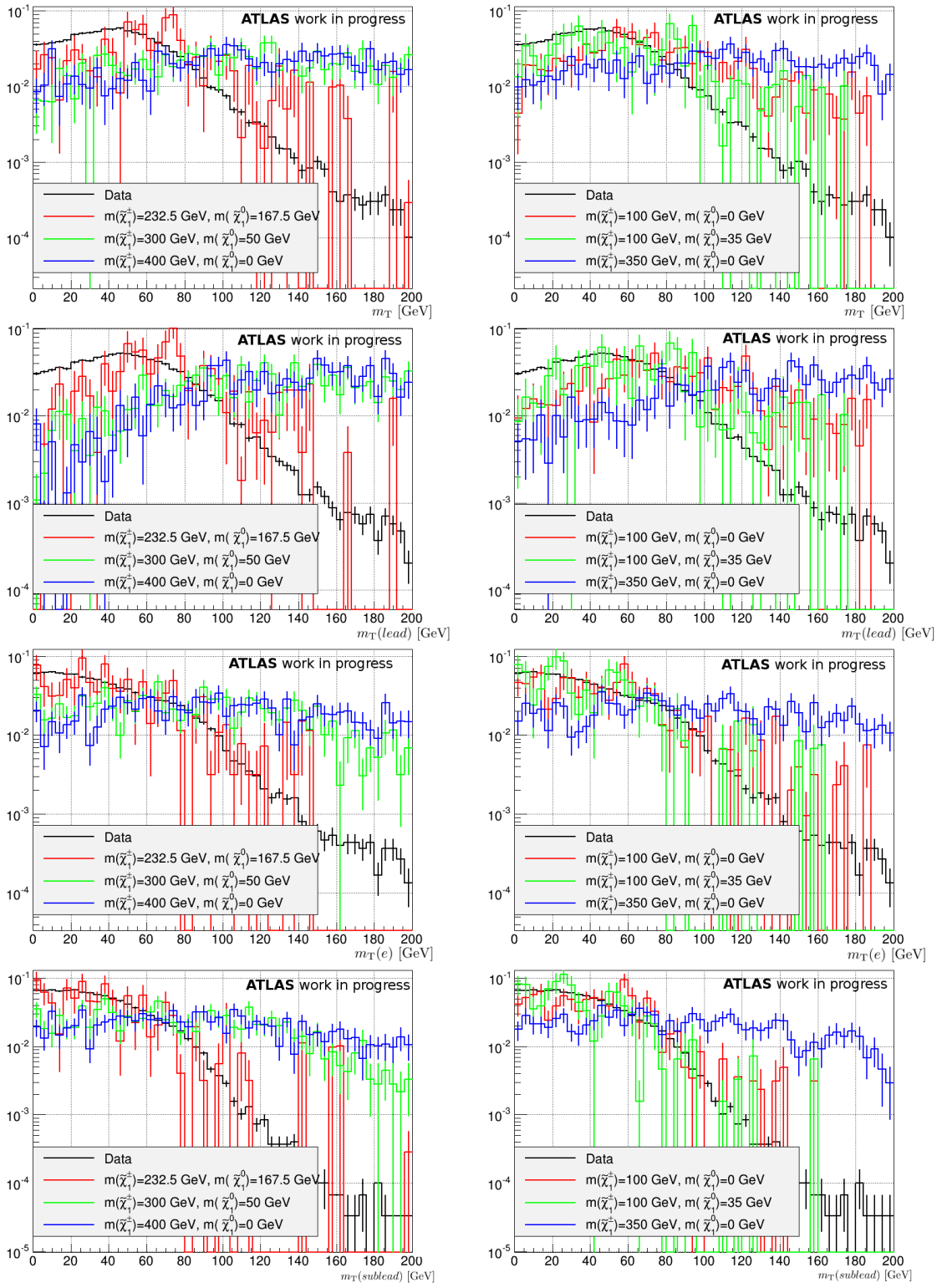

Figure A.4.: Normalized m_T distributions for different possibilities to define m_T in the $\tau + e$ channel. On the left side for a selection of high mass points and on the right side a selection of low mass points for the simplified model targeting $\tilde{\chi}_1^\pm \tilde{\chi}_1^\mp$ production. From top to bottom: the transverse mass of the hadronically decaying τ, the transverse mass of the leading p_T lepton, the transverse mass of the electron and the transverse mass of the sub-leading lepton.

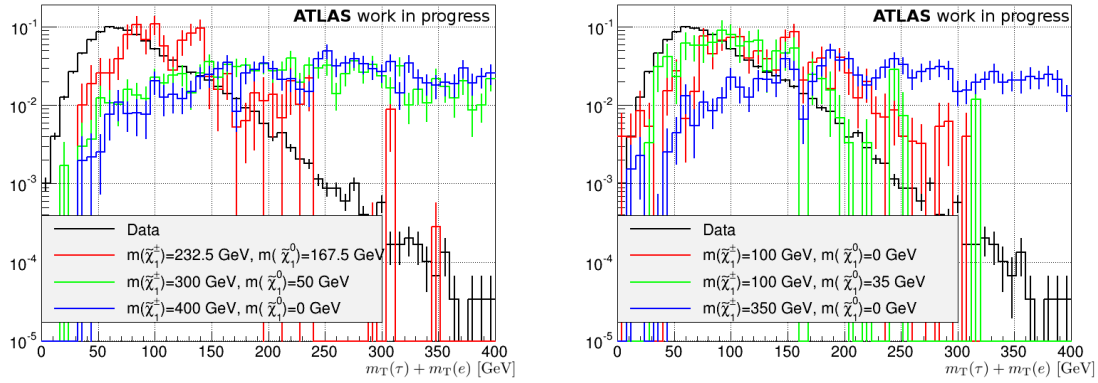

Figure A.5.: Normalized $\sum m_T$ distributions. On the left a selection of higher mass grid points, on the right the same for a selection of lower mass grid points.

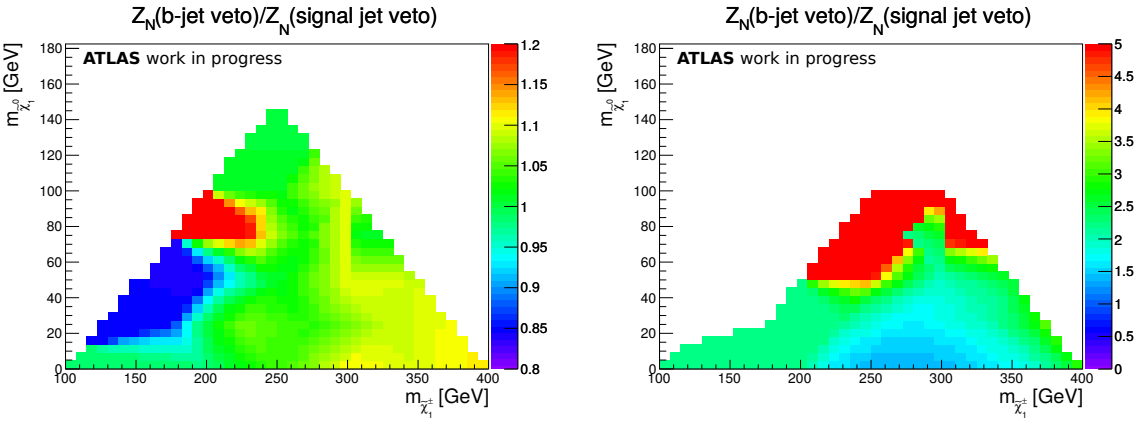

Figure A.6.: Z_N(b-jet veto)/Z_N(signal-jet veto) in the SR-TL-highMass signal region. The left plot shows the improvement when combining all three channels, the right plot shows the improvement when combining only the tau + light lepton channels.

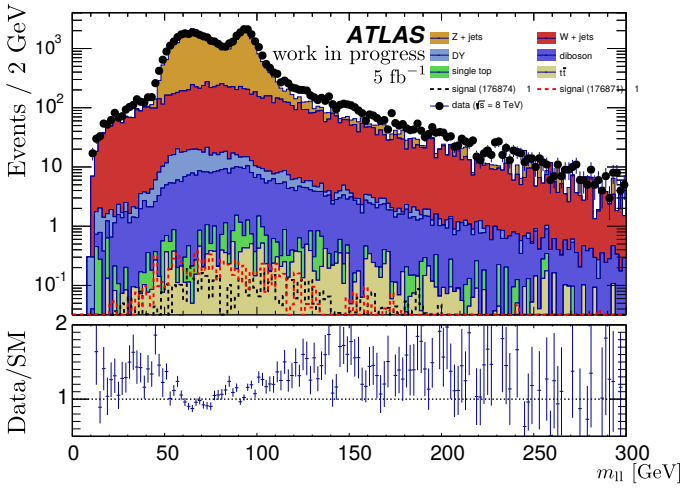

Figure A.7.: Invariant mass of the dilepton system in the $\tau + e$ channel before applying the Z-veto.

Improvement when Replacing the Z-Veto by a cut on m_{T2}

Since the distribution of the invariant mass of the two leptons is smeared by the additional neutrino, see Figure A.7, a possible improvement might be achieved by using m_{T2}. The m_{T2} distribution of the Z+jetsbackground, as depicted in Figure 7.17, is rather narrow, while for signal it is rather broad.
In Figure A.8 the ratio of the significances with and without a Z-veto in the SR-TL-highMass is shown (which applies a cut on m_{T2}), on the left the case of all three channels combined and on the right the case of combining only the tau + light lepton channels. An improvement can be seen in the tau + light lepton channels. However, the statistics are low in the tau + light lepton channels, therefore minor changes in the number of events passing a cut lead to large changes in the significance. In the case of combining all three channels, there is no improvement, but instead a loss of significance in this signal region. In this channel the contribution from Z+jets events extends to high values of m_{T2} (see Figure 7.17), and therefore cannot be efficiently suppressed by a cut on m_{T2}.

Using Asymmetric m_{T2}

One of the most important variables employed in this analysis, with very high discrimination power between signal and background, is m_{T2} [117, 201]. It is defined to be a generalization of the transverse mass to events with two invisible particles, as is the case in SUSY events when R-parity is conserved. It is sometimes called the "stransverse mass". The decay topology in the SUSY events which are considered is not quite the one m_{T2} was designed for, as there is a number of additional invisible particles (the neutrinos) and not only the two immediate neutralinos from the SUSY decay chains. Still, in the di-tau channel it proved very useful to distinguish between signal and background.
In the computation of m_{T2}, one has to make an assumption on the mass of the invisible

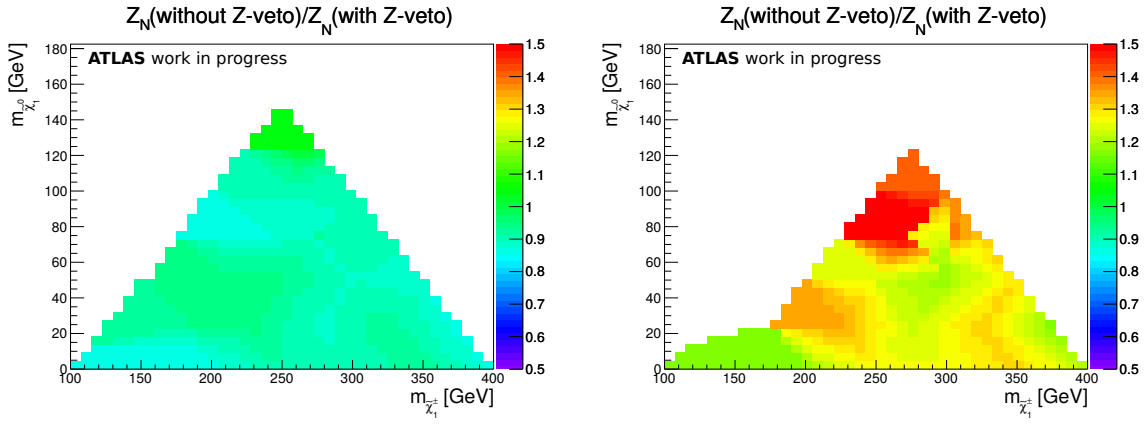

Figure A.8.: The ratio of the significances without and with a Z-veto. Left: for the combination of all three channels. Right: for the combination of only the tau + light lepton channels.

particle. In the definition of m_{T2}used in the presented analyses, this mass is taken to be the same in both decay branches of the event. When looking at chargino pair production, this is the case in the di-tau channel, and also in the tau + light lepton channel the invisible particle is the same in both branches, the lightest neutralino. However, the two decay branches in events from the tau + light lepton channels are not symmetric due to the additional neutrino in the branch where the tau decays to a lighter lepton. One may therefore hope that an asymmetric m_{T2} definition may be able to cope better with this event topology. There are generalizations of m_{T2} [202, 203] which take into account either different parent particle masses or different invisible particle masses. Their application to the tau + light lepton channel is studied in the following. Note that [202] states that in the case of non-identical daughters but common-mass parents, one could use the standard m_{T2} definition. It is still possible though to use a different value for the invisible mass in the two branches, as was done e.g. in [204].
Distributions of m_{T2} when varying the assumed mass of the invisible particles, m_{invis}, in the calculation of $m_{\mathrm{T2}}$are shown in Figure A.9. The ratio of the masses of the two invisible particles has been set to 1. Going from lower to higher values of m_{invis}, the onset of the m_{T2} distribution is shifted to the right. In fact, the onset of the distributions is and has to be equal to m_{invis} if the ratio of the masses of the invisible particles is equal to 1. However, the discrimination power of m_{T2} does not increase by varying m_{invis}, because this affects all distributions in the same way. The m_{T2} distribution for the W+jets background is still very similar to the ones of the signal samples. Therefore, varying m_{invis} does not help to increase the discrimination power of m_{T2}.
Another modification of the standard symmetric m_{T2} studied, is to vary the ratio of the parent masses, while setting m_{invis} to 0 GeV. The results are shown in Figure A.10. Increasing the ratio of the masses of the parent particles broadens the resulting m_{T2} distributions. However, as before, this affects all processes in the same way. As a result, it does not help in discriminating background and signal. Note that this modification does not have a direct physical motivation, as in our case in both branches the parent particle

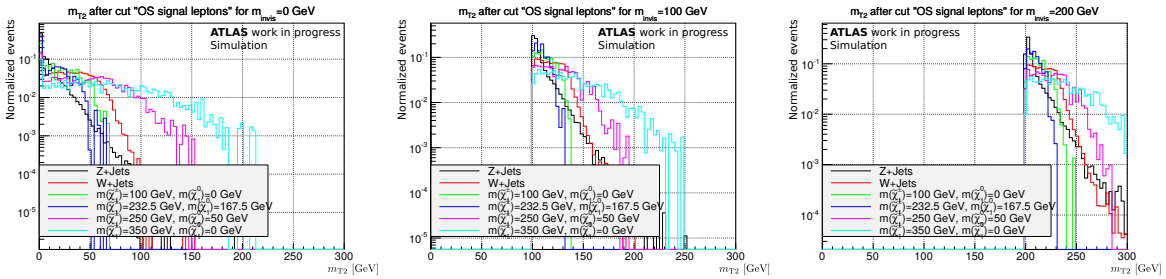

Figure A.9.: Normalized m_{T2} distributions for different samples from the simplified model targeting $\tilde{\chi}_1^{\pm}\tilde{\chi}_1^{\mp}$ production and two of the main backgrounds in the $\tau + e$ channel. The mass of the invisible particles is varied from left to right: 0 GeV, 100 GeV, 200 GeV. The mass of both invisible particles is assumed to be equal.

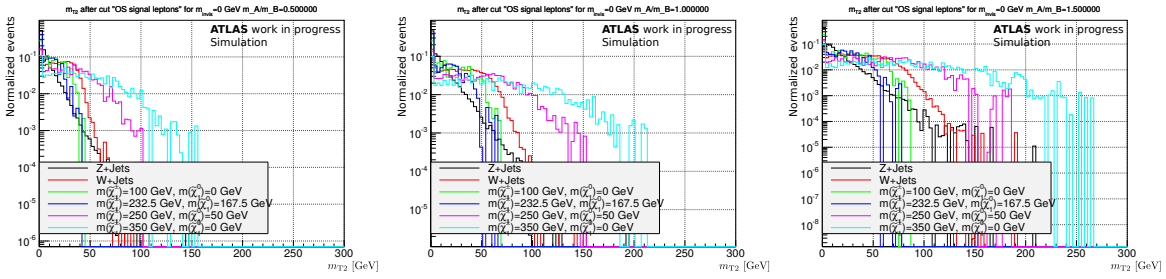

Figure A.10.: Normalized m_{T2} distributions for different samples from the simplified model targeting $\tilde{\chi}_1^{\pm}\tilde{\chi}_1^{\mp}$ production and two of the main backgrounds in the $\tau + e$ channel. The mass ratio of the parent masses is varied from left to right: 0.5, 1.0, 1.5. The mass of the invisible particles is assumed to be zero.

is a $\tilde{\chi}_1^{\pm}$. However, as the subsequent decays of the parent particles are asymmetric in tau + light lepton events, this variation of m_{T2} was taken into account for completeness. Yet another modification of the standard symmetric m_{T2} studied, is by varying the assumed masses of the invisible particles independently. This is motivated by the fact that a different number of invisible particles is created in the two branches of the targeted decays. As can be seen in Figure A.11, the effect on all distributions is again the same and, as to be expected from the definition of m_{T2}, the lower end of the distribution is given by the assumed mass of the heavier invisible particle. Therefore, the discrimination power of m_{T2} between signal and background does not increase by assuming different masses for the invisible particles.

A.3. Estimating the Sensitivity at $\sqrt{s} = 13$ TeV

Using the re-weighting technique explained in section 7.8, the expected sensitivity at $\sqrt{s} = 13$ TeV has been estimated for a luminosity of 5 fb^{-1} and different multi-jet scaling factors, the results are depicted in Figure A.12.

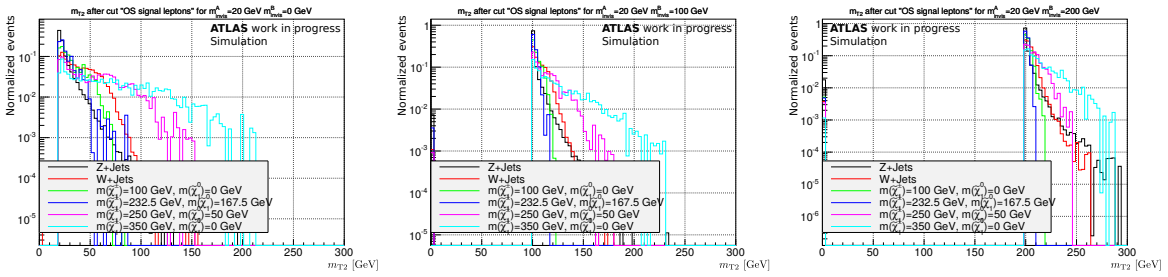

Figure A.11.: Normalized m_{T2} distributions for different samples from the simplified model targeting $\tilde{\chi}_1^{\pm}\tilde{\chi}_1^{\mp}$ production and two of the main backgrounds in the $\tau + e$ channel. The mass of the two assumed invisible particles is varied independently. For all three plots the mass of one of the invisible particles is set to 20 GeV, while the other is varied from left to right: 0 GeV, 100 GeV, 200 GeV.

A.4. The Search for Strongly Produced Taus

A.4.1. QCD Estimate

JetSmearing Estimate

The explanation of the technique, as well as the explanation of the seed-selection are closely following the explanations found in [205].

Technique Given the large cross section for multi-jet production at the LHC, it is not convenient to make direct use of simulation in order to estimate their background contribution. Even in the hypothetical situation of sufficiently large MC samples, the fact that the multi-jet selection efficiency heavily depends on jets mis-identified as taus and on instrumental $\not{E}_{\mathrm{T}}$ would lead to very large uncertainties in the prediction. Multi-jet events contain neither prompt taus nor $\not{E}_{\mathrm{T}}$ (except in the case of heavy-flavour jets). Hence, for such events to end up in one of the signal regions, at least two taus have to be faked by jets and in addition jets have to mis-measured. Although both are unlikely cases to happen, yet, the multi-jet contribution cannot be neglected, because its cross section is very large.
Fake $\not{E}_{\mathrm{T}}$ in multi-jet events is a common problem in many SUSY searches. The so-called "jet smearing" technique [206] has been developed in the context of the search for supersymmetry in events with $\not{E}_{\mathrm{T}}$, multiple jets and no light leptons (0-lepton search). This method is based on the idea that the dominant source of $\not{E}_{\mathrm{T}}$ in multi-jet events is a mis-measurement of the energy of one or multiple jets. Following this reasoning, one can produce "multi-jet pseudo-data" with fake $\not{E}_{\mathrm{T}}$ by smearing well-measured jets in the data within their calorimeter response function. They are computed as ratios between calibrated jet p_{T} and truth jet p_{T}, where truth jets include neutrinos, and both reconstructed and truth jets include muons which are especially relevant for b-jets. Jet response functions are initially derived using di-jet Monte Carlo samples. However, corrections are needed to better describe the response distributions in data, especially the

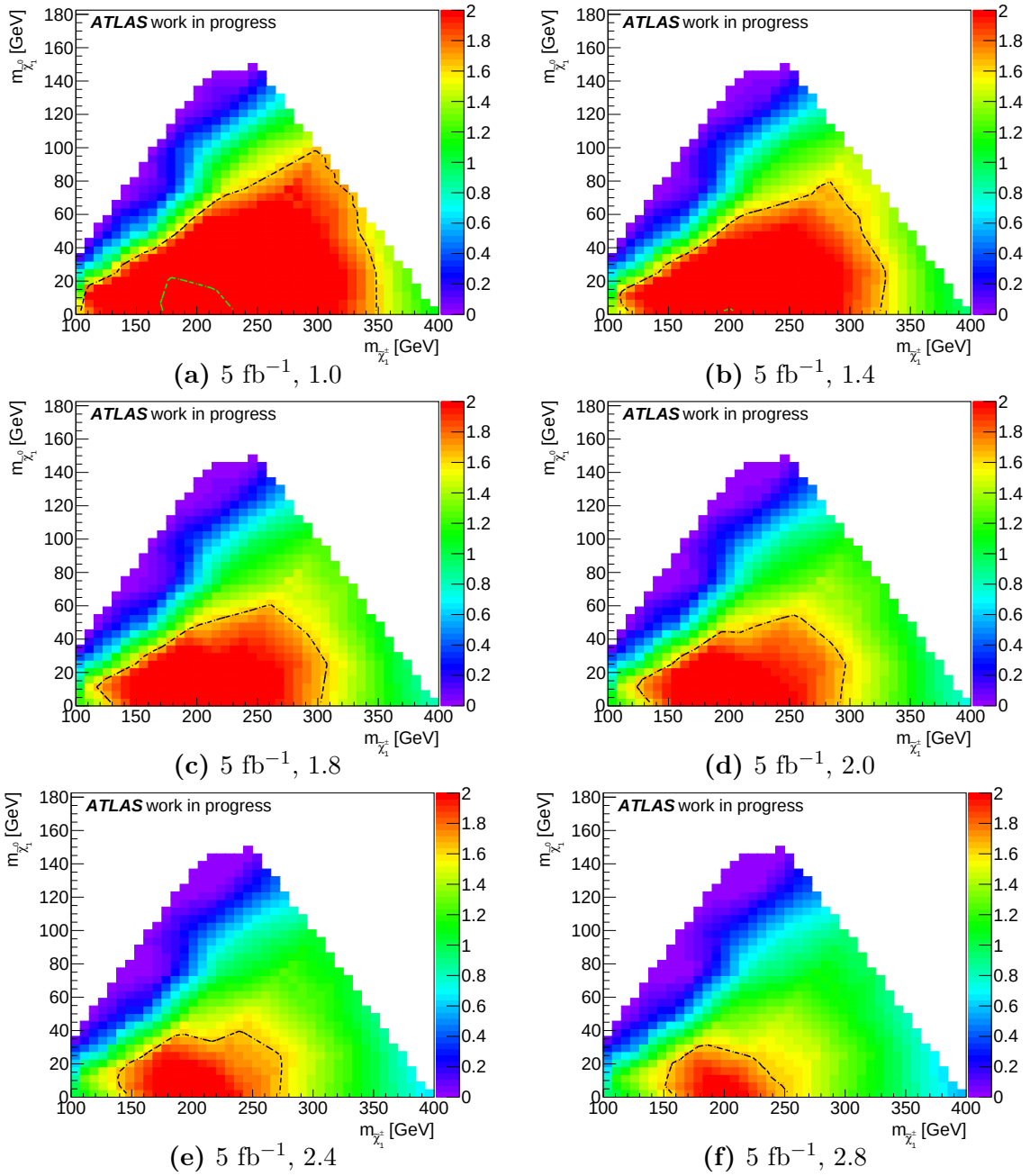

(a) 5 fb^{-1}, 1.0 **(b)** 5 fb^{-1}, 1.4

(c) 5 fb^{-1}, 1.8 **(d)** 5 fb^{-1}, 2.0

(e) 5 fb^{-1}, 2.4 **(f)** 5 fb^{-1}, 2.8

Figure A.12.: Expected significance obtained by weighting the Standard Model backgrounds taken from Monte Carlo to a center-of-mass energy of 13 TeV and using the multi-jet estimate from Run I multiplied by different factors for an integrated luminosities of 5 fb^{-1}. The scaling factors are: (a) 1.0, (b) 1.4, (c) 1.8, (d) 2.0, (e) 2.4, (f) 2.8. The black-dashed line corresponds to the region which can potentially be excluded, while the green-dashed line corresponds to the region where one can potentially claim evidence for supersymmetry if it exists within that region.

tails of response distributions. These data-driven corrections are not yet available for Run II and are consequently not used. More details about the technique, the measurements and the Run I parametrization can be found in [206].
In the context of the Run II search presented in this thesis, the only difference with the above is the presence of reconstructed taus. In multi-jet events, these taus are misidentified jets. One advantage of using data to estimate the multi-jet background is that the fake tau content is well modeled, because the seed events are not simulated, thus there is no need for a jet-to-tau fake-rate correction.

Seed Selection As a starting point, multi-jet "seed events" are selected. Seed events are required to have well-measured jets, i.e. they should not have a significant amount of missing transverse energy. Studies showed that imposing a cut directly on $\not{E}_{\mathrm{T}}$ results in a bias in the jet p_{T}. Instead, a cut on the $\not{E}_{\mathrm{T}}$ significance

$$S_{1/2} = \frac{\not{E}_{\mathrm{T}}}{\sqrt{\sum E_{\mathrm{T}}}} , \quad \text{or} \quad S_{1/3} = \frac{\not{E}_{\mathrm{T}}}{(\sum E_{\mathrm{T}})^{1/3}}$$

is applied. In Run I, the $\not{E}_{\mathrm{T}}$ resolution was essentially following $\sqrt{\sum E_{\mathrm{T}}}$, which motivated the use of $S_{1/2}$. In Run II, selecting seed events by cutting on $S_{1/2}$ was found to induce biases in pseudo-data distributions, especially on the leading jet p_{T} [207]. This might be due to the fact that the $\not{E}_{\mathrm{T}}$ soft term changed: now it is based on tracks, and not clusters like in Run I. The alternative definition $S_{1/3}$ was found not to introduce such biases, although the fundamental reason is still being investigated. Therefore this latter definition is used for the seed selection.
Seed events are selected using all single-jet triggers available throughout 2015. Pre-scales are taken into account by weighting events according to the pre-scale of the highest-threshold trigger that fired. Trigger plateau cuts are applied to ensure that each of the triggers is working in its plateau region.

Results A p_{T} threshold of 18 GeV is used to select jet candidates for smearing, Smearing only jets as well as smearing jets and taus has been studied. For the latter case, the assumption is made that taus in multi-jet events are simply jets which have been misidentified as taus and therefore the same response function was used for jets and taus.
Although getting some distributions like $\not{E}_{\mathrm{T}}$, m_{Tsum} and $\frac{\not{E}_{\mathrm{T}}}{m_{\mathrm{eff}}}$ right with the jet- and tau-smearing technique, lots of variables are mismodeled, like e.g. the leading jet p_{T} or the ΔR between the two leading taus, as can be seen in Figure A.13. This is caused by limited seed statistics. Only about 1200 multi-jet events containing two taus and jets were selected prior to applying the $\not{E}_{\mathrm{T}}$ significance cut. Even using $\not{E}_{\mathrm{T}}$-based triggers to complement the single jet ones does not improve the situation much. One or two orders of magnitude more seed events are needed. What limits the usable statistics so strongly is the requirement of two fake taus, because the jet-to-tau fake-probability is low. In addition the large pre-scales of events triggered by the low threshold jet triggers also contribute to the problem, since these result in large per-event weights and in low

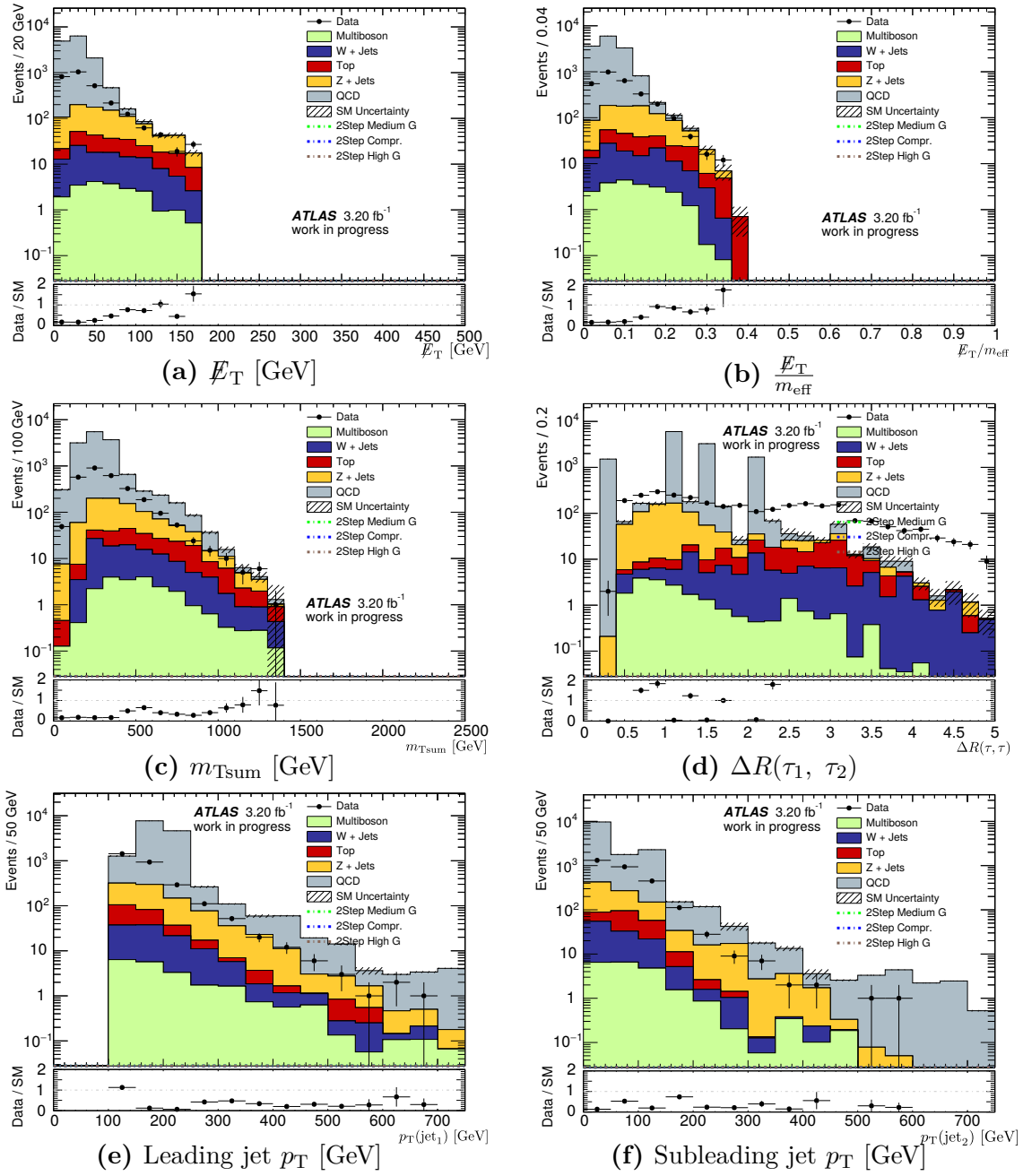

(a) $\not{E}_T$ [GeV] **(b)** $\frac{\not{E}_T}{m_{eff}}$

(c) m_{Tsum} [GeV] **(d)** $\Delta R(\tau_1,\ \tau_2)$

(e) Leading jet p_T [GeV] **(f)** Subleading jet p_T [GeV]

Figure A.13.: Performance of the jet-smearing method in the QCD-dominated two tau selection, based on single-jet triggers and two-tau selection. Jets as well as taus are smeared, using the same response function. The QCD contribution has been scaled by a factor 10 to exaggerate the spiky behavior. Depicted uncertainties are only of statistical nature.

	Contribution [%]	Stat. Error [%]
Process		
Top	52.18	23.54
Z + Jets	9.49	1.46
W + Jets	28.12	7.97
QCD	7.90	4.37
Multiboson	2.30	0.79
SM Total	100.00	-

Table A.1.: Background composition in SR-mTSum. QCD has been estimated using the jet-fake method. Complements Table 9.5.

	Contribution [%]	Stat. Error [%]
Process		
Top	28.46	20.15
Z + Jets	7.47	1.60
W + Jets	55.02	7.14
QCD	2.37	0.61
Multiboson	6.68	4.00
SM Total	100.00	-

Table A.2.: Background composition in SR-highMass. QCD has been estimated using the jet-fake method. Complements Table 9.5.

statistics in the low leading jet p_{T} bins. Therefore, alternative approaches for estimating QCD in the two-tau channel are used, as discussed in section 9.3.2.

Jet-Fake Method

Additional Plots Figure A.14 complements Figure 9.9 (a) and (b) by showing the performance of the jet-fake method in the multi-jet dominated control region for additional variables.

Estimates in the Signal/Control Regions The following tables supplement the ones found in section 9.3.2, giving a detailed breakdown of the individual contributions of each process to the individual control and signal regions. To be more specific the tables Table 9.5 and Table 9.7 are supplemented by tables A.1, A.2, and A.3 and tables A.4, A.5, A.6 and A.7 respectively. Table 9.8, showing the multi-jet contributions to the fake tau control regions, is complemented by Table A.8 and Table A.9 for the electron and muon channel, respectively.

OS-SS Method

Additional Plots Figure A.15 complements Figure 9.9 (c) and (d) by showing the performance of the jet-fake method in the multi-jet dominated control region for additional

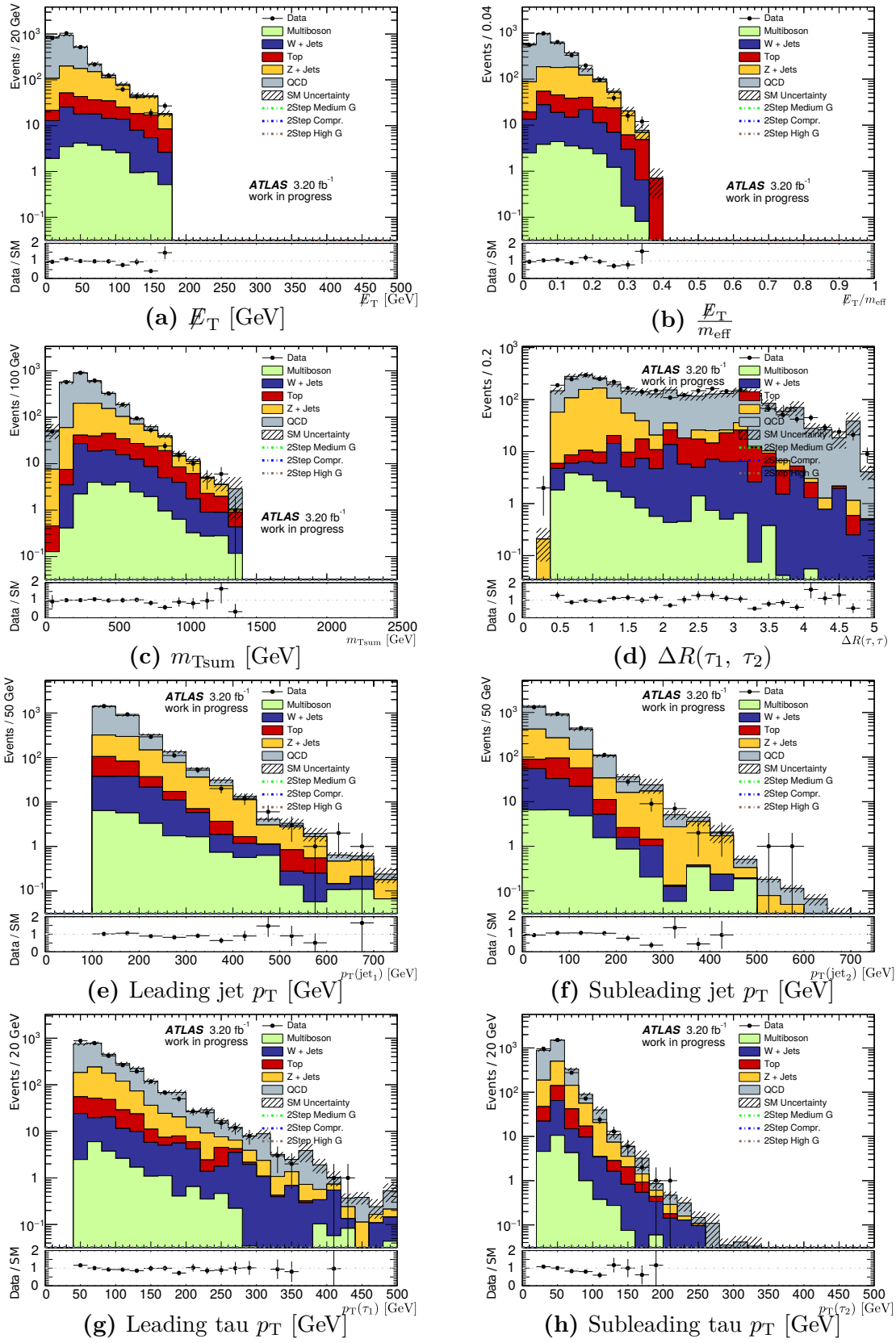

(a) $\not{E}_T$ [GeV] **(b)** $\frac{\not{E}_T}{m_{\text{eff}}}$

(c) m_{Tsum} [GeV] **(d)** $\Delta R(\tau_1,\ \tau_2)$

(e) Leading jet p_T [GeV] **(f)** Subleading jet p_T [GeV]

(g) Leading tau p_T [GeV] **(h)** Subleading tau p_T [GeV]

Figure A.14.: Performance of the jet-fake method in the multi-jet dominated control region, as defined in section 9.3.2. Complements Figure 9.9 (a) and (b). Depicted uncertainties are only of statistical nature.

	Contribution [%]	Stat. Error [%]
Process		
Top	19.90	11.49
Z + Jets	11.51	3.76
W + Jets	57.83	14.99
QCD	2.36	0.75
Multiboson	8.40	5.84
SM Total	100.00	-

Table A.3.: Background composition in SR-GMSB. QCD has been estimated using the jet-fake method. Complements Table 9.5.

	Contribution[%]	Stat. Error[%]	Contribution[%]	Stat. Error[%]
	W CR		Top CR	
Top	6.68	0.18	64.91	0.69
Z + Jets	6.40	0.51	2.32	0.35
W + Jets	84.32	0.85	22.43	0.36
Single Top	1.20	0.04	9.13	0.15
QCD	0.81	0.06	0.99	0.07
Multiboson	0.59	0.03	0.22	0.03
SM Total	100.00	-	100.00	-

Table A.4.: Background composition in the true tau W and Top control regions. QCD has been estimated using the jet-fake method. Complements Table 9.7.

	Contribution[%]	Stat. Error[%]	Contribution[%]	Stat. Error[%]
	W CR		Top CR	
Top	6.99	0.09	67.80	0.34
Z + Jets	1.15	0.09	0.41	0.08
W + Jets	86.23	0.54	21.66	0.22
Single Top	1.16	0.03	8.24	0.09
QCD	0.02	0.00	0.02	0.00
Multiboson	4.44	0.14	1.87	0.12
SM Total	100.00	-	100.00	-

Table A.5.: Background composition in the kinetic W and Top control regions. QCD has been estimated using the jet-fake method. Complements Table 9.7.

	Contribution[%]	Stat. Error[%]	Contribution[%]	Stat. Error[%]
	W CR		Top CR	
Top	13.60	0.82	67.33	1.97
Z + Jets	9.65	1.12	1.83	0.74
W + Jets	54.54	1.83	9.65	0.54
Single Top	1.74	0.17	7.37	0.38
QCD	17.00	0.81	12.71	0.74
Multiboson	3.46	0.21	1.12	0.20
SM Total	100.00	-	100.00	-

Table A.6.: Background composition in the fake tau W and Top control regions. QCD has been estimated using the jet-fake method. Complements Table 9.7.

	Contribution[%]	Stat. Error[%]
	Z CR	
Top	8.52	1.24
Z + Jets	52.02	5.36
W + Jets	27.89	2.77
Single Top	1.21	0.26
QCD	6.49	8.06
Multiboson	3.87	0.54
SM Total	100.00	-

Table A.7.: Background composition in the Z control region. QCD has been estimated using the OS-SS method, because the Z control region requires an oppositely charged tau pair. Complements Table 9.7.

	Contribution[%]	Stat. Error[%]	Contribution[%]	Stat. Error[%]
	W CR		Top CR	
Top	13.50	1.10	62.20	2.61
Z + Jets	7.34	0.97	1.73	0.13
W + Jets	47.62	2.23	9.15	0.74
Single Top	1.65	0.22	7.21	0.51
QCD	26.78	1.38	18.99	1.26
Multiboson	3.11	0.27	0.71	0.15
SM Total	100.00	-	100.00	-

Table A.8.: Background composition in the fake tau W and Top control regions when requiring one electron instead of one electron or one muon. QCD has been estimated using the jet-fake method. The QCD contribution is significantly larger than in the combined selection. Complements Table 9.8.

	Contribution[%]	Stat. Error[%]	Contribution[%]	Stat. Error[%]
	W CR		Top CR	
Top	14.06	1.24	72.84	2.96
Z + Jets	12.41	2.15	1.94	1.52
W + Jets	62.42	3.00	10.16	0.79
Single Top	1.84	0.26	7.51	0.56
QCD	5.41	0.68	6.01	0.72
Multiboson	3.86	0.34	1.54	0.37
SM Total	100.00	-	100.00	-

Table A.9.: Background composition in the fake tau W and Top control regions when requiring one muon instead of one electron or one muon. QCD has been estimated using the jet-fake method. The QCD is significantly lower than in the electron channel. Complements Table 9.8.

	Contribution [%]	Stat. Error [%]
Process		
Top	61.54	35.03
Z + Jets	9.10	1.96
W + Jets	26.43	11.29
QCD	0	0
Multiboson	2.93	1.14
SM Total	100.00	-

Table A.10.: Background composition in SR-mTSum. QCD has been estimated using the OS-SS method. Complements Table 9.6.

variables.

Estimates in the Signal/Control Regions The following tables supplement the ones found in section 9.3.2, giving a detailed breakdown of the individual contributions of each process to the signal regions. To be more specific the tables Table 9.6 is supplemented by tables A.10, A.11, and A.12.

A.4.2. Comparison Between Jet-Fake and OS-SS Methods

Additional Plots Additional plots are presented which supplement the ones in the main text concerning the comparison between the jet-fake method and the OS-SS method to estimate multi-jet events in section 9.3.2. Figure A.16 shows a "side-by-side" comparison of different variables of the jet-fake method on the left and the OS-SS method on the right. It complements Figure 9.9 (a-d). Figure A.17 complements the normalized comparison of solely the multi-jet contribution estimated using the jet-fake and OS-SS method shown in Figure 9.9 (e) and (f).

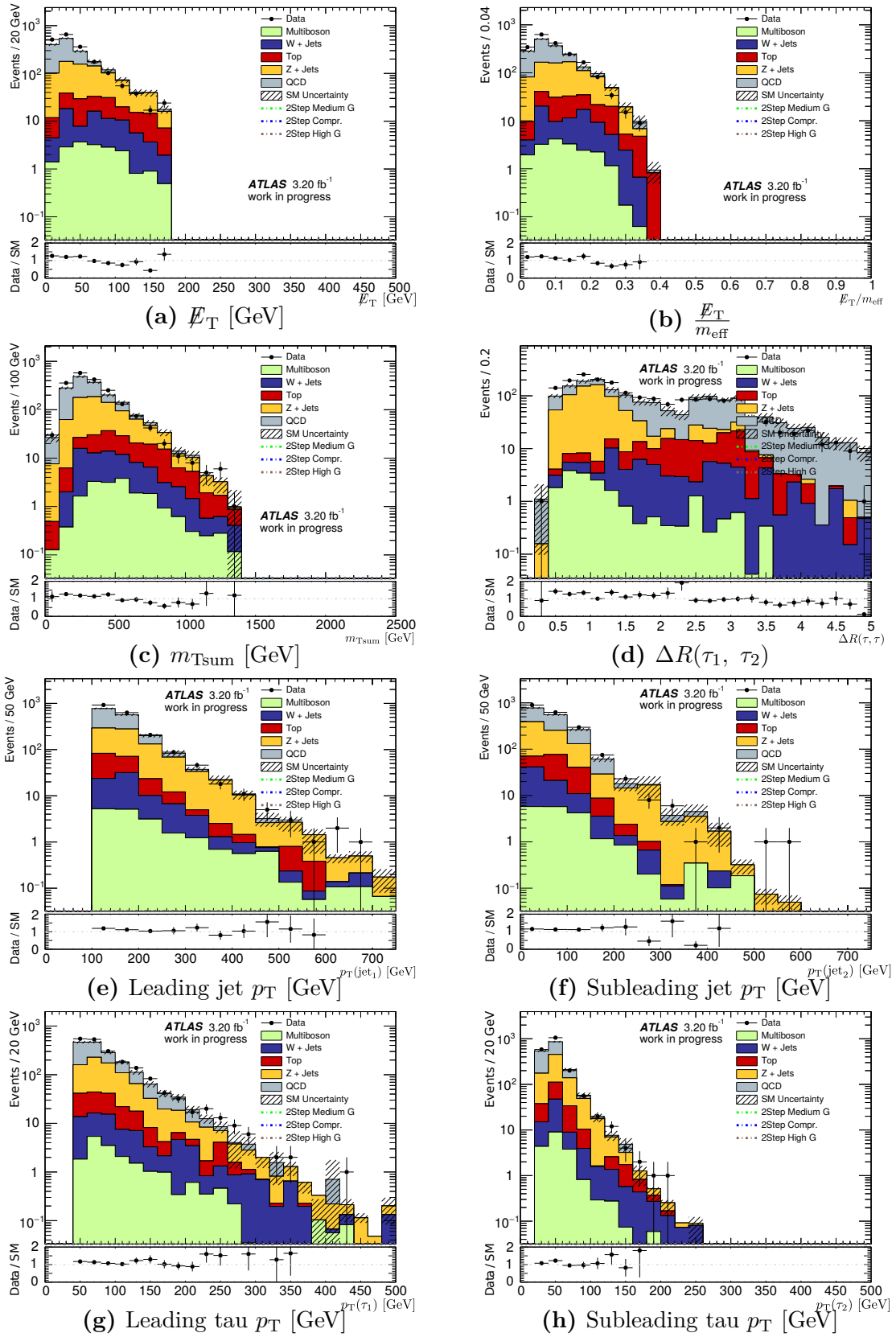

(a) $\not{E}_{\mathrm{T}}$ [GeV] **(b)** $\frac{\not{E}_{\mathrm{T}}}{m_{\mathrm{eff}}}$

(c) m_{Tsum} [GeV] **(d)** $\Delta R(\tau_1,\ \tau_2)$

(e) Leading jet p_{T} [GeV] **(f)** Subleading jet p_{T} [GeV]

(g) Leading tau p_{T} [GeV] **(h)** Subleading tau p_{T} [GeV]

Figure A.15.: Performance of the OS-SS method in the QCD-dominated two tau selection. The QCD estimate has not yet been normalized in a separate control region. Complements Figure 9.9 (c) and (d). Depicted uncertainties are only of statistical nature.

	Contribution [%]	Stat. Error [%]
Process		
Top	36.88	33.02
Z + Jets	7.35	2.28
W + Jets	44.67	7.27
QCD	0	0
Multiboson	11.11	6.69
SM Total	100.00	-

Table A.11.: Background composition in SR-highMass. QCD has been estimated using the OS-SS method. Complements Table 9.6.

	Contribution [%]	Stat. Error [%]
Process		
Top	11.35	11.35
Z + Jets	10.85	4.80
W + Jets	63.36	21.06
QCD	0	0
Multiboson	14.44	10.06
SM Total	100.00	-

Table A.12.: Background composition in SR-GMSB. QCD has been estimated using the OS-SS method. Complements Table 9.6.

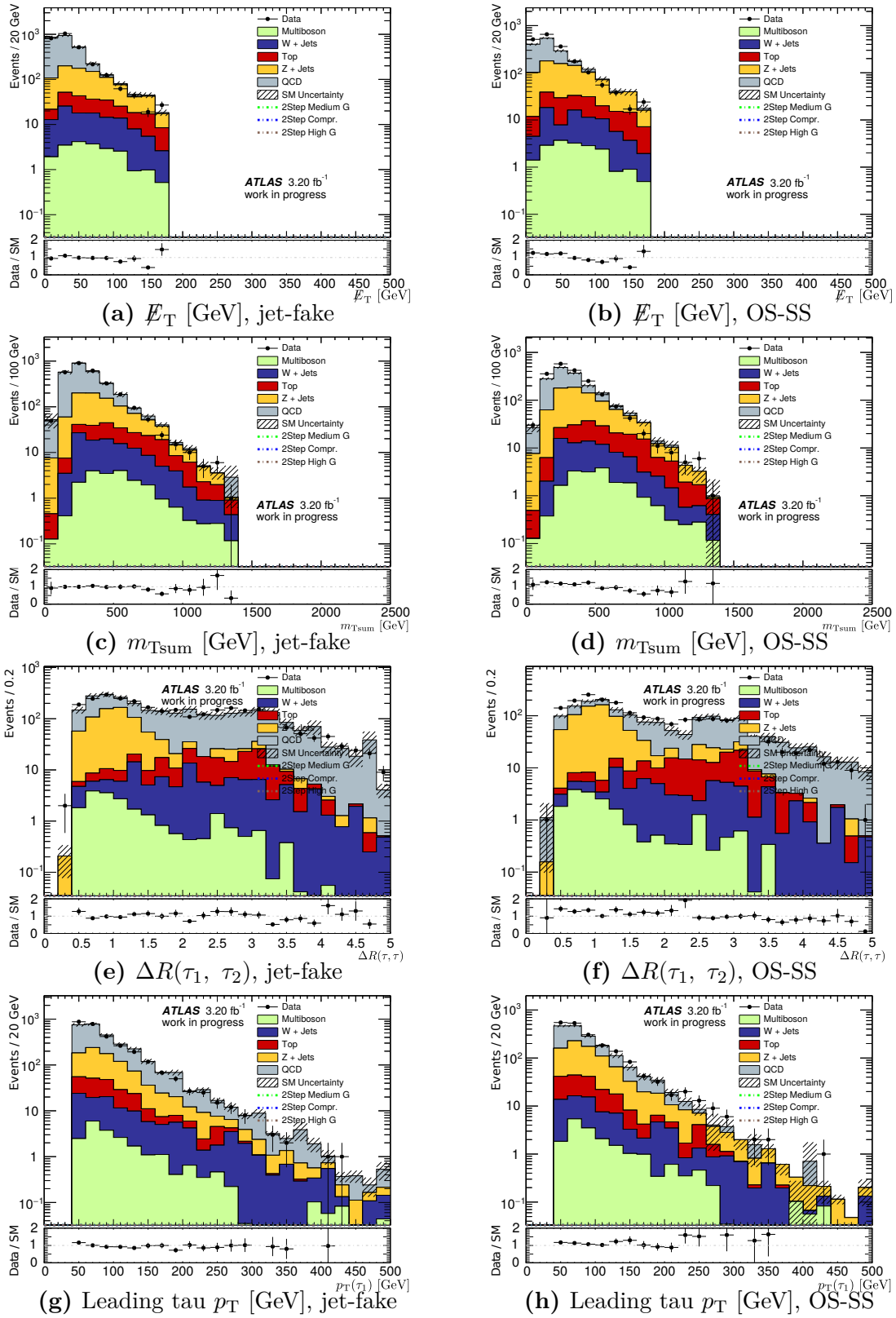

(a) $\not{E}_T$ [GeV], jet-fake **(b)** $\not{E}_T$ [GeV], OS-SS

(c) m_{Tsum} [GeV], jet-fake **(d)** m_{Tsum} [GeV], OS-SS

(e) $\Delta R(\tau_1,\ \tau_2)$, jet-fake **(f)** $\Delta R(\tau_1,\ \tau_2)$, OS-SS

(g) Leading tau p_T [GeV], jet-fake **(h)** Leading tau p_T [GeV], OS-SS

Figure A.16.: Side-by-side comparison of the jet-fake method (left) and the OS-SS method (right) for several different kinematic variables in the QCD-enriched two-tau control region. To be able to focus on the comparison of the performance of both methods, all backgrounds have been stacked and data is also shown. The QCD estimate from the OS-SS estimate has not been normalized from a QCD control region. Depicted uncertainties are only of statistical nature. Complements Figure 9.9 (a-d).

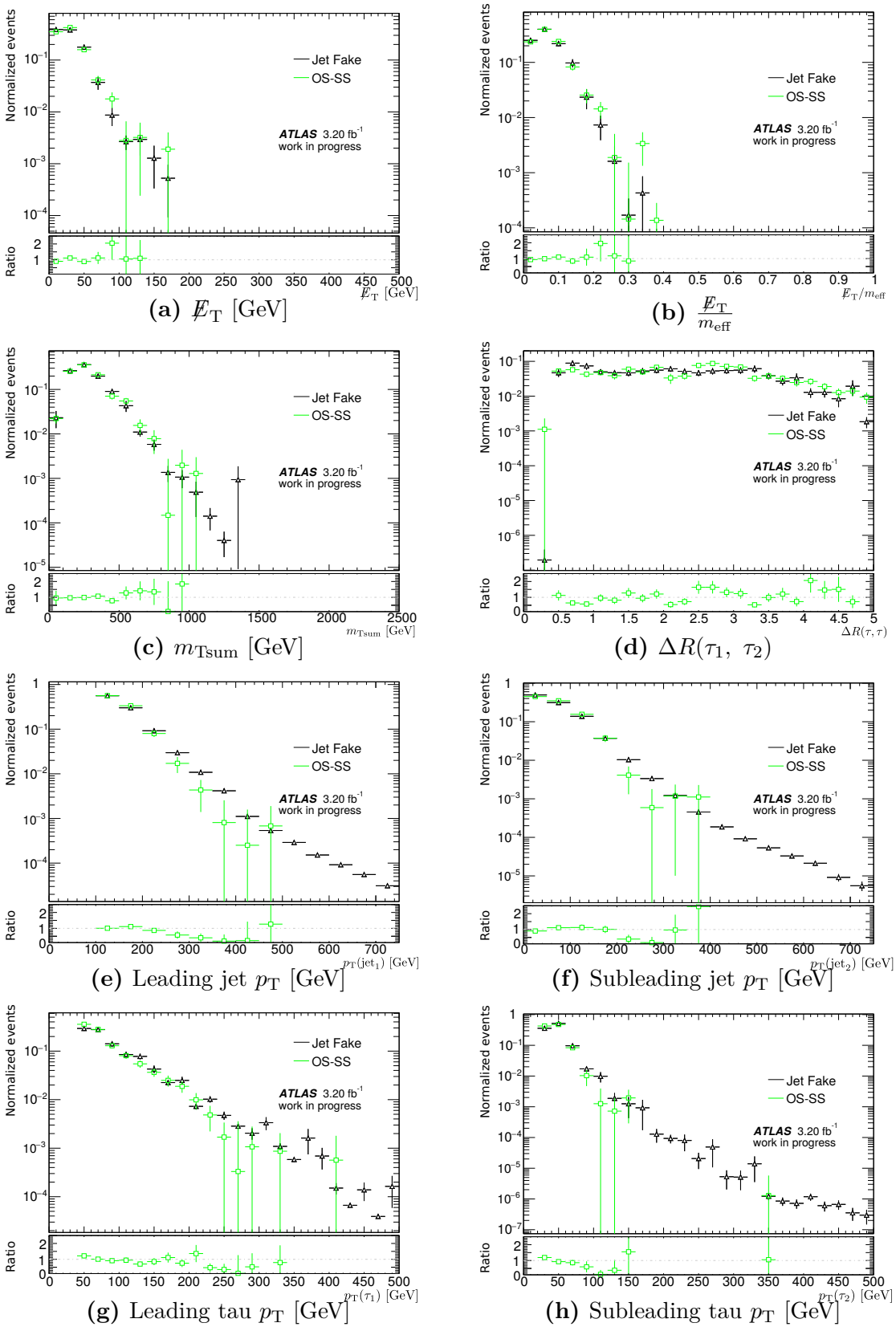

(a) $\not{E}_T$ [GeV] (b) $\frac{\not{E}_T}{m_{eff}}$

(c) m_{Tsum} [GeV] (d) $\Delta R(\tau_1,\ \tau_2)$

(e) Leading jet p_T [GeV] (f) Subleading jet p_T [GeV]

(g) Leading tau p_T [GeV] (h) Subleading tau p_T [GeV]

Figure A.17.: Normalized comparison of the jet-fake method and the OS-SS method of several kinematic variables. This comparison focusses on the modelling of the multi-jet estimates for several different variables. Depicted uncertainties are only of statistical nature. Complements Figure 9.9 (e) and (f).

Bibliography

[1] D. Griffiths, *Introduction to Elementary Particles*. Wiley VCH Verlag GmbH, 2008. [Online]. Available: http://www.ebook.de/de/product/4008107/david_griffiths_introduction_to_elementary_particles.html

[2] S. P. Martin, "A Supersymmetry primer," 1997, [Adv. Ser. Direct. High Energy Phys.18,1(1998)].

[3] W. de Boer, "The Discovery of the Higgs Boson with the CMS Detector and its Implications for Supersymmetry and Cosmology," in *Time and Matter 2013 (TAM2013) Venice, Italy*, 2013. [Online]. Available: https://inspirehep.net/record/1252561/files/arXiv:1309.0721.pdf

[4] LHCb Collaboration Collaboration, "Observation of $j/\psi p$ resonances consistent with pentaquark states in $\Lambda_b^0 \to j/\psi K^- p$ decays," *Phys. Rev. Lett.*, vol. 115, p. 072001, Aug 2015. [Online]. Available: http://link.aps.org/doi/10.1103/PhysRevLett.115.072001

[5] LHCb Collaboration Collaboration, "Observation of the resonant character of the $z(4430)^-$ state," *Phys. Rev. Lett.*, vol. 112, p. 222002, Jun 2014. [Online]. Available: http://link.aps.org/doi/10.1103/PhysRevLett.112.222002

[6] Particle Data Group Collaboration, "Review of Particle Physics," *Chin. Phys.*, vol. C38, p. 090001, 2014.

[7] D. Griffiths, *Introduction to Elementary Particles*. Wiley VCH Verlag GmbH, 2008, ch. 1, p. 54. [Online]. Available: http://www.ebook.de/de/product/4008107/david_griffiths_introduction_to_elementary_particles.html

[8] J. E. Augustin *et al.*, "Discovery of a narrow resonance in e^+e^- annihilation," *Phys. Rev. Lett.*, vol. 33, pp. 1406–1408, Dec 1974. [Online]. Available: http://link.aps.org/doi/10.1103/PhysRevLett.33.1406

[9] J. J. Aubert *et al.*, "Experimental observation of a heavy particle j," *Phys. Rev. Lett.*, vol. 33, pp. 1404–1406, Dec 1974. [Online]. Available: http://link.aps.org/doi/10.1103/PhysRevLett.33.1404

[10] B. Bjørken and S. Glashow, "Elementary particles and SU(4)," *Physics Letters*, vol. 11, no. 3, pp. 255–257, aug 1964. [Online]. Available: http://dx.doi.org/10.1016/0031-9163(64)90433-0

[11] S. L. Glashow, J. Iliopoulos, and L. Maiani, "Weak interactions with lepton-hadron symmetry," *Phys. Rev. D*, vol. 2, pp. 1285–1292, Oct 1970. [Online]. Available: http://link.aps.org/doi/10.1103/PhysRevD.2.1285

[12] M. L. Perl *et al.*, "Evidence for anomalous lepton production in $e^+ - e^-$ annihilation," *Phys. Rev. Lett.*, vol. 35, pp. 1489–1492, Dec 1975. [Online]. Available: http://link.aps.org/doi/10.1103/PhysRevLett.35.1489

[13] S. W. Herb *et al.*, "Observation of a dimuon resonance at 9.5 gev in 400-gev proton-nucleus collisions," *Phys. Rev. Lett.*, vol. 39, pp. 252–255, Aug 1977. [Online]. Available: http://link.aps.org/doi/10.1103/PhysRevLett.39.252

[14] A. Buras, W. Słominski, and H. Steger, "mixing, CP violation and the b-meson decay," *Nuclear Physics B*, vol. 245, pp. 369–398, jan 1984. [Online]. Available: http://dx.doi.org/10.1016/0550-3213(84)90437-1

[15] A. Buras, W. Słominski, and H. Steger, "B-meson decay, CPviolation, mixing angles and the top quark mass," *Nuclear Physics B*, vol. 238, no. 3, pp. 529–560, jun 1984. [Online]. Available: http://dx.doi.org/10.1016/0550-3213(84)90334-1

[16] J. Ellis, G. Fogli, and E. Lisi, "Updated prediction of the top quark mass and implications of its possible confirmation," *Physics Letters B*, vol. 292, no. 3-4, pp. 427–434, oct 1992. [Online]. Available: http://dx.doi.org/10.1016/0370-2693(92)91199-J

[17] J. Ellis and G. Fogli, "The mass of the top quark from electroweak radiative corrections," *Physics Letters B*, vol. 213, no. 4, pp. 526–530, nov 1988. [Online]. Available: http://dx.doi.org/10.1016/0370-2693(88)91304-4

[18] F. Abe *et al.*, "Observation of top quark production in p $^{-}$ p collisions with the collider detector at fermilab," *Phys. Rev. Lett.*, vol. 74, no. 14, pp. 2626–2631, apr 1995. [Online]. Available: http://dx.doi.org/10.1103/PhysRevLett.74.2626

[19] S. Abachi *et al.*, "Observation of the top quark," *Phys. Rev. Lett.*, vol. 74, no. 14, pp. 2632–2637, apr 1995. [Online]. Available: http://dx.doi.org/10.1103/PhysRevLett.74.2632

[20] A. Salam, "Elementary particle theory,(ed) n. svartholm, stockholm, almquist and wiksell, 1968," *S. Weinberg*, vol. 196, p. 367, 1967.

[21] S. Weinberg, "A model of leptons," *Phys. Rev. Lett.*, vol. 19, no. 21, pp. 1264–1266, nov 1967. [Online]. Available: http://dx.doi.org/10.1103/PhysRevLett.19.1264

[22] S. L. Glashow, "Partial-symmetries of weak interactions," *Nuclear Physics*, vol. 22, no. 4, pp. 579–588, feb 1961. [Online]. Available: http://dx.doi.org/10.1016/0029-5582(61)90469-2

[23] G. Arnison *et al.*, "Experimental observation of isolated large transverse energy electrons with associated missing energy at," *Physics Letters B*, vol. 122, no. 1, pp. 103–116, feb 1983. [Online]. Available: http://dx.doi.org/10.1016/0370-2693(83)91177-2

[24] G. Arnison *et al.*, "Experimental observation of lepton pairs of invariant mass around 95 GeV/c2 at the CERN SPS collider," *Physics Letters B*, vol. 126, no. 5, pp. 398–410, jul 1983. [Online]. Available: http://dx.doi.org/10.1016/0370-2693(83)90188-0

[25] TOPAZ Collaboration Collaboration, "Measurement of the electromagnetic coupling at large momentum transfer," *Phys. Rev. Lett.*, vol. 78, pp. 424–427, Jan 1997. [Online]. Available: http://link.aps.org/doi/10.1103/PhysRevLett.78.424

[26] The OPAL Collaboration Collaboration, "Tests of the standard model and constraints on new physics from measurements of fermion-pair production at 189-209 GeV at LEP," *The European Physical Journal C - Particles and Fields*, vol. 33, no. 2, pp. 173–212, mar 2004. [Online]. Available: http://dx.doi.org/10.1140/epjc/s2004-01595-9

[27] SLD Electroweak Group, DELPHI, LEP, ALEPH, SLD Heavy Flavour Group, OPAL, LEP Electroweak Working Group, L3 Collaboration, "A Combination of preliminary electroweak measurements and constraints on the standard model," 2004.

[28] E. Stückelberg and A. Petermann, "Stückelberg 1953," *Helv. Phys. Acta*, vol. 26, p. 499, 1953.

[29] M. Gell-Mann and F. E. Low, "Quantum electrodynamics at small distances," *Phys. Rev.*, vol. 95, pp. 1300–1312, Sep 1954. [Online]. Available: http://link.aps.org/doi/10.1103/PhysRev.95.1300

[30] N. Bogolyubov and D. Shirkov, "Application of the renormalization group to improvement of perturbation theory formulae," in *Dokl. Akad. Nauk SSSR*, vol. 103, 1955, pp. 391–394.

[31] P. Higgs, "Broken symmetries, massless particles and gauge fields," *Physics Letters*, vol. 12, no. 2, pp. 132–133, sep 1964. [Online]. Available: http://dx.doi.org/10.1016/0031-9163(64)91136-9

[32] P. W. Higgs, "Broken symmetries and the masses of gauge bosons," *Phys. Rev. Lett.*, vol. 13, no. 16, pp. 508–509, oct 1964. [Online]. Available: http://dx.doi.org/10.1103/PhysRevLett.13.508

[33] F. Englert and R. Brout, "Broken symmetry and the mass of gauge vector mesons," *Phys. Rev. Lett.*, vol. 13, no. 9, pp. 321–323, aug 1964. [Online]. Available: http://dx.doi.org/10.1103/PhysRevLett.13.321

[34] G. S. Guralnik, C. R. Hagen, and T. W. B. Kibble, "Global conservation laws and massless particles," *Phys. Rev. Lett.*, vol. 13, no. 20, pp. 585–587, nov 1964. [Online]. Available: http://dx.doi.org/10.1103/PhysRevLett.13.585

[35] ALEPH Collaboration DELPHI Collaboration L3 Collaboration OPAL Collaboration and The LEP Working Group for Higgs Boson Searches Collaboration, "Search for the standard model higgs boson at lep," *Physics Letters B*, vol. 565, pp. 61 – 75, 2003. [Online]. Available: http://www.sciencedirect.com/science/article/pii/S0370269303006142

[36] R. C. Lopes de Sa, "Precise measurements of the W mass at the Tevatron and indirect constraints on the Higgs mass," in *Proceedings, 47th Rencontres de Moriond on QCD and High Energy Interactions: La Thuile, France, March 10-17, 2012*, 2012, pp. 3–10. [Online]. Available: http://lss.fnal.gov/cgi-bin/find_paper.pl?conf-12-103

[37] D. P. Fernando B. Moringo, *Feynman Lectures on Gravitation*. WESTVIEW PR, 2002. [Online]. Available: http://www.ebook.de/de/product/4324825/fernando_b_moringo_david_pines_feynman_lectures_on_gravitation.html

[38] H. W. Hamber, *Quantum Gravitation*. Springer Berlin Heidelberg, 2008. [Online]. Available: http://www.ebook.de/de/product/11431381/herbert_w_hamber_quantum_gravitation.html

[39] P. K. Townsend, "Four lectures on m-theory," 2008.

[40] M. J. Duff, "M-theory (the theory formerly known as strings)," *Int.J.Mod.Phys.A*, vol. 11:5623-5642,1996, Int.J.Mod.Phys.A11:5623-5642,1996.

[41] D. Griffiths, *Introduction to Elementary Particles*. Wiley VCH Verlag GmbH, 2008, ch. 12, p. 405 f. [Online]. Available: http://www.ebook.de/de/product/4008107/david_griffiths_introduction_to_elementary_particles.html

[42] N. M. A. 2014. (2016) The 2004 nobel prize in physics - popular information. [Online]. Available: http://www.nobelprize.org/nobel_prizes/physics/laureates/2004/popular.html

[43] F. Zwicky, "Die Rotverschiebung von extragalaktischen Nebeln," *Helv. Phys. Acta*, vol. 6, pp. 110–127, 1933.

[44] H. W. Babcock, "The rotation of the Andromeda Nebula," *Lick Observatory Bulletin*, vol. 19, pp. 41–51, 1939.

[45] V. C. Rubin and W. K. Ford, Jr., "Rotation of the Andromeda Nebula from a Spectroscopic Survey of Emission Regions," *The Astrophysical Journal*, vol. 159, p. 379, Feb. 1970.

[46] V. C. Rubin *et al.*, "Motion of the Galaxy and the local group determined from the velocity anisotropy of distant SC I galaxies. I - The data," *The Astronomic Journal*, vol. 81, pp. 687–718, Sep. 1976.

[47] V. C. Rubin, W. K. J. Ford, and N. . Thonnard, "Rotational properties of 21 SC galaxies with a large range of luminosities and radii, from NGC 4605 /R = 4kpc/ to UGC 2885 /R = 122 kpc/," *The Astrophysical Journal*, vol. 238, pp. 471–487, Jun. 1980.

[48] V. C. Rubin *et al.*, "Rotation velocities of 16 SA galaxies and a comparison of Sa, Sb, and SC rotation properties," *The Astrophysical Journal*, vol. 289, pp. 81–98, Feb. 1985.

[49] E. Corbelli and P. Salucci, "The extended rotation curve and the dark matter halo of m33," *Monthly Notices of the Royal Astronomical Society*, vol. 311, no. 2, pp. 441–447, 2000. [Online]. Available: http://mnras.oxfordjournals.org/content/311/2/441.abstract

[50] NASA. (2016) Chandra photo album - 1e 0657-56. [Online]. Available: http://chandra.harvard.edu/photo/2006/1e0657/index.html

[51] ESA and the Planck Collaboration Collaboration, (2016) Simple but challenging: The universe according to planck. [Online]. Available: http://sci.esa.int/jump.cfm?oid=51551

[52] D. Griffiths, *Introduction to Elementary Particles*. Wiley VCH Verlag GmbH, 2008, ch. 11.2, p. 390 f. [Online]. Available: http://www.ebook.de/de/product/4008107/david_griffiths_introduction_to_elementary_particles.html

[53] S. Alekhin, A. Djouadi, and S. Moch, "The top quark and higgs boson masses and the stability of the electroweak vacuum," *Physics Letters B*, vol. 716, no. 1, pp. 214–219, sep 2012. [Online]. Available: http://dx.doi.org/10.1016/j.physletb.2012.08.024

[54] F. Iachello, "Dynamical supersymmetries in nuclei," *Phys. Rev. Lett.*, vol. 44, pp. 772–775, Mar 1980. [Online]. Available: http://link.aps.org/doi/10.1103/PhysRevLett.44.772

[55] R. Bijker, "Supersymmetry in nuclear physics," *Journal of Physics: Conference Series*, vol. 237, no. 1, p. 012005, 2010. [Online]. Available: http://stacks.iop.org/1742-6596/237/i=1/a=012005

[56] H. Baer, V. Barger, and A. Mustafayev, "Neutralino dark matter in msugra/cmssm with a 125 gev light higgs scalar," vol. 2012, no. 5, pp. 1–24, 2012. [Online]. Available: http://dx.doi.org/10.1007/JHEP05(2012)091

[57] S. Akula, P. Nath, and G. Peim, "Implications of the higgs boson discovery for msugra," *Physics Letters B*, vol. 717, no. 1–3, pp. 188 – 192, 2012. [Online]. Available: http://www.sciencedirect.com/science/article/pii/S0370269312009410

[58] H. Baer *et al.*, "Post-lhc7 fine-tuning in the minimal supergravity/cmssm model with a 125 gev higgs boson," *Phys. Rev. D*, vol. 87, p. 035017, Feb 2013. [Online]. Available: http://link.aps.org/doi/10.1103/PhysRevD.87.035017

[59] A. Samanta, S. K. Mandal, and H. Manna, "Is mSUGRA under tension for testing at colliders?" 2014.

[60] B. C. Allanach, "SOFTSUSY: a program for calculating supersymmetric spectra," *Comput. Phys. Commun.*, vol. 143, pp. 305–331, 2002.

[61] S. Ambrosanio *et al.*, "Aspects of GMSB phenomenology at TeV colliders," in *1st Les Houches Workshop on Physics at TeV Colliders (PhysTeV 1999) Les Houches, France, June 7-18, 1999*, 2000. [Online]. Available: http://weblib.cern.ch/abstract?CERN-TH-2000-054

[62] J. Alwall, P. C. Schuster, and N. Toro, "Simplified models for a first characterization of new physics at the lhc," *Phys. Rev. D*, vol. 79, p. 075020, Apr 2009. [Online]. Available: http://link.aps.org/doi/10.1103/PhysRevD.79.075020

[63] D. Alves *et al.*, "Simplified models for lhc new physics searches," *Journal of Physics G: Nuclear and Particle Physics*, vol. 39, no. 10, p. 105005, 2012. [Online]. Available: http://stacks.iop.org/0954-3899/39/i=10/a=105005

[64] G. Cowan and E. Gross, "Discovery significance with statistical uncertainty in the background estimate," 2008. [Online]. Available: http://www.pp.rhul.ac.uk/~cowan/stat/notes/SigCalcNote.pdf

[65] G. Cowan *et al.*, "Asymptotic formulae for likelihood-based tests of new physics," *The European Physical Journal C*, vol. 71, no. 2, pp. 1–19, 2011. [Online]. Available: http://dx.doi.org/10.1140/epjc/s10052-011-1554-0

[66] CERN. (2016) Root reference guide v.6.07/1 - roostats::numbercountingutils. [Online]. Available: https://root.cern.ch/doc/v606/namespaceRooStats_1_1NumberCountingUtils.html

[67] CERN. (2016) About cern. [Online]. Available: http://home.cern/about

[68] C. Lefèvre, "The CERN accelerator complex. Complexe des accélérateurs du CERN," Dec 2008. [Online]. Available: https://cds.cern.ch/record/1260465

[69] LHC Study Group Collaboration, "The Large Hadron Collider: conceptual design," Tech. Rep. CERN-AC-95-05-LHC, Oct 1995. [Online]. Available: https://cds.cern.ch/record/291782

[70] CERN. (2016) The accelerator complex. [Online]. Available: https://home.cern.ch/about/accelerators

[71] C. Lefevre, "LHC: the guide," Jan 2008. [Online]. Available: https://cds.cern.ch/record/1092437

[72] ATLAS Collaboration Collaboration, "The atlas experiment at the cern large hadron collider," *Journal of Instrumentation*, vol. 3, no. 08, p. S08003, 2008. [Online]. Available: http://stacks.iop.org/1748-0221/3/i=08/a=S08003

[73] ATLAS Collaboration Collaboration, *ATLAS detector and physics performance: Technical Design Report, 1*, ser. Technical Design Report ATLAS. Geneva: CERN, 1999. [Online]. Available: https://cds.cern.ch/record/391176

[74] G. Aad *et al.*, "Studies of the performance of the atlas detector using cosmic-ray muons," *The European Physical Journal C*, vol. 71, no. 3, pp. 1–36, 2011. [Online]. Available: http://dx.doi.org/10.1140/epjc/s10052-011-1593-6

[75] ATLAS Collaboration Collaboration, *ATLAS inner detector: Technical Design Report, 1*, ser. Technical Design Report ATLAS. Geneva: CERN, 1997. [Online]. Available: https://cds.cern.ch/record/331063

[76] J. Pequenao, "Computer generated image of the ATLAS inner detector," Mar 2008. [Online]. Available: https://cds.cern.ch/record/1095926

[77] M. Capeans *et al.*, "ATLAS Insertable B-Layer Technical Design Report," Tech. Rep. CERN-LHCC-2010-013. ATLAS-TDR-19, Sep 2010. [Online]. Available: https://cds.cern.ch/record/1291633

[78] ATLAS Collaboration Collaboration, *ATLAS liquid-argon calorimeter: Technical Design Report*, ser. Technical Design Report ATLAS. Geneva: CERN, 1996. [Online]. Available: https://cds.cern.ch/record/331061

[79] ATLAS Collaboration Collaboration, *ATLAS tile calorimeter: Technical Design Report*, ser. Technical Design Report ATLAS. Geneva: CERN, 1996. [Online]. Available: https://cds.cern.ch/record/331062

[80] J. Pequenao, "Computer Generated image of the ATLAS calorimeter," Mar 2008. [Online]. Available: https://cds.cern.ch/record/1095927

[81] J. Pequenao, "Computer generated image of the ATLAS Muons subsystem," Mar 2008. [Online]. Available: https://cds.cern.ch/record/1095929

[82] Y. Nakahama, "The ATLAS Trigger System: Ready for Run-2: Talk draft in CHEP2015," CERN, Geneva, Tech. Rep. ATL-COM-DAQ-2015-021, Mar 2015, for CHEP2015, staring on 13/04/2015. [Online]. Available: https://indico.cern.ch/event/382472/contributions/1809089/attachments/762480/1046036/CHEP2015.pdf

[83] ATLAS Collaboration Collaboration, "2015 start-up trigger menu and initial performance assessment of the ATLAS trigger using Run-2 data," CERN, Geneva, Tech. Rep. ATL-DAQ-PUB-2016-001, Mar 2016. [Online]. Available: https://cds.cern.ch/record/2136007

[84] ATLAS Collaboration Collaboration, (2016) Atlas trigger operation public results. [Online]. Available: https://twiki.cern.ch/twiki/bin/view/AtlasPublic/TriggerOperationPublicResults

[85] Y. Nakahama, "The atlas trigger system: Ready for run-2," *Journal of Physics: Conference Series*, vol. 664, no. 8, p. 082037, 2015. [Online]. Available: http://stacks.iop.org/1742-6596/664/i=8/a=082037

[86] W. P. Office. (2016) Welcome to the worldwide lhc computing grid. [Online]. Available: http://wlcg.web.cern.ch/

[87] CERN. (2016) The worldwide lhc computing grid. [Online]. Available: https://home.cern/about/computing/worldwide-lhc-computing-grid

[88] DESY. (2016) Lhc computing grid. [Online]. Available: http://www.weltmaschine.de/experimente/lhc_computing_grid/

[89] I. Bird. (2016) Lhc computing, cern, & federated identities. [Online]. Available: http://indico.cern.ch/event/358127/contributions/848185/attachments/713125/979037/WLCG-FIM4R-030215.pdf

[90] T. Sjostrand, "Monte Carlo Generators," in *High-energy physics. Proceedings, European School, Aronsborg, Sweden, June 18-July 1, 2006*, 2006, pp. 51–74. [Online]. Available: http://weblib.cern.ch/abstract?CERN-LCGAPP-2006-06

[91] W. Lukas, "Fast simulation for atlas: Atlfast-ii and isf," *Journal of Physics: Conference Series*, vol. 396, no. 2, p. 022031, 2012. [Online]. Available: http://stacks.iop.org/1742-6596/396/i=2/a=022031

[92] ATLAS Collaboration Collaboration, "Measurement of hard double-parton interactions in $w(\rightarrow l\nu) + 2 - \text{jet}$ events at $\sqrt{s} = 7$ tev with the atlas detector," vol. 15, no. 3, p. 033038, 2013. [Online]. Available: http://stacks.iop.org/1367-2630/15/i=3/a=033038

[93] ATLAS Collaboration, "Study of hard double-parton scattering in four-jet events in pp collisions at $\sqrt{s} = 7$ TeV with the ATLAS experiment," 2016.

[94] GEANT4 Collaboration, "GEANT4: A simulation toolkit," *Nucl. Instrum. Meth.*, vol. A 506, p. 250, 2003.

[95] ATLAS Collaboration, "The simulation principle and performance of the ATLAS fast calorimeter simulation FastCaloSim," ATL-PHYS-PUB-2010-013, 2010. [Online]. Available: http://cds.cern.ch/record/1300517

[96] ATLAS Collaboration, "Performance of the Fast ATLAS Tracking Simulation (FATRAS) and the ATLAS Fast Calorimeter Simulation (FastCaloSim) with single particles," ATL-SOFT-PUB-2014-01, 2014. [Online]. Available: http://cdsweb.cern.ch/record/1669341

[97] ATLAS Collaboration, "Vertex Reconstruction Performance of the ATLAS Detector at $\sqrt{s} = 13$ TeV," ATL-PHYS-PUB-2015-026, 2015. [Online]. Available: http://cdsweb.cern.ch/record/2037717

[98] ATLAS Collaboration Collaboration, "Electron efficiency measurements with the ATLAS detector using the 2012 LHC proton-proton collision data," CERN, Geneva, Tech. Rep. ATLAS-CONF-2014-032, Jun 2014. [Online]. Available: https://cds.cern.ch/record/1706245

[99] ATLAS Collaboration Collaboration, "Electron identification measurements in ATLAS using $\sqrt{s} = 13$ TeV data with 50 ns bunch spacing," CERN, Geneva, Tech. Rep. ATL-PHYS-PUB-2015-041, Sep 2015. [Online]. Available: https://cds.cern.ch/record/2048202

[100] ATLAS Collaboration Collaboration, "Electron efficiency measurements with the ATLAS detector using the 2015 LHC proton-proton collision data," CERN, Geneva, Tech. Rep. ATLAS-CONF-2016-024, Jun 2016. [Online]. Available: https://cds.cern.ch/record/2157687

[101] G. Aad *et al.*, "Measurement of the muon reconstruction performance of the ATLAS detector using 2011 and 2012 LHC proton–proton collision data," *Eur. Phys. J. C*, vol. 74, no. 11, nov 2014. [Online]. Available: http://dx.doi.org/10.1140/epjc/s10052-014-3130-x

[102] R. Nicolaidou *et al.*, "Muon identification procedure for the ATLAS detector at the LHC using muonboy reconstruction package and tests of its performance using cosmic rays and single beam data," *J. Phys.: Conf. Ser.*, vol. 219, no. 3, p. 032052, apr 2010. [Online]. Available: http://dx.doi.org/10.1088/1742-6596/219/3/032052

[103] ATLAS Collaboration Collaboration, "Muon reconstruction performance in early $\sqrt{s}$ =13 TeV data," CERN, Geneva, Tech. Rep. ATL-PHYS-PUB-2015-037, Aug 2015. [Online]. Available: http://cds.cern.ch/record/2047831

[104] S. Hassani *et al.*, "A muon identification and combined reconstruction procedure for the ATLAS detector at the LHC using the (MUONBOY, STACO, MuTag) reconstruction packages," *Nuclear Instruments and Methods in Physics Research Section A: Accelerators, Spectrometers, Detectors and Associated Equipment*, vol. 572, no. 1, pp. 77–79, mar 2007. [Online]. Available: http://dx.doi.org/10.1016/j.nima.2006.10.340

[105] B. Resende, "Muon identification algorithms in ATLAS," CERN, Geneva, Tech. Rep. ATL-PHYS-PROC-2009-113, Sep 2009. [Online]. Available: https://cds.cern.ch/record/1209632

[106] ATLAS Collaboration, "Identification and energy calibration of hadronically decaying tau leptons with the ATLAS experiment in *pp* collisions at $\sqrt{s} = 8$ TeV," *Eur. Phys. J. C*, vol. 75, p. 303, 2015.

[107] ATLAS Collaboration Collaboration, "Reconstruction, Energy Calibration, and Identification of Hadronically Decaying Tau Leptons in the ATLAS Experiment for Run-2 of the LHC," CERN, Geneva, Tech. Rep. ATL-PHYS-PUB-2015-045, Nov 2015. [Online]. Available: https://cds.cern.ch/record/2064383

[108] M. Cacciari, G. P. Salam, and G. Soyez, "The anti-k_t jet clustering algorithm," *JHEP*, vol. 0804, p. 063, 2008.

[109] ATLAS Collaboration, "Jet energy measurement with the ATLAS detector in proton–proton collisions at $\sqrt{s} = 7$ TeV," *Eur. Phys. J. C*, vol. 73, p. 2304, 2013.

[110] ATLAS Collaboration, "Jet energy resolution in proton–proton collisions at $\sqrt{s} =$ 7 TeV recorded in 2010 with the ATLAS detector," *Eur. Phys. J. C*, vol. 73, p. 2306, 2013.

[111] ATLAS Collaboration, "Pile-up subtraction and suppression for jets in ATLAS," ATLAS-CONF-2013-083, 2013. [Online]. Available: http://cdsweb.cern.ch/record/1570994

[112] ATLAS Collaboration, "Tagging and suppression of pileup jets with the ATLAS detector," ATLAS-CONF-2014-018, 2014. [Online]. Available: http://cdsweb.cern.ch/record/1700870

[113] ATLAS Collaboration, "Calibration of *b*-tagging using dileptonic top pair events in a combinatorial likelihood approach with the ATLAS experiment," ATLAS-CONF-2014-004, 2014. [Online]. Available: http://cdsweb.cern.ch/record/1664335

[114] ATLAS Collaboration, "Calibration of the performance of *b*-tagging for *c* and light-flavour jets in the 2012 ATLAS data," ATLAS-CONF-2014-046, 2014. [Online]. Available: http://cdsweb.cern.ch/record/1741020

[115] ATLAS Collaboration, "Commissioning of the ATLAS high performance *b*-tagging algorithms in the 7 TeV collision data," ATLAS-CONF-2011-102, 2011. [Online]. Available: http://cdsweb.cern.ch/record/1369219

[116] ATLAS Collaboration, "Expected performance of the ATLAS *b*-tagging algorithms in Run-2," ATL-PHYS-PUB-2015-022, 2015. [Online]. Available: http://cdsweb.cern.ch/record/2037697

[117] C. Lester and D. Summers, "Measuring masses of semi-invisibly decaying particle pairs produced at hadron colliders," *Physics Letters B*, vol. 463, no. 1, pp. 99–103, sep 1999. [Online]. Available: http://dx.doi.org/10.1016/S0370-2693(99)00945-4

[118] C. G. Lester and A. J. Barr, "m t gen : mass scale measurements in pair-production at colliders," *Journal of High Energy Physics*, vol. 2007, no. 12, pp. 102–102, dec 2007. [Online]. Available: http://dx.doi.org/10.1088/1126-6708/2007/12/102

[119] ATLAS Collaboration, "Search for the direct production of charginos, neutralinos and staus in final states with at least two hadronically decaying taus and missing transverse momentum in pp collisions at $\sqrt{s} = 8$ TeV with the ATLAS detector," *JHEP*, vol. 1410, p. 096, 2014.

[120] A. Djouadi, J.-L. Kneur, and G. Moultaka, "SuSpect: A fortran code for the supersymmetric and higgs particle spectrum in the MSSM," *Computer Physics Communications*, vol. 176, no. 6, pp. 426–455, mar 2007. [Online]. Available: http://dx.doi.org/10.1016/j.cpc.2006.11.009

[121] C. F. Berger *et al.*, "Supersymmetry without prejudice," *Journal of High Energy Physics*, vol. 2009, no. 02, pp. 023–023, feb 2009. [Online]. Available: http://dx.doi.org/10.1088/1126-6708/2009/02/023

[122] S. S. AbdusSalam *et al.*, "Fitting the phenomenological MSSM," *Physical Review D*, vol. 81, no. 9, may 2010. [Online]. Available: http://dx.doi.org/10.1103/PhysRevD.81.095012

[123] ATLAS Collaboration, "Performance of the ATLAS tau trigger in 2011," ATLAS-CONF-2013-006, 2013. [Online]. Available: http://cdsweb.cern.ch/record/1510157

[124] ATLAS Collaboration, "Search for direct production of charginos, neutralinos and sleptons in final states with two leptons and missing transverse momentum in pp collisions at $\sqrt{s} = 8$ TeV with the ATLAS detector," *JHEP*, vol. 1405, p. 071, 2014.

[125] ATLAS Collaboration, "Search for direct production of charginos and neutralinos in events with three leptons and missing transverse momentum in $\sqrt{s} = 8$ TeV pp collisions with the ATLAS detector," *JHEP*, vol. 1404, p. 169, 2014.

[126] ATLAS Collaboration Collaboration, "Identification of the Hadronic Decays of Tau Leptons in 2012 Data with the ATLAS Detector," CERN, Geneva, Tech. Rep. ATLAS-CONF-2013-064, Jul 2013. [Online]. Available: https://cds.cern.ch/record/1562839

[127] D. R. Tovey, "On measuring the masses of pair-produced semi-invisibly decaying particles at hadron colliders," *Journal of High Energy Physics*, vol. 2008, no. 04, pp. 034–034, apr 2008. [Online]. Available: http://dx.doi.org/10.1088/1126-6708/2008/04/034

[128] G. Polesello and D. R. Tovey, "Supersymmetric particle mass measurement with the boost-corrected contransverse mass," *Journal of High Energy Physics*, vol. 2010, no. 3, mar 2010. [Online]. Available: http://dx.doi.org/10.1007/JHEP03(2010)030

[129] LEP SUSY Working Group (ALEPH, DELPHI, L3, OPAL), Notes LEPSUSYWG/01-03.1, 04-01.1, http://lepsusy.web.cern.ch/lepsusy/Welcome.html.

[130] A. Mann, private communication and ATLAS internal note, 2013.

[131] A. Buckley *et al.*, "LHAPDF6: parton density access in the LHC precision era," *Eur. Phys. J. C*, vol. 75, no. 3, mar 2015. [Online]. Available: http://dx.doi.org/10.1140/epjc/s10052-015-3318-8

[132] A. Hoecker, private communication, 2016.

[133] ATLAS Collaboration Collaboration, (2016) Atlas public results - supersymmetry searches. [Online]. Available: https://twiki.cern.ch/twiki/bin/view/AtlasPublic/SupersymmetryPublicResults

[134] G. Aad *et al.*, "Summary of the atlas experiment's sensitivity to supersymmetry after lhc run 1 — interpreted in the phenomenological mssm," *Journal of High Energy Physics*, vol. 2015, no. 10, pp. 1–76, 2015. [Online]. Available: http://dx.doi.org/10.1007/JHEP10(2015)134

[135] ATLAS Collaboration, "Search for squarks and gluinos in events with hadronically decaying tau leptons, jets and missing transverse momentum in proton-proton collisions at $\sqrt{s} = 13$ TeV recorded with the ATLAS detector," 2016.

[136] ATLAS Collaboration, "Search for Supersymmetry in Events with Large Missing Transverse Momentum, Jets, and at Least One Tau Lepton in 7 TeV Proton–Proton Collision Data with the ATLAS Detector," *Eur. Phys. J. C*, vol. 72, p. 2215, 2012.

[137] ATLAS Collaboration, "Search for supersymmetry in events with large missing transverse momentum, jets, and at least one tau lepton in 20 fb^{-1} of $\sqrt{s} = 8$ TeV proton–proton collision data with the ATLAS detector," *JHEP*, vol. 1409, p. 103, 2014.

[138] D. A. Vásquez, G. Bélanger, and C. Bœhm, "Revisiting light neutralino scenarios in the MSSM," *Physical Review D*, vol. 84, no. 9, nov 2011. [Online]. Available: http://dx.doi.org/10.1103/PhysRevD.84.095015

[139] ATLAS Collaboration, "Summary of the searches for squarks and gluinos using $\sqrt{s} = 8$ TeV pp collisions with the ATLAS experiment at the LHC," *JHEP*, vol. 1510, p. 054, 2015.

[140] S. Schaepe, private communication and ATLAS internal note, 2016.

[141] M. Baak *et al.*, "HistFitter software framework for statistical data analysis," *Eur. Phys. J. C*, vol. 75, no. 4, apr 2015. [Online]. Available: http://dx.doi.org/10.1140/epjc/s10052-015-3327-7

[142] ATLAS Collaboration, "The ATLAS Simulation Infrastructure," *Eur. Phys. J. C*, vol. 70, p. 823, 2010.

[143] GEANT4 Collaboration, "GEANT4: A simulation toolkit," *Nucl. Instrum. Meth. A*, vol. 506, p. 250, 2003.

[144] T. Gleisberg *et al.*, "Event generation with sherpa 1.1," *JHEP*, vol. 0902, p. 007, 2009.

[145] T. Binoth *et al.*, "Gluon-induced W-boson pair production at the LHC," *JHEP*, vol. 0612, p. 046, 2006.

[146] J. Alwall *et al.*, "MadGraph 5 : Going Beyond," *JHEP*, vol. 1106, p. 128, 2011.

[147] T. Sjostrand, S. Mrenna, and P. Z. Skands, "PYTHIA 6.4 Physics and Manual," *JHEP*, vol. 0605, p. 026, 2006.

[148] T. Sjostrand, S. Mrenna, and P. Skands, "Brief Introduction to PYTHIA 8.1," *Comput. Phys. Comm.*, vol. 178, p. 852, 2008.

[149] S. Frixione and B. R. Webber, "Matching NLO QCD computations and parton shower simulations," *JHEP*, vol. 0206, p. 029, 2002.

[150] S. Frixione, P. Nason, and B. R. Webber, "Matching NLO QCD and parton showers in heavy flavour production," *JHEP*, vol. 0308, p. 007, 2003.

[151] S. Frixione *et al.*, "Single-top production in MC@NLO," *JHEP*, vol. 0603, p. 092, 2006.

[152] B. P. Kersevan and E. Richter-Was, "The Monte Carlo event generator AcerMC versions 2.0 to 3.8 with interfaces to PYTHIA 6.4, HERWIG 6.5 and ARIADNE 4.1," *Comp. Phys. Commun.*, vol. 184, p. 919, 2013.

[153] M. L. Mangano *et al.*, "Alpgen, a generator for hard multiparton processes in hadronic collisions," *JHEP*, vol. 0307, p. 001, 2003.

[154] S. Frixione, P. Nason, and C. Oleari, "Matching NLO QCD computations with Parton Shower simulations: the POWHEG method," *JHEP*, vol. 0711, p. 070, 2007.

[155] ATLAS Collaboration, "ATLAS tunes of PYTHIA 6 and Pythia 8 for MC11," 2011.

[156] P. Z. Skands, "Tuning Monte Carlo Generators: The Perugia Tunes," *Phys. Rev. D*, vol. 82, p. 074018, 2010.

[157] H.-L. Lai *et al.*, "New parton distributions for collider physics," *Phys. Rev.*, vol. D 82, p. 074024, 2010.

[158] J. Pumplin *et al.*, "New generation of parton distributions with uncertainties from global QCD analysis," *JHEP*, vol. 0207, p. 012, 2002.

[159] S. Catani *et al.*, "Vector boson production at hadron colliders: a fully exclusive QCD calculation at NNLO," *Phys. Rev. Lett.*, vol. 103, p. 082001, 2009.

[160] A. Martin, W. Stirling, R. Thorne and G. Watt, "Update of parton distributions at NNLO," *Phys. Lett.*, vol. B 652, p. 292, 2007.

[161] M. Czakon and A. Mitov, "Top++: A Program for the Calculation of the Top-Pair Cross-Section at Hadron Colliders," *Comput. Phys. Commun.*, vol. 185, p. 2930, 2014.

[162] J. M. Campbell and R. K. Ellis, "An Update on vector boson pair production at hadron colliders," *Phys. Rev.*, vol. D 60, p. 113006, 1999.

[163] J. M. Campbell, R. K. Ellis, and C. Williams, "Vector boson pair production at the LHC," *JHEP*, vol. 1107, p. 018, 2011.

[164] J. M. Campbell and R. K. Ellis, "$t\bar{t}W^{\pm}$ production and decay at NLO," *JHEP*, vol. 1207, p. 052, 2012.

[165] M. Garzelli *et al.*, "$t\bar{t}$ $W^{\pm}$ and $t\bar{t}$ Z hadroproduction at NLO accuracy in QCD with parton shower and hadronization effects," *JHEP*, vol. 1211, p. 056, 2012.

[166] M. Bahr *et al.*, "Herwig++ Physics and Manual," *Eur. Phys. J. C*, vol. 58, p. 639, 2008.

[167] W. Beenakker *et al.*, "The Production of charginos/neutralinos and sleptons at hadron colliders," *Phys. Rev. Lett.*, vol. 83, pp. 3780–3783, 1999.

[168] B. Fuks *et al.*, "Gaugino production in proton-proton collisions at a center-of-mass energy of 8 TeV," *JHEP*, vol. 1210, p. 081, 2012.

[169] B. Fuks *et al.*, "Precision predictions for electroweak superpartner production at hadron colliders with Resummino," *Eur. Phys. J. C*, vol. 73, p. 2480, 2013.

[170] B. Fuks *et al.*, "Revisiting slepton pair production at the Large Hadron Collider," *JHEP*, vol. 1401, p. 168, 2014.

[171] T. Sjöstrand, S. Ask, J. R. Christiansen, R. Corke, N. Desai, P. Ilten, S. Mrenna, S. Prestel, C. O. Rasmussen, and P. Z. Skands, "An Introduction to PYTHIA 8.2," *Comput. Phys. Commun.*, vol. 191, p. 159, 2015.

[172] ATLAS Collaboration, "Summary of ATLAS Pythia 8 tunes," ATL-PHYS-PUB-2012-003, 2012. [Online]. Available: http://cds.cern.ch/record/1474107

[173] A. D. Martin, W. J. Stirling, R. S. Thorne, and G. Watt, "Parton distributions for the LHC," *Eur. Phys. J. C*, vol. 63, p. 189, 2009.

[174] T. Gleisberg *et al.*, "Event generation with SHERPA 1.1," *JHEP*, vol. 0902, p. 007, 2009.

[175] F. Cascioli, P. Maierhofer, and S. Pozzorini, "Scattering Amplitudes with Open Loops," *Phys. Rev. Lett.*, vol. 108, p. 111601, 2012.

[176] T. Gleisberg and S. Höche, "Comix, a new matrix element generator," *JHEP*, vol. 0812, p. 039, 2008.

[177] Z. Czyczula, T. Przedzinski, and Z. Was, "TauSpinner Program for Studies on Spin Effect in tau Production at the LHC," *Eur. Phys. J. C*, vol. 72, p. 1988, 2012.

[178] S. Schumann and F. Krauss, "A Parton shower algorithm based on Catani-Seymour dipole factorisation," *JHEP*, vol. 0803, p. 038, 2008.

[179] S. Höche *et al.*, "QCD matrix elements + parton showers: The NLO case," *JHEP*, vol. 1304, p. 027, 2013.

[180] H.-L. Lai *et al.*, "New parton distributions for collider physics," *Phys. Rev. D*, vol. 82, p. 074024, 2010.

[181] C. Anastasiou *et al.*, "High precision QCD at hadron colliders: Electroweak gauge boson rapidity distributions at NNLO," *Phys. Rev. D*, vol. 69, p. 094008, 2004.

[182] S. Alioli *et al.*, "A general framework for implementing NLO calculations in shower Monte Carlo programs: the POWHEG BOX," *JHEP*, vol. 1006, p. 043, 2010.

[183] P. Artoisenet *et al.*, "Automatic spin-entangled decays of heavy resonances in Monte Carlo simulations," *JHEP*, vol. 1303, p. 015, 2013.

[184] T. Sjöstrand, S. Mrenna, and P. Z. Skands, "PYTHIA 6.4 Physics and Manual," *JHEP*, vol. 0605, p. 026, 2006.

[185] J. Pumplin *et al.*, "New generation of parton distributions with uncertainties from global QCD analysis," *JHEP*, vol. 0207, p. 012, 2002.

[186] J. Alwall *et al.*, "The automated computation of tree-level and next-to-leading order differential cross sections, and their matching to parton shower simulations," *JHEP*, vol. 1407, p. 079, 2014.

[187] ATLAS Collaboration, "ATLAS Pythia 8 tunes to 7 TeV data," ATL-PHYS-PUB-2014-021, 2014. [Online]. Available: http://cdsweb.cern.ch/record/1966419

[188] NNPDF Collaboration, "Parton distributions with QED corrections," *Nucl. Phys. B*, vol. 877, p. 290, 2013.

[189] L. Lonnblad, "Correcting the color dipole cascade model with fixed order matrix elements," *JHEP*, vol. 0205, p. 046, 2002.

[190] S. Gieseke, C. Rohr, and A. Siodmok, "Colour reconnections in Herwig++," *Eur. Phys. J. C*, vol. 72, p. 2225, 2012.

[191] W. Porod and F. Staub, "SPheno 3.1: Extensions including flavour, CP-phases and models beyond the MSSM," *Comput. Phys. Commun.*, vol. 183, p. 2458, 2012.

[192] G. Marchesini and B. R. Webber, "Simulation of QCD Jets Including Soft Gluon Interference," *Nucl. Phys. B*, vol. 238, p. 1, 1984.

[193] G. Marchesini and B. R. Webber, "Monte Carlo Simulation of General Hard Processes with Coherent QCD Radiation," *Nucl. Phys. B*, vol. 310, p. 461, 1988.

[194] S. Gieseke, P. Stephens, and B. Webber, "New formalism for QCD parton showers," *JHEP*, vol. 0312, p. 045, 2003.

[195] W. Beenakker *et al.*, "Squark and gluino production at hadron colliders," *Nucl. Phys. B*, vol. 492, p. 51, 1997.

[196] A. Kulesza and L. Motyka, "Threshold resummation for squark-antisquark and gluino-pair production at the LHC," *Phys. Rev. Lett.*, vol. 102, p. 111802, 2009.

[197] A. Kulesza and L. Motyka, "Soft gluon resummation for the production of gluino-gluino and squark-antisquark pairs at the LHC," *Phys. Rev. D*, vol. 80, p. 095004, 2009.

[198] W. Beenakker *et al.*, "Soft-gluon resummation for squark and gluino hadroproduction," *JHEP*, vol. 0912, p. 041, 2009.

[199] W. Beenakker *et al.*, "Squark and gluino hadroproduction," *Int. J. Mod. Phys.*, vol. A26, p. 2637, 2011.

[200] M. Kramer *et al.*, "Supersymmetry production cross sections in pp collisions at $\sqrt{s} = 7$ TeV," 2012.

[201] A. Barr, C. Lester, and P. Stephens, "m_{T2} : The Truth behind the glamour," *J. Phys.*, vol. G 29, p. 2343, 2003.

[202] A. J. Barr, B. Gripaios, and C. G. Lester, "Transverse masses and kinematic constraints: from the boundary to the crease," *JHEP*, vol. 0911, p. 096, 2009.

[203] P. Konar *et al.*, "Dark Matter Particle Spectroscopy at the LHC: Generalizing m_{T2} to Asymmetric Event Topologies," *JHEP*, vol. 1004, p. 086, 2010.

[204] ATLAS Collaboration, "Search for direct top squark pair production in final states with one isolated lepton, jets, and missing transverse momentum in $\sqrt{s} = 8$ TeV pp collisions using 13 fb^{-1} ATLAS data," ATLAS-CONF-2012-166, 2012. [Online]. Available: http://cdsweb.cern.ch/record/1497732

[205] A. Kastanas, private communication and ATLAS internal note, 2016.

[206] O. S., private communication and ATLAS internal note.

[207] M. Tripiana, private communication, 2016.

Danksagung

An dieser Stelle möchte ich mich bei allen bedanken die meine Promotion möglich gemacht und mich während meiner Promotion, sowie während der Anfertigung dieser Arbeit unterstützt haben. Vielen herzlichen Dank an:

- Prof. Dr. Dorothee Schaile dafür, dass sie mich an Ihrem Lehrstuhl aufgenommen hat, für die durchgängige und gute Betreuung, für die Möglichkeiten auch in der Lehre mitzuwirken, sowie für die tollen Erfahrungen die sie mir mit dem Aufenthalt am CERN, durch Konferenzbesuche und den Besuch von Sommerschulen ermöglicht hat.
- Prof. Dr. Martin Fässler für die schnelle Zusage in meiner Promotionskommission mitzuwirken und das Zweitgutachten zu verfassen.
- Den weiteren Mitgliedern meiner Promotionskommission, Prof. Dr. Gerhard Buchalla, Prof. Dr. Thomas Kuhr und Prof. Dr. Jochen Weller, für ihre prompten Zusagen und auch für ihre Mitwirkung bei der Erlangung meines Doktorgrads.
- Dr. Alexander Mann für die großartige Zusammenarbeit, dafür, dass er mir immer mit Rat und Tat zur Seite stand, für all die ausgiebigen Diskussionen, für seine unendliche Geduld, für das Korrekturlesen dieser Arbeit und vor allem für alles was ich vergessen habe zu erwähnen.
- Dr. Christoph A. Weber für all die stundenlangen Diskussionen während meiner Masterarbeit, seine unendliche Geduld, die vielen nützlichen Ratschläge und auch für alles was ich vergessen habe.
- Balthasar Maria Schachtner dafür, dass er es so lange alleine mit mir in einem Büro ausgehalten, aber auch für all die guten Vorschläge zu meinem Code und dafür, dass mein Software-Framework durch dich weiter gepflegt wird.
- allen "Mensa-Mitläufern", denn alleine essen macht dick und ist nicht so spaßig.
- allen aktiven und ehemaligen Mitgliedern des Lehrstuhls Schaile für die vielen guten Diskussionen, für die Hilfsbereitschaft, für die tolle Zeit und auch das super Arbeitsklima.
- meiner Mutter, meinem Vater und meinen Geschwistern, dafür dass sie mich immer unterstützen und immer für mich da sind, egal was passiert.
- meine Tochter Emily die immer ein Lächeln auf den Lippen hat und jeden einzelnen Tag nur noch unvergesslicher macht. Sie lässt in Windeseile alle Sorgen und Probleme vergessen sein.
- meine Frau Andrea die mir während der stressigen Zeiten immer den Rücken frei gehalten hat, für Ihre moralische Unterstützung während meiner Promotion und vor allem für deine Liebe! Danke für alles mein Schatz!